eman ta zabal zazu

Universidad del País Vasco
Euskal Herriko Unibertsitatea

NAZIOARTEKO BIKAINTASUN CAMPUSA
CAMPUS DE EXCELENCIA INTERNACIONAL

# Quantum simulation of two-dimensional electronic lattices

**Candidate's name:**

Miguel Ángel Jiménez Herrera

**Supervisors:**

Dr. Dario Bercioux

&

Dr. Aitzol García-Etxarri

Theoretical Study of Structural and Electronic Properties of Nanostructures

2024

# Resumen

Las redes bidimensionales son arreglos periódicos de puntos en el plano. Cuando colocamos especies atomicas en esos puntos, hablamos de redes bidimensionales electrónicas, o cristales bidimensionales. Las redes electrónicas bidimensionales han desempeñado un papel crucial en el desarrollo de la física de la materia condensada moderna y en el estudio de materiales con interesantes propiedades electrónicas. El estudio de las redes electrónicas bidimensionales es actualmente un área activa de investigación, con descubrimientos en curso en el campo de los aislantes topológicos, el efecto Hall cuántico de espín y otros fenómenos electrónicos intrigantes. Uno de los aspectos intrigantes de las redes electrónicas bidimensionales es su conexión con el campo de la topología, que describimos en las siguiente lineas.

En este contexto, la topología se refiere al estudio de las propiedades que permanecen inalteradas bajo deformaciones continuas. Las estructuras de bandas electrónicas en dos dimensiones pueden tener carácter topológico, lo que conduce a la aparición de fenómenos intrigantes como el efecto Hall cuántico y los aislantes topológicos. La topología de los estados electrónicos en estos materiales da lugar a comportamientos exóticos, como estados de borde protegidos topológicamente y propiedades de transporte electrónico robustas. Esta robustez es particularmente intrigante porque es insensible a las perturbaciones locales, lo que hace que estos materiales sean potencialmente valiosos para aplicaciones en computación cuántica y espintrónica.

Comenzamos con el Capítulo 1, con una breve introducción presentando el estado del arte de los temas que tratamos en esta tesis. A continuación, pasamos al Capítulo 2, donde desarrollamos todos los antecedentes teóricos. Este capítulo sirve para establecer la notación que hemos utilizado a lo largo de todo el documento. Dentro de este capítulo, tratamos temas como la ecuación de Schrödinger para una función de onda electrónica en presencia de un potencial bidimensional. Usando esto como base, empezamos a construir los diferentes métodos que podemos usar para aproximarnos al problema de la física de los electrones en dos dimensiones.

En primer lugar, introducimos el método de expansión en ondas planas que nos permitirá comprender la simulación de redes bidimensionales de forma sintética. La principal motivación es el hecho de que algunas redes electrónicas bidimensionales no existen en la naturaleza, ya que no son químicamente estables. Por este motivo, se necesitan técnicas de simulación cuántica para

comprender la física que subyace a las redes bidimensionales y hacer realidad estos sistemas con experimentos en el laboratorio. Entre las numerosas plataformas de simulación cuántica disponibles en la actualidad, cabe destacar el simulador cuántico de CO/Cu(111). Esta plataforma consiste en manipular moléculas de CO utilizando la punta de un microscopio de barrido de efecto túnel, creando pozos de potencial que presentan niveles de energía imitando orbitales atómicos.

Otra posible aproximación al estudio de las propiedades espectrales de las redes electrónicas es el uso del método de enlace fuerte. Esta potente herramienta, bastante sencilla, permite reproducir fácilmente a bajas energías la física de los electrones que se mueven de un sitio de la red a otro. En este sentido, podemos hablar de amplitudes de salto entre los sitios de vecinos con diferentes ordenes de cercanía. Diagonalizando el Hamiltoniano de enlace fuerte, que se escribe como la matriz de conectividad entre los diferentes orbitales atómicos, se puede tener acceso a la dispersión de energía de los electrones que se mueven dentro de una determinada red.

Evidentemente, este Hamiltoniano de enlace fuerte está estrechamente relacionado con las simetrías de la red, ya que dichas simetrías rigen la conectividad de la propia red. En todo momento, se puede establecer un modelo de enlace fuerte que proporcione ciertas predicciones sobre el espectro de energía de cualquier red. Hablamos de predicciones porque los Hamiltonianos de enlace fuerte actúan como modelos juguete y, ajustando los parámetros, podemos reproducir los resultados experimentales con gran precisión. Finalmente, este ajuste puede realizarse mediante técnicas de minimización, lo que permite reproducir los resultados del simulador cuántico con un modelo simple de enlace fuerte. En el caso del simulador cuántico, las amplitudes están relacionadas con las interacciones entre las estructuras que imitan los sitios de la red y los orbitales atómicos.

Al diagonalizar el Hamiltoniano de enlace fuerte, se pueden estudiar sus vectores propios, que son la clave para el siguiente tema: la topología. La topología desempeña un papel crucial en el campo de la simulación cuántica electrónica y los modelos de enlace fuerte. Como hemos afirmado antes, el simulador cuántico electrónico basado en el CO/Cu(111) está profundamente conectado con las simetrías cristalinas de la red que se simula. La conexión entre topología y simetrías cristalinas se introdujo en el formalismo de la química cuántica topológica [1]. Esta teoría establece una conexión directa y biyectiva entre las características topológicas de una estructura de bandas y la distribución en el espacio real de los orbitales atómicos en términos de objetos matemáticos llamados representaciones de banda del grupo espacial. Dado que tanto el conjunto de todos los grupos espaciales como el número de representaciones de banda es finito, pueden calcularse todas las configuraciones posibles. Todas estas configuraciones posibles están tabuladas en el Servidor Cristalográfico de Bilbao.

En este sentido, la biyección se realiza en los siguientes términos: un conjunto de orbitales atómicos bajo la periodicidad de un determinado grupo espacial da lugar a una estructura de bandas con determinadas propiedades de simetría (ya presentes en el Servidor Cristalográfico de Bilbao), y viceversa. Por el contrario, si una estructura de bandas posee propiedades de simetría que no se encuentran en el Cristalográfico de Bilbao, se debe a su carácter topológico.

La presencia de un bulk topológico está relacionada con la aparición de estados límite que son robustos frente a la dispersión cuando el sistema se corta en una muestra de tamaño finito. Se trata de la correspondencia entre bulk y la frontera de los aislantes topológicos, por la que los modos de frontera son robustos frente a perturbaciones debidas a la protección topológica. Una red bidimensional, cuando se estudia en una muestra de tamaño finito, puede mostrar dos tipos diferentes de fronteras: bordes, cuya dimensión es 1, y esquinas, con dimensión 0. Por lo tanto, un aislante topológico puede tener, al menos, modos de borde con protección topológica. Si el aislante topológico muestra también modos de esquina, nos referiremos a él como un aislante topológico de orden superior. Este orden se define en términos de la diferencia entre las dimensiones del bulk y la dimensión del modo de borde.

Por estas razones, decidimos aplicar el formalismo de simulación cuántica a un red bidimensional que presenta interesantes características topológicas asociadas a la presencia de modos de frontera de orden superior localizados en las esquinas de una muestra de tamaño finito. Este es el caso de la red kagome, una red bidimensional construida a partir de una red triangular con una base de tres átomos. Cuando esta red está sometida a una distorsión aplicada a las integrales de solapamiento entre orbitales, la red presenta dos fases diferentes. En el bulk, cada fase se caracteriza por el valor de la polarización eléctrica, un invariante topológico relacionado con el desplazamiento de la carga negativa con respecto al centro de carga positiva. Además, estas dos fases presentan el mismo espectro; por lo tanto, no se puede distinguir entre ellas simplemente comprobando las propiedades espectrales.

Sin embargo, las propiedades espectrales de una muestra de tamaño finito cambian entre las dos fases. Más concretamente, una de las fases muestra estados dentro del gap energético localizados en las esquinas de la muestra, lo que ha desconcertado a la comunidad científica, ya que se pensaba que los modos de las esquinas eran consecuencia de un bulk topológico de orden superior.

El trabajo que se presenta en el capítulo 3 está relacionado con la caracterización de la topología de la red de kagome tanto en el bulk como en una muestra de tamaño finito. En el bulk, caracterizamos la red kagome en términos de invariantes topológicos y argumentos de teoría de grupos basados en la formulación de la química cuántica topológica. Los invariantes topológicos revelan que el bulk no

presenta ninguna topología robusta, por lo que concluimos que en términos de la correspondencia bulk-frontera, los estados de esquina no están relacionados con la topología del bulk. Además, complementamos estos resultados con los proporcionados por la aplicación de la teoría de grupos y la química cuántica topológica. Los resultados obtenidos arrojan las mismas conclusiones: la topología del bulk en las dos fases corresponde a dos límites atómicos diferentes conectados a través del cierre del gap energético, cada uno con una representación de banda bien definida. Por lo tanto, estos dos límites atómicos no están conectados adiabáticamente, por lo que corresponden a dos fases diferentes, cada una caracterizada por un valor diferente de la polarización del bulk.

En el caso de la muestra de tamaño finito, añadimos integrales de solapamiento de mayor alcance que preservan o rompen ciertas simetrías, y estudiamos los efectos que estos términos tienen sobre el espectro. Observamos que estas perturbaciones desplazan los estados dentro del gap energético a las bandas del bulk, y concluimos que las integrales de solapamiento que respetan las simetrías y la conectividad de la red, generalizados hasta cualquier orden de vecinos más próximos, preservan los modos de esquina en el gap energético. Por tanto, la protección de esos modos de esquina está relacionada con las simetrías y la conectividad y no se debe a una protección topológica.

El capítulo 4 está dedicado al estudio de una red bidimensional que presenta propiedades espectrales muy interesantes, todas ellas enraizadas en las simetrías de la red. Algunos grupos espaciales, llamados no simórficos, contienen ciertos elementos que implican traslaciones fraccionarias a lo largo de los vectores directos de la red. Estos elementos de simetría tienen consecuencias muy interesantes en el espectro de la red, como pliegues en las bandas con cruces dentro de los límites de la primera zona de Brillouin que están protegidos contra la hibridación. Utilizando un Hamiltoniano de enlace fuerte, utilizamos integrales de solapamiento entre vecinos más cercanos para describir el espectro de la red, denominado red en espiga, o *herringbone lattice*, en inglés.

Entre las diferentes características que muestra el espectro, encontramos un par de conos de Dirac fijados en posiciones dentro del camino de alta simetría. La investigación llevada a cabo en este capítulo trata sobre los diferentes efectos que la ruptura de las simetrías tiene sobre las propiedades espectrales de la red, tanto en el bulk como en geometrías en forma de cinta. La ruptura de las simetrías se realiza, en primer lugar, cambiando las energías de los sitios de la red. En este sentido, se preserva la conectividad de la red y, simplemente aplicando diferentes potenciales, somos capaces de mover los conos de Dirac a través de la primera zona de Brillouin e incluso fusionarlos formando semi-conos Dirac, donde la dispersión cambia de lineal a parabólica a medida que rodeamos el cono, o semi-conos de Dirac desplegados, que pueden considerarse como una línea

nodal enre dos bandas más un semi-cono de Dirac. Todos estos resultados obtenidos en el bulk se proyectan en las geometrías en forma de cinta, donde hemos elegido los vectores de la red para definir los bordes de las mismas.

Un enfoque diferente para la ruptura de las simetrías es una técnica de distorsión aplicada a las integrales de solapamiento, como la que introdujimos anteriormente en el capítulo 3 en la red kagome. Sin embargo, la distorsión aplicada a esta red es un poco diferente a la aplicada en el entramado kagome, y está relacionada con la distinción entre orientaciones horizontales/verticales de las integrales de solapamiento. utilizando esta distorsión, somos capaces de mover los conos fuera del camino de alta simetría. Más concretamente, los conos describen una trayectoria cuasi-hiperbólica dentro de la primera zona de Brillouin, y se funden en semi-conos de Dirac en las esquinas de la misma.

Finalmente, presentamos una generalización de todas las perturbaciones aplicadas a la red, además de una posible implementación de la red en espiga en el CO/Cu(111). Una vez caracterizados los efectos que las distintas simetrías tienen en el espectro, encontramos que la propuesta puede incluir una cierta dimerización al quedar los conos fuera del camino de alta simetría.

En el último capítulo presentamos el concepto de topología frágil. Como introdujimos anteriormente, la topología no trivial del bulk de una red tiene sus consecuencias en las fronteras del sistema. Al mismo tiempo, las propiedades de simetría de una estructura de bandas topológica no están relacionadas con ninguna combinación de representaciones de bandas. En general, las propiedades topológicas se denominan robustas ya que los invariantes topológicos sólo cambian cuando se produce un proceso no adiabático en el sistema,*i. e.*, el cierre del gap energetico. Sin embargo, en dos dimensiones, sin acoplamiento espín-órbita y preservando la simetría de inversión temporal, todavía podemos encontrar cierta topología que parece ser frágil bajo la adición de grados de libertad triviales. Esta es una característica bastante interesante ya que el diagnóstico de esta topología se realiza a través de los mismos invariantes, tanto topológicos como los basados en las simetrías.

El modelo que presentamos se basa en la red kagome con un orbital extra que forma una red triangular. Tras estudiar el espectro utilizando un modelo de enlace fuerte con integrales de solapamiento tanto a primeros como a segundos vecinos, encontramos un conjunto de dos bandas intermedias separadas del resto. A continuación, aplicando invariantes topológicos y química cuántica topológica, verificamos que estas dos bandas son efectivamente frágiles: la topología se rompe tras la adición de grados de libertad triviales.

Terminamos este capítulo con una propuesta de la red en la plataforma de simulación cuántica CO/Cu(111). En esta ocasión, mostramos varias propuestas que pueden dar lugar a una fase frágil. Aplicando invariantes topológicos, verificamos que la propuesta sí respeta la topología frágil de la red.

Finalmente, como conclusión, esperamos que esta tesis ayude a la comprensión de las redes bidimensionales a través de un discurso claro y directo, a través del compendio de redes que hemos estudiado en profundidad y trasladado a una plataforma de simulación cuántica.

# Abstract

Two-dimensional lattices are periodic arrangements of points in the Euclidean plane. When those points are populated with atomic species, one can talk about two-dimensional atomic crystals, where the gas of electrons is delocalized across the whole lattice. For this reason, they are usually called two-dimensional electronic lattices, which have played a crucial role in the development of modern condensed matter physics and in the study of novel materials. The study of two-dimensional electronic lattices is currently an active area of research, with ongoing discoveries in the field of topological insulators, quantum spin Hall effect, and other intriguing electronic phenomena. One of the intriguing aspects of two-dimensional electronic lattices is their connection to the field of topology.

In this context, topology refers to the study of properties that remain unchanged under continuous deformations. Electronic band structures in two dimensions can be topologically classified, leading to the emergence of intriguing phenomena such as the quantum Hall effect and topological insulators. The topology of electronic states in these materials gives rise to exotic behaviors, such as protected edge states and robust electronic transport properties. This robustness is particularly intriguing because it is insensitive to local perturbations, making these materials potentially valuable for applications in quantum computing and spintronics.

We begin this thesis with a brief introduction and state-of-the-art of the topics that we cover in Chapter 1. Next, we move on to Chapter 2, where all the theoretical background is developed. At the same time, this chapter serves to establish the notation we have used throughout the whole document. Within this Chapter, we cover topics like the Schrödinger equation for an electronic wavefunction in the presence of a two-dimensional periodic potential. Using this as a basis, we start building the different methods we can use to approach the problem of the energy physics of electrons in two dimensions.

In the first place, we introduce the plane-wave expansion method that will allow us to comprehend the solution to the energy spectrum of two-dimensional electron gases under the action of periodic potentials. in particular, we are interested in a certain kind of potentials that mimic the shape of two-dimensional lattices. The main motivation is the fact that some two-dimensional electronic lattices do not exist in nature since they are not chemically stable. For this reason, quantum

simulating techniques are required to understand the physics underneath two-dimensional lattices and to realize these systems with tabletop experiments. Among the many quantum simulation platforms currently available, a noteworthy example is the CO/Cu(111) quantum simulator. This platform involves manipulating CO molecules using the tip of a scanning tunneling microscope, creating potential wells that exhibit energy levels mimicking atomic orbitals.

Another possible approach to the study of the spectral properties of electronic lattices is the use of the tight-binding method. This powerful, rather simple tool allows one to easily reproduce the low-energy profile of electrons hopping from one lattice site to another. In this sense, we can talk about hopping amplitudes between nearest, next-to-nearest, etc, neighboring lattice sites. By diagonalizing the tight-binding Hamiltonian, which is written as the connectivity matrix between the different atomic orbitals, one can have access to the energy dispersion of the electrons moving inside a certain lattice.

Clearly, this tight-binding Hamiltonian is closely related to the symmetries of the lattice, since those symmetries rule the connectivity of the lattice itself. At all times, one can always establish a tight-binding model providing certain predictions about the energy spectrum of any lattice. We talk about predictions since the tight-binding Hamiltonians act as toy models, and by tuning the hopping amplitudes, we can reproduce the experimental results with high accuracy. Finally, this tuning can be done by fitting techniques, which allows the reproduction of the quantum simulated results with a simple tight-binding model. In the case of the quantum simulator, hopping amplitudes are related to the interactions between the engineered atomic-like structures, mimicking the lattice sites and atomic orbitals.

By diagonalizing the tight-binding Hamiltonian, one can study its eigenvectors, which are the key to the next topic: topology. Topology plays a crucial role in the field of quantum materials, and in particular in electronic quantum simulation and tight-binding models. As we have claimed before, the electronic quantum simulator based on the CO/Cu(111) is deeply connected with the crystalline symmetries of the lattice being simulated. The connection between topology and crystalline symmetries was introduced in the topological quantum formalism [1]. This theory establishes both a straightforward and bijective connection between the topological features of a band structure and the real space distribution of the atomic orbitals in terms of mathematical objects called band representations of the space group. Since both the set of all space groups and the number of band representations is finite, all the possible configurations can be calculated. All these possible configurations are tabulated in the Bilbao Crystallographic Server.

In this sense, the bijection is done in the following terms: a set of atomic orbitals under the

periodicity of a certain space group gives rise to a band structure with certain symmetry properties already present in the Bilbao Crystallographic server, and vice-versa. On the contrary, if a band structure possesses symmetry properties that cannot be found in the Bilbao Crystallographic, it is due to its topological character.

The presence of a topological bulk is connected with the appearance of boundary states that are robust against back-scattering when the system is cut into a finite-size sample. This is the bulk-boundary correspondence of topological insulators, by which boundary modes are robust against perturbations due to topological protection. A two-dimensional lattice, when cut from the bulk, it may display two different types of boundaries: edges, whose dimension is 1, and corners, with dimension 0. Hence, a topological insulator may have, at least, edge modes with topological protection. If the topological insulator shows as well corner modes, we will refer to it as a higher-order topological insulator. This order is defined in terms of the difference between the dimensions of the bulk and the dimension of the boundary mode.

For these reasons, we decided to apply the quantum-simulation formalism to a two-dimensional lattice that presents interesting topological features associated with the presence of higher-order boundary modes localized in the corners of a finite-size flake. This is the case of the *breathing* kagome lattice, a two-dimensional lattice built from a triangular lattice plus a set of three atoms under a breathing distortion applied to the hopping amplitudes. The breathing distortion is controlled through a parameter that increases and decreases the hopping amplitude between neighboring lattice sites. When this lattice is under a breathing distortion applied to the hoppings, the lattice presents two different phases. In the bulk, each phase is characterized by the value of the bulk polarization, a topological invariant that is related to the displacement of the negative charge with respect to the positive charge center. Additionally, these two phases display the same spectrum; hence, one cannot distinguish between them just by checking the spectral properties.

However, the spectral properties of a finite-size flake do change between the two phases. More specifically, one of the phases displays in-gap states localized in the corners of the flake, which puzzled the scientific community since the corner modes were thought to be the consequence of a higher-order topological order.

The work presented in Chapter 3 is related to the characterization of the topology of the breathing kagome lattice both in the bulk and in the finite size flake. In the bulk, we characterize the breathing kagome lattice in terms of topological invariants and group theory arguments based on the topological quantum chemistry formulation. The topological invariants reveal that the bulk does not present any robust topology, so we conclude that in terms of the bulk-boundary correspondence, the

corner states are not related to the bulk topology. Additionally, we complement these results with the ones provided by the application of group theory and topological quantum chemistry. The results obtained yield the same conclusions: the topology of the bulk in the two phases corresponds to two different atomic limits connected through the closing of the energy gap, each with a well-defined band representation. Hence, these two atomic limits are not connected adiabatically, and thus they correspond to two different phases, each characterized by a different value of the bulk polarization.

In the case of the finite-size flake, we add long-range hoppings that preserve or break certain symmetries of the flake and study the effects on the spectrum. We observe that these perturbations move the in-gap states into the bulk bands, and conclude that hoppings that respect the symmetries and connectivity of the lattice, generalised up to any order of next-nearest neighbors, preserve the corner modes in the gap. Hence, the protection of those corner modes is related to the symmetries and connectivity and not due to topological protection.

Chapter 4 is devoted to the study of a two-dimensional lattice that presents very interesting spectral properties, which are all rooted in the symmetries of the lattice. Some space groups, called non-symmorphic, contain certain elements that involve fractional translations along the direct lattice vectors. These symmetry elements have very interesting consequences in the spectrum of the lattice, as band-foldings with crossings inside the first Brillouin zone boundaries that are protected against hybridization. From a tight-binding perspective, we use the easiest nearest-neighbor Hamiltonian to describe the spectrum of the lattice, called the herringbone lattice.

Among the different features the spectrum displays, we find a pair of Dirac cones pinned at positions inside the high-symmetry path. The research carried out in this Chapter covers the different effects that the breaking of the symmetries have on the spectral properties of the lattice, both in the bulk and in ribbon geometries. The breaking of the symmetries is first done by tuning the onsite energies of the lattice sites. In this sense, the connectivity of the lattice is preserved and just by applying different onsite potentials, we are able to gap the Dirac cones, move them across the first Brillouin zone, and even merge them into very interesting spectral features: semi-Dirac cones, where the dispersion changes from linear to parabolic as we go around the cone, or unfolded semi-Dirac cone, which can be thought of as a nodal line plus a semi-Dirac cone. All these bulk results are projected into the ribbon geometries, where we have chosen the lattice vectors to define the edges of the ribbons.

A different approach to the breaking of the symmetries is a breathing technique, as we introduced previously in Chapter 3 in the kagome lattice. The breathing distortion applied to this lattice is a bit different to the one applied in the kagome lattice, and it is related to the distinction between

horizontal/vertical orientations of the hoppings. using this distortion, we are able to move the cones out of the high-symmetry path. More precisely, the cones describe a quasi-hyperbolic trajectory inside the first Brillouin zone, and merge into semi-Dirac cones in the corners of it.

Finally, we present a generalization of all the perturbations applied to the lattice, plus a possible implementation of the herringbone lattice in the CO/Cu(111) platform. Once we have characterized the effects that the different symmetries have in the spectrum, We find that the proposal may include a certain dimerization since the cones are out of the high-symmetry path.

In the last Chapter, we present the concept of fragile topology. As we introduced previously, the non-trivial topology of the bulk of a lattice has its consequences in the boundaries of the system. At the same time, the symmetry properties of a topological band structure are not related to any combination of band representations. In general, topological properties are called robust since topological invariants only change when an adiabatic process occurs in the system,*i. e.*, the closing of a gap. However, in two-dimensions, without spin-orbit coupling and preserving time-reversal symmetry we can still find certain topology that appears to be fragile under the addition of trivial degrees of freedom. This is a quite interesting feature since the diagnosis of this topology is done through the same invariants, both topological and symmetry-based.

The model we present is based on the kagome lattice with an extra orbital forming a triangular lattice. After studying the spectrum using a tight-binding model with both nearest and next-to-nearest hopping amplitudes, we find a set of two intermediate bands detached from the rest. Then, by applying topological invariants and topological quantum chemistry, we verify that these two bands are indeed fragile: the topology breaks down after the addition of trivial degrees of freedom.

We finish this chapter with a proposal of the lattice in the CO/Cu(111) quantum simulating platform. This time, we show several proposals that may give rise to the fragile phase. By applying topological invariants, we verify that the proposal does respect the fragile topology of the lattice.

Finally, in conclusion, we expect that this thesis helps the comprehension of two-dimensional lattices through clear and direct speech, plus the compendium of lattices that we have deeply studied and mapped into a quantum simulation platform.

# List of related publications

Publications related to this thesis:

1. **Herrera, M. A. J.**, Kempkes, S. N., de Paz, M. B., García-Etxarri, A., Swart, I., Smith, C. M., & Bercioux, D. (2022). Corner modes of the breathing kagome lattice: Origin and robustness. In Physical Review B (Vol. 105, Issue 8). American Physical Society (APS).
2. **Herrera, M. A. J.**, & Bercioux, D. (2023). Tunable Dirac points in a two-dimensional non-symmorphic wallpaper group lattice. In Communications Physics (Vol. 6, Issue 1). Springer Science and Business Media LLC.

Other publications:

1. Blanco de Paz, M., **Herrera, M. A. J.**, Arroyo Huidobro, P., Alaeian, H., Vergniory, M. G., Bradlyn, B., Giedke, G., García-Etxarri, A., & Bercioux, D. (2022). Energy density as a probe of band representations in photonic crystals. In Journal of Physics: Condensed Matter (Vol. 34, Issue 31, p. 314002). IOP Publishing.
2. Martínez-Strasser, C., **Herrera, M. A. J.**, García-Etxarri, A., Palumbo, G., Kunst, F. K., & Bercioux, D. (2023). Topological Properties of a Non-Hermitian Quasi-1D Chain with a Flat Band. In Advanced Quantum Technologies. Wiley.

# Contents

# CHAPTER 1

# Introduction

Quantum mechanics is the field of physics that comprehends the study of the building blocks of matter, the subatomic particles, and their interactions. It was developed in the 20th century, and though there is no *proof* of the quantum theory, it has proven to cover all experimental observations. One of the main claims of quantum theory is the particle/wave duality of subatomic particles, known as de Broglie's hypothesis. The proposal is that massive particles can show wave or particle nature depending on the experiment. This hypothesis was demonstrated three years later by Thomson by means of diffraction techniques [2]. At the same time, Davisson reached the same conclusion after collecting a diffraction pattern from scattered electrons using thin films [3] at Bell Labs. These two experimental milestones confirmed de Broglie's hypothesis.

Back in 1790, we found the first experiment that questioned the particle nature of, in this case, light. The experiment was developed by Young and defied Newton's conception of light as particles. There, a beam of light is shot against a screen with a double slit. Another screen collecting the light after crossing the double slit shows a diffraction pattern, characteristic of a wave's nature.

It was not until the 60's of last century that the first Young-inspired experiment with electrons was developed [4, 5]. Several years later, a group of researchers from the University of Bologna corroborated these findings [6]. Subsequent enhancements were achieved over a decade later in an experiment conducted at the Hitachi lab by Tonomura *et al.* [7].

The wave interpretation of subatomic particles is one of the pillars of the Copenhagen interpretation of quantum mechanics, and its mathematical background was developed by physicists like Erwin Schrödinger, Werner Heisenberg, or Max Born. The description of the quantum state of a quantum system is done in terms of wave functions, which are complex-valued functions of position $\mathbf{r}$ and time $t$, among other variables. The Copenhagen interpretation of the wave function claims that its square modulus describes the probability density of finding a particle at position $\mathbf{r}$ and

time $t$. The evolution of the wave function is ruled by a differential equation called the Schrödinger equation, published in 1926 [8]. The most general case is the time-dependent Schrödinger equation, which describes the time evolution of a wave function. It involves first-order derivatives in time and second-order derivatives in space. We can write that equation in terms of the Hamiltonian operator as the total energy of a quantum state according to its kinetic and potential energies. Usually, for stationary problems, one can decouple the time dependence from the spatial dependence by separation of variables. In this case, we arrive at the time-independent Schrödinger equation. This decoupling is often done assuming that the dependence in time is harmonic and/or if the Hamiltonian operator is not explicitly dependent on time. In this case, the wave functions are stationary states that are eigenstates of the Hamiltonian operator. The associated eigenvalues of the Hamiltonian are the energies of such quantum state.

In this thesis, we study the wave behavior of electrons when they are confined in a crystal, which is a set of atoms arranged periodically in space. Solid-state physics is a wide field of physics that focuses on the large-scale effects (electric conductance, resistance, etc.) and how they arise from the atomic-scale interactions. Quantum mechanics is a fundamental tool in solid-state physics since we can describe the behavior of electrons in a crystal in terms of a time-independent Schrödinger equation with a periodic potential term. More precisely, we study the electronic properties of two-dimensional crystals, where electrons are confined in the $x$, $y$ plane. A well-known two-dimensional material is graphene, a one-atom-thick layer of carbon atoms arranged in a honeycomb lattice. The unique properties of a single graphene sheet lie on the fact that the system is a two-dimensional crystal, which has sparked a wide range of potential applications for graphene in fields such as electronics, materials science, energy storage, sensors, and more. All these properties are rooted on the electronic properties of graphene, which can be described using quantum mechanics. Band theory is built around the Schrödinger equation with a periodic potential term, in the sense that the solution to such equation returns the relation of the energy of the electrons and their wave vectors. This relation is usually called dispersion relation, but in the context of solid-state physics, it is called band structure.

Band structures are the characteristic signature of the wave behavior of electrons in a periodic media, *i. e.*, crystals. Bands are separated by band gaps, regions in energy space that cannot be reached by any wave vector. Band gaps are of very much interest because they allow for a classification of materials according to the filling of the bands, in terms of the position of the chemical potential or Fermi level. The band below the Fermi level is called the valence band, and the one immediately above is called the conduction band. In this classification, we find insulators, where the Fermi level lies in a band gap (the conduction band is empty), or metals, where the

Fermi level crosses the conduction band. The case of graphene is known as semimetal, where the gap closes at a single point. In a few words, band theory gave a simple explanation of how some crystals are electric insulators, in contrast to electric conductors, even if, in both cases, electrons can move through the material. Figure 1.1 represents some of the different configurations we can find concerning the position of the Fermi level ($E_{\mathrm{F}}$) and the band structure of materials. Adapted from [9].

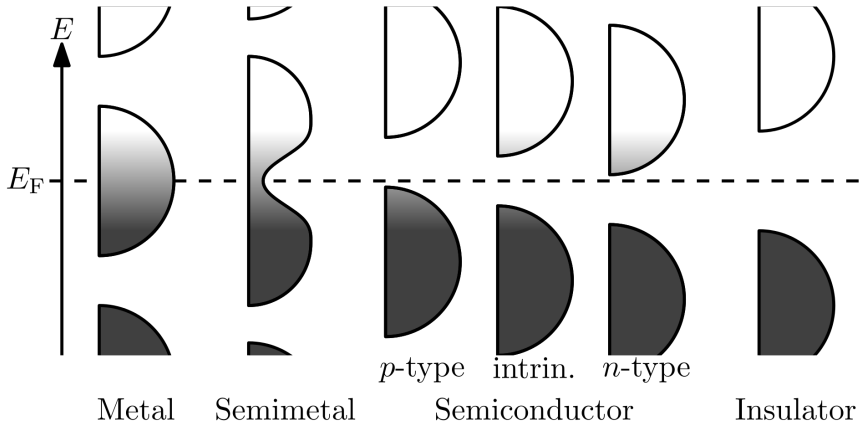


*Figure 1.1:* Distribution of the band structure in comparison with the position of the Fermi level for different materials. Adapted from [9].

However, in 1980, Klaus von Klitzing's discovery required a deeper classification of materials farther from just metallic/insulating characters. It is the case of the quantum Hall effect, by which a two-dimensional material under very strong magnetic fields and at very low temperatures shows plateaus of transverse resistivity, instead of the expected linear behavior predicted by Drude's theory. Not only Drude's theory broke down but also Landau theory about phase transitions. Here, phase transitions are detected whenever a certain order parameter characterizing the system presents discontinuities at the so-called critical points. At these critical points, some symmetries break spontaneously which changes the value of the order parameter abruptly. Back to the quantum Hall effect, these plateaus were the signature of phase transitions that Landau's theory could not describe, since no symmetry was breaking during the phase transition. A later work by Thouless *et al.* [10] related the Hall conductivity to the derivatives of wave functions of the two-dimensional electron gas, using a Kubo formula [11]. In that work, the macroscopic effect (Hall conductivity) is related to the microscopic properties of electrons (quantum mechanical wave functions). Due to the mathematical properties of the wave functions, the Hall conductivity can be written in terms of a so-called *topological* invariant, an integer-valued quantity that cannot change unless a quantum phase transition occurs. This is the birth of topological insulators, materials that present phase transitions ruled by invariants rooted in the topology of the Hilbert space spanned by the wave functions describing the system.

The prediction, study, and classification of topological materials is mostly based on computational methods to solve the Schrödinger equation. This is also the main constraint since realistic samples of materials have a huge number of atoms, requiring tremendous computational power. This sets the path for the search of new computational tools that allow for a simple but realistic description of materials. For instance, density functional theory has served as one of the most powerful tools to obtain the band structure of materials. However, density functional theory calculations are usually slow, with low accuracy at determining band gaps, making band structures less reliable. Another practical tool is the use of tight-binding methods to compute the band structure of materials. In one and two dimensions, tight-binding Hamiltonians are widely used since the complexity of those materials is lowered due to the low dimensionality of the systems. The term *toy model* comes in handy since one can *play* and modify quite easily the properties of a tight-binding model by tuning hopping terms, onsite energies, or spin-orbit coupling to the atomic positions in the lattice.

There is, however, a practical way to study one and two-dimensional materials, both experimentally and theoretically, by simulating the system in a platform that is easy to manipulate. This may give us access to all the degrees of freedom of the system, similar to a tight-binding model. This is a bottom-up approach to the study of low-dimensional systems at the atomic scale. It is the case of quantum simulators, a series of platforms where real materials are simulated by artificially designed atom-like structures. The idea to simulate quantum matter can be traced back to Richard Feynman when he gave his speech "there is plenty of room at the bottom" in 1959 and his insight to use quantum computers to calculate the properties of materials in 1982 [12]. The key contribution came in 1981 when Feynman published a paper titled "Simulating Physics with Computers" in the International Journal of Theoretical Physics[13]. In this paper, he discussed the limitations of classical computers in simulating quantum systems and proposed the idea of using a quantum computer to simulate quantum physics more efficiently.

Among the many quantum simulation platforms currently available, we want to highlight the CO/Cu(111) quantum simulator. In such platform, CO molecules are manipulated with the tip of a scanning tunneling microscope to design potential wells that show energy levels that behave as atomic orbitals. Hopping amplitudes are modeled by the interaction between these artificial atomic-like structures, and are always of long-range nature. This platform is thoroughly studied throughout this thesis. One of the many interesting features of this quantum-simulating platform is the role of crystalline symmetries in band theory and in this platform in particular. The design of the potential wells describing the artificial atoms has to be done respecting the symmetries of the lattice to be simulated. In this sense, the results that this platform produces are straightforwardly related to the symmetry properties of the lattice.

As mentioned above, this thesis is focused on the study of two-dimensional systems, together with their spectral, symmetry and topological features, and how to simulate them using the CO/Cu(111) quantum simulating platform. Hence, the outline of this thesis is as follows:

1. In **Chapter 2** we present the theoretical background for the study of two-dimensional electronic lattices, based on the Schrödinger equation and tight-binding models. Next, we discuss topological invariants and topological quantum chemistry, and apply those concepts to the Su-Schrieffer-Heeger model, a one-dimensional chain that displays very interesting topological features. We conclude by discretizing the continuum expressions for the topological invariants to be able to compute them numerically.

2. **Chapter 3** is devoted to the study of the breathing kagome lattice, a two-dimensional system that displays boundary modes in both the edges and the corners of a finite-size triangular flake. By means of topological invariants and topological quantum chemistry, we characterize the different phases of this system realized in a quantum simulating platform.

3. **Chapter 4** covers the study of the spectral properties of a non-symmorphic two-dimensional lattice called the herringbone lattice. By applying different perturbations to the bulk Hamiltonian, we are able to gap the Dirac cones characterizing the band structure, move them within the first Brillouin zone, and eventually merge them into more exotic cone-like structures, like semi-Dirac cones or unfolded semi-Dirac cones. Additionally, we study the ribbon and flake geometries in terms of the edge-projected spectral function, a relevant tool to evaluate the localization of the wave functions. Finally, a proposal for the realization of the herringbone lattice in the CO/Cu(111) quantum simulator is presented, along with the energy spectrum.

4. Finally, **Chapter 5** is focused on the study of a very interesting type of topology known as fragile topology. Contrary to robust topology, we are able to get rid of this kind of topology by the addition of trivial bands. We study a tight-binding Hamiltonian plus its realization of the CO/Cu(111) quantum simulating platform and recover the fragile character from a band structure that is not induced from atomic orbitals.

# CHAPTER 2

# Two-dimensional electronic lattices: characterization and topology

## 2.1 Introduction

This chapter is devoted to the study and characterization of electrons confined in two-dimensional lattices. Usually, this confinement is achieved by a two-dimensional potential term that is added to the single-particle free electron Hamiltonian. This potential is periodic since it is built over a two-dimensional lattice. The periodicity confers certain properties to the electronic wave functions that we will cover in this chapter. A well-known example of a two-dimensional material is graphene, a one-atom-thick layer of graphite. This material has shown to have a plethora of properties based on the fact that it is genuinely a two-dimensional material. There are plenty of other two-dimensional materials that can be found in nature; however, further in the text, we will consider "synthetic" two-dimensional lattices in a platform that is called electronic quantum simulator.

In the following sections, we introduce the notation and concepts commonly used in the study of electronic lattice physics in two dimensions. In section 2.2, we introduce the concept of two-dimensional lattices and write the Schrödinger equation for an electron confined to hop inside such lattices. Additionally, we present a different approach to the study of electronic lattice physics in two dimensions by using tight-binding models. In section 2.3, we will explain the concept of electronic quantum simulators based on the so-called muffin-tin electronic potentials, which will be essential throughout this thesis. Section 2.4 covers the idea of bulk-boundary correspondence, a crucial connection between non-trivial topological invariants and physically measurable quantities. Sections 2.5 and 2.6 are devoted to the tools used to characterize the topological phases that electronic lattices can display. Those tools are topological invariants and Topological Quantum Chemistry [14], introduced in respective sections. In section 2.7, we apply the concepts presented

in previous sections to the Su-Schrieffer-Heeger model, a one-dimensional bipartite chain that succinctly encodes quite interesting physics. In section 2.8, we show how to compute topological invariants over a discrete domain. Finally, in section 2.9, we introduce the projected spectral function, a helpful concept that will allow us to study the localization of boundary modes. This chapter has been built around the concepts of electronic band theory and adapted from several references [15, 16, 17, 18, 19, 20].

## 2.2 Electrons in two-dimensional crystals: the nearly-free electron model

This thesis is focused on the study of two-dimensional lattices. From a mathematical point of view, a lattice is an infinite discrete set of points arranged periodically in space (Bravais lattice) plus a motif placed at each of these positions [15]. Back to the example in the introduction, graphene consists of a motif of two carbon atoms connected by a covalent bond distributed over a triangular lattice. The separation between the atoms is called interatomic distance or lattice constant, represented by $a_0$. The minimal unit of periodicity in the Bravais lattice, which includes a single motif, is called unit cell. Any Bravais lattice is generated by a set of vectors called primitive or direct lattice vectors. In two dimensions, two vectors, namely $\{\mathbf{a}_1, \mathbf{a}_2\}$, define any position in the lattice as $\mathbf{R}_{m,n} = m\mathbf{a}_1 + n\mathbf{a}_2$, for $m, n$ integers describing how many copies of the direct lattice vectors conform the generic $\mathbf{R}_{m,n}$ vector. If a basis of atoms is defined by a set of $N_{\text{at}}$ positions inside the unit cell: $\tau_i$ for $i = 1, ..., N_{\text{at}}$, the most generic atomic position inside the lattice is described by a vector $\mathbf{R}_{m,n;i} = m\mathbf{a}_1 + n\mathbf{a}_2 + \tau_i$. However, from now on, the subscripts $m, n, i$ will be removed for simplicity and will be made explicit when necessary.

### 2.2.1 The Schrödinger equation in a periodic potential

The most generic way to describe the physics of electrons in two-dimensional lattices is by considering a potential $\mathcal{V}(\mathbf{r})$ that confines the electrons in the $(x, y)$ plane. A gas of electrons confined in two spatial dimensions is called a two-dimensional electron gas. The single-particle time-independent Schrödinger equation that describes the physics of a two-dimensional electron gas confined to a potential can be written as

$$\mathcal{H}\psi(\mathbf{r}) = \left(\frac{-\hbar^2}{2m_e}\nabla^2 + \mathcal{V}(\mathbf{r})\right)\psi(\mathbf{r}) = \mathcal{E}\psi(\mathbf{r}). \tag{2.1}$$

In this equation, $\mathcal{H}$ is the Hamiltonian operator, $\psi(\mathbf{r})$ is the electronic wave function, $\hbar$ is the reduced Planck's constant, $m_e$ is the electron mass, $\nabla^2$ is the Laplacian operator, $\mathcal{V}(\mathbf{r})$ represents

the potential, which is periodic according to a certain lattice periodicity, and $\mathcal{E}$ is the energy of the electron in the state described by $\psi(\mathbf{r})$.

The solution to this eigenvalue problem is a set of energies $\{\mathcal{E}_\ell\}$ (the eigenvalues of the Hamiltonian operator) and a set of eigenstates $\{\psi_\ell(\mathbf{r})\}$, labeled by an integer $\ell$. Each of the energies has either a single eigenstate associated $\psi_\ell(\mathbf{r})$ (non-degenerated eigenvalue) or a discrete set of $g$ eigenstates $\{\psi^i_\ell(\mathbf{r})\}$ for $i = 1, ..., g$ (degenerated eigenvalue of degeneracy $g$).

The fact that the potential is periodic makes the Hamiltonian operator periodic as well, and this is inherited by its eigenvalues and eigenstates. Whenever an operator is periodic, we can apply Fourier analysis and decompose it into plane waves $e^{i\mathbf{K}\cdot\mathbf{r}}$ for generic momentum $\mathbf{K}$ (or wave vector), since plane waves form a complete set of functions. However, not all plane waves yield a fair plane-wave expansion since these plane waves have to respect the periodicity of the direct lattice. Position and momentum are conjugate variables so that the periodicity of the direct lattice imposes conditions over the periodicity in momentum space. Hence, the set of all possible waves that oscillate with a wave vector that respects the periodicity of a given Bravais lattice is another Bravais lattice, called reciprocal lattice. The reciprocal lattice has the same dimensions as the real space one (the latter being called the direct lattice when studied from the reciprocal lattice perspective). This condition can be expressed as:

$$e^{i\mathbf{G}\cdot\mathbf{r}} = e^{i\mathbf{G}\cdot(\mathbf{r}+\mathbf{R})} \Rightarrow e^{i\mathbf{G}\cdot\mathbf{R}} = 1 \Rightarrow \mathbf{G}\cdot\mathbf{R} = 2\pi p \text{ for } p \in \mathbb{Z} \tag{2.2}$$

for any $\mathbf{R}$ in the Bravais lattice. The reciprocal lattice points are generated by a basis of vectors, called reciprocal lattice vectors, and labeled here by $\{\mathbf{b}_1, \mathbf{b}_2\}$. In this way, the wave vectors of a reciprocal lattice $\mathbf{G}$ can be expressed as a linear combination of the elements of the basis, such that $\mathbf{G} = p\mathbf{b}_1 + q\mathbf{b}_2$, for $p, q$ integers (same as the lattice positions in real space $\mathbf{R}_{m,n}$). The construction of the basis $\{\mathbf{b}_1, \mathbf{b}_2\}$ is done by considering that a wave vector $\mathbf{G}$ has to respect the lattice periodicity (condition in Eq. (2.2)). Substituting the linear combination $\mathbf{G} = p\mathbf{b}_1 + q\mathbf{b}_2$ in equation (2.2) and after some algebra, we find that the reciprocal lattice vectors are related to the (direct) lattice vectors via $\mathbf{a}_i \cdot \mathbf{b}_j = 2\pi\delta_{i,j}$, where $\delta_{i,j}$ is the Kronecker delta function over the indices $i, j = x, y$.

One can define the minimal unit of periodicity in the reciprocal space, called the first Brillouin zone. The first Brillouin zone is the Wigner-Seitz unit cell constructed in reciprocal space [15]. The whole reciprocal space can be decomposed into an infinite set of first Brillouin zones centered at each of the reciprocal lattice vectors $\mathbf{G}$. We label wave vectors inside the first Brillouin zone as $\mathbf{k}$ so that a generic wave vector $\mathbf{K}$ can be written as $\mathbf{K} = \mathbf{G} + \mathbf{k}$. Since, by construction, $e^{i\mathbf{G}\cdot\mathbf{R}} = 1$, the physics related to a wave vector $\mathbf{K}$ are the same as if we consider just the wave vector $\mathbf{k}$. Then, we will just consider the momenta inside the first Brillouin zone.

The wave vector $\mathbf{k}$ labels both the eigenvalues and the eigenstates. For fixed $\ell$, the eigenvalues $\mathcal{E}_\ell$ and eigenvectors $\psi_\ell(\mathbf{r})$ are functions of the momentum $\mathbf{k}$. The function $\mathcal{E}_\ell(\mathbf{k})$ is called an energy band, and the set of all bands is called band structure. We define isolated bands as energy bands that do not present any degeneracies with the rest of the bands. Band degeneracies appear when, at a certain (set of) $\mathbf{k}$ point(s), two or more bands present the same eigenvalue. Band degeneracies can occur at single $\mathbf{k}$ points, like Dirac or semi-Dirac cones, or at a set of $\mathbf{k}$ points, like nodal lines or totally degenerated bands, when the set of degeneracy points is the whole first Brillouin zone. Accordingly, we define a set of degenerated bands when a set of bands presents at least one degeneracy point. They are usually called composite groups of bands.

A generic band structure can present isolated bands, isolated composite groups of bands, or a combination of both isolated bands and composite groups. We define the energy gap $\Delta E$ as the energy difference between the maximum and the minimum of two consecutive sets of isolated bands or isolated groups of bands. When the maximum and the minimum occur at the same $\mathbf{k}$ point, the band gap is called direct. On the contrary, the band gap is called indirect.

### 2.2.2 Boundary conditions and Bloch theorem

In this section, we study the consequences of the periodicity on the eigenstates of the Hamiltonian. The Bloch theorem applies to any problem that presents periodicity. In the case of electronic wave functions, the eigenstates of the Hamiltonian can be chosen to have the form of a plane wave with wave vector $\mathbf{k}$, times a periodic function with the lattice periodicity [15], *i. e.*,

$$\psi_{\ell,\mathbf{k}}(\mathbf{r}) = \mathrm{e}^{\mathrm{i}\mathbf{k}\cdot\mathbf{r}} u_{\ell,\mathbf{k}}(\mathbf{r}). \tag{2.3}$$

We will refer to $\psi_{\ell,\mathbf{k}}(\mathbf{r})$ written in this form as the Bloch wave function or Bloch eigenstate and to $u_{\ell,\mathbf{k}}(\mathbf{r})$ as the periodic part of the Bloch eigenstate or the cell-periodic part of the wave function. The fact that the function $u_{\ell,\mathbf{k}}(\mathbf{r})$ respects the lattice periodicity is formulated as:

$$u_{\ell,\mathbf{k}}(\mathbf{r}+\mathbf{R}) \overset{\text{def}}{=} u_{\ell,\mathbf{k}}(\mathbf{r}). \tag{2.4}$$

Since the electronic wave function $\psi_{\ell,\mathbf{k}}(\mathbf{r})$ is related to the probability amplitude of finding an electron at position $\mathbf{r}$, the amplitude of the electronic wave function for momentum $\mathbf{K} = \mathbf{G} + \mathbf{k}$ is the same as the amplitude for momentum $\mathbf{k}$. This leaves gauge freedom over the phase of the wave function after the addition of a reciprocal lattice vector. The most common gauge choice is to define the Bloch wave function to be periodic in reciprocal space (periodic gauge [16]):

$$\psi_{\ell,\mathbf{k}+\mathbf{G}}(\mathbf{r}) \overset{\text{def}}{=} \psi_{\ell,\mathbf{k}}(\mathbf{r}). \tag{2.5}$$

The Bloch wave function is an eigenstate of the Hamiltonian operator presented in (2.1), periodic with the lattice periodicity. However, the cell-periodic part is an eigenstate of a *different* Hamiltonian, which depends parametrically on the wave vector $\mathbf{k}$. It can be obtained by applying the Hamiltonian (2.1) to (2.3):

$$\mathcal{H}_{\mathbf{k}} u_{\ell,\mathbf{k}}(\mathbf{r}) = \left( \frac{\hbar^2}{2m_e} \left(-i\nabla + \mathbf{k}\right)^2 + \mathcal{V}(\mathbf{r}) \right) u_{\ell,\mathbf{k}}(\mathbf{r}) = \mathcal{E}_{\ell,\mathbf{k}} u_{\ell,\mathbf{k}}(\mathbf{r}). \tag{2.6}$$

The Hamiltonian $\mathcal{H}_{\mathbf{k}}$ is defined as $\mathcal{H}_{\mathbf{k}} = \mathrm{e}^{-\mathrm{i}\mathbf{k}\cdot\mathbf{r}} \mathcal{H} \mathrm{e}^{\mathrm{i}\mathbf{k}\cdot\mathbf{r}}$. In general, an operator $O$ acting on the Bloch wave function $\psi_{\ell,\mathbf{k}}(\mathbf{r})$ can be written as an operator $O_{\mathbf{k}}$ acting on $u_{\ell,\mathbf{k}}(\mathbf{r})$ by applying such transformation:

$$O_{\mathbf{k}} = \mathrm{e}^{-\mathrm{i}\mathbf{k}\cdot\mathbf{r}} O \mathrm{e}^{\mathrm{i}\mathbf{k}\cdot\mathbf{r}}. \tag{2.7}$$

Since the electronic wave function $\psi_{\ell,\mathbf{k}}(\mathbf{r})$ is defined to be periodic in reciprocal space as presented in Eq. (2.5), the cell-periodic part $u_{\ell,\mathbf{k}}(\mathbf{r})$ presents a *twisted* boundary condition in reciprocal space as a consequence:

$$u_{\ell,\mathbf{k}+\mathbf{G}}(\mathbf{r}) = \mathrm{e}^{-\mathrm{i}\mathbf{G}\cdot\mathbf{r}} u_{\ell,\mathbf{k}}(\mathbf{r}). \tag{2.8}$$

Similarly, since the cell-periodic part of the wave function $u_{\ell,\mathbf{k}}(\mathbf{r})$ is defined to be periodic in real space as presented in Eq. (2.4), the electronic wave function $\psi_{\ell,\mathbf{k}}(\mathbf{r})$ presents a *twisted* boundary condition in real space as a consequence:

$$\psi_{\ell,\mathbf{k}}(\mathbf{r}+\mathbf{R}) = \mathrm{e}^{\mathrm{i}\mathbf{k}\cdot\mathbf{R}} \psi_{\ell,\mathbf{k}}(\mathbf{r}). \tag{2.9}$$

As a final remark, the wave vector $\mathbf{k}$ is usually called the *crystal* momentum. This naming comes from the fact that $\mathbf{k}$ is *not* the eigenvalue of the momentum operator $\hat{\mathbf{p}} = -\mathrm{i}\hbar\nabla$ when applied to the Bloch wave function:

$$\hat{\mathbf{p}} \psi_{\ell,\mathbf{k}}(\mathbf{r}) = -\mathrm{i}\hbar\nabla \left[ \mathrm{e}^{\mathrm{i}\mathbf{k}\cdot\mathbf{r}} u_{\ell,\mathbf{k}}(\mathbf{r}) \right] = \hbar\mathbf{k} \psi_{\ell,\mathbf{k}}(\mathbf{r}) - \mathrm{i}\hbar \mathrm{e}^{\mathrm{i}\mathbf{k}\cdot\mathbf{r}} \nabla u_{\ell,\mathbf{k}}(\mathbf{r}). \tag{2.10}$$

Since the extra term $-\mathrm{i}\hbar \mathrm{e}^{\mathrm{i}\mathbf{k}\cdot\mathbf{r}} \nabla u_{\ell,\mathbf{k}}(\mathbf{r})$ is not necessarily zero, $\hbar\mathbf{k}$ is not the momentum eigenvalue of the electron inside the crystal. Hence, it is called *crystal* momentum since the extra term depends on the crystal periodicity.

### 2.2.3 Born-Von Karman boundary conditions

Once we have introduced the boundary conditions that the Bloch wave function respects in both real and reciprocal space, let's present a new set of boundary conditions related to the fact that the electrons are confined inside a finite macroscopic two-dimensional crystal. Practically,

the translational invariance of the lattice is broken at the boundaries of the crystal. This affects the electronic wave function at the boundary because we cannot apply the boundary conditions presented in the previous section[1].

However, if the number of unit cells is large enough (usually of the order of Avogadro's number), the effects of the boundaries will have little impact on the properties of the electrons since they decay exponentially into the inner part of the crystal. Contrary to the boundary, we define the bulk of a crystal as a region of the crystal where the environment of the electron is practically periodic, *i. e.*, the electronic wave function behaves as if there were no trace of any boundaries. Hence, in the bulk, the boundary conditions presented in the previous section are totally fulfilled.

Mathematically, we model a finite two-dimensional crystal as a supercell formed by a finite amount of $N_1$ unit cells along $x$ and $n-2$ along $y$. Now, we repeat the supercell periodically along $x$ and $y$. We impose periodic boundary conditions in the supercell geometry. This can be expressed as:

$$\psi_{\ell,\mathbf{k}}(\mathbf{r}+N_1\mathbf{a}_1)=\psi_{\ell,\mathbf{k}}(\mathbf{r}), \tag{2.11a}$$

$$\psi_{\ell,\mathbf{k}}(\mathbf{r}+N_2\mathbf{a}_2)=\psi_{\ell,\mathbf{k}}(\mathbf{r}). \tag{2.11b}$$

These conditions are called Born-Von Karman boundary conditions and impose some restrictions over the wave vectors. In the boundary between supercells, the condition presented in Eq. (2.9) for any direction $i=x,y$ yields:

$$\psi_{\ell,\mathbf{k}}(\mathbf{r}+N_i\mathbf{a}_i)=\mathrm{e}^{\mathrm{i}N_i\mathbf{k}\cdot\mathbf{a}_i}\psi_{\ell,\mathbf{k}}(\mathbf{r}) \implies \mathrm{e}^{\mathrm{i}N_i\mathbf{k}\cdot\mathbf{a}_i}=1. \tag{2.12}$$

The momentum $\mathbf{k}$ can be written as a linear combination of the reciprocal lattice vectors as $\mathbf{k}=u_1\mathbf{b}_1+u_2\mathbf{b}_2$, for generic $(u_1,u_2)$. Hence, we define $\mathbf{q}$ to be the wave vectors that respect the Born-Von Karman periodic boundary conditions:

$$\mathbf{q}=\frac{v_1}{N_1}\mathbf{b}_1+\frac{v_2}{N_2}\mathbf{b}_2,\ \text{for } v_1,\ v_2 \text{ integers: } \begin{cases} v_1=0,\ldots,N_1-1 \\ v_2=0,\ldots,N_2-1 \end{cases}. \tag{2.13}$$

The Born-von Karman boundary conditions can be understood as if we glued together the boundaries of the two-dimensional crystal since when an electron approaches the boundary of the supercell, it enters the adjacent supercell. Since all the supercells are identical, the electron behaves as if it re-enters the crystal but on the opposite boundary.

[1]The main consequence of the breaking of the periodicity is the appearance of electronic states that can decay into the vacuum, or both into the bulk and the vacuum. These states are called Shockley states [21] or Tamm states [22], and will be described in detail further in the text.

As a final remark, the Born-von Karman boundary conditions allow us to study the propagation of electrons inside finite crystals with wave vectors that are compatible with the size of the crystal. We now present a practical application of the Born-von Karman boundary conditions and the Bloch theorem to compute the Bloch wave function.

### 2.2.4 Plane wave expansion of the Schrödinger equation

So far, we have studied how the periodicity of the potential affects the properties of the eigenstates of the Hamiltonian. We now present a practical application of the Bloch theorem, combined with the Born-von Karman boundary conditions, to compute the Bloch wave function starting from the Schrödinger equation. Once we have defined the wave vectors $\mathbf{q}$ allowed by the Born-von Karman periodic boundary conditions, we are able to expand the Bloch wave function into a set of plane waves with momentum $\mathbf{q}$, that is,

$$\psi_{\ell,\mathbf{q}}(\mathbf{r}) = \sum_{\mathbf{q}} C^{\ell}_{\mathbf{q}} e^{i\mathbf{q}\cdot\mathbf{r}}, \tag{2.14}$$

where the coefficients $C^{\ell}_{\mathbf{q}}$ are unknown and will be obtained by solving the Schrödinger equation. Accordingly, we expand the periodic potential into plane wave components $V_{\mathbf{G}}$ of the form:

$$\mathcal{V}(\mathbf{r}) = \sum_{\mathbf{G}} V_{\mathbf{G}} e^{i\mathbf{G}\cdot\mathbf{r}}, \tag{2.15a}$$

$$V_{\mathbf{G}} = \frac{1}{A_{\mathrm{UC}}} \int_{\mathrm{UC}} d\mathbf{r}\ e^{-i\mathbf{G}\cdot\mathbf{r}} \mathcal{V}(\mathbf{r}), \tag{2.15b}$$

where $\mathbf{G}$ are the reciprocal lattice vectors, UC stands for unit cell, and $\mathrm{A_{UC}}$ is the area of the unit cell.

Practically, the solution to the Schrödinger equation using the plane wave expansion is obtained by defining a set of reciprocal lattice vectors $\mathbf{G}$ with norm shorter than a cut-off length. This truncation of the expansion in Eq. (2.15a) is done since waves with long wave vectors oscillate rapidly, and thus, their contribution to the Fourier expansion can be neglected. Plugging these two expansions into the Hamiltonian in (2.1) we transform the eigenvalue problem of a continuous operator into a finite set of coupled linear equations. After some algebra, we arrive at the expression that defines the coefficients $C^{\ell}_{\mathbf{q}-\mathbf{G}}$ of the wave function at momenta $\mathbf{q} - \mathbf{G}$:

$$\left( \frac{\hbar^2 |\mathbf{q} - \mathbf{G}|^2}{2m_e} - \mathcal{E} \right) C^{\ell}_{\mathbf{q}-\mathbf{G}} + \sum_{\mathbf{G}'} V_{\mathbf{G}'-\mathbf{G}}\, C^{\ell}_{\mathbf{q}-\mathbf{G}} = 0, \tag{2.16}$$

With this procedure, we can reconstruct the expression of the Bloch wave function at each $\mathbf{q}$ and also find an analytic expression for the periodic part of the Bloch wave function under the plane-wave

expansion method:

$$\psi_{\ell,\mathbf{q}}(\mathbf{r}) = \sum_{\mathbf{G}} C^{\ell}_{\mathbf{q}-\mathbf{G}} e^{i(\mathbf{q}-\mathbf{G})\cdot\mathbf{r}} = e^{i\mathbf{q}\cdot\mathbf{r}} \left( \sum_{\mathbf{G}} C^{\ell}_{\mathbf{q}-\mathbf{G}} e^{-i\mathbf{G}\cdot\mathbf{r}} \right) = e^{i\mathbf{q}\cdot\mathbf{r}} u_{\ell,\mathbf{q}}(\mathbf{r}), \tag{2.17}$$

$$u_{\ell,\mathbf{q}}(\mathbf{r}) = \sum_{\mathbf{G}} C^{\ell}_{\mathbf{q}-\mathbf{G}} e^{-i\mathbf{G}\cdot\mathbf{r}}. \tag{2.18}$$

As we stated before, this is an approximation due to the truncation in the summation over the components of the potential. Chapters 3, 4, and 5 contain different examples where these formulas have been used to reconstruct the Bloch wave function and its periodic part.

### 2.2.5 Tight-binding Hamiltonians

So far, we have presented the Schrödinger equation and its solution in two dimensions in terms of a periodic potential. The plane-wave expansion allows the decomposition of the periodic potential in Fourier components of the reciprocal lattice vectors and the electronic wave function in the momenta allowed by the Born-von Karman periodic boundary conditions.

Now, we take a different approach to the study of periodic systems by using tight-binding Hamiltonians[1]. Instead of solving the Schrödinger equation with a periodic potential term, the main idea is to consider that the unit cell is populated by a set of $n_{\text{orb}}$ atomic orbitals at each of the $N_{\text{at}}$ atomic positions inside the unit cell. Each of these orbitals is described by a function $\phi_{\mathbf{R},i;\alpha}(\mathbf{r}) = \phi_{\alpha}(\mathbf{r} - (\mathbf{R} + \tau_i))$, where $\mathbf{R}$ labels the unit cell, $i = 1, ..., N_{\text{at}}$ labels the atomic position $\tau_i$, and $\alpha = 1, ..., n_{\text{orb}}$ labels the species of the orbital per atom. In total, there are $N_{\text{orb}} = N_{\text{at}} n_{\text{orb}}$ orbitals per unit cell. These orbitals are usually assumed to be tightly bound to the atomic nuclei, so we begin by assuming that no overlap between the orbitals exist ($s$ orbitals are the most common choice): this is why the method is called tight-binding.

We introduce the Dirac notation to write $\langle \mathbf{r} | \phi_{\mathbf{R},i;\alpha} \rangle = \phi_{\mathbf{R},i;\alpha}(\mathbf{r})$, where $\langle \mathbf{r}|$ is the bra associated to the coordinate representation and $|\phi_{\mathbf{R},i;\alpha}\rangle$ is the ket representing the orbital in the Hilbert space. The orbitals are assumed to be orthonormal such that the following relation is fulfilled:

$$\langle \phi_{\mathbf{R},i;\alpha} | \phi_{\mathbf{R}',j;\beta} \rangle = \delta_{\mathbf{R},\mathbf{R}'} \delta_{i,j} \delta_{\alpha,\beta}, \tag{2.19}$$

where $\delta_{\mathbf{R},\mathbf{R}'}$ is the Kronecker delta function over the unit cell vectors $\mathbf{R}, \mathbf{R}'$; $\delta_{i,j}$ is the Kronecker delta function over the atomic positions $\tau_i, \tau_j$, and $\delta_{\alpha,\beta}$ is the Kronecker delta function over the orbitals $\alpha, \beta$. This orthonormality relation makes the position operator block-diagonal and degenerated over

[1] Tight-binding Hamiltonians are closely related to the LCAO method, or linear combination of atomic orbitals method, used in quantum chemistry to calculate molecular orbitals.

the orbital degrees of freedom since, as we described above, there are $n_{\text{orb}}$ orbitals placed at the same $\tau_i$ position inside the unit cell. Thus, each block corresponding to the unit cell located at $\mathbf{R}$ contains $N_{\text{at}}$ blocks of dimension $n_{\text{orb}}$. Each of the $N_{\text{at}}$ blocks has position operator eigenvalue $\mathbf{R} + \tau_j$. Hence, we can write:

$$\langle \phi_{\mathbf{R},i;\alpha} | \mathbf{r} | \phi_{\mathbf{R}',j;\beta} \rangle = (\mathbf{R} + \tau_i) \delta_{\mathbf{R},\mathbf{R}'} \delta_{i,j} \delta_{\alpha,\beta}. \tag{2.20}$$

Now the Schrödinger equation comes to play: the interaction between the orbitals is mediated by the Hamiltonian operator. Its matrix elements are called hopping amplitudes, usually defined as $t_{i,\alpha;j,\beta}$:

$$t_{i,\alpha;j,\beta} = H_{i,\alpha;j,\beta}(\mathbf{R}) = \langle \phi_{\mathbf{R}',i;\alpha} | \mathcal{H} | \phi_{\mathbf{R}'+\mathbf{R},j;\beta} \rangle = \langle \phi_{\mathbf{0},i;\alpha} | \mathcal{H} | \phi_{\mathbf{R},j;\beta} \rangle, \tag{2.21}$$

where in the last step we have used the periodicity of the Hamiltonian and shifted the hopping amplitude between two generic positions $\mathbf{R}'$ and $\mathbf{R}' + \mathbf{R}$ to the unit cell labeled by $\mathbf{R} = \mathbf{0}$. The matrix element as written in Eq. (2.21) represents the hopping amplitude of an electron from the orbital $\beta$ at position $\mathbf{R} + \tau_j$ to the $\alpha$ orbital placed at atom $i$ inside the unit cell labeled by $\mathbf{R} = \mathbf{0}$.

Since the positions of the atomic orbitals inside the lattice are discrete, we classify the hopping amplitudes according to the neighborhood of each atom. We find nearest, next-to-nearest,... interactions according to the distance between the atomic positions. We define the coordination number as the number of nearest-neighboring atoms surrounding a certain atomic position. Usually, the hopping interactions are assumed to be of nearest-neighbor character, since the atomic orbitals decay exponentially with distance.

Now, we Fourier-transform the problem by constructing Bloch-like basis functions $\varphi_{\mathbf{k},i;\alpha}(\mathbf{r})$ in the form of linear combinations of the atomic orbitals:

$$\varphi_{\mathbf{k},i;\alpha}(\mathbf{r}) = \sum_{\mathbf{R}} \mathrm{e}^{\mathrm{i}\mathbf{k}\cdot(\mathbf{R}+\tau_i)} \phi_\alpha(\mathbf{r} - (\mathbf{R} + \tau_i)), \tag{2.22}$$

where $\mathbf{R}$ is summed over all the lattice vectors inside the $N_1 \times N_2$ lattice. We introduce Dirac notation to simplify the expressions:

$$\varphi_{\mathbf{k},i;\alpha}(\mathbf{r}) = \langle \mathbf{r} | \varphi_{\mathbf{k},i;\alpha} \rangle, \tag{2.23a}$$

$$|\varphi_{\mathbf{k},i;\alpha}\rangle = \sum_{\mathbf{R}} \mathrm{e}^{\mathrm{i}\mathbf{k}\cdot(\mathbf{R}+\tau_i)} |\phi_{\mathbf{R},i;\alpha}\rangle. \tag{2.23b}$$

The matrix elements of the Hamiltonian introduced in (2.21) now are $\mathbf{k}$ dependent:

$$H_{i,\alpha;j,\beta}(\mathbf{k}) = \langle \varphi_{\mathbf{k}';\alpha} | \mathcal{H} | \varphi_{\mathbf{k};\beta} \rangle = \sum_{\mathbf{R}} \mathrm{e}^{\mathrm{i}\mathbf{k}\cdot(\mathbf{R}+\tau_j-\tau_i)} H_{i,\alpha;j,\beta}(\mathbf{R}), \tag{2.24}$$

Finally, the Bloch eigenstates will be a linear combination of the basis functions:

$$|\psi_{\mathbf{k},\ell;\omega}\rangle = \sum_{l}^{N_{\text{at}}} \sum_{\omega}^{n_{\text{orb}}} C^{\ell}_{l,\omega}(\mathbf{k})|\varphi_{\mathbf{k},l;\omega}\rangle, \tag{2.25}$$

where $C^{\ell}_{l,\omega}$ are the coefficients of the expansion. Defining $C^{\ell}(\mathbf{k})$ as the $N_{\text{orb}}$-component vector containing the coefficients of the Bloch basis functions, we can calculate it by diagonalizing the matrix Hamiltonian, whose elements are given by equation (2.24):

$$H(\mathbf{k})C^{\ell}(\mathbf{k}) = E_{\ell}(\mathbf{k})C^{\ell}(\mathbf{k}). \tag{2.26}$$

With this formulation, we obtain both the eigenenergies $E_{\ell}(\mathbf{k})$ of the Hamiltonian and the coefficients of the expansion. Finally, the condition in expression (2.19) can be relaxed, allowing the orbitals to overlap, thus being non-orthogonal. This translates into adding an overlap matrix $S(\mathbf{k})$ to the right-hand side of (2.26), and the problem transforms into a generalized eigenvalue problem.

We present now a more intuitive form to write tight-binding Hamiltonians, which is to use the second quantization formalism or occupation number representation. It is widely used in many-body physics, although single-particle states can also be treated within this framework. Up to now, we have not distinguished between particles with bosonic or fermionic character since we have considered only single-particle states. In many-body physics, the bosonic and fermionic of quasiparticles nature is crucial for the description of a many-body state: permutations of indistinguishable fermionic particles change sign, contrary to bosonic ones. In addition, in the case of fermionic particles, these many-body states are formed by all possible combinations of single-particle states (Slater determinants). The usual representation of the many-body states is known as the occupation number representation, formed by an ordered list of the occupation numbers of each single-particle state.

All the possible many-body states form a basis of a generalized Hilbert space, known as Fock space. Hence, it is natural to build occupation number operators that have such basis vectors as eigenstates and the occupation number as eigenvalues. These operators are called number operators, and their properties depend on the nature of the particle: for bosonic particles, the eigenvalues of the number operator are the non-negative numbers, while for fermionic particles, Pauli's principle limits them to 0 or 1. The number operators are formed by the product of two operators, creation and annihilation operators, that respectively increase and decrease by 1 the occupation number of a state. We refer the reader to references [23, 24] for a complete introduction to many-body physics.

We focus now on the creation and annihilation operators since they are the main ingredients for the second quantization formalism we adopt for the tight-binding formulation. Since we are working with electrons, we use the general notation, where $c^{\dagger}$, $c$ denote the fermionic creation and

annihilation operators, respectively[1]. Now, the hopping amplitudes of the tight-binding Hamiltonian acquire a different interpretation: a matrix element as in Eq (2.21) is associated with the annihilation process of a particle in orbital $\beta$ at position $\mathbf{R}+\tau_j$, represented by $c_{\mathbf{R}+\tau_j,\beta}$, and the creation process of a particle in orbital $\alpha$ at position $\mathbf{0}+\tau_i$, represented by $c^\dagger_{\mathbf{0}+\tau_i,\alpha}$. Finally, the total process is represented by a number operator of the form $c^\dagger_{\mathbf{0}+\tau_i,\alpha}c_{\mathbf{R}+\tau_j,\beta}$. The total Hamiltonian contains a sum over all possible processes, thus being a sum over pairs of lattice sites.

Having introduced this formalism, we show below the tight-binding Hamiltonian built over a two-dimensional square lattice with a single $s$ orbital per unit cell, as shown in Figure 2.1a. The interatomic distance coincides with the lattice periodicity, and it is labeled as $a_0$. In a square lattice, the coordination number is 4, so each lattice site is surrounded by 4 lattice sites. Under these considerations, the expression of the Hamiltonian in the second quantization formalism under the nearest-neighbor approximation is:

$$\mathcal{H} = t\sum_{\mathbf{R}} c^\dagger_{\mathbf{R}}c_{\mathbf{R}+\mathbf{a}_1} + c^\dagger_{\mathbf{R}}c_{\mathbf{R}+\mathbf{a}_2} + \text{h.c.} = t\sum_{\langle m,n\rangle} c^\dagger_{m,n}c_{m+1,n} + c^\dagger_{m,n}c_{m,n+1} + \text{h.c.}, \tag{2.27}$$

where $t$ is the hopping amplitude, "h.c." stands for Hermitian conjugate, and $\langle\ldots\rangle$ denotes nearest neighbors. We have again used the discrete indices $m, n$ to label the unit cells along the two directions, $m$ for $\mathbf{a}_1$ and $n$ for $\mathbf{a}_2$. In order to find the energies and the eigenstates of the Hamiltonian, we apply the Fourier transform to the creation and annihilation operators since the system is periodic in both real and reciprocal space. If we denote the first Brillouin zone as FBZ, the Fourier transform of the annihilation operator, $c_{\mathbf{k}}$, is defined through:

$$c_{\mathbf{R}} = c_{m,n} = \frac{1}{\sqrt{N_1N_2}}\sum_{\mathbf{k}\in\text{FBZ}} \mathrm{e}^{\mathrm{i}\mathbf{k}\cdot\mathbf{R}_{m,n}}c_{\mathbf{k}}. \tag{2.28}$$

For the creation operator, we need to take the adjoint of the previous expression. Substituting (2.28) into the Hamiltonian in (2.27), and after some algebra, we diagonalize the Hamiltonian and obtain the energy bands or the dispersion relation of the electrons:

$$\mathcal{H}(\mathbf{k}) = \sum_{\mathbf{k}} E(\mathbf{k})c^\dagger_{\mathbf{k}}c_{\mathbf{k}} \tag{2.29a}$$

$$E(\mathbf{k}) = E(k_x,k_y) = 2t\left[\cos(k_xa_0) + \cos(k_ya_0)\right]. \tag{2.29b}$$

Equation (2.29b) represents the bulk band structure of the square lattice, composed by a single electronic band, which can be viewed as a surface in the $k_x$, $k_y$ plane. Figure 2.1c represents this

[1] In Chapters 3, 4, and 5, we have replaced the letter $c$ with the species of the orbital or the labeling of the lattice site. With this in mind, the number operator $c^\dagger_{\mathbf{0}+\tau_i,\alpha}c_{\mathbf{R}+\tau_j,\beta}$ would be written as $\alpha^\dagger_{\mathbf{0}+\tau_i}\beta_{\mathbf{R}+\tau_j}$. At all times, we use fermionic operators, although the fermionic/bosonic character is irrelevant for us since we are working under the single-particle picture.

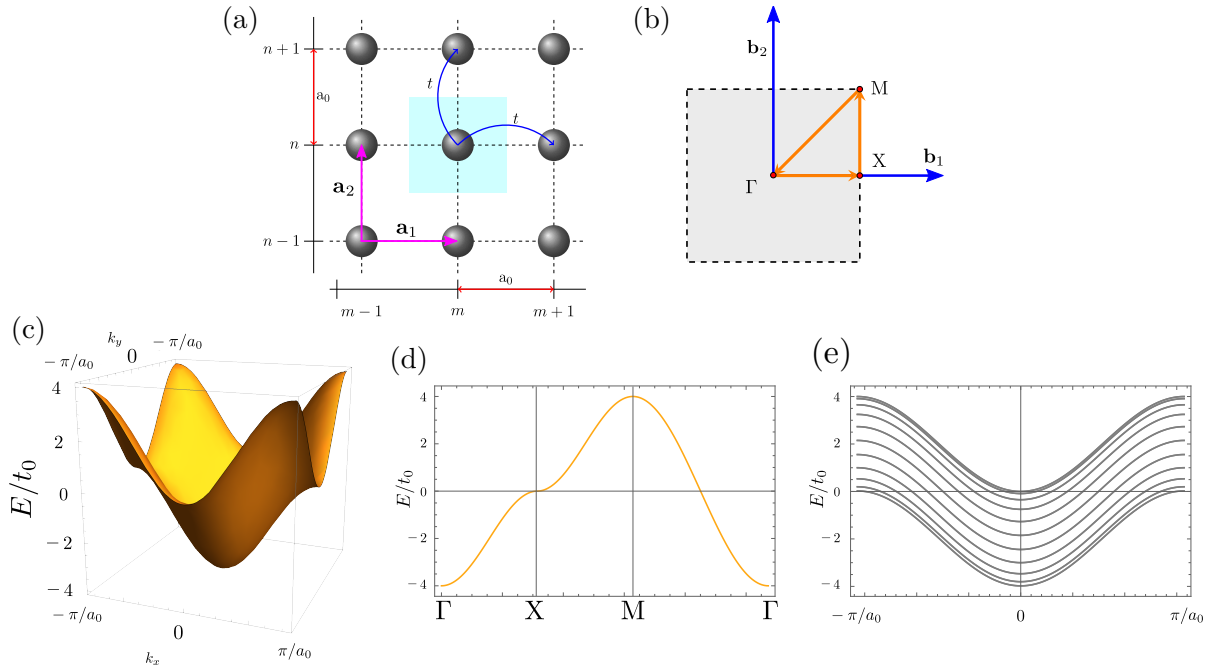


*Figure 2.1:* (a) Square lattice in real space. The pink arrows represent the direct lattice vectors, the light-blue square represents the unit cell and the interatomic distance has been made explicit in both real space directions. The blue arrows represent the possible hopping amplitudes under the nearest neighbors approximation (horizontal and vertical hopping amplitudes) (b) Reciprocal space of the square lattice, with reciprocal lattice vectors in blue and the high-symmetry path highlighted in orange. The high-symmetry points have been labeled as well according to the criteria present in the literature [25, 26, 27] (c) Overview of the band structure of the square lattice in the whole first Brillouin zone. (d) Spectrum of the square lattice along the high-symmetry path. (e) Spectrum of the square lattice ribbon when the bulk is cut along $\mathbf{a}_1$. We have taken $N_2 = 22$ units in the orthogonal direction.

band inside the first Brillouin zone. In two dimensions, the energy bands are surfaces; however, in three-dimensional crystals, three-dimensional plots of bands are difficult to represent. Instead, there is a way to plot the whole band structure by plotting the cut of such band structure along a particular path in reciprocal space. This path is called high-symmetry path and it is the boundary of a region called irreducible Brillouin zone. The corners of the irreducible Brillouin zone are certain $\mathbf{k}$ points called high-symmetry points, special $\mathbf{k}$ points inside the first Brillouin zone that present high-symmetry properties. Both high-symmetry points and irreducible Brillouin zone will be introduced properly in Sec. 2.6. For the square lattice, those high-symmetry points are:

- the Γ point, placed at the origin of the first Brillouin zone. The Γ point is unique in the first Brillouin zone, *i. e.*, there are no copies of the Γ point inside the first Brillouin zone.
- the X point, located at half of the reciprocal lattice vectors. There are four copies of the X

point inside the first Brillouin zone.

- the M point, located at half the sum of the reciprocal lattice vectors. As well, there are four copies of the M point inside the first Brillouin zone.

We show in figure 2.1b the high-symmetry path of the square lattice. The region inside the high-symmetry path is called irreducible Brillouin zone, and it is the minimal part of the first Brillouin zone that contains all the features of the band structure[1]. Finally, the plot of the band structure along the high-symmetry path is shown in figure 2.1d.

### 2.2.6 Cutting the bulk into different geometries: ribbons and flakes

In Eq. (2.28), we have introduced the Fourier transform definition we use throughout the text. Due to the periodicity of the two-dimensional lattice, this Fourier transform is done along the two real-space directions $x, y$. In this way, two-component wave vectors are necessary for the construction of such Fourier transform. In other words, since both real space directions are periodic, also the two reciprocal space directions are periodic. With this formulation, we describe the bulk-like properties of the system, where the periodicity of the direct lattice is unperturbed by the presence of boundaries. However, there are situations where the Fourier transform needs to be modified because there are systems where only one of the real space directions is periodic. The physical realization of this mathematical manipulation corresponds to cutting the bulk of the system into a finite-size sample, also known as a ribbon.

Back to the square lattice example, taking the $x$ direction to be periodic, we may introduce a one-dimensional momentum $k_x$, or simply $k$ that ranges inside the interval $[-\pi/a_0, \pi/a_0)$. This interval is the projection over the periodic direction of the two-dimensional first Brillouin zone describing the bulk of the system. The Fourier transform is applied along the direction that remains periodic after the cut (the $x$ direction):

$$c_{\mathbf{R}} = c_{R_x,R_y} = \frac{1}{\sqrt{N_1}} \sum_{k_x} \mathrm{e}^{\mathrm{i}k_x R_x} c_{k_x,R_y} \tag{2.30}$$

We fix the width of the ribbon to $N_2$ unit cells so that there are $N_2$ unit cells along the $y$ direction. The Hamiltonian in momentum space is a $k_x$-dependent matrix of order $N_2 \times N_2$, and the band structure is formed by precisely $N_2$ equally-spaced cuts of the bulk band structure in $\mathbf{k}$ space, all projected over the one-dimensional Brillouin zone. Figure 2.1e presents the band structure of the ribbon geometry with $N_2 = 22$ unit cells cut from a square lattice. There are only 11 curves in the

[1] We refer the reader to Sec. 2.6 for a deeper explanation of these concepts from a group theory perspective

plot since all of them are doubly degenerated. This is because the equally spaced cuts are symmetric, and thus, after the projection, they lie on top of each other in pairs. In Chapter 4 we present a study on the ribbon geometry of a more complex two-dimensional lattice.

Finally, if none of the spatial directions are periodic, no Fourier transform can be applied. The system corresponds to a finite-size flake cut from the bulk of the system. Assuming there are $N_1$ unit cells along $\mathbf{a}_1$ and $N_2$ along $\mathbf{a}_2$, the Hamiltonian has matrix elements given by Eq 2.21, so it is a square matrix of dimension $N_1 N_2 N_{orb}$, and it is no longer $\mathbf{k}$ dependent. In Chapters 3 and 4 we present results for flake geometries of different lattices.

### 2.2.7 Wannier functions

Up to now, we have studied the properties of two-dimensional crystals in reciprocal space in terms of Bloch wave functions or the energy dispersion, both functions of the momentum $\mathbf{k}$. Nevertheless, we can also adopt a picture where the description of the crystal is done in real space, by simply Fourier-transforming back to real space the concepts we have presented so far. Accordingly, we define the Wannier functions as the Fourier transform of the Bloch wave functions. We use the notation $W_{\ell,\mathbf{R}}(\mathbf{r}) = \langle \mathbf{r}|\ell\mathbf{R}\rangle$ to refer to the Wannier functions associated with the $\ell$-th band, same as the Bloch wave function. The $\mathbf{R}$ vector denotes the unit cell where the Wannier function is defined. We begin by presenting the single-band definition of the Wannier functions. If we denote the first Brillouin zone as FBZ, and we use a similar notation for the Bloch wave functions, namely $\psi_{\ell,\mathbf{k}}(\mathbf{r}) = \langle \mathbf{r}|\ell\mathbf{k}\rangle$, the definition of the Wannier function associated to band index $\ell$ reads:

$$|\ell\mathbf{R}\rangle = \sum_{\mathbf{k}\in \mathrm{FBZ}} \mathrm{e}^{-\mathrm{i}\mathbf{k}\cdot\mathbf{R}} |\ell\mathbf{k}\rangle. \tag{2.31}$$

Similarly to the Bloch wave functions, the Wannier functions are not unique since there is gauge freedom in the phase: we can multiply the Wannier functions by $\mathrm{e}^{\mathrm{i}\theta(\mathbf{k})}$ and the physical observables related to the transformed Wannier functions would not change. For simplicity, we have assumed $\theta(\mathbf{k}) = 0$ in Eq. (2.31).

If we work with a set of $J$ degenerated bands instead of a single band, we need a set of $J$ Wannier functions that expand the same space as the set of degenerated Bloch functions. Using $r, s$ as band indices, we can write:

$$|r\mathbf{R}\rangle = \sum_{\mathbf{k}\in \mathrm{FBZ}} \mathrm{e}^{\mathrm{i}\mathbf{k}\cdot\mathbf{R}} U_{r,s}(\mathbf{k}) |s\mathbf{k}\rangle. \tag{2.32}$$

The gauge freedom present in the single-band definition also applies to the multi-band formulation: it is encoded in the $U_{r,s}(\mathbf{k})$ matrix, which is usually called unitary mixing since it is a unitary matrix that mixes the Bloch wave functions at each $\mathbf{k}$ point.

The Wannier functions are defined to be periodic in real space, as $W_{\ell,\mathbf{R}+\mathbf{R}'}(r) = W_{\ell,\mathbf{R}}(r-\mathbf{R}')$. This means that we can simply work with a Wannier function restricted to a single unit cell, which is taken to be the origin $\mathbf{R} = \mathbf{0}$. The Wannier functions expand the same subspace as the Bloch functions from which they are built. In terms of the projection operator onto band $\ell$, $P_\ell$, we can write:

$$P_\ell = \sum_{\mathbf{k}} |\ell\mathbf{k}\rangle\langle\ell\mathbf{k}| = \sum_{\mathbf{R}} |\ell\mathbf{R}\rangle\langle\ell\mathbf{R}|. \tag{2.33}$$

Since the Bloch wave functions are extended in the reciprocal space (linear combinations of plane waves), the Wannier functions are localized in real space. This comes directly from Heisenberg principle and Fourier analysis, where a plane wave, defined to be extended (delocalized) in real space, has a well-defined wave vector, thus localized in reciprocal space. Hence, we can define the center of charge of the Wannier function associated to the $\ell$-th band, $\bar{\mathbf{r}}_{\ell\mathbf{0}}$, analogous to the center of mass of an object, as the expectation value of the position operator. For a single-band formulation:

$$\bar{\mathbf{r}}_{\ell\mathbf{0}} = \langle\ell\mathbf{0}|\hat{\mathbf{r}}|\ell\mathbf{0}\rangle, \tag{2.34}$$

while for a multi-band we have to trace over the band index. Denoting $\mathcal{J}$ the set of $J$ bands, the Wannier center is:

$$\bar{\mathbf{r}}_{\mathcal{J}\mathbf{0}} = \sum_{\ell=1}^{J} \langle\ell\mathbf{0}|\hat{\mathbf{r}}|\ell\mathbf{0}\rangle. \tag{2.35}$$

Due to translational invariance, the Wannier center of a Wannier function $|\ell\mathbf{R}\rangle$ is defined as $\bar{\mathbf{r}}_{\ell\mathbf{R}} = \bar{\mathbf{r}}_{\ell\mathbf{0}} + \mathbf{R}$. Expressions (2.34) and (2.35) are clearly gauge invariant so they may be related to any measurable quantity. In particular, the position of the Wannier center is closely related to the topological order of the system and will be used in Secs. 2.5 and 2.6.

As we have mentioned previously, the Wannier functions are localized in real space. The localization of a Wannier function can be defined as its quadratic spread, also called localization functional $\Omega\left[U_{r,s}(\mathbf{k})\right]$:

$$\Omega\left[U_{r,s}(\mathbf{k})\right] = \sum_{\ell=1}^{J} \Omega_\ell = \sum_{\ell=1}^{J} \left[\langle\ell\mathbf{0}|\hat{\mathbf{r}}^2|\ell\mathbf{0}\rangle - \bar{\mathbf{r}}_{\ell\mathbf{0}}^2\right], \tag{2.36}$$

where $\hat{\mathbf{r}}^2$ is the square of the norm of the position operator $\hat{\mathbf{r}}$. We have assumed a multi-band picture, so the total quadratic spread is the sum of the individual quadratic spreads. Due to the gauge freedom, the total quadratic spread can be minimized by finding the best unitary mixing $U_{r,s}(\mathbf{k})$ in a process described in detail in [28]. When the spread reaches a minimum, the Wannier functions are called maximally localized Wannier functions. These optimal Wannier functions are the closest to a quantum chemistry orbital, characterized for being exponentially localized at the atomic positions[1].

[1]This configuration is called atomic limit, and it will be described in Sec 2.6.

In reciprocal space, the best unitary mixing makes the Bloch wave functions as smooth as possible as a function of **k**. This equivalence (maximally localized Wannier function and smooth gauge choice for Bloch wave functions) comes from Fourier analysis and will be used throughout the text.

The existence of maximally localized Wannier functions describing a crystal is not always guaranteed [29, 30], and it is crucial for the construction of a tight-binding model. In the following sections, we will describe under which conditions such maximally localized Wannier functions can be constructed.

## 2.3 Electronic quantum simulators and muffin-tin potentials

Tight-binding Hamiltonians are a very useful tool to study the physics of electrons under the action of periodic potentials. A system that allows a description in terms of maximally localized Wannier functions can be reproduced by a tight-binding model up to any order of nearest-neighboring hoppings, since all possible Hamiltonian matrix elements (hopping amplitudes) can be built using as a basis its associated maximally localized Wannier functions.

Tight-binding models can be built over any lattice with any basis of atoms and orbitals. However, not all lattices, all atoms, or orbitals can combine to yield a description of a realistic two-dimensional electron system since a particular choice of lattice may not be stable in nature. As well, a particular choice of atoms or orbitals may not be compatible from the chemical point of view. Hence, the associated tight-binding Hamiltonians will be just toy models that will predict the physics of the electrons under that certain lattice structure, with no possible experiment that will support the tight-binding results.

However, there is a way to study electrons under the action of a periodic potential but in a platform that does not account for the number of hoppings, orbitals, or atomic species. This platform also allows a physical realization of those lattices that do not appear in nature, as if we were simulating a two-dimensional structure.

Let's suppose that we have a two-dimensional electron gas and the possibility to confine it to any potential one may desire. We could recreate the physics of graphene, for example, without having actually in the lab a layer of carbon atoms arranged in a particular way. This is precisely the main idea behind a set of experiments called electronic quantum simulators. This family of experiments is based on the fact that a two-dimensional electron gas can be confined using a potential that mimics the properties (connectivity and symmetries) of a certain lattice. Since there is freedom over the

design of such potential, any two-dimensional lattice could potentially be recreated.

Two-dimensional electron gases are naturally found in noble metals when they are cut in a certain direction. For example, when a three-dimensional piece of copper is cut along the (111) direction, the surface hosts a surface state that behaves as a two-dimensional electron gas [31]. These surface states are known as Shockley states [21] and are due to the termination of the crystal since the periodicity of the potential is broken at the surface. Figure 2.2a shows the projected band structure and the surface state of the Cu(111) surface, which appears as a parabolic dispersion in a small range of energies, and thus the electrons behave as a nearly-free two-dimensional electron gas. It has been adapted from reference [31].

The way to confine the two-dimensional electron gas is to build barriers on top of the metallic surface. These barriers are built by chemisorbing atoms (adatoms) or molecules to the surface, which act as repulsive potentials or scatterers of the electronic wave function. These scatterers can be manipulated with the tip of a scanning tunneling microscope (STM) [32, 33, 34]. The very first experiment where the tip of a STM was used to place atoms on top of a surface was the famous IBM experiment, run by Eigler and Schweizer in the late 80s, where the initialism of the IBM company was reproduced on top of a Ni(110) surface using 35 xenon atoms [35]. As well, other experiments, like quantum corrals and quantum mirages [36, 37, 38, 39] show the possibility of manipulating with atomic precision the properties of two-dimensional electron gases.

Up to now we have considered attractive potentials between the atomic nuclei and the electron gas. However, this electronic quantum simulating technique works as the particle-in-a-box experiment, where the box is actually the negative picture of the lattice we want to simulate. Then, in the framework of these electronic simulators, in order to simulate a certain lattice, one has to design the negative picture of the lattice. Usually, the negative picture of a lattice is called the dual lattice. For example, the dual lattice of the honeycomb lattice is the triangular lattice. Let's study now surface states in different media and the modeling of these potentials.

### 2.3.1 Surface states in metallic substrates

We first introduce the electronic quantum simulation platform where the substrate is the Cu(111) surface, which naturally hosts a surface state. This surface state is shown in Figure 2.2a and can be fit to a parabola, reflecting the nearly-free character of the two-dimensional electron gas:

$$E(k) = \frac{\hbar^2 k^2}{2m_e^*} + E_0, \tag{2.37}$$

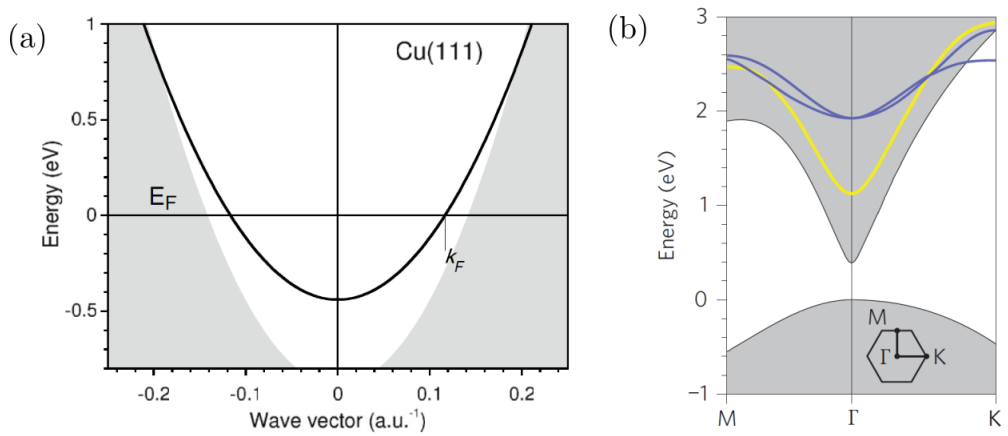


*Figure 2.2:* (a) Shockley state of the Cu(111) surface in black over projected bulk band structure, in gray. Adapted from [31]. (b) Surface band structure of the reconstructed InAs(111)$A-2\times2$. Adapted from [40].

where $k$ is the crystal momentum parallel to the (111) plane, $E_0 = -0.45\,\text{eV}$ is the onset energy, and $m_e^* = 0.42m_e$ is the effective mass of the electron in units of the bare electron mass [36, 41, 42, 43]. This substrate was used by Crommie *et al.* in the design of the quantum corral [37]. In their experiment, 48 Fe atoms confined the surface state displaying standing wave patterns, which are precisely the solution to the problem of a particle in a two-dimensional circular box – Figure 2.3a.

Instead of iron or xenon atoms, the scatterers we have worked with are CO molecules vertically chemisorbed into the substrate, with the carbon atom facing the surface [47, 48, 49, 50]. This platform – Cu(111) substrate plus CO scatterers– has been used widely in the literature, where we find experiments like molecular graphene [51], the Lieb lattice [44, 52] (see Fig. 2.3b), the kagome lattice [45, 53] (see Fig. 2.3c) or even lattices with fractal dimensions and quasicrystals [46] (see Fig. 2.3d). Each of the molecules is modeled by a cylinder of radius $a = 0.3$ nm and height $V_0 = 0.9$ eV placed at position $\mathbf{r}_\alpha$. In this way, the unit cell is populated by a set of molecules, and the potential total inside the unit cell, $V_{\text{UC}}^{\text{CO}}(\mathbf{r})$ is the superposition of all the individual potentials coming from each molecule $V_\alpha^{\text{CO}}(\mathbf{r})$:

$$V_\alpha^{\text{CO}}(\mathbf{r}) = \begin{cases} V_0 > 0 & \text{if } |\mathbf{r}-\mathbf{r}_\alpha| < a, \\ 0 & \text{otherwise} \end{cases}. \tag{2.38}$$

The full potential is the superposition of the potential created by each molecule, as in Eq (2.39):

$$V_{\text{UC}}^{\text{CO}}(\mathbf{r}) = \sum_\alpha V_\alpha^{\text{CO}}(\mathbf{r}). \tag{2.39}$$

Once the potential is defined, one solves the Schrödinger equation as we presented in Section 2.3 using the plane-wave expansion. The coefficients $V_{\mathbf{G}}^{\text{CO}}$ can be computed analytically using the

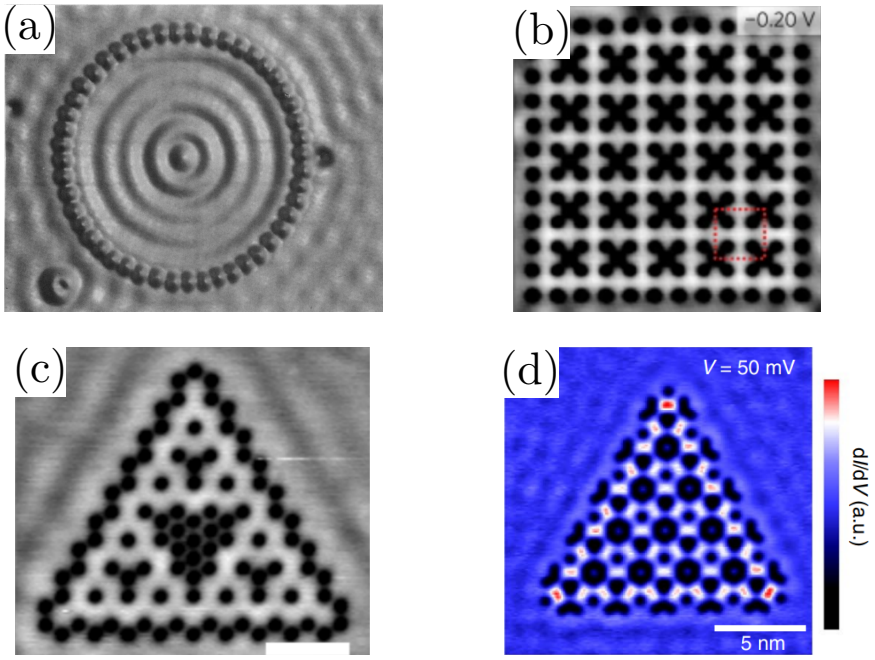


*Figure 2.3:* Set of experiments built on the Cu(111) surface. (a) Quantum corral built with 48 iron atoms on top of the Cu(111) surface. The ripples are the standing wave solutions to the particle-in-a-box problem. Adapted from [36]. (b) Local density of states of the Lieb lattice. Adapted from [44]. (c) Local density of states of the breathing kagome lattice displaying corner localized modes. Adapted from [45] (d) Local density of states of the Sierpinski lattice built on the Cu(111) substrate. Adapted from [46]..

definition in Eq. (2.15b). We obtain:

$$V_{\mathbf{G}}^{\mathrm{CO}} = \frac{2\pi V_0 a}{A_{\mathrm{UC}}|\mathbf{G}|} J_1(|\mathbf{G}|a), \tag{2.40}$$

where $A_{\mathrm{UC}}$ is the area of the unit cell, $|\mathbf{G}|$ is the norm of the wave vector $\mathbf{G}$ and $J_1(|\mathbf{G}|a)$ is the Bessel function of the first kind of order 1, evaluated on the dimensionless parameter $x = |\mathbf{G}|a$. We refer the reader to Appendix A.1 for a detailed derivation of equation (2.40).

The process of populating the unit cell depends on the purpose of the experiment, but it should include as least molecules as possible because they can be deadsorbed from the surface and leave due to temperature fluctuations [54, 55, 56, 57]. In this particular platform, the molecules are stable below 40K.

This family of experiments does not involve either atomic orbitals, species, or chemical bonds between them. The lattice sites are potential wells, and the orbitals are the energy levels of these artificial atoms [58], connected by hopping amplitudes, which are always long-range and modeled by potential wells or barriers. Further in the text, we present a guide on how to place the molecules based on symmetry arguments (see Sec. 3.6).

Nevertheless, the Cu(111)/CO platform has a drawback: the surface state, which is in the scale of 0.8 eV, is coupled to the bulk. Also, the coupling of the surface state with the bulk modes and the phonon modes, together with the presence of scatterers populating the surface (the CO molecules), results in a broadening of the signal of $\approx 80$ meV [51], by which two different states may appear as a single one (bad energy resolution). See figure 2.2a for the energy scale of this particular platform, which is usually $E_0 < E < 0.3$ eV.

### 2.3.2 Surface states in semiconductor substrates

Another possible platform that overcomes the limitations of the metallic substrate is to use the surface of a semiconductor. Here we present the indium-terminated InAs(111) surface, also called InAs(111)A in the literature. Compared to the surface state of copper, the broadening reduces to 20 meV [59, 60, 61]. This surface presents a two-dimensional electron gas, presented as the yellow parabolic band shown in Figure 2.2b (adapted from reference [40]). This surface presents a $2 \times 2$ Indium vacancy reconstruction, which can be populated with atoms like indium or cesium. These atoms donate electrons to the surface state, thus bending the band structure and pulling down the surface state to the projected band gap.

In this platform, the two-dimensional electron gas is confined using an *attractive* potential. The shape of this attractive potential can be assumed to have a Gaussian profile $\mathcal{V}^{\mathrm{In}}_{\mathrm{UC}}(\mathbf{r})$, with a certain depth ($V_0$) and full width at half maximum $d$:

$$\log_2\left(\frac{\mathcal{V}^{\mathrm{In}}_{\alpha}(\mathbf{r})}{V_0}\right) = -\frac{4|\mathbf{r}-\mathbf{r}_\alpha|^2}{d^2}, \tag{2.41a}$$

$$V^{\mathrm{In}}_{\mathrm{UC}}(\mathbf{r}) = \sum_{\alpha} V^{\mathrm{In}}_{\alpha}(\mathbf{r}), \tag{2.41b}$$

$$V^{\mathrm{In}}_{\mathbf{G}} = \frac{\pi V_0 d^2}{4A_{\mathrm{UC}}\ln 2}\exp\left(-\frac{d^2|\mathbf{G}|^2}{16\ln 2}\right). \tag{2.41c}$$

Same as in the cylindrical potential, the Schrödinger equation is expanded in plane waves. This time we use equation (2.41c) to define the components of the Gaussian potential. In this expression, $A_{\mathrm{UC}}$ is the area of the unit cell, and $|\mathbf{G}|$ is the norm of the wave vector $\mathbf{G}$. We refer the reader to Appendix A.2 for a detailed derivation of equation (2.41c).

## 2.4 Bulk-boundary correspondence

Up to now, we have described the bulk of systems, where the periodicities of the real and reciprocal spaces are translated into the electronic wave functions. We can study finite-size systems

that are cut from the bulk (see Sec. 2.2.6), like ribbons or finite-size flakes, thus displaying boundaries. In two dimensions, these boundaries can be classified into edges of dimension 1, and into corners of dimension 0. The bulk-boundary correspondence establishes a connection between the properties of the bulk and the boundaries of the system.

The Hall effect is an example of a physical phenomenon related to bulk-boundary correspondence. The classical Hall effect is the phenomenon by which an electrical conductor, under the action of a magnetic field, displays a transversal resistance (Hall resistance) proportional to the value of the applied magnetic field. However, in the 80s, von Klitzing discovered that a two-dimensional electron gas under very high magnetic fields and very low temperatures displays plateaus of quantized Hall resistance as a function of the applied magnetic field [62], contrary to the expected linear behavior. A later work by Thouless *et al.* [10] related the Hall conductivity to the derivatives of wave functions of the two-dimensional electron gas, using a Kubo formula [11]. The formulation is the following: whenever the Fermi energy lies in the gap between two Landau levels, the Hall conductivity $\sigma_{\mathrm{H}}$ of a 2DEG is quantized and can be written as:

$$\sigma_{\mathrm{H}} = \frac{\mathrm{i}e^2}{A_0\hbar} \sum_{E_\alpha < E_{\mathrm{F}}} \sum_{E_\beta > E_{\mathrm{F}}} \frac{(\partial_{k_1}\mathcal{H})_{\alpha\beta}(\partial_{k_2}\mathcal{H})_{\beta\alpha} - (\partial_{k_2}\mathcal{H})_{\alpha\beta}(\partial_{k_1}\mathcal{H})_{\beta\alpha}}{(E_\alpha - E_\beta)^2}, \tag{2.42}$$

where $e$ is the charge of the electron, $\hbar$ is the reduced Planck's constant, $A_0$ is the area of the unit cell, $\partial_{k_i}$ is the partial derivative with respect to the $k_i$ variable, where $i = 1, 2$; $\alpha, \beta$ are band indices and $E_{\mathrm{F}}$ is the value of the Fermi level. This formulation relates a physical observable (the Hall conductance) to the bulk properties of the material (derivatives of the bulk Hamiltonian). An interpretation of the quantized Hall conductance was given by Laughlin's pumping argument [63], by which a quantum of magnetic flux pumps a single electron, and thus the conductivity is quantized. Those electrons are forced to move through the edges of the system since the Fermi level lies in an energy gap where no bulk states are allowed. These conducting channels can be visualized semiclassically by the skipping orbit picture, where the cyclotron orbits of the electrons at the edges are broken, and the effective circulation of electrons in the edges of the sample is achieved. This is precisely the claim of the bulk-boundary correspondence: the number of conducting edge states in a finite-size sample of a material is related to the properties of the bulk of the system.

Topological insulators are characterized by displaying conducting boundary modes while the bulk remains in an insulating phase. The term *topological* comes from the fact that the existence of conducting boundary modes lies directly on purely mathematical concepts, namely, topological invariants, which are defined in the bulk of the system. For instance, Eq. (2.42) can be cast in such a way that the appearance of a purely topological concept is made explicit (the Berry curvature). This and other concepts will be introduced in the next section.

Finally, the quantized Hall effect is an example of a certain bulk-boundary correspondence that can be called of first order, in the sense that the difference between the dimensions of the bulk (2) and the edges (1) is 1. The difference between the dimension of the bulk and the dimension of the boundary is called the co-dimension of the boundary mode. Nevertheless, more exotic topological phases display what are called higher-order boundary modes, displaying conducting modes with co-dimension greater than one. In two dimensions, the only possible allowed higher-order topological modes are corner modes, which do not propagate. In three dimensions, first-order topological modes are surface states, while higher-order topological modes include hinge modes, which propagate along the hinges of the crystal, and corner modes, which are again non-conducting.

## 2.5 Topological Invariants

Topology is the field of mathematics that studies what transformations can be applied to a system that leave certain properties invariant. We say that such system is *robust* under those transformations. Two different systems can be topologically equivalent if they share topological properties. A typical example of this topological equivalence is represented with the mug and doughnut: these two objects are topologically identical since both share the same number of holes (formally called genus). One can continuously deform a doughnut into a mug and vice versa without changing the genus (closing or opening holes in the system).

Band theory allows a description in terms of topological invariants as well. More precisely, each band (or group of degenerated bands) can be characterized by topological invariants, which take integer values due to the internal symmetries of the system: time-reversal symmetry, chiral symmetry, or particle-hole symmetry. The full classification of materials according to these symmetries in any dimension was introduced in the ten-fold way by Altland and Zirnbauer [64, 65, 66], which was then generalized to systems with topological phases protected by crystalline symmetries, called topological crystalline insulators [67, 68, 69, 70].

In this thesis, we have used topological invariants based on the Berry connection, such as the Berry curvature, Berry phase and Chern numbers, the Wilson loop operator and its spectrum, to comprehend the topological properties.

### 2.5.1 Berry connection, Berry curvature and Chern number

The Berry connection is a mathematical object that represents the local potential associated with the non-trivial geometry of the Hilbert space spanned by the eigenvectors of a certain Hamiltonian. To define the Berry connection, the Hamiltonian has to be a function of a set of parameters $\mathcal{H}(\{\alpha_i\})$

that vary periodically, *i. e.*, after a certain period $T$, $\mathcal{H}(\{\alpha_i\} + T) = \mathcal{H}(\{\alpha_i\})$. In two-dimensional crystalline systems, we use the coordinates $\mathbf{k} = (k_x,\ k_y)$ since the Hamiltonian is a function of $\mathbf{k}$.

The parameter space is the first Brillouin zone since as we showed in Sec. 2.2.1, we can work with just the values of the crystal momentum that are restricted to the first Brillouin zone due to the periodicity of the reciprocal lattice. The first Brillouin zone can be mapped to the surface of a torus, a closed orientable surface with the shape of a doughnut represented by $\mathbb{T}^2$. This is because both $(k_x,\ k_y)$ are periodic in reciprocal space. In coordinates, we write $(k_x + 2\pi, k_y + 2\pi) = (k_x, k_y)$ (we have assumed that the lattice constant $a_0$ is unity). We can visualize this mapping from the first Brillouin zone to the torus by taking the sides of the first Brillouin zone and gluing together the line $k_y = 0$ with the line $k_y = 2\pi$. This yields a cylinder along the $k_x$ axis. If we now bend this cylinder and glue together its edges (lines described by $k_x = 0$ and $k_x = 2\pi$), we arrive at the torus. This process is described step by step in figure 2.4.

In order to detect the non-trivial geometry of the Hilbert space, we perform the (adiabatic) parallel transport of an eigenstate around a loop in the parameter space. A loop is defined as a path where the start and finish points correspond to the same locus. Figure 2.4a shows an example of a possible closed loop, labeled as $\gamma_3$. After a single turn along the loop, the eigenvectors of the Hamiltonian undergo a geometric transformation, which is reflected on a complex phase that the eigenvectors acquire after following such path [71]. This concept is called holonomy[1] and will be used further in the text. For now, we focus on the phase: it is called the Berry phase and comes from the integral of the so-called Berry connection. For a two-dimensional crystal, the single-band Berry connection can be written as:

$$\mathcal{A}_\ell(\mathbf{k}) = \mathrm{i}\langle u_\ell(\mathbf{k})|\nabla_{\mathbf{k}}|u_\ell(\mathbf{k})\rangle, \tag{2.43}$$

where $\ell$ is the band index, $\mathcal{A}_\ell(\mathbf{k})$ is the Berry connection, $|u_\ell(\mathbf{k})\rangle$ is the periodic part of the Bloch wave function associated to the $r$-th band, $\nabla_{\mathbf{k}}$ is the gradient operator in the parameter space. The Berry connection is a gauge-dependent quantity: after changing $|u'_\ell(\mathbf{k})\rangle \to \mathrm{e}^{\mathrm{i}\beta(\mathbf{k})}|u_\ell(\mathbf{k})\rangle$, where $\beta(\mathbf{k})$ is periodic and depends smoothly on $\mathbf{k}$, the single-band Berry connection transforms under $\mathcal{A}'_\ell(\mathbf{k}) = \mathcal{A}_\ell(\mathbf{k}) + \nabla_{\mathbf{k}}\beta(\mathbf{k})$.

If we are working with a set of degenerated bands, running from band indices $r$ through $s$, the multi-band Berry connection, or non-Abelian Berry connection is defined as:

$$\mathcal{A}_{r,s}(\mathbf{k}) = \mathrm{i}\langle u_r(\mathbf{k})|\nabla_{\mathbf{k}}|u_s(\mathbf{k})\rangle. \tag{2.44}$$

[1] More specifically, the Berry phase is related to the concept of anholonomy, which is the impossibility to return to the same state after parallel-transporting such state along a closed path.

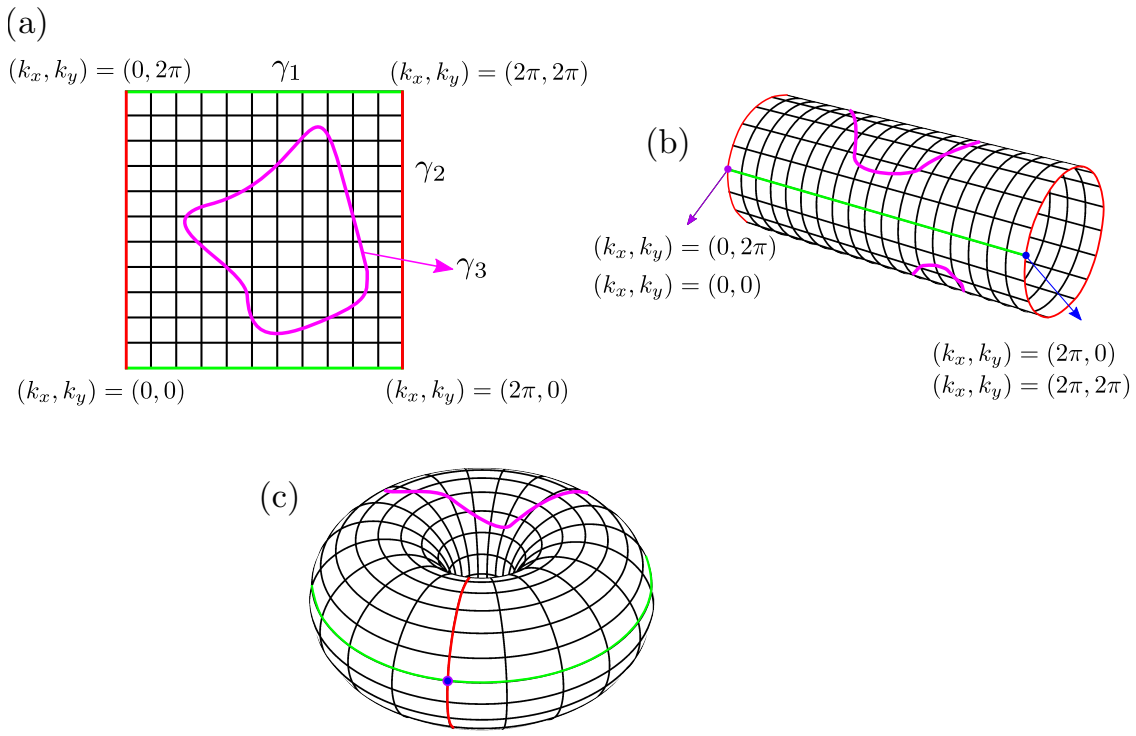


*Figure 2.4:* Mapping between the two-dimensional first Brillouin zone to the torus surface by gluing together the edges. (a) Two-dimensional Brillouin zone with its corners labeled by the values of the coordinates of the crystal momentum. The curves $\gamma_1$ and $\gamma_2$ represent non-contractible loops, while $\gamma_3$ represents a contractible one. (b) The resulting cylinder after gluing together the green edges. The purple and blue dots represent the coordinates of the crystal momentum that have the same value: $k_y = k_y + 2\pi$. (c) Torus resulting from gluing the edges of the cylinder (in red). The blue dot with purple edge represents all the corners of the two-dimensional first Brillouin zone, all mapped to the same point in the torus' surface. Coordinates have been suppressed for the sake of clarity.

In the multi-band definition, the gauge is performed via a unitary mixing of the wave functions, represented with a unitary matrix $U(\mathbf{k})$. The change in the Berry connection is $\mathcal{A}'_{r,s}(\mathbf{k}) = \mathcal{A}_{r,s}(\mathbf{k}) + U^\dagger(\mathbf{k})\nabla_{\mathbf{k}}U(\mathbf{k})$.

Conversely, the integral of the Berry connection over a closed loop is gauge invariant modulo $2\pi$. For this reason, the Berry phase is a physical quantity that can be measured. It can also be called the Zak phase in the context of band theory (often when referring to one-dimensional systems). It is computed as the integral of the Berry connection over a closed loop in reciprocal space:

$$\phi = \oint_\gamma \mathrm{Tr}\, \mathcal{A}_{r,s}(\mathbf{k}) \cdot \mathrm{d}\mathbf{k} \mod 2\pi, \tag{2.45}$$

where $\phi$ is the Berry phase associated to the set of bands spanned by indices $r, s$. The trace over the

band indices is taken since the bands are degenerate. For a single-band definition, one takes $r = s$.

One may be tempted to apply Stokes' theorem to Eq. (2.45). If so, one arrives at the definition of the Berry curvature $\mathbf{\Omega}_{r,s}(\mathbf{k})$, a gauge invariant quantity:

$$\mathbf{\Omega}_{r,s}(\mathbf{k}) = \nabla_{\mathbf{k}} \times \mathcal{A}_{r,s}(\mathbf{k}), \tag{2.46a}$$

$$\phi = \oint_{\gamma} \mathrm{Tr}\, \mathcal{A}_{r,s}(\mathbf{k}) \cdot \mathrm{d}\mathbf{k} = \mathrm{Tr} \iint_{S} \nabla_{\mathbf{k}} \times \mathcal{A}_{r,s}(\mathbf{k}) \cdot \mathbf{dS} = \iint_{S} \mathrm{Tr}\, \mathbf{\Omega}_{r,s}(\mathbf{k}) \cdot \mathbf{dS} \tag{2.46b}$$

The Berry phase can be defined as well as the flux of Berry curvature $\mathbf{\Omega}_{r,s}(\mathbf{k})$ across the surface enclosed by the closed-loop $\gamma$. In other words, the Berry curvature is the surface density of the Berry phase. Again, for the single-band case, one takes $r = s$.

Since the Berry curvature is fully gauge-invariant, there is no modulo $2\pi$ in the definition of the Berry phase, unlike in Eq. (2.45). This is because integrating the Berry curvature inside the loop forces to choose a smooth gauge everywhere, so that there is no ambiguity in the definition of the Berry phase. Contrarily, if we compute the wave function *only* along the path, the Berry phase is defined modulo $2\pi$.

Let's discuss more formally the use of Stoke's theorem in equation (2.46b). As previously mentioned, the parameter space (the two-dimensional first Brillouin zone) is topologically equivalent to a torus, a closed orientable surface. According to Stokes' theorem, the net flow of any continuous vector field integrated over such a surface must be zero. This leads to the assertion that the total Berry phase must be zero for any two-dimensional lattice: if we divide the torus into two halves along the toroidal plane, the flow across the upper half must balance the flow across the lower half, with opposite sign, resulting in a vanishing total flow. However, this statement is not always true since it only holds if the eigenstates are defined smoothly across the entire torus. Conversely, if the eigenstates are multivalued functions of the crystal momentum, it is possible for the difference between the flows across the two halves of the torus to be nonzero.

In the following, we present a proof of the non-zero valued integral of the Berry curvature. We start from the abovementioned situation: the torus is divided into two halves through the toroidal plane, $\mathcal{R}_1$ being the lower half, and $\mathcal{R}_2$ being the upper one. We define the Berry connections of the lower and upper halves to be $\mathcal{A}_1(\mathbf{k})$ and $\mathcal{A}_2(\mathbf{k})$, respectively. Each of the halves has two boundaries, the inner one (smaller circle) and the outer one (bigger circle), called respectively $\partial\mathcal{R}^{\mathrm{I}}$ and $\partial\mathcal{R}^{\mathrm{O}}$, so that the total boundary is the formal sum $\partial\mathcal{R}_i = \partial\mathcal{R}_i^{\mathrm{I}} \oplus \partial\mathcal{R}_i^{\mathrm{O}}$, where we have used $\oplus$ to denote the formal sum. We have depicted this situation in Figure 2.5, where we have shown the two halves of the torus and the boundaries introduced above. The inner boundaries have been colored in blue to

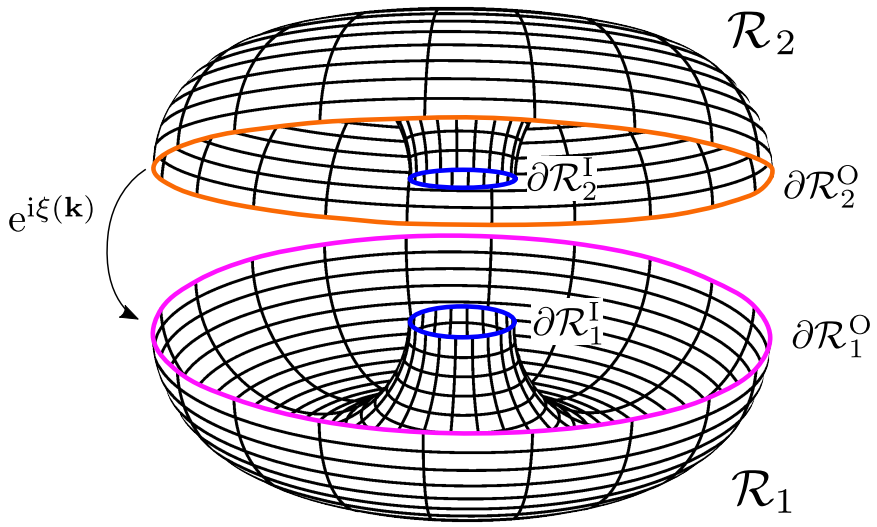


*Figure 2.5:* Torus divided into two halves with the labeling of the boundaries and the gauge connecting the eigenstates in the outer boundary.

reflect the fact that the eigenvectors are smooth across these two boundaries, while the outer ones have been colored differently to reflect the opposite. We can assume that the gauge choice makes the eigenvectors smooth across the inner boundary so that we only have to study the outer boundary. At the outer boundary, we can relate the eigenvectors by a transformation $\xi(\mathbf{k})$ such that:

$$|\psi(\partial\mathcal{R}_1^{\mathrm{O}})\rangle = e^{i\xi(\mathbf{k})}|\psi(\partial\mathcal{R}_2^{\mathrm{O}})\rangle. \tag{2.47}$$

This transformation $e^{i\xi(\mathbf{k})}$ is represented in Figure 2.5 as the difference in color between the eigenvectors in the upper half (colored in orange) and the ones in the lower half (colored in pink).

We compute the integral of the Berry curvature by splitting it into two terms since the Berry connection in one half can be related to the Berry connection in the other half via the transformation in the boundary:

$$\mathcal{A}_2(\mathbf{k}) = \mathcal{A}_1(\mathbf{k}) + \nabla_{\mathbf{k}}\xi(\mathbf{k}). \tag{2.48}$$

Hence, we can write:

$$\begin{aligned}\int \Omega(\mathbf{k}) \cdot \mathbf{dS} &= \int \mathcal{A}_1(\mathbf{k}) \cdot \mathrm{d}\mathbf{k} + \int \mathcal{A}_2(\mathbf{k}) \cdot \mathrm{d}\mathbf{k} \\ &= \int \mathcal{A}_1(\mathbf{k}) \cdot \mathrm{d}\mathbf{k} + \int (\mathcal{A}_1(\mathbf{k}) + \nabla_{\mathbf{k}}\xi(\mathbf{k})) \cdot \mathrm{d}\mathbf{k} \\ &= \int \nabla_{\mathbf{k}}\xi(\mathbf{k}) \cdot \mathrm{d}\mathbf{k} = 2\pi C,\end{aligned} \tag{2.49}$$

where $C$ is an integer, and we have used the fact that, without loss of generality, the Berry connection $\mathcal{A}_1(\mathbf{k})$ can be taken to be zero, so that $\mathcal{A}_2(\mathbf{k}) = \nabla_{\mathbf{k}}\xi(\mathbf{k})$. The final result is the winding number of the gauge choice connecting the two halves, which is restricted to integer values since it is a periodic function. This is the Chern theorem, and this integer is called the Chern number, a topological invariant associated with the manifold of eigenstates. The definition of the Chern number is:

$$C = \frac{1}{2\pi}\int_{\mathrm{FBZ}} \Omega(\mathbf{k}) \cdot \mathrm{d}\mathbf{S} \in \mathbb{Z}, \tag{2.50}$$

where FBZ stands for the first Brillouin zone. In certain cases, $C \neq 0$, and thus the wave functions are not smooth functions of the crystal momentum, so there exists a function $\xi(\mathbf{k})$ as in Eq. (2.47), that glues together the wave functions at the boundary, to make them smooth across the whole first Brillouin zone. When the Chern number of a band or a set of bands is different from zero, such set of bands is said to be *topological*. The main requirement for the Chern number to be different from zero is that time reversal symmetry ($\mathcal{T}$) is broken, for instance, using a magnetic field. The behavior of the Berry curvature under time reversal imposes $\mathcal{T}\Omega(\mathbf{k}) = -\Omega(-\mathbf{k})$. If time reversal is conserved $\mathcal{T}\Omega(\mathbf{k}) = \Omega(\mathbf{k}) = -\Omega(-\mathbf{k})$, and thus the Chern number is zero, as it is the integral of an odd function inside its domain of definition. Contrarily, if inversion symmetry ($\mathcal{I}$) is present in the system, the Berry curvature transforms as $\mathcal{I}\Omega(\mathbf{k}) = \Omega(-\mathbf{k})$. Thus if both $\mathcal{T}$ and $\mathcal{I}$ are present, the integral of the Berry curvature is zero, but because the Berry curvature is identically zero in all $\mathbf{k}$ points, since $\Omega(-\mathbf{k}) = -\Omega(-\mathbf{k})$.

As a final comment, we have seen how the quantization of the Chern number implies that there is no global gauge that makes the Bloch wave functions to behave smoothly inside the first Brillouin zone. This is quite remarkable since in Sec. 2.2.7 we mentioned that a smooth gauge choice (unitary mixing of the Bloch wave functions) is necessary to build maximally localized Wannier functions. Thus, if the Chern number is different from zero, no smooth gauge can be found, and thus no maximally localized Wannier functions can be constructed. In other words, a non-zero Chern number conforms an obstruction to the construction of a globally smooth gauge for the Bloch wave functions, and thus, it is also an obstruction to the maximal localization of the Wannier functions corresponding to the considered set of bands. This does not mean that the construction of Wannier functions is not allowed, just that the localization will be poor and not exponential as in the maximally localized case [72].

### 2.5.2 Wilson loop operator and its spectrum

Another topological marker related to the Berry connection and the Wannier center is the Wilson loop operator and its spectrum. Formally, the multi-band or non-Abelian Wilson loop operator is

defined as:

$$\hat{W}^{r,s}_{\mathbf{k+G}\leftarrow\mathbf{k}} = \mathcal{P}\,\exp\left(-\mathrm{i}\int_{\mathbf{k}}^{\mathbf{k+G}} \mathcal{A}_{r,s}(\mathbf{k})\cdot \mathrm{d}\mathbf{k}\right), \tag{2.51}$$

where $\hat{W}^{r,s}_{\mathbf{k+G}\leftarrow\mathbf{k}}$ is the Wilson loop operator, $\mathcal{A}_{r,s}(\mathbf{k})$ is the non-Abelian Berry connection, integrated from $\mathbf{k}$ to $\mathbf{k}+\mathbf{G}$. The Wilson loop operator is defined as the path-ordered ($\mathcal{P}$) integral of the Berry connection across a line of the first Brillouin zone. Due to its non-Abelian character, the path-ordered operator ensures the ordering of the integration from $\mathbf{k}$ to $\mathbf{k}+\mathbf{G}$. For a single-band definition, we take $r = s$.

We recall now the short discussion at the beginning of section 2.5.1 about the adiabatic transport of eigenstates in parameter space: the Wilson loop operator is closely related to the parallel transport theorem [71]. In a curved space, when a vector is parallel-transported along a closed loop, the ending vector presents a rotation with respect to the starting vector. In terms of wave functions, after the transport along the loop, the final state acquires a phase related to the curvature of the space. This concept is called holonomy (or anholonomy), and the Wilson loop operator describes precisely the holonomy of the Berry connection as the Berry phase associated to the path. More precisely, the eigenvalues of the Wilson loop operator are the phases acquired by each of the bands included in the calculation of Eq.(2.51) (general non-Abelian case).

In the torus, there are two different non-contractible paths. They form a basis that generates all possible non-contractible paths. The elements of this basis have been presented in Figure 2.5 as the paths $\gamma_1$ (green) and $\gamma_2$ (red). Formally, they can be described as the set of points that fulfill:

$$\gamma_1 = \{\mathbf{k}_1(t) = \mathbf{k}_0 + \mathbf{b}_1 t, t \in [0,1]\}, \tag{2.52a}$$

$$\gamma_2 = \{\mathbf{k}_2(t) = \mathbf{k}_0 + \mathbf{b}_2 t, t \in [0,1]\}, \tag{2.52b}$$

where $\mathbf{k}_0 = (k_x^0, k_y^0)$ is the origin of the path, which can be taken as a free parameter in the following way: since $\gamma_1$ is a horizontal path, it can be placed at any $k_y$, so that $\mathbf{k}_0 = (0, k_y^0)$. At the same time, $\gamma_2$ can be placed at any $k_x$ so that $\mathbf{k}_0 = (k_x^0, 0)$. Hence, we define the spectrum of the Wilson loop operator, not as its set of eigenvalues[1] but as the behavior of its eigenvalues as a function of the "free" parameter $\mathbf{k}_0$.

We compute the Wilson spectrum taking the $\gamma_2$ path as an example and placing $N$ copies of this path $\gamma_2^i$ at $\mathbf{k}_0 = (k_{x,i}, 0)$, with $k_{x,i} = 2\pi i/N$ for $i = 0, N-1$[2]. Since the eigenvalues of the Wilson loop operator are the Berry phases associated to the path, we integrate the Berry connection along

[1] This is the usual definition of the spectrum of an operator.

[2] The index $i$ runs from 0 to $N-1$ since due to periodicity $k_{x,N}$ is the same as $k_{x,0}$.

each $\gamma_2^i$ and associate the resulting phase $\phi_i$ with the index $i$. Taking the continuum limit $N \to \infty$, each $\gamma_2^i$ is a $\mathrm{d}k_x$ apart, so the discrete set of all Berry phases $\{\phi_i\}$ becomes a continuous function of the $k_x$ variable, called the Wilson loop spectrum $\Phi(k_x)$:

$$\Phi(k_x) = \int_0^{2\pi} \mathcal{A}(k_x, k_y)\mathrm{d}k_y, \tag{2.53}$$

The same procedure can be done for the Berry phase calculated along $\gamma_1$, thus obtaining $\Phi(k_y)$ as the Wilson loop spectrum. The relation between the two functions depends on the symmetries of the system [73].

For an interpretation of the Wilson loop operator, we start from one dimension, where the Wilson loop, the Berry phase, and the Zak phase share the definition. All these concepts represent the geometric phase that a certain state acquires after crossing the one-dimensional first Brillouin zone. This phase has also a meaning related to the Wannier functions: it can be shown that the Berry phase $\phi$ divided by $2\pi$ corresponds to the position of the Wannier center $\bar{r}_{\mathcal{J}}$ associated with the set of Bloch functions considered $\mathcal{J}$:

$$\bar{r}_{\mathcal{J}} = \frac{\phi}{2\pi} a_0, \tag{2.54}$$

where $a_0$ is the lattice constant. This result is used in the modern theory of polarization in solids, introduced in [74, 75]. The way to generalize this result to higher dimensions is to realize that along the lines of the first Brillouin zone, we should obtain a quantity related to the position of the Wannier center. More precisely, we can always relate the eigenvalues of the Wilson loop operator with the eigenvalues of the projected position operator into the occupied set of bands. The eigenvalues of the projected position operator are precisely the coordinates of the Wannier center along the coordinate of the operator. For example, in two dimensions, we know that even if the operators $\hat{x}$ and $\hat{y}$ commute, their projections onto the occupied bands, $P\hat{x}P$ and $P\hat{y}P$ with $P = \sum_{\ell \in \mathrm{occ}} |\psi_{\ell,\mathbf{k}}\rangle\langle\psi_{\ell,\mathbf{k}}|$, do not commute, so one cannot obtain simultaneously the $x$, $y$ coordinates of the Wannier center. We refer the reader to references [69, 76] for a more pedagogical understanding of this concept.

We now relate the Wilson loop spectrum to the Chern number in the following way:

$$\begin{aligned} C =& \frac{1}{2\pi} \iint \left( \partial_{k_x} \mathcal{A}_y(k_x, k_y) - \partial_{k_y} \mathcal{A}_x(k_x, k_y) \right) \mathrm{d}k_x \mathrm{d}k_y \\ =& \frac{1}{2\pi} \int_0^{2\pi} \partial_{k_x} \left( \int_0^{2\pi} \mathcal{A}_y(k_x, k_y)\mathrm{d}k_y \right) \mathrm{d}k_x \\ =& \frac{1}{2\pi} \int_0^{2\pi} \partial_{k_x} \Phi(k_x)\mathrm{d}k_x = \frac{1}{2\pi} \left( \Phi(2\pi) - \Phi(0) \right) \in \mathbb{N}, \end{aligned} \tag{2.55}$$

which is precisely the integral of the Wilson loop spectrum, as introduced in Eq. (2.53). The Chern number is the net number of windings of the Wilson loop spectrum, *i. e.*, the number of times that the Wilson loop spectrum wraps around the torus.

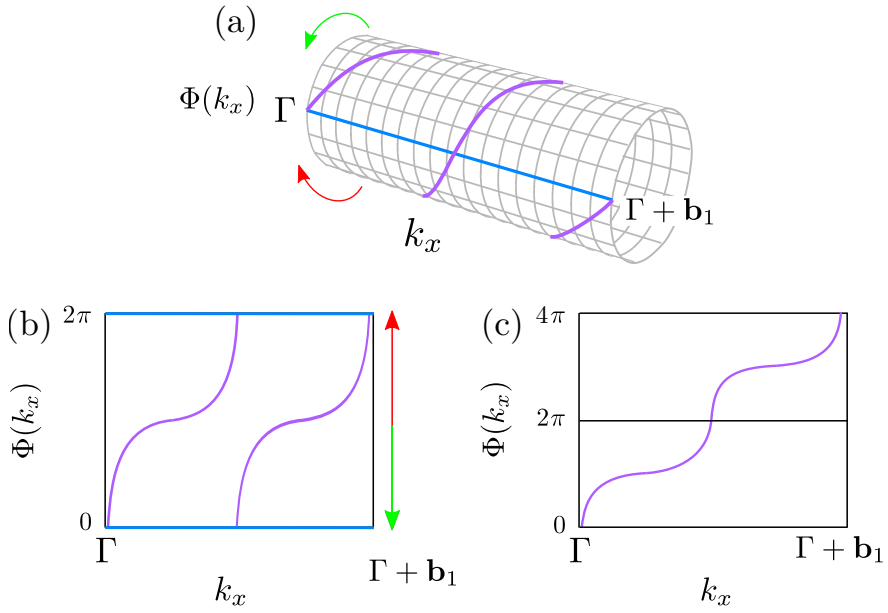


*Figure 2.6:* (a) Wrapping of the Wilson loop spectrum in the first Brillouin zone along the free parameter $k_x$. In purple, the Wilson loop spectrum from $\mathbf{k} = \Gamma$ to $\mathbf{k} + \mathbf{G} = \Gamma + \mathbf{b}_1$ showing two windings, so the Chern number corresponds to $C = 2$. (b) Representation of the Wilson loop spectrum in (a) but with the modulo $2\pi$ definition of the Berry phase. The two windings present in (a) transform into the discontinuity of the Wilson loop spectrum. The blue lines correspond to the periodicity of the Wilson loop spectrum. By gluing together the blue lines in panel (b) according to the red/green arrow, we obtain panel (a) from panel (b). (c) Computation of the Wilson loop spectrum without the modulo-$2\pi$ step. We can obtain te Chern number as we claimed in the text: $\Phi(\mathbf{k} + \mathbf{G}) - \Phi(\mathbf{k}) = \Phi(\Gamma + \mathbf{b}_1) - \Phi(\Gamma) = \Phi(2\pi) - \Phi(0) = 4\pi - 0 = 4\pi = 2\pi C$, so $C = 2$. So, by removing the modulo-$2\pi$ step, the Berry phase has to range from 0 to $2\pi C$, in order to compute the Chern number as the difference between the Wilson loop spectrum at the limits of the path.

This calculation has to be done carefully: to relate the number of windings of the Wilson loop spectrum to the difference of its values at $k_x = 2\pi$ and at $k_x = 0$, the definition of the Berry phase has to be done *without* the modulo-$2\pi$ step. This is because the modulo-$2\pi$ step constrains the Berry phase to lie within the $[0, 2\pi)$ interval. Without the modulo step, the Berry phase will range from 0 to $2\pi C$ and thus $\Phi(k_x = 2\pi) - \Phi(k_x = 0) = 2\pi C$. In other words, the number of times that the Wilson loop spectrum winds along the free coordinate determines the absolute value of the Chern number, while the sign of the slope determines its sign. Finally, as we have connected the Chern number to the winding of the Wilson loop spectrum, we can claim that a Wilson loop spectrum that winds represents a non-zero Chern number. Thus, a Wilson loop spectrum that winds represents the same obstruction we described previously in Sec. 2.5.1, by which neither a smooth gauge can be

found for the Bloch wave functions nor a maximally localized Wannier function can be built for the chosen set of bands.

## 2.6 Topological quantum chemistry

Topological quantum chemistry is a formalism that allows to predict and classify band structures according to their topological character, based exclusively on group theory and symmetry arguments. It was introduced in reference [14] and has allowed for an exhaustive classification of materials according to their topological character, without and with magnetic character [77, 78]. By determining the symmetry properties of the wave functions at the high-symmetry points of the first Brillouin zone, one is able to tell whether a band structure is topological or not. Let's begin by presenting the building blocks of this theory, starting from group theory concepts.

### 2.6.1 Group theory

All two-dimensional lattices belong to the 17 different two-dimensional space groups, called plane or wallpaper groups, and labeled as $\mathcal{G}$. The elements of these groups are combinations of isometries plus translations, and are denoted by Seitz symbols as $g = \{R|\mathbf{t}\}$, where $R$ is the isometry or linear part, and $\mathbf{t}$ is the translational part in the form of $\mathbf{t} = \mathbf{R}_{m,n}$ (see Sec. 2.2). Hence, a generic space group element is represented by a Seitz symbol and is usually written as $g = \{R|mn\}$. These elements act in all the real space elements that we have defined so far (unit cell, lattice vectors, wave functions, periodic potential, Hamiltonian), and thus impose certain constraints that these elements must preserve.

The set of isometries of a certain space group is formed by elements of the space group that have the zero vector as the translational part, represented by Seitz symbols of the form $\{R|\mathbf{0}\}$. This set forms a group and is isomorphic to a point group, labeled as $G$. In two dimensions, there are 11 point groups, which can be classified into:

- symmorphic, if after applying all its elements to a point inside the unit cell, it remains in the same position or in an equivalent one. Since the lattice is translational invariant, the starting point and the resulting one are equivalent;
- non-symmorphic, where at least one element has a translational part by a fraction of a lattice vector (elements of the form $\{R|mn\}$ where $m, n$ are fractional numbers). In this way, the transformed point does not fall into a lattice point so the whole lattice has translated a fraction

of a lattice vector. We find glide symmetries, where the linear part is a mirror, and screw symmetries, where the linear part is any rotation.

Chapter 3 is focused on a lattice whose space group is symmorphic, while Chapter 4 is dedicated to a lattice belonging to a non-symmorphic space group.

Certain points inside the unit cell inherit the symmetry properties of the point group of the lattice. These are called Wyckoff positions, denoted by $\mathbf{w}$. Each of them has a point group associated, called the site-symmetry group (or stabilizer group) labeled as $G_{\mathbf{w}}$ and composed by all the operations from the point group of the lattice $G$ that leave such position invariant:

$$G_{\mathbf{w}} = \{g \in G | g\mathbf{w} = \mathbf{w}\}. \tag{2.56}$$

The elements of the site-symmetry group $G_{\mathbf{w}}$ can contain translations proportional to the lattice vectors (elements of the form $\{R|mn\}$ with $m, n \neq 0$). Any site-symmetry group is a subgroup of the point group of the lattice $G_{\mathbf{w}} \subseteq G$. The Wyckoff positions can be decomposed into two subsets:

- Maximal Wyckoff positions ($\mathbf{w}_{\mathrm{M}}$) are those Wyckoff positions whose site-symmetry group $G_{\mathbf{w}_{\mathrm{M}}}$ is a maximal subgroup of the point group of the lattice, *i. e.*, whose site-symmetry group is not a subgroup of any other site-symmetry group [79]. We can write $G_{\mathbf{w}_{\mathrm{M}}} \subseteq G$.
- The rest of the Wyckoff positions are called non-maximal since their site-symmetry groups are a subgroup of another Wyckoff positions' site-symmetry group. If we label non-maximal Wyckoff positions as $\mathbf{w}_{\mathrm{m}}$ and its site-symmetry group as $G_{\mathbf{w}_{\mathrm{m}}}$, we can write $G_{\mathbf{w}_{\mathrm{m}}} \subset G_{\mathbf{w}_{\mathrm{M}}} \subseteq G$.

The Wyckoff positions are represented with a number related to how many of them are inside the unit cell, and a letter that allows one to distinguish between different Wyckoff positions. The set of Wyckoff positions of the same species defines the concept of orbit: the orbit of a Wyckoff position is the set of positions inside the unit cell generated by the elements of the point group that are *not* inside the site-symmetry group of the Wyckoff position. The elements that generate the orbit of a Wyckoff position are called coset representatives of the site-symmetry group of the Wyckoff position. Let's apply these group theory concepts to a two-dimensional lattice populated by atomic orbitals.

### 2.6.2 From atomic orbitals to band structures

Atoms in a lattice are usually placed at the maximal Wyckoff positions. This reduces the symmetry of the atomic orbitals from $O(3)$ to the point group of the lattice, so we cannot talk about

(isolated) atomic orbitals anymore. We introduce the concept of crystal orbital in the same way as molecular orbital is introduced in chemistry [80]: the hybridization of the atomic orbitals from the individual atoms, placed at the lattice sites, form an orbital called crystal orbital, which is periodic with the lattice periodicity. However, in Sec. 2.2.7 we introduced the concept of maximally localized Wannier function as a real-space valued function that represents the localization of the charge in the lattice and is periodic with the lattice periodicity. We can thus form a linear combination of maximally localized Wannier functions to describe such crystal orbital, which transforms according to the symmetries of the lattice. This set of maximally localized Wannier functions has associated a certain band structure in reciprocal space. Since the Wannier functions respect the symmetry of the space group, the band structure inherits the symmetry properties of the space group. This is where topological quantum chemistry comes into play: by choosing a lattice and populating different Wyckoff positions with different crystal orbitals, we arrive at different band structures, each with its symmetry properties inherited from the space group.

This process (called induction) induces a representation of the space group, called band representation, a concept introduced by Zak [81, 82, 83, 84]. A band representation is a mathematical object that dictates the symmetry properties of the wave functions in real and reciprocal space.

More formally, the induction process happens in the following way: some crystal orbital, placed at a certain maximal Wyckoff position $\mathbf{w}$[1], has certain symmetry properties, ruled by the elements of its site-symmetry group $G_{\mathbf{w}}$. The action of each of the symmetry elements of the point group is represented by a square matrix. The set of matrices for all the symmetry elements of the point group form a representation of the point group. This representation, which we call $\rho$, dictates the properties of the symmetry elements of the site-symmetry group. Since the crystal orbital respects the symmetry of the site-symmetry group, and the site-symmetry group is a subgroup of the full space group, $G_{\mathbf{w}} \subseteq \mathcal{G}$, the representation $\rho$ from the site-symmetry group is induced into the full space group. This is called band representation of the full space group $\rho_{\mathcal{G}}$ and is represented by:

$$\rho_{\mathcal{G}} = (\rho \uparrow \mathcal{G})_{\mathbf{w}}, \tag{2.57}$$

where $\rho_{\mathcal{G}}$ is the induced band representation, and $\uparrow$ represents the induction process.

Representations are objects that can be reduced into simpler elements, called irreducible representations. Accordingly, band representations can be decomposed into simpler elements, called elementary band representations. In order to find the symmetry properties in reciprocal space, it is necessary to decompose the band representation into elementary band representations. Then, it can

[1]We have removed the subindex M since we do not work with non-maximal Wyckoff positions, so at all times a Wyckoff position denoted by $\mathbf{w}$ will be maximal.

be Fourier transformed into reciprocal space, so that one can determine the symmetry properties of the wave functions at certain **k** points. These are called high-symmetry points, analogous to the Wyckoff positions in real space since they inherit the symmetry properties of the reciprocal lattice. Each high-symmetry point $\Lambda_j$ has a point group associated, called little group, denoted as $G_{\Lambda_j}$ (analogous to the site-symmetry group of the Wyckoff positions $G_{\mathbf{w}}$).

The symmetry properties of the wave functions at each high-symmetry point are determined by a process called subduction ($\downarrow$), by which the band representation $(\rho \uparrow \mathcal{G})_{\mathbf{q}}$ is decomposed into a linear combination of irreducible representations $\{\sigma_i^{\mathbf{k}}\}$ of the little group $G_{\Lambda_j}$ of each of the high-symmetry points:

$$(\rho \uparrow \mathcal{G})_{\mathbf{w}} \downarrow G_{\Lambda_j} \approx \bigoplus_i m_i \sigma_i^{\Lambda_j}, \tag{2.58}$$

where $m_i$ is the multiplicity of the irreducible representations in the decomposition. This subduction process must be done for each of the high-symmetry points inside the irreducible Brillouin zone. In this way, the irreducible representation assignment determines how the wave functions associated with each band transform under the action of the symmetry elements at each high-symmetry point.

We want to point out that the subduction process ($\downarrow$) is not restricted to reciprocal space. Actually, when we place atomic orbitals in Wyckoff positions with a certain site-symmetry group, we are *subducing* the representation from the $O(3)$ point group, which is called the vector representation or $V$, to the set of irreducible representations of the site symmetry group: $V \downarrow G_{\mathbf{w}}$. In general, the subduction process happens when a representation is restricted or decomposed into irreducible representations of a different group. After the subduction process, the irreducible character of a representation can change: an irreducible representation of a group can become reducible when it is expressed into irreducible representations of one of its subgroups.

### 2.6.3 From band structures to crystal orbitals

Up to now, we have determined the symmetry properties of a band structure from real space, where the symmetry of the crystal orbital determines the symmetry properties of the band structure in reciprocal space. However, this process can be reversed: if one is able to characterize the symmetry properties in reciprocal space, by determining the irreducible representations at each high-symmetry point, this uniquely defines the band representation in real space. As we presented previously, the band representation is characterized by the symmetry of the crystal orbital, described by a certain representation of the site-symmetry group, $\rho$, and the Wyckoff position where such band representation is induced, **w**.

This leads to a criterion to characterize the symmetry properties of a band structure based on the location of the Wyckoff position. This is because the Wyckoff position associated with a band representation represents the location of the Wannier center of the maximally localized Wannier function (crystal orbital):

- We define a *trivial* atomic limit as a situation where the band structure corresponds to a band representation induced from an *occupied* Wyckoff position, that is, when there is an atom with a set of orbitals located in such Wyckoff position.
- On the contrary, we define an *obstructed* atomic limit as a band structure corresponding to a band representation that is induced from an *unoccupied* Wyckoff position: the Wyckoff position is empty and no atom or orbitals are located in such Wyckoff position.

These two limits correspond to (topologically) different phases that accept, by definition, a set of maximally localized Wannier functions, so they do not present robust topology. These two atomic limits are not adiabatically connected: by studying the behavior of the symmetry eigenvalues, one can detect band inversions, which are the typical signature of phase transitions between trivial/obstructed atomic limits. This criterion applies only to non-topological materials.

### 2.6.4 Topological classification: topological quantum chemistry

At the beginning of this section, we claimed that topological quantum chemistry allows for a topological classification of materials according to their symmetry properties. So far, we have described the symmetry properties of band representations induced from occupied/unoccupied Wyckoff positions which accept a representation in terms of maximally localized Wannier functions.

As we described previously, elementary band representations form a basis of all possible band representations, so any band representation is expected to be decomposed into a linear combination of elementary band representations with positive integer coefficients. Those coefficients are called multiplicities, in the same sense as in Eq (2.58).

However, this is not always the case: topological band structures (whose topology can be diagnosed using symmetry indicators) do not allow a decomposition of their band representation into a linear combination of elementary band representations with positive integer coefficients. Each elementary band representation represents a set of bands that are connected inside the first Brillouin zone [85, 86]. However, it was proven that elementary band representations can be disconnected [14], and thus whenever an elementary band representation is said to be disconnected, at least one of

the disconnected set of bands has to present non-trivial topological features, again, diagnosable via symmetry indicators.

As we introduced in Sec. 2.2.7, robust topological bands do not accept a description in terms of maximally localized Wannier functions. In terms of elementary band representations, the impossibility of assigning a well-defined band representation to the topological bands is the key to the poor localization of the Wannier function. Thus, no center can be assigned to them.

As a final remark, the "direct" way (induction of a band representation, subduction into little groups at high-symmetry points) allows to study the topology of a band structure induced from real space. On the contrary, the "inverse" way allows to characterize band structures that do not necessarily come from electronic orbitals in real space, as in photonic systems or quantum simulators. Chapter 3 is devoted to the characterization of a system in the absence of atomic species or orbitals (electronic quantum simulator).

## 2.7 Su-Schrieffer-Heeger (SSH) model

This section is devoted to the application of the concepts introduced in the previous sections to a very simple model, called the SSH model due to the authors who used it to describe solitons in polyacetylene [87]. A sketch of such polymer is shown in Figure 2.7(a). This model encodes a very simple description of the basic concepts of topology, as described in Secs. 2.5, 2.6 and 2.4. We begin by presenting the tight-binding Hamiltonian used in the study of the model. We cover as well the symmetries of the chain, and then we present the two different topological phases of the system according to the quantization of the Berry phase (in this case called Zak phase). Finally, we apply topological quantum chemistry to characterize these two phases fully.

### 2.7.1 Hamiltonian and symmetries

We start by presenting the tight-binding Hamiltonian with nearest neighbor hoppings. The unit cell is populated by two orbitals, A and B. These orbitals are placed at $x = \pm a_0/4$ respectively, where $a_0$ is the lattice constant, taken to be unity. There is an intra-cell hopping, called $t$, and an intercell hopping, called $t'$. We can write the matrix elements of the Hamiltonian as $t_{m,n} = \langle m\mathrm{A}|\mathcal{H}|n\mathrm{B}\rangle = t\delta_{m,n} + t'\delta_{m+1,n}$, for $\langle m\mathrm{A}|$, $|n\mathrm{B}\rangle$ being the Dirac notation for orbitals at species A or B, $m, n$ indexing the unit cells, and $\delta_{m,n}$ being the Kronecker $\delta$ function over the cell indices. If

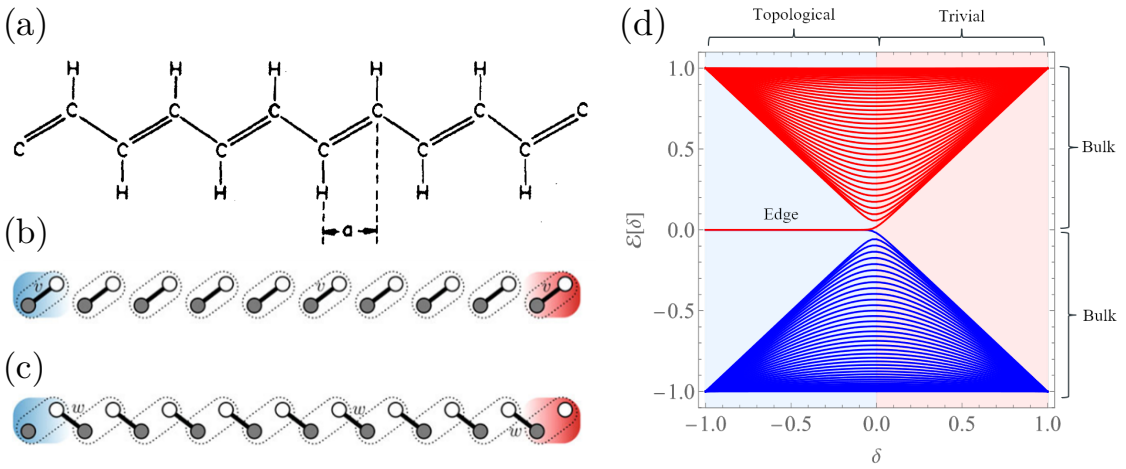


*Figure 2.7:* (a) Configuration of a polyacetylene molecule displaying the unit cell. Adapted from [87]. (b) Trivial phase of the SSH model containing disconnected dimers. (c) Phase displaying the boundary modes lying on the disconnected orbitals in the boundaries. Both have been adapted from [20]. (d) Phase diagram of the SSH model under a dimerization technique such that $t_{m,n} = \langle m\mathrm{A}|\mathcal{H}|n\mathrm{B}\rangle = t\delta_{m,n} + t'\delta_{m+1,n} = t_0(1+\delta)\delta_{m,n} + t_0(1-\delta)\delta_{m+1,n}$, where $\delta \in (-1,1)$ is the dimerization parameter. When $\delta = \pm 1$ the SSH chain reaches the two limiting cases of disconnected dimers. At $\delta < 0$ two zero energy states appear and localize at the boundaries of the chain–light blue region.

we Fourier transform the Hamiltonian in the basis A, B, we obtain:

$$\mathcal{H}(k) = \begin{pmatrix} 0 & q(k) \\ q^\dagger(k) & 0 \end{pmatrix} = \sigma_+ q(k) + \sigma_- q^\dagger(k), \tag{2.59}$$

$$q(k) = t + t'\mathrm{e}^{-\mathrm{i}k}, \tag{2.60}$$

where $\sigma_\pm$ is an even/odd combination of the $x$, $y$ Pauli matrices, and $k$ is the one-dimensional wave vector. The Hamiltonian has been written in such a form that makes explicit the sublattice symmetry or chiral symmetry, which makes the Hamiltonian off-diagonal. This can be generalized for any even number of atoms in the unit cell, as it will be shown in Chapter 4. The chiral symmetry can be expressed as:

$$\Gamma^{-1}\mathcal{H}_1\Gamma = \mathcal{H}_2, \tag{2.61}$$

$$\mathcal{H}_1 + \mathcal{H}_2 = 0, \tag{2.62}$$

where $\Gamma$ is thus the chiral operator in a diagonal form. We find $\mathcal{H}_2 = -\mathcal{H}_1$, and as $\mathrm{Tr}(\mathcal{H}_1 + \mathcal{H}_2) = 0$, the two possible eigenvalues verify $E_2 = -E_1 = E$, and thus a single Hamiltonian can be considered as $\Gamma^{-1}\mathcal{H}\Gamma = -\mathcal{H}$. The operator $\Gamma$ does not commute with $\mathcal{H}$, but its square does, and so, for a $2\times 2$ chiral-symmetric matrix, the shape of $\Gamma$ is the Pauli matrix $\sigma_z$. The spectrum of a chiral-symmetric Hamiltonian is always energy-symmetric, since for an eigenvector $|\phi\rangle$ with eigenenergy $E$, there is

always a chiral-symmetric one $\Gamma|\phi\rangle$ with eigenenergy $-E$. In this sense, whenever the energy is different from zero, the eigenvectors $\phi$ and $\Gamma|\phi\rangle$ are orthogonal:

$$\langle\phi|\Gamma|\phi\rangle = \begin{pmatrix}\phi_1^* & \phi_2^*\end{pmatrix}\sigma_z\begin{pmatrix}\phi_1\\ \phi_2\end{pmatrix} = |\phi_1|^2 - |\phi_2|^2 = 0 \quad \Rightarrow \quad |\phi_1|^2 = |\phi_2|^2. \tag{2.63}$$

This last expression means that the wave function will have the same weight in both sublattices whenever $E \neq 0$. However, if the energy is zero, $\mathcal{H}|\phi\rangle = 0$ implies that $\mathcal{H}\Gamma|\phi\rangle = 0$ and thus $\mathcal{H} = \Gamma\mathcal{H}$. Therefore, the eigenvectors of $\mathcal{H}$ can be taken to be the same as the ones from $\Gamma$:

$$|\gamma_1\rangle = \begin{pmatrix}1\\0\end{pmatrix} \quad |\gamma_2\rangle = \begin{pmatrix}0\\1\end{pmatrix}, \tag{2.64}$$

and thus the wave function will have only weight in just one of the sublattices.

With this explanation in mind, the spectrum of the SSH chain is computed diagonalizing the Hamiltonian in (2.59). The result is two energy-symmetric bands that gap when $t \neq t'$. Indeed, taking $a_0 = 1$, the spectrum reads

$$E_\pm(k) = \pm\sqrt{t^2 + (t')^2 + 2tt'\cos(k)}. \tag{2.65}$$

The subindex $\pm$ corresponds to the lower and upper bands and will also be used to distinguish between the eigenstates associated to the respective band. The spectrum closes at $k = \pm\pi$ when $t = t'$, and is gapped at any other case. The width of the gap is $\Delta_g = 2|t - t'|$. Let's now apply the concepts of topology and group theory to this system in the gapped phases.

### 2.7.2 Topological analysis of the phases of the SSH model

The topology of a system is encoded in the eigenvectors of the Hamiltonian. Therefore, we diagonalize and solve for the eigenvectors of expression (2.59). We obtain:

$$|\psi\rangle_\pm(k) = \frac{1}{\sqrt{2}}\begin{pmatrix}\frac{E_\pm(k)}{t + t'e^{ik}} & 1\end{pmatrix}^{\mathrm{T}}. \tag{2.66}$$

We now compute the Zak phase (Berry phase along the one-dimensional first Brillouin zone) for the two limiting cases where $t' = 0$, $t = t_0$ (phase I), and for the case $t = 0\,t' = t_0$ (phase II). In both cases, the bulk spectra of the two phases are identical, displaying a gap of $\Delta_g = 2|t_0|$.

In phase I, $t' = 0$, the SSH chain is decomposed into an infinite set of dimers A−B. The eigenvectors can be written as

$$|\psi\rangle_\pm(t' = 0, k) = \frac{1}{\sqrt{2}}\begin{pmatrix}\pm 1 & 1\end{pmatrix}^{\mathrm{T}}, \tag{2.67}$$

and thus the Berry connection is 0, as the eigenvectors do not depend on $k$. Therefore, the Zak phase is zero and the associated Wannier center is zero as well, meaning that the maximally localized Wannier function is located in the center of the unit cell, coinciding with one of the centers of inversion of the system.

In phase II, where $t = 0$, the SSH chain is decomposed again into an infinite set of dimers, but this time the dimers are B−A. The eigenvectors can be written as

$$|\psi\rangle_{\pm}(t = 0, k) = \frac{1}{\sqrt{2}} \begin{pmatrix} \pm e^{-ik} & 1 \end{pmatrix}^{T}. \tag{2.68}$$

Now, the Berry connection for the lower band is:

$$\mathcal{A}_{-}(k) = \frac{1}{2}. \tag{2.69}$$

Therefore, the Zak phase is:

$$\phi = \int \mathcal{A}_{-}(k)\mathrm{d}k = \int_{0}^{2\pi} \frac{1}{2}\mathrm{d}k = \pi, \tag{2.70}$$

and the associated Wannier center is thus $\bar{r}_{-} = a_0/2$, which means that the maximally localized Wannier function is located at the border of the unit cell. This position is the other center of inversion of the system.

These two bulk topologies have different consequences in the boundaries of a finite-size system, as specified in Sec. 2.4. If we take a finite size sample of $N$ unit cells and study the two limiting cases, we observe the following: phase II presents boundary modes localized in the sublattice defining the end of the chain, *i. e.*, A on the left and B on the right of the chain. These two modes are both at zero energy because they correspond to orbitals disconnected from the rest of the dimers since the dimers are formed between adjacent unit cells.

According to the bulk-boundary correspondence presented in Sec. 2.4, we can call phase I topologically *trivial*, since there is no signature of non-trivial topological bulk at the boundaries of the system. On the contrary, we call phase II topologically *non-trivial* since there is indeed a boundary signature of a non-trivial topological bulk. However, since we are in one dimension, no robust topology can be encoded in these systems. Another way to understand the actual "lack" of robust topology in the system is to make a shift of the unit cell in real space. In this way, the physics of the phases would be exchanged and so the topological markers. Since topology must not depend on the choice of unit cell, we conclude that no topology is encoded in the SSH chain, just a non-zero bulk polarization resulting in the appearance of two boundary modes.

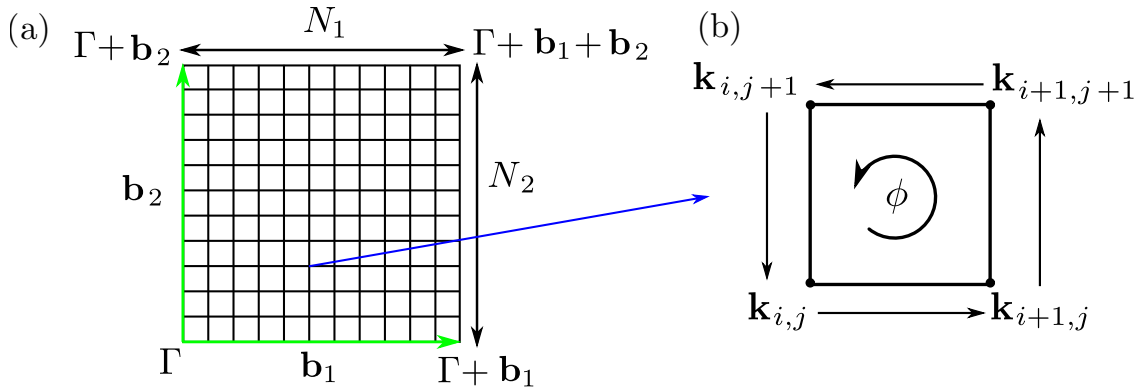


*Figure 2.8:* (a) $N_1 \times N_2$ discretization of a square first Brillouin zone. (b) Infinitesimal plaquette pinned at $k_{i,j}$ reflecting the Berry phase $\phi$ acquired after a loop pinned at $k_{i,j}$.

### 2.7.3 Symmetry analysis of the phases of the SSH model

When we computed the Berry connections and Zak phases of the two distinct phases of the SSH model, we obtained quantized values, due to inversion symmetry since it maps $k$ to $-k$. By taking a topological quantum chemistry perspective of the problem, we compare the obtained Wannier centers with the maximal Wyckoff positions and the atomic positions. The center of the unit cell corresponds to the $1a$ maximal Wyckoff position, while the edges correspond to the $1b$ maximal Wyckoff position. The atomic positions are located at the $2c$ Wyckoff positions, which are non-maximal, so no band representation can be induced from them. This sheds light on the actual configuration of the system: since none of the maximal Wyckoff positions are occupied, strictly speaking, both phases are different obstructed atomic limits, one with zero bulk polarization (phase I) and the other with non-zero bulk polarization (phase II).

## 2.8 Sampling over a discretized two-dimensional Brillouin zone

So far we have introduced the topological invariants in the continuum, using the SSH model as an example. This is because we have been able to obtain analytic expressions for the eigenvectors and the topological invariants. However, in two or more dimensions, this is not always possible. In this section we present the discretized version of the topological invariants introduced in Sec. 2.5. We begin by discretizing the two-dimensional first Brillouin zone into a $(N_1 \times N_2)$ grid[1]. The first Brillouin zone is now a set of points in the form:

$$\mathbf{k}_{i,j} = \frac{i}{N_1}\mathbf{b}_1 + \frac{j}{N_2}\mathbf{b}_2, \qquad \text{for } i = 0, ..., N_1 - 1, \quad j = 0, ..., N_2 - 1. \tag{2.71}$$

[1]Usually $N_1 = N_2 = N$ but we keep a different notation to distinguish them.

The Bloch wave function is periodic in the first Brillouin zone (periodic gauge). However, all the topological quantities depend on the cell-periodic part of the Bloch wave function, and thus we need to overcome the fact that the gauge is chosen to be twisted, not periodic. This can be achieved by defining the cell-periodic part along the lines $\{N_1, j\}$ and $\{i, N_2\}$ as the cell-periodic part computed along $\{0, j\}$ and $\{i, 0\}$ times a phase factor in the form $\exp(-\mathrm{i}\mathbf{b}_{1,2} \cdot \hat{\mathbf{r}})$. This phase is an operator since it is a function of the operator $\hat{\mathbf{r}}$, so when it acts on the cell-periodic part of the Bloch wave function, it returns the exponential of the positions in the real space unit cell of the crystal orbitals. In this way, we can account for the gauge choice of the cell periodic part and include it in the calculations. This procedure needs to be done since the diagonalization routines include random phases, which need to be balanced to get rid of them [16, 88].

The most important element of the discretized versions of the topological invariants is the overlap elements between wave functions at adjacent $\mathbf{k}$ points of the first Brillouin zone. We can define them according to [88, 89]. For a single band, we have the Abelian $U(1)$ link variable:

$$U(\mathbf{k}_i, \mathbf{k}_j) = \frac{\langle u(\mathbf{k}_i)|u(\mathbf{k}_j)\rangle}{|\langle u(\mathbf{k}_i)|u(\mathbf{k}_j)\rangle|}. \tag{2.72}$$

For a $J$ multi-band description of the overlap (non-Abelian definition), we perform all the possible combinations of the overlaps between all the degenerated bands. In this way, we build a $U(J)$ link variable in the shape of a square matrix, and take the determinant (back to $U(1)$ link variables):

$$\mathcal{S}^{(J)}(\mathbf{k}_i, \mathbf{k}_j) = \begin{pmatrix} \langle u_1(\mathbf{k}_i)|u_1(\mathbf{k}_j)\rangle & \dots & \langle u_1(\mathbf{k}_i)|u_J(\mathbf{k}_j)\rangle \\ \vdots & \ddots & \vdots \\ \langle u_N(\mathbf{k}_i)|u_1(\mathbf{k}_j)\rangle & \dots & \langle u_J(\mathbf{k}_i)|u_N(\mathbf{k}_j)\rangle \end{pmatrix}, \tag{2.73a}$$

$$U^{(J)}(\mathbf{k}_i, \mathbf{k}_j) = \frac{\det \mathcal{S}^{(J)}(\mathbf{k}_i, \mathbf{k}_j)}{|\det \mathcal{S}^{(J)}(\mathbf{k}_i, \mathbf{k}_j)|}. \tag{2.73b}$$

Let's now write down the expressions for the Berry phase along a closed loop. This closed loop is represented as a small plaquette formed by a set of $\mathbf{k}$ points, as presented in Figure 2.8b. This plaquette is pinned at $\mathbf{k}_{i,j}$ placed in the lower left corner. The naming of the rest of the corners is done counter-clockwise $\square = \left\{\mathbf{k}_{i,j}, \mathbf{k}_{i+1,j}, \mathbf{k}_{i+1,j+1}, \mathbf{k}_{i,j+1}\right\} = \{\mathbf{k}_0, \mathbf{k}_1, \mathbf{k}_2, \mathbf{k}_3\}$. The total Berry phase after completing the loop is:

$$\phi(\mathbf{k}_0) = \mathrm{Im}\ \ln\ \left[U(\mathbf{k}_0, \mathbf{k}_3)U(\mathbf{k}_3, \mathbf{k}_2)U(\mathbf{k}_2, \mathbf{k}_1)U(\mathbf{k}_1, \mathbf{k}_0)\right], \tag{2.74a}$$

$$\phi^{(J)}(\mathbf{k}_0) = \mathrm{Im}\ \ln\ \left[U^{(N)}(\mathbf{k}_0, \mathbf{k}_3)U^{(N)}(\mathbf{k}_3, \mathbf{k}_2)U^{(N)}(\mathbf{k}_2, \mathbf{k}_1)U^{(N)}(\mathbf{k}_1, \mathbf{k}_0)\right], \tag{2.74b}$$

for single-band and multi-band calculations respectively, The order of the $\mathbf{k}$ points is crucial since it determines the criterion for the sign. Also, in Eq. (2.74b) due to the non-Abelian origin of the $U^{(J)}(\mathbf{k}_i, \mathbf{k}_j)$ link variable, the order of the matrices actually matter.

For the definition of the Berry curvature, we compute the Berry phase for all the plaquettes inside the first Brillouin zone and divide it by the area of each plaquette. Finally, the Chern number is just the integral of the Berry curvature inside the first Brillouin zone, or the sum of all the Berry phases associated with each plaquette. This definition is a consequence of the Ambrose-Singer theorem [90] by which the holonomy of a connection is related to the curvature of the connection. In other words, the Berry phase along the plaquette represents an infinitesimal Wilson loop, which is precisely the holonomy of the Berry connection. We refer the reader to Sec. 2.5 for more details.

However, we can write an analytic expression of the Berry curvature: we can use the expression (2.42) introduced in Sec. 2.4. The derivatives of the Hamiltonian can be related to the velocity operator $\hbar \mathbf{v}_{r,s}(\mathbf{k}) = \langle r\mathbf{k}|\nabla_{\mathbf{k}}\mathcal{H}_{\mathbf{k}}|s\mathbf{k}\rangle$. Averaging over the whole first Brillouin zone, we obtain:

$$\sigma_{\mathrm{H}}^{\alpha\beta} = \frac{1}{N_1 N_2}\sum_{\mathbf{k}} \sigma_{\mathrm{H}}^{\alpha\beta}(\mathbf{k}), \tag{2.75a}$$

$$\sigma_{\mathrm{H}}^{\alpha\beta}(\mathbf{k}) = \frac{e^2\hbar}{A_0}\Omega(\mathbf{k}), \tag{2.75b}$$

$$\Omega(\mathbf{k}) = \mathrm{i}\sum_{r,s} \frac{v_{s,r}^{\alpha}(\mathbf{k}) v_{r,s}^{\beta}(\mathbf{k})}{(E_r(\mathbf{k}) - E_s(\mathbf{k}))^2}, \tag{2.75c}$$

where $\sigma_{\mathrm{H}}^{\alpha\beta}$ is the total Hall conductance, $\sigma_{\mathrm{H}}^{\alpha\beta}(\mathbf{k})$ is the $\mathbf{k}$ resolved Hall conductance and $\Omega(\mathbf{k})$ is the $\mathbf{k}$ resolved *exact* Berry curvature. This is because the definition of the Berry curvature through the Ambrose-Singer theorem, by which the Berry curvature is built by computing the Berry phase for small plaquettes that tile the whole first Brillouin zone, is just the leading term in a series expansion, where the terms of the order $O(\delta k^3)$ have been neglected.

For the Wilson loop and its spectrum, we decompose it into the product of Wilson lines in the first Brillouin zone. Then, the Wilson loop along a straight line across the first Brillouin zone is just a generalization of Eqs. (2.74a) and (2.74b) where now the starting and end points are related by a reciprocal lattice vector. Assuming that the lines are located at $k_{2,j} = 2\pi j/N_2$, for $j = 0, \ldots, N_2$, and extend along $\mathbf{b}_1$ with $N_1$ points, we have:

$$\begin{aligned}\hat{W}_{(k_1+2\pi,k_2)\leftarrow(k_1,k_2)}(k_{2,j}) = \hat{W}_{\mathbf{b}_1}(k_{2,j}) = \\ = \prod_{i=0}^{N_1} U(\{k_1^{i+1}, k_{2,j}\}, \{k_1^{i}, k_{2,j}\}) \\ = \prod_{i=0}^{N_1} \langle u(k_1^{i+1}, k_{2,j})|u(k_1^{i}, k_{2,j})\rangle\end{aligned}$$

$$= \langle u_n(k_1 + 2\pi, k_{2,j})| \prod_{i=1}^{N_k-1} P(k_1^i, k_{2,j})|u_n(k_1, k_{2,j})\rangle. \tag{2.76}$$

Since the operator is unitary, we work with the phase associated with it, or Im ln $\hat{W}_{\mathbf{b}_1}(k_2)$. Expression (2.76) is a way to recast the Wilson loop operator as a product of infinitesimally separated one-particle projection operators, which is a reminder that the Wilson loop is related to the transport of an eigenstate of the Hamiltonian through multiple projections. The expression of each operator is thus $P(k_1, k_2) = |u(k_1, k_2)\rangle\langle u(k_1, k_2)|$. Since we are dealing with just one band, the Wilson loop spectrum is just a curve for all the set of $k_{2,j}$ which may or may not wind due to the topology of the system (see Fig. 2.9a and 2.9b).

For a non-Abelian expression, we need to compute as well the eigenvalues of the resulting matrix $W^{(J)}_{\mathbf{b}_1}(k_2)$:

$$\hat{W}^{(J)}_{(k_1+2\pi,k_2)\leftarrow(k_1,k_2)}(k_{2,j}) = \hat{W}^{(J)}_{\mathbf{b}_1}(k_{2,j}) = \\ = \mathcal{P}\left(\prod_{i=0}^{N_1-1} \mathcal{S}^{(J)}(\{k_1^{i+1}, k_{2,j}\}, \{k_1^i, k_{2,j}\})\right), \tag{2.77}$$

where we have recovered the path ordering operator due to the non-Abelian origin of the variables. Finally, once the operator is built, we compute its eigenvalues, which must not be mistaken as the Wilson loop spectrum, since the spectrum is defined as the variation of the Wilson operator along a path in reciprocal space. Hence, for a set of $J$ bands, we have a set of $J$ curves reflecting the Wilson loop of the total set of bands, not the individual ones. In figure 2.9c we present the Wilson loop spectrum of a set of 3 bands[1]. In all of these calculations, the cell-periodic part of the Bloch wave function has to be corrected with the extra phase factor in order to cancel the random phases introduced by the diagonalization routines.

We now recall the discussion about trivial/obstructed atomic limits presented in Sec. 2.6. Since the band representation is well-defined, its Wyckoff position is identified. Hence, it is possible to associate a Wilson loop spectrum with the coordinates of the Wyckoff position. This is possible since the Wilson loop spectrum does not wind and thus no Wannier center shifts from one unit cell to the adjacent one. Certain crystals (namely $C_n$-symmetric crystals) present a non-zero bulk polarization, which suggests that the centers of positive and negative charge are not in the same position. This is the same as saying that the electrons are displaced from where the atomic nuclei are. Since atomic nuclei are located at the maximal Wyckoff positions, whenever a $C_n$-symmetric crystal presents a non-zero bulk polarization, it corresponds to an obstructed atomic limit (necessary

[1]This is the typical Wilson loop spectrum of an obstructed atomic limit [88].

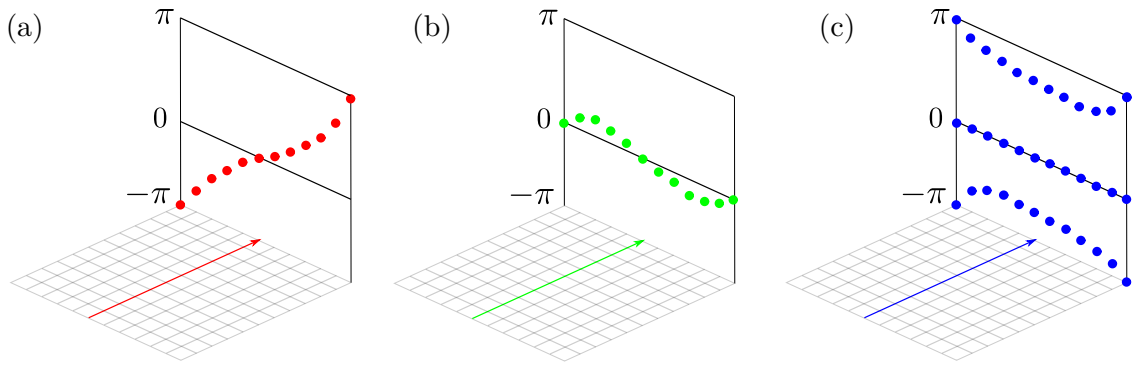


*Figure 2.9:* Examples of Wilson loop spectra. In all the cases, the arrow represents the direction along the Zak phase is computed. The orthogonal direction represents the direction of the spectrum. (a) Wilson loop spectrum of a single band, belonging to a system with broken time-reversal symmetry. As it presents a winding of 1, the corresponding Chern number is $C = +1$, where we have established the sign criterion according to the sign of the derivative of the Wilson loop spectrum. (b) Wilson loop spectrum of a single band belonging to a system that is symmetric under time-reversal symmetry. This Wilson loop spectrum is mappable to a constant value of zero, so we can associate a Wannier center that lies in the origin of the system of coordinates chosen. (c) Wilson loop spectrum of three bands presenting no winding.

but not sufficient). More precisely, the bulk polarization of those systems is related to the symmetry of the crystal, since the value of the polarization will be a $\mathbb{Z}_n$-quantized quantity [73, 91, 92, 93].

In general, after computing the Wilson loop spectrum for a system in an atomic limit, we can estimate the value of the bulk polarization as the averaged Wilson loop spectrum [94]:

$$p = \frac{1}{2\pi N_k} \sum_{j=1}^{N_k} \sum_{m=1}^{N_{\text{occ}}} \nu_{1,2}^{m}(k_{2,1}^{j}) \qquad \text{mod } 1. \tag{2.78}$$

We have expressed the eigenvalue problem of the (non-Abelian) Wilson loop as

$$W_{\mathbf{b}_1}(k_2)|\nu_1^j(k_1,k_2)\rangle = \mathrm{e}^{\mathrm{i}\nu_1^j(k_2)}|\nu_1^j(k_1,k_2)\rangle, \tag{2.79}$$

where $\nu_1^j(k_2)$ is the component of the Wannier center of the $j$-th Wannier function along the $\mathbf{a}_1$ direction. We refer the reader to Chapter 3 for an example of the application of this last formulation.

## 2.9 Projected spectral function

A very useful tool in band theory is the spectral function $A(E, \mathbf{k})$. It provides information about the probability that an electron of momentum $\mathbf{k}$ has energy $E$. In a many-body problem, it can be seen as an indication of how well the excitation created by adding a particle can be described within the free non-interacting particle picture. It can be seen as a distribution since, experimentally, such

probability is not always one due to the principle of uncertainty. In the following lines, we describe how to obtain the spectral function from the Green's function for free electrons. We refer the reader to Refs. [23, 24] for a more pedagogical introduction to this topic.

The spectral function is related to the imaginary part of the Green's function that describes the system. For a given Hamiltonian $\mathcal{H}$, we define the Green's function or resolvent operator as $G(z) = (z - \mathcal{H})^{-1}$, where $z = E + i\eta$ and $\eta \to 0^+$. The spectral function is then:

$$A(E, \mathbf{k}) \propto \operatorname{Im} \operatorname{Tr} G(z) = \operatorname{Im} \sum_{\ell} \langle \psi_{\ell,\mathbf{k}} | G(z) | \psi_{\ell,\mathbf{k}} \rangle = \operatorname{Im} \sum_{\ell} \frac{1}{E - E_{\ell,\mathbf{k}} + i\eta}, \tag{2.80}$$

where $E_{\ell,\mathbf{k}}$ is the eigenvalue associated to the state $|\psi_{\ell,\mathbf{k}}\rangle$. Practically, the $\eta$ parameter is related to the finite lifetime of the excitation, but for our purposes will be treated as a parameter to control the resolution of the plot.

We will work further in the text with the so-called projected spectral function. In this case, the spectral function is projected over a region of the system. This is interesting when the system presents more than one region, as we can find in ribbons and flakes, where we can identify bulk and different species of boundaries. The projection is done by adding a projection operator $\mathcal{P}_R$ in the numerator of Eq. (2.80) (the subscript $R$ denotes the region of the projection). This operator will be formed by the composition of projection operators that project into the individual orbitals present at the desired region.

The spectral function is presented in an energy *vs.* momentum plot. However, if the Hamiltonian depends on a set of parameters, the momentum can be replaced by any other of these parameters. With this in mind, we can study the spectral function of a certain Hamiltonian at fixed $\mathbf{k}$ points. The most general expression for the projected spectral function $A_R(E, \{\alpha_j\})$ is thus:

$$A_R(E, \{\alpha_j\}) = \operatorname{Im} \sum_{i} \frac{\langle \psi_i(\{\alpha_j\}) | \mathcal{P}_R | \psi_i(\{\alpha_j\}) \rangle}{\omega - E_i(\{\alpha_j\}) + \mathrm{i}\eta}, \tag{2.81}$$

where $\{\alpha_j\}$ is a set of parameters. The matrix element in the numerator represents the projection of the spectral function over the region $R$. We refer the reader to chapter 4 for an application of the spectral function to a specific lattice where we compute the localization of states in the edges of a ribbon. As well, we present there different projection operators to distinguish between the edges of the region (in the cases this distinction is possible).

# CHAPTER 3

# Corner modes of the breathing kagome lattice: origin and robustness

This chapter is devoted to the study of a lattice belonging to a symmorphic space group, namely the kagome lattice, belonging to the *p*6*mm* wallpaper group. The work presented here is published in Ref. [53]. This chapter is organized as follows: in section 3.1, we introduce the kagome lattice, a well-known two-dimensional lattice that displays many interesting features. In section 3.2, we present the tight-binding model we used to describe the pristine and *breathing* kagome lattice kagome lattice, where we introduce a certain perturbation that breaks some of the symmetries of the lattice. Next, we study the bulk spectrum of both the pristine and breathing kagome lattice. Additionally, we study the finite-size spectrum of the breathing which displays gapped boundary modes localized in the edges and, most importantly, in the corners. In section 3.3, we describe the spatial symmetries of the breathing kagome lattice, and how to study them starting from the breaking of the symmetries of the pristine kagome lattice. In section 3.4, we present the discussion about the properties of the corner modes in terms of the generalized chiral symmetry. Additionally, we present a study on different hopping terms that can be added to the Hamiltonian that do and do not perturb the corner modes. In section 3.5, we present the breathing kagome lattice implemented on a nearly-free electron gas platform, using a muffin tin potential to describe the lattice, as it was introduced in section 2.3. Finally, in section 3.6 we present the discussion, conclusions and outlook of this chapter.

## 3.1 Introduction

The kagome lattice, named after the bamboo-basket woven pattern shown in Fig. 3.1(a) [95] has attracted a lot of interest due to the variety of phases that it can describe, ranging from frustrated

antiferromagnets to spin liquids [96, 97, 98, 99] or nematic superconductors [100]. Due to its simplicity, it has also been realized in several experimental setups, like optical lattices [101, 102, 103], mechanical, electrical, and acoustic metamaterials [104, 105, 106] and even colloidal crystals [107, 108]. Another interesting platform where the kagome lattice has also taken an important role is in the field of photonic crystals [109, 110, 111, 112], where light propagation without backscattering even with disorder has been achieved in bosonic systems [113, 114].

The kagome lattice is also known because it is able to host higher-order topological boundary modes [115, 116] that are localized in the corners of a finite size sample–see Sec. 2.4 and figure 3.1(b). In the case of photonic crystals, these robust corner modes behave as stationary cavity modes. The robustness against perturbations was claimed to be due to higher-order topological protection [45, 105, 117, 118].

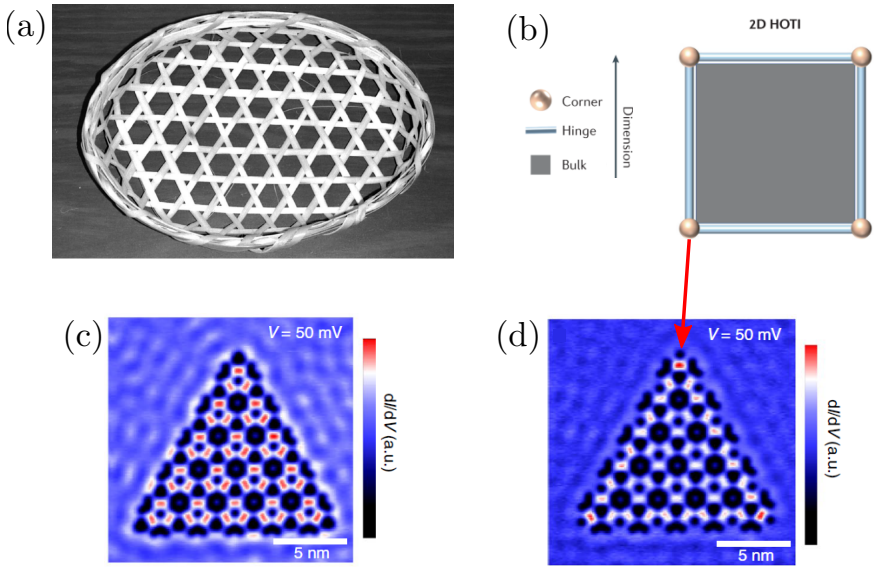


*Figure 3.1:* Kagome and breathing kagome lattices. (a) Bamboo-basket woven pattern adapted from [95]. The orbitals are placed in the corners of the triangular crossings. (b) Boundary states of a two-dimensional higher-order topological insulator. Adapted from [116]. Panels (c) and (d) present the two distinct phases that the breathing kagome lattice displays, studied in this chapter. Panel (c) represents the trivial phase while (d) shows the non-trivial phase, with the corner states highlighted. Both panels have been adapted from [45].

In this chapter, we have investigated the corner modes of the electronic *breathing* kagome lattice [117], which is a kagome lattice with alternating intra- and inter-cell hopping amplitudes, in contrast with the *canonical* kagome lattice, where all the hoppings have the same value. As we mentioned previously, the key feature of the breathing kagome lattice is that by tuning the breathing parameter, we are able to describe a phase that exhibits corner localized zero-energy states when it is built over a finite-size sample. We will call this phase topologically non-trivial in contrast with

the topologically trivial phase, where no corner modes appear. It could also be called topological in the same way as the SSH model is called so; however, we will show later in the chapter that the non-triviality of the phase does not correspond to any topology encoded in the system, exactly as in the case of the SSH model. See section 2.7 for the details of the SSH model.

A recent experimental realization of the kagome lattice is within the framework of artificially designed electronic lattices [45]. This technique has its origin in the manipulation of adatoms on metallic surfaces [39]. The main idea behind these experiments is to confine the surface state of a metal, which behaves as a two-dimensional electron gas, using a user-defined potential that patterns the lattice. The theoretical framework used in this work is known as the muffin-tin technique, presented in section 2.3.

## 3.2 The breathing kagome model: bulk and boundaries

The *breathing* kagome lattice is a two-dimensional lattice with alternating strong and weak hoppings in a kagome pattern [95, 117]. In Fig. 3.2(a), we present the unit cell and the choice of lattice vectors. The unit cell contains three lattice sites, labeled A, B, and C, respectively. The shape of the unit cell is considered to be a rhombus centered in the 1b Wyckoff position. In the simplest tight-binding formulation, where we consider only nearest-neighbor hopping terms, the Hamiltonian reads:

$$\begin{aligned}\mathcal{H} = -\sum_{\langle m,n\rangle} (\varepsilon_a a^\dagger_{m,m} a_{m,m} + \varepsilon_b b^\dagger_{m,m} b_{m,m} + \varepsilon_c c^\dagger_{m,m} c_{m,m}) + \\ + t_a \left(a^\dagger_{m,n} b_{m,n} + a^\dagger_{m,n} c_{m,n} + b^\dagger_{m,n} c_{m,n}\right) + \\ + t_b \left(a^\dagger_{m,n}(b_{m-1,n+1} + c_{m,n-1}) + b^\dagger_{m,n} c_{m,n-1}\right) + \text{h.c.},\end{aligned} \tag{3.1}$$

where $m, n$ index the unit cell, the notation $\langle m, n\rangle$ means nearest-neighbors, and h.c. stands for hermitian conjugate. The first line corresponds to the onsite energies, the second to the intracell hoppings, associated with $t_a$, and the last line corresponds to the intercell hoppings, associated by $t_b$. If we Fourier transform the previous Hamiltonian by choosing the basis $\Psi = \{a_{\mathbf{k}}, b_{\mathbf{k}}, c_{\mathbf{k}}\}^{\mathrm{T}}$, we obtain the $\mathbf{k}$ dependent Hamiltonian $h(\mathbf{k})$ that reads

$$h(\mathbf{k}) = -\begin{pmatrix} \varepsilon_a & t_a + t_b e^{i\mathbf{k}\cdot\mathbf{a}_3} & t_a + t_b e^{-i\mathbf{k}\cdot\mathbf{a}_2} \\ t_a + t_b e^{-i\mathbf{k}\cdot\mathbf{a}_3} & \varepsilon_b & t_a + t_b e^{-i\mathbf{k}\cdot\mathbf{a}_1} \\ t_a + t_b e^{i\mathbf{k}\cdot\mathbf{a}_2} & t_a + t_b e^{i\mathbf{k}\cdot\mathbf{a}_1} & \varepsilon_c \end{pmatrix}, \tag{3.2}$$

where $\mathbf{k}$ the crystal momentum and $\mathbf{a}_{1,2} = (\pm\frac{1}{2}, \frac{\sqrt{3}}{2})$ the lattice vectors. The vector $\mathbf{a}_3 = \mathbf{a}_2 - \mathbf{a}_1 =$

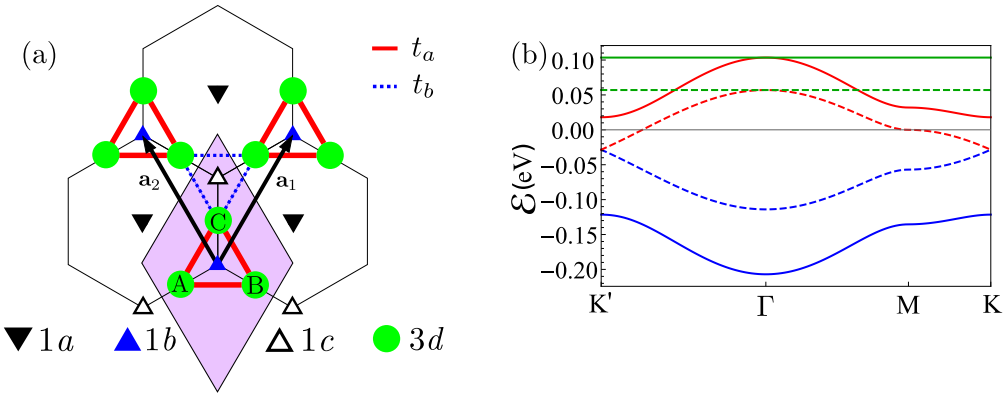


*Figure 3.2:* The breathing kagome model (bulk). (a) Lattice model with three sublattice sites A, B, and C, and hopping parameters $t_a$ and $t_b$. The black triangles represent the $1a$ Wyckoff position, the blue triangles represent the $1b$ Wyckoff position and the empty triangles represent the $1c$ Wyckoff position. The lattice sites fall on the $3d$ Wyckoff positions, represented with green circles. The purple-shaded rhombus is the choice of unit cell. (b) Band structure of the kagome model for the breathing (solid lines) and non-breathing (dashed lines) phases. Notice that the non-breathing phase is gapless at the **K** and **K′** points. The corresponding values of $t_a = 0.38t_b$ and $t_b = 0.075\,\text{eV}$ are obtained from Ref. [45] by fitting the bands calculated within the tight-binding approach with the ones derived using the muffin-tin method. This corresponds to $\delta \approx -0.45$ and $t_0 \approx 52$ meV.

$(-1, 0)$ has been added to simplify the expression of the Hamiltonian in momentum space. We show in Fig. 3.2(b) the band structure for a periodic lattice both in the *breathing* phase ($t_a \neq t_b$) (solid lines) and in the *canonical* or pristine phase ($t_a = t_b$) (dashed lines). As we can see, the breathing kagome lattice displays a gap that closes at **K**, **K′** points when the hoppings are the same (canonical kagome lattice). This will be explained using group theory arguments in Sec. 3.3. Both the canonical and breathing phases display a flat band at $E_{\text{flat}} = t_a + t_b$. By changing the values of the hoppings we can shift the position in energy of this flat band. Additionally, it can acquire a certain dispersion with the addition of next-to-nearest neighbor hoppings.

We will now apply the breathing dimerization technique to the canonical/pristine kagome lattice. Figure 3.3 presents the energy bands of a finite-size lattice obtained using the following breathing parametrization of the hopping amplitudes: $t_{a,b} = (1 \pm \delta)t_0$ with $t_0 < 0$. The parameter $\delta$ is the called the breathing factor: it allows us to study the different phases of the breathing kagome lattice by changing its sign. This dimerization technique has been used before in the SSH model back in Section 2.7 in order to obtain the boundary modes in the chain. In the limiting case where $\delta = -1$, the breathing kagome lattice is decomposed into isolated sets of atoms[1]: single atoms in the corners of the flake, dimers along the edges, and trimers in the bulk-like part of the flake.

[1] In the case of the SSH we obtained single atoms in the boundaries of the chain and dimers in the bulk-like part of the chain. We refer the reader to section 2.7 for a simpler version of the effects of this dimerization technique applied to the SSH model.

Particularly, for this calculation, we have chosen a size of 630 lattice sites, or 20 unit cells along the side of the triangle. After diagonalizing the Hamiltonian built over the finite-size sample, we show in Figures 3.3(c) to 3.3(e) the spatial localization of selected states for $\delta = -0.5$, revealing the existence of bulk–Fig.3.3(c), edge–Fig.3.3(d)– and corner modes–Fig.3.3(d). We have assigned a different color for each lattice site: red for lattice site A, green for lattice site B and blue for lattice site C. For the case of the corner modes, we notice that the wave function has non-zero weight in only one sublattice (A, B, or C), precisely the sublattice species located on the lattice site at the corner. More precisely, the flake ends in an A-site in the upper corner, and so the corner mode has non-zero weight in the A sublattice. The same happens on the left corner with the B-species and on the right one with the C-species. This fact will be used further in the text to fathom whether a zero energy mode is truly a corner mode or not in terms of localization. In this sense, if the mode has non-zero weight in a different sublattice, it will not be considered a proper corner mode, even if the localization decays exponentially towards the bulk-like part of the flake.

Figure 3.3(b) is a zoom-in over the energy scale to reveal that the corner modes are truly pinned to zero energy, with no bending in the spectrum. For $\delta = -1$, the fully disconnected case is recovered (strict dimerization), and the corner modes remain at zero energy, also for a wide range of values of the dimerization parameter, and, eventually, they hybridize with the bulk modes. Hence the breathing kagome has two distinct phases, one featuring zero-energy corner-localized modes and edge modes (non-trivial with $\delta < 0$) and one where such modes are absent (trivial with $\delta > 0$), separated by a gapless one (canonical with $\delta = 0$).

In appendix B we present a possible interpretation of the (breathing) kagome lattice as a set of stacked SSH chains with varying lengths coupled to each other through an extra lattice site.

## 3.3 Spatial symmetries of the kagome/breathing kagome lattice

We now discuss the symmetry properties of the model. The canonical kagome lattice ($\delta = 0$) belongs to the space group $p6mm$ (#183 in the ITA [119]). The point group associated to this space group is $C_{6v}$, characterized by a six-fold rotational symmetry $C_6$ that closes the gap at the $\mathbf{K}$ and $\mathbf{K}'$ points in the first Brillouin zone–see dashed lines in Fig. 3.2(b).

After introducing the breathing distortion, the symmetry is reduced, and hence the space group of the breathing kagome lattice is a subgroup of $p6mm$, *i. e.*, space group $p3m1$ (#156 in the ITA [119]). As mentioned, this space group is a subgroup of $p6mm$ and has a three-fold rotation operation. Now, $C_6$ is not a symmetry anymore, and the point group is reduced from $C_{6v}$ to $C_{3v}$: the

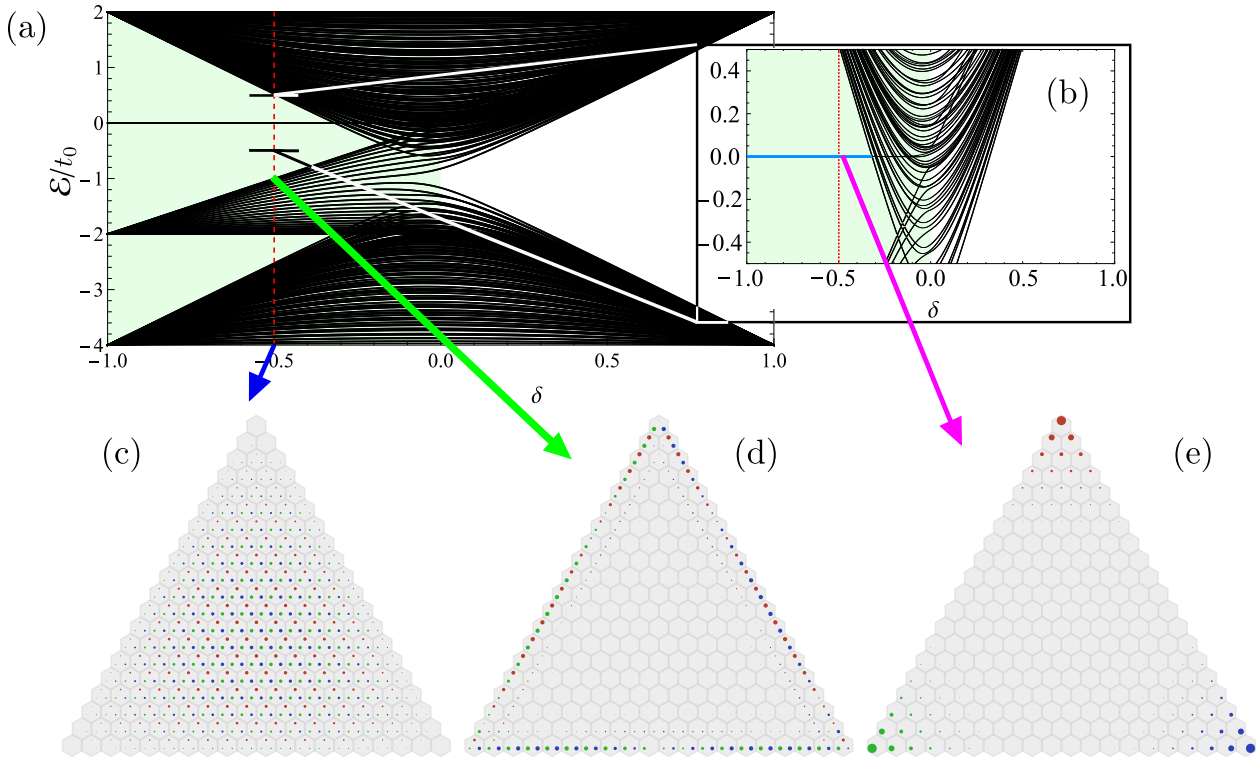


*Figure 3.3:* The breathing kagome model (finite size flake) (a) Spectrum of a finite-size lattice and (b) zoom-in for low-energy scale. For $\delta < 0$, three-fold degenerated energy eigenvalues can be found pinned at zero. These zero energy modes have been highlighted in light blue. Panels (c), (d), (e) show the exponential decay of the wave function for $\delta = -0.5$ in the bulk, edge, and corner, respectively. The size of the dots is set for convenience proportional to $|\psi|^{0.2}$.

two-dimensional irreducible representation that protected the degeneracies at the **K** and **K′** points, now splits into two one-dimensional ones (see table 3.1) and thus the gap opens at the **K** and **K′** points–see solid lines in Fig. 3.2(b).

The group/subgroup relation between $p6mm$ and $p3m1$ also affects the naming of the Wyckoff positions [25, 26, 27]. For this case, the $2b$ Wyckoff position from $p6mm$ splits into two non-equivalent Wyckoff positions of $p3m1$, *i. e.*, $1b$ and $1c$, both with site-symmetry group $C_{3v}$. This distinction will be crucial for studying the character of the bands, which will be discussed in Sec. 3.5 where we apply the concepts introduced in Sec. 2.6 to the lattice. Additionally, the $3c$ Wyckoff position is now called $3d$ since its site-symmetry group reduces from $C_{2v}$ to $C_m$. This last case reflects how a maximal Wyckoff position now becomes a non-maximal one since $C_m \subset C_{3v}$, $C_{2v}$. Figure 3.2(a) shows the Wyckoff positions of $p3mm$ distributed in space. We have used symbols with the same symmetry as the point group of the Wyckoff position. In the case of the $3d$ Wyckoff position, we have used a circle for simplicity due to the reduced symmetry of this Wyckoff position.

## 3.4 The generalized chiral symmetry and its consequences

A possible explanation for the pinning of the corner modes to zero energy is based on the concept of generalized chiral symmetry. It follows the same line of reasoning as the chiral symmetry in the SSH model [20, 120, 87], as introduced in Sec. 2.7. Here, we repeat how to generalize the chiral symmetry for a unit cell containing three sites, in line with Ref. [105].

### 3.4.1 Generalized chiral symmetry

First of all, it should be noted that chiral symmetry, also known as sublattice symmetry, is *not* a symmetry operation: instead of commuting with the Hamiltonian, the chiral symmetry operator anti-commutes with it. Nevertheless, in this chapter, we will refer to this operation as chiral symmetry for consistency with existing literature. To introduce the generalized chiral symmetry for the case of the kagome lattice, we use the Bloch Hamiltonian (3.2) and define $\mathcal{H}_1 = \hat{\mathcal{H}}$. The kagome lattice is not bipartite; it has an odd number of lattice sites in the unit cell, unlike the one- and two-dimensional SSH models, which show an even number of lattice sites. The generalized chiral symmetry is defined as some operator $\Gamma_3$ that satisfies

$$\Gamma_3^{-1}\mathcal{H}_1\Gamma_3 = \mathcal{H}_2, \tag{3.3a}$$

$$\Gamma_3^{-1}\mathcal{H}_2\Gamma_3 = \mathcal{H}_3, \tag{3.3b}$$

$$\mathcal{H}_1 + \mathcal{H}_2 + \mathcal{H}_3 = 0. \tag{3.3c}$$

When combining the last equation with the previous two, it follows that $\Gamma_3^{-1}\mathcal{H}_3\Gamma_3 = \mathcal{H}_1$. Following this reasoning, the generalized chiral symmetry introduced in Eqs. (3.3) is completely analogous to the chiral symmetry of the SSH model [20] (see Sec. 2.7). However, in this case $[\mathcal{H}_1, \Gamma_3^3] = 0$, which implies $\Gamma_3^3 = \mathbb{I}_3$ and the eigenvalues are given by $1, \exp[\pm 2\pi\mathrm{i}/3]$. Therefore, up to a unitary transformation, we can write

$$\Gamma_3 = \begin{pmatrix} 1 & 0 & 0 \\ 0 & \mathrm{e}^{2\pi\mathrm{i}/3} & 0 \\ 0 & 0 & \mathrm{e}^{-2\pi\mathrm{i}/3} \end{pmatrix}. \tag{3.4}$$

Furthermore, we now have three eigenvalues to consider ($\mathcal{H}_1$, $\mathcal{H}_2$, and $\mathcal{H}_3$ each have the same set of eigenvalues $\epsilon_1$, $\epsilon_2$ and $\epsilon_3$, since the Hamiltonians differ by a unitary transformation). By taking the trace of Eq. (3.3c), we find

$$\mathrm{Tr}[\mathcal{H}_1 + \mathcal{H}_2 + \mathcal{H}_3] = 3\mathrm{Tr}[\mathcal{H}_1] = 0, \tag{3.5}$$

where we used the first two lines of Eqs. (3.3) and the fact that the trace is cyclic. This means that the sum of the three eigenvalues vanishes, $\epsilon_1 + \epsilon_2 + \epsilon_3 = 0$.

Now, the same reasoning could apply to the eigenstates. However, there is one crucial difference. If $\mathcal{H}_1|\psi\rangle = \epsilon_1|\psi\rangle$, with $|\psi\rangle$ being an eigenstate, the wave functions $\Gamma_3|\psi\rangle$ and $\Gamma_3^2|\psi\rangle$ are not necessarily also eigenstates of $\mathcal{H}_1$. In the SSH chain, this relationship is guaranteed by the relation $H_1 = -H_2$. This does not hold for the generalized chiral symmetry, since

$$\mathcal{H}_1\Gamma_3|\psi\rangle = \Gamma_3\mathcal{H}_2|\psi\rangle, \tag{3.6}$$

and since $|\psi\rangle$ is not per se an eigenstate of $\mathcal{H}_2$, it is not proven that $\Gamma_3|\psi\rangle$ is an eigenstate of $\mathcal{H}_1$. Therefore, the generalized chiral symmetry does not work in the same way as the chiral symmetry, and there is no guarantee that a zero-energy mode will remain pinned to zero.

### 3.4.2 Perturbating the corner modes

In the last part of this section, we study the influence of perturbations on the electronic structure of a finite-size triangular flake, similar to what was done in Ref. [121]. Since boundary modes appear in boundaries that respect the symmetries of the lattice, we use a triangular flake, which preserves the $C_{3v}$ point group of the lattice.

We begin with Fig. 3.4, where all the perturbations that have been added break different sets of symmetries. In Fig. 3.4(a) we add random onsite energies to all lattice sites of the flake, all of them ranging between 0 and $0.2t_0$. After finding similar results for several different disorder realizations, we only show a single possible realization of random onsite energies. This perturbation breaks all possible spatial symmetries while preserving the connectivity of the kagome lattice. This means that the generalized chiral symmetry is preserved in terms of connectivity, but spatial symmetries are no longer mapping the lattice to itself. We observe that the corner modes are neither pinned to zero energy nor degenerate; each one departs from zero at a different energy. If we look at the localization of the eigenstate around the corner, we see that the wave function has non-zero weight in the three sublattices and that each circle has a different diameter as a consequence of the breaking of the symmetries. This may not be distinguished easily in the plot, but was confirmed numerically. As mentioned previously, we don't consider this mode to be truly localized at the corner.

Figures 3.4(b) to 3.4(f) show other types of perturbations: we introduce new hopping terms that change the connectivity of the lattice while preserving both $C_{3v}$ and/or generalized chiral symmetry. The intensity of those hopping terms has been selected to the same value of the maximum random onsite energy ($0.2t_0$) used in Fig. 3.4(a).

In Fig. 3.4(b), we show a perturbation that couples sites of the same sublattices up to the nearest neighboring cells (not neighboring lattice sites), thus breaking generalized chiral symmetry. As

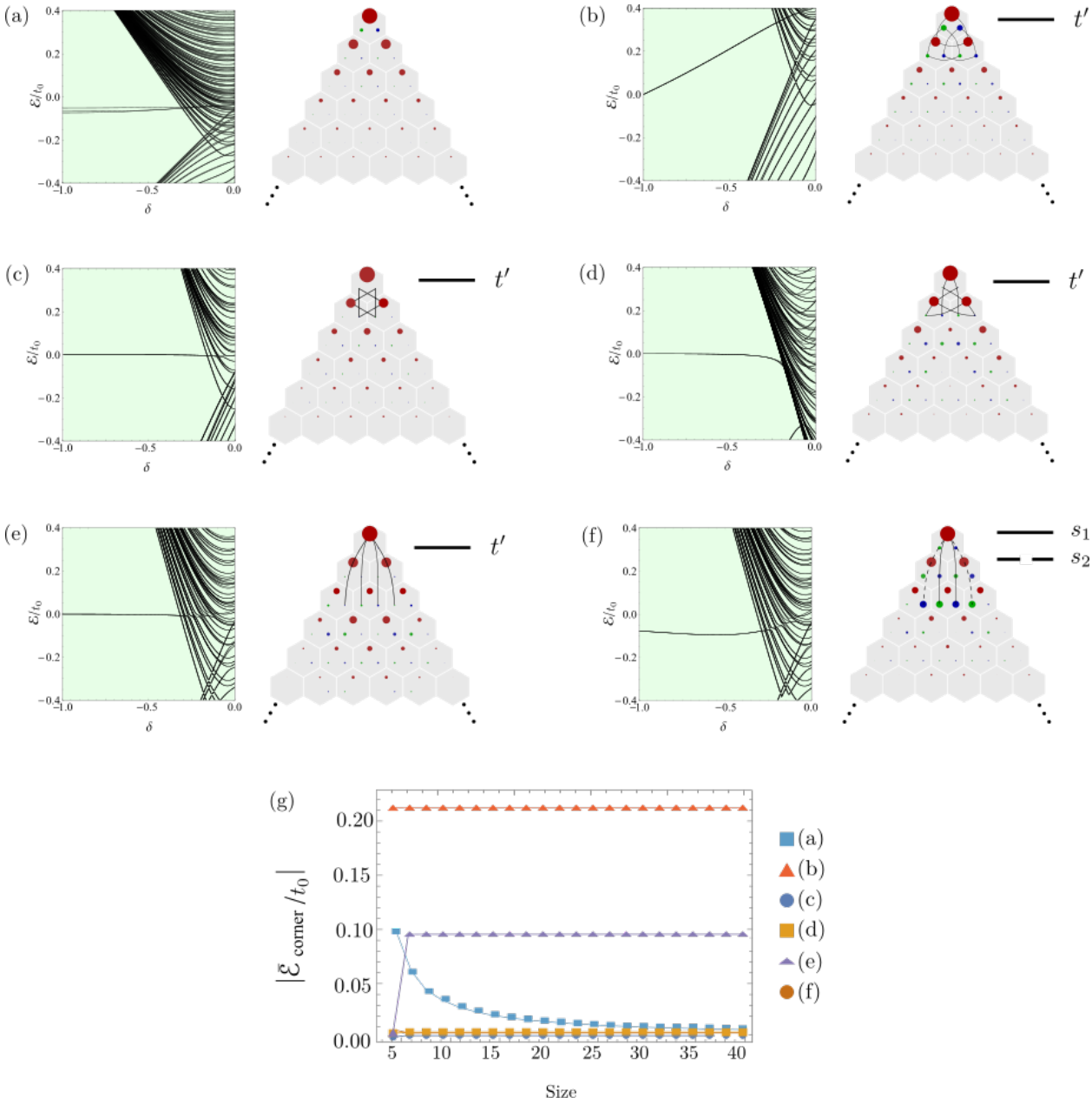


*Figure 3.4:* Set of perturbations that have been studied to detect the protection mechanisms of the corner modes. Each panel displays the close-up of the spectrum plus the localization in real space of the wave function, thus, a visualization of the local density of states. (a) random disorder in all lattice sites, (b) perturbation breaking generalized chiral symmetry, thus connecting lattice sites of the same species, (c) perturbation connecting second-order nearest neighbors, (d) perturbation connecting third-order nearest neighbors, (e) long-range local perturbation with different sign, (f) long-range local perturbation with same sign, (g) influence of the size on the average energy, in absolute value, of the corner modes on each of the perturbations.

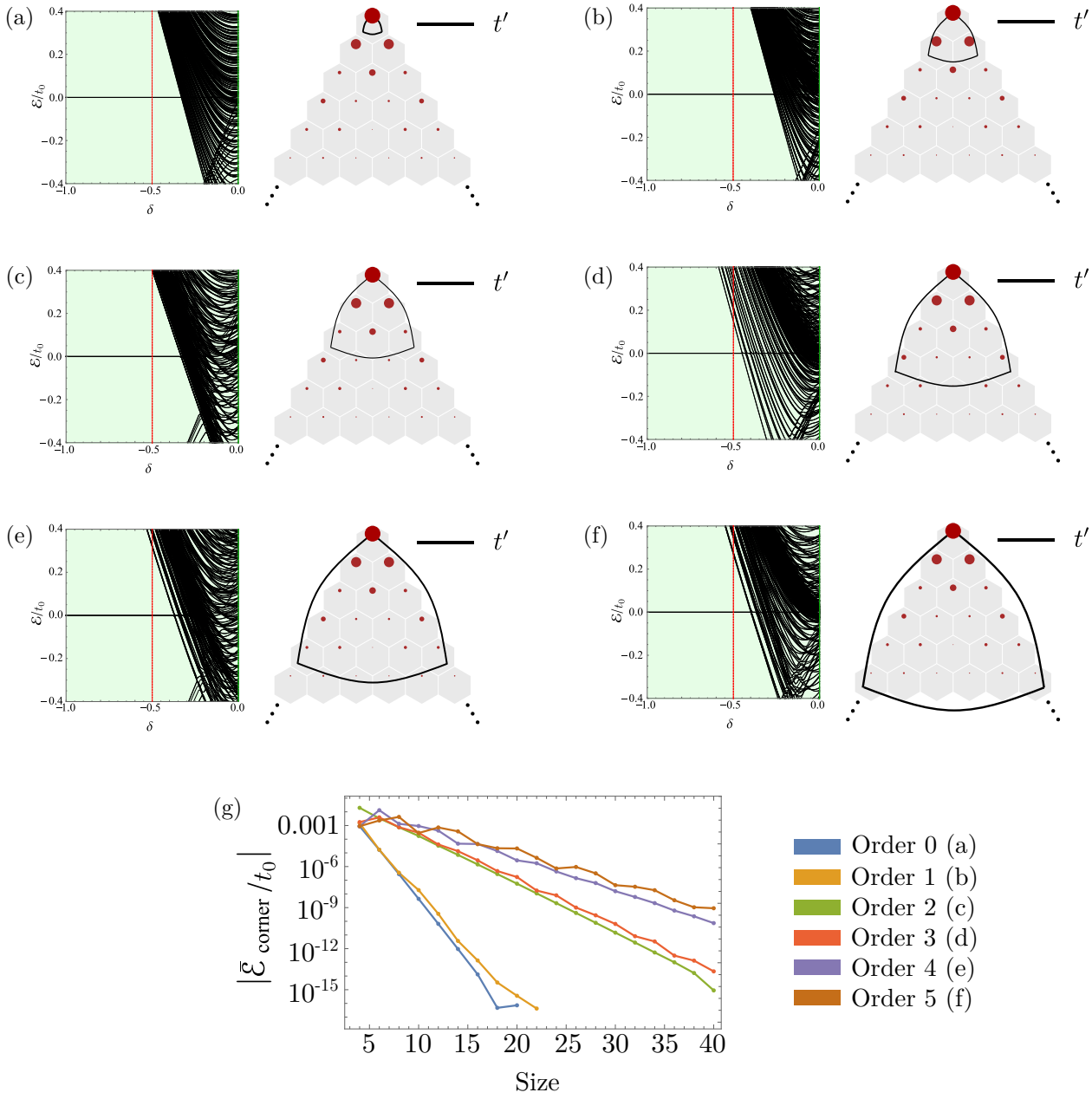


*Figure 3.5:* Set of perturbations that have been studied to detect the protection mechanisms of the corner modes. Each panel displays the close-up of the spectrum plus the localization in real space of the wave function, thus, a visualization of the local density of states. From (a) to (f) the order of the neighboring unit cell increases from 0 to 5. Panel (g) displays the influence of the size on the average energy, in absolute value, of the corner modes on each of the perturbations. The scale is logarithmic since the dependence is exponential.

soon as we depart from the fully dimerized case ($\delta = -1$), the corner modes are no longer pinned at zero energy, but they are still degenerate since the flake remains $C_{3v}$ symmetric. Again, the wave function has nonzero weight in all three sublattices, but this time the size of the circles is related by a mirror symmetry that crosses the flake vertically.

Figures 3.4(c) to 3.4(e) show different choices of long-range hopping terms in increasing order of neighbor coupling, which preserves both generalized chiral symmetry and $C_{3v}$ symmetries. However, the wave function shows nonzero weight in the three sublattices due to the different connectivity of the lattice.

The cases in Figs. 3.4(e) and 3.4(f) correspond to the perturbations introduced in Ref. [121], which are used as immunity checks for the robustness of the corner modes. These are long-range hopping amplitudes $s_1$ and $s_2$ applied locally at the corners. We have studied two different configurations: in Fig. 3.4(f) the spectrum is generated using $s_1 = -s_2$, with $|s_1| = |s_2| = 0.2t_0$, while the spectrum in Fig. 3.4(e) is generated using the same sign for the perturbations. The perturbation shown in Fig. 3.4(f) leads to degenerate modes, which are, however, no longer pinned to zero energy (not even in the fully dimerized case). When using the same sign for the perturbation, the modes are degenerate and located at zero energy in the fully dimerized case, but move away as $\delta$ increases. In both cases, the wave function is delocalized over all three sublattices. These last perturbations respect the generalized chiral symmetry and the $C_{3v}$ symmetry of the flake but are applied only locally to the corners.

Finally, we present in Fig. 3.4(g) the evolution of the energy of the corner modes of the different perturbations with increasing size of the flake. We plot the average of the three closest-to-zero eigenvalues versus the number of unit cells along the edge of the flake. None of them show an exponential behavior with the size. Some of the perturbations pin the corner modes to values different from zero, but no dependence on size is detected. The light blue curve in Fig. 3.4(g) shows the evolution of the energies of the flake with random onsite energies. To perform this calculation, we generated 20 configurations for each size, and then, we took the average of the energies of the corner modes. We see a $1/N$ evolution of the eigenvalues, where $N$ is the total number of unit cells. This precise evolution suggests that for small sizes, the corner modes are not pinned to zero due to poor localization. In the thermodynamic limit, where $N \to \infty$, the long tails of the modes will eventually remain isolated, even if the intercell hopping is not zero, and thus the corner modes approach the onsite energies of the corner, as if they were properly isolated.

We present now in Fig. 3.5 a total different type of perturbation that respects spatial symmetries, connectivity, and generalized chiral symmetry. This perturbation is presented in six different orders

of neighboring unit cells. The first case is the pristine breathing kagome lattice. The rest of the cases are a generalization of this connectivity, closing an ABC loop. It is remarkable how the three closer-to-zero eigenvalues remain pinned to zero for the whole range of values of $\delta$ considered and show an exponential localization in just the sublattice conforming to the corner. Also, the averaged value of them decays to zero exponentially with size–shown in Fig. 3.5(g)–, which proves that the hoppings considered pin the modes to zero energy.

In addition to these results, we refer to the supplementary material of Ref. [45] for a similar study of the perturbation of the corner modes. In the field of photonic crystals, we refer to Ref. [118] for a similar analysis of the robustness of corner modes in a photonic breathing honeycomb lattice. In addition, in the field of plasmonics, we refer to Ref. [122] for a realization of the breathing kagome lattice in such framework, as well as for a study of the robustness of corner modes. We refer to Ref. [123] and the supplementary material of Ref. [124] for a complementary study of the robustness of the corner modes in waveguide arrays. Finally, other geometries may also host robust corner modes, as is the case of Ref. [125, 126, 127, 128]. In these geometries, chiral symmetry, in addition to spatial symmetries, yields further protection of the corner modes.

## 3.5 The muffin-tin method applied to the breathing kagome lattice

In this final section, we will analyze the breathing kagome lattice (Ref. [45]) within the framework of the nearly-free two-dimensional electron gas confined to a muffin-tin potential. As presented in Sec. 2.3, the muffin-tin technique describes a specific class of experiments, where a two-dimensional electron gas hosted on the surface of a noble metal is patterned by molecules or atoms arranged in a precise and periodic fashion [33, 45, 129, 34]. Specifically, in the experimental setup of Ref. [45], the two-dimensional electron gas is the surface state hosted by the (111) surface of Cu, and it was decorated with a set of CO molecules adsorbed at certain positions, using the tip of a scanning tunneling microscope [129]. The muffin-tin method does not involve atomic orbitals or species, nor chemical bonds between them. The lattice sites are built with artificial interacting quantum dots (also known as artificial atoms [58]) connected by hopping amplitudes, which are always long-range and modeled by potential wells or barriers. It is possible to work with $s$-like or $p$-like orbitals, which allow us to study more complex interactions [129, 52]. Practically, this is achieved by changing the size of the potential wells, which brings the energy levels up or down. This property suggests that the muffin-tin method always considers all the possible hopping terms between all the lattice sites, namely those respecting generalized chiral symmetry and those that do not. Therefore, only the

spatial symmetry properties of the potential will affect the behavior of the two-dimensional electron gas.

### 3.5.1 Muffin-tin potentials for canonical and breathing kagome lattices: a guide

To study the breathing kagome lattice, we have considered three different configurations of CO molecules, accounting for the canonical gapless phase and the two breathing ones. Each molecule is modeled by a cylinder of radius $a = 0.3$ nm and height $V_0 = 0.9$ eV [45] placed at position $\mathbf{r}_n$:

$$V_n(\mathbf{r}) = \begin{cases} V_0 > 0 & \text{if } |\mathbf{r} - \mathbf{r}_n| < a, \\ 0 & \text{otherwise.} \end{cases}$$

The full landscape is the superposition of the potential of each molecule. The design of the potential well is done by placing CO molecules forming the negative image of the lattice (a muffin-tin). Once the potential well defining the unit cell is built, the full lattice is constructed by translating it along the direct lattice vectors $\mathbf{a}_{1,2} = \mathrm{a}_0/2(\pm 1, \sqrt{3})$, where $\mathrm{a}_0/2 = 6\sqrt{3}\ \mathrm{a}_0^{\mathrm{Cu}}$ and $\mathrm{a}_0^{\mathrm{Cu}} = 0.265$ nm is the interatomic distance of the substrate.

Let's now define the steps followed to realize the kagome lattice within the muffin-tin technique, both for the canonical and the breathing phases, using CO molecules on top of the Cu (111) surface.

### 3.5.2 Canonical phase

We begin by studying the geometry of the kagome lattice in terms of Wyckoff positions. In the canonical form, the kagome lattice is a triangular lattice belonging to the *p*6*mm* plane space group. Such space group has the following maximal Wyckoff positions: 1*a*, 2*b*, 3*c*. In the case of the kagome lattice, the lattice sites are the 3*c* Wyckoff position, so artificial atoms must be constructed around these positions, leaving the remaining ones unoccupied. To realize the muffin-tin potential, we place CO molecules to block the wave function from localizing in the unoccupied Wyckoff positions. Thus, we have placed six CO molecules forming a hexagon around the 1*a* Wyckoff position and a single molecule on the 2*b* Wyckoff position, thus leaving the 3*c* Wyckoff position free. In this way, the two-dimensional electron gas will be confined to the lattice formed by the 3*c* Wyckoff positions, reproducing the canonical kagome lattice. We have built three interacting artificial atoms located at the 3*c* maximal Wyckoff positions. The connection between these artificial atoms is the same within the unit cell and between them, reflecting the fact that in the tight-binding model the intra- and intercell hopping must be the same to build the canonical/pristine kagome lattice. The left panel of Fig. 3.6 represents this process step by step, in panels from (a) to (f). To be

consistent with the text, we have represented Wyckoff positions with elements with the same point group symmetry as the site-symmetry group of each maximal Wyckoff position.

### 3.5.3 Breathing phase

When we introduce the breathing distortion in the kagome lattice, we break the $C_6$ symmetry, so the space group is reduced from $p6mm$ to $p3m1$, one of its subgroups. This group/subgroup relation splits the $2b$ Wyckoff position into two Wyckoff positions, namely $1b$ and $1c$, which are now non-equivalent. Additionally, the symmetry of the $3c$ Wyckoff position, now called $3d$, reduces from $C_{2v}$ to $C_m$. The $1b$ Wyckoff position is surrounded by three $3d$ Wyckoff positions, so if we place a single molecule in the $1b$, and three molecules in the $1c$, we make the effective intercell hopping amplitude smaller than the intracell one, since the wider potential well formed inside the unit cell displays more energy levels. The intercell hopping is modeled by a potential well that is very narrow, thus displaying less energy levels and making the hopping amplitude smaller. This situation corresponds to the trivial phase of the breathing kagome lattice, which does not show corner modes.

The non-trivial case can be achieved by inverting the feature at the $1b$ and $1c$ Wyckoff positions. Now the $3d$ Wyckoff positions have a smaller effective intracell hopping amplitude compared to the intercell one, so the corners would host zero energy modes since they are weakly connected to the rest of the lattice. Again, we have confined the two-dimensional electron gas to a lattice formed by the $3d$ Wyckoff positions, thus reproducing the breathing kagome lattice.

The right panel of Fig. 3.6 represents this process step by step, in panels from (a) to (i). To be consistent with the text, we have represented Wyckoff positions with elements with the same point group symmetry as the site-symmetry group of the Wyckoff position. We have used circles in the 3d case. Panels (d), (f), and (h) correspond to the trivial phase while (e), (g), and (i) correspond to the non-trivial phase. Panels (a), (b), and (c) are common to the two situations.

Once the potentials are built, we show in Figs. 3.7(a), 3.7(c) and 3.7(e) the choice of unit cells that we have used to build the corresponding potential that reproduces the canonical kagome lattice, and the two breathing phases, respectively. Many other choices can be realized, either by changing the molecule set-up or choosing different lattice vectors or different origins. We use configurations symmetric with respect to the mirror plane $m_{\bar{1}1}$ centered either at the $1b$ or at the lower $2b$ Wyckoff positions, depending on whether we work with $p3m1$ or $p6mm$, respectively. Such geometric locus represents the center of mass of the three lattice sites inside the choice of unit cell, as well as the

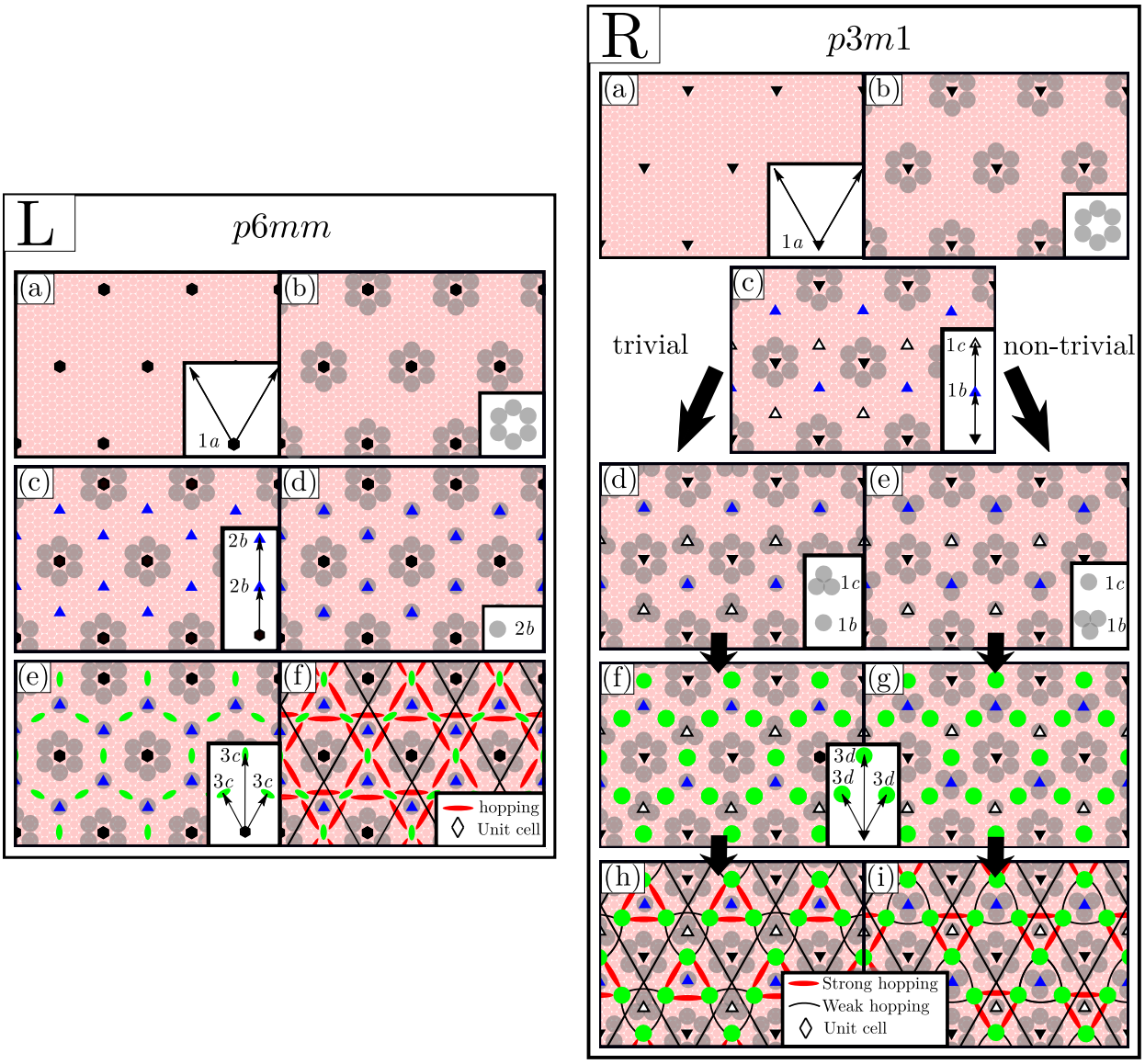


*Figure 3.6:* Steps for realizing the muffin-tin potential for the kagome lattice in the canonical and breathing phases using CO molecules. On the left we show the process for building the potential well for the canonical kagome lattice: (a) define the 1$a$ Wyckoff position in the substrate. (b) Accommodate 6 molecules around it to block such Wyckoff position. (c) Locate the 2$b$ Wyckoff position and (d) block it with a single CO molecule. (e) The remaining Wyckoff positions are the 3$c$ ones. Finally, (f) displays the rhomboidal choice of unit cell and the effective hopping in red. On the right we start again by (a) locating the 1$a$ Wyckoff position and accommodating six molecules around it. Next, we identify where the 1$b$, 1$c$ Wyckoff positions are (c). Depending on the trivial/non-trivial breathing phase we want to explore, we place one or three molecules in the 1$b$ and three or one in the 1$c$, reflected in panels (d) and (e), respectively. The remaining Wyckoff positions are 3d, as it is shown in panels (f) and (g). Finally, panels (h) and (i) show the unit cell and the strong/weak effective hoppings built in the lattice.

center of “positive" charge [1], since it represents the center of mass and charge of the atomic nuclei in an actual kagome lattice.

We solve the Schrödinger equation by expanding the potential in Fourier components in reciprocal space [15] (see Sec. 2.3). By obtaining the coefficients of such expansion, we can reconstruct the band structure and the Bloch wave functions for the three different configurations. In Figs. 3.7(g), 3.7(h), and 3.7(i), we show the band structures along the high-symmetry path. In the bulk, the two set-ups of molecules are related by a $m_{11}$ mirror passing through the upper lattice site (geometric transformation). This explains why the eigenvalues of the two phases are the same. We nevertheless expect the eigenstates to behave differently, so we will distinguish these two phases via topological and symmetry markers, such as Wilson loops, bulk polarization, and Topological Quantum Chemistry.

### 3.5.4 Topology and symmetries of the muffin-tin potentials

Let’s study now the Wilson loop operator and its spectrum applied to the breathing kagome lattice. As we introduced in the previous chapter, this method is widely used in the literature to distinguish topological phases [17, 88, 76]. The spectrum of the Wilson operator allows to determine the topological character of a band structure, depending on its behavior.

We recall the expressions for the Wilson loop operator for both single and degenerated bands since we are interested in describing the Wilson spectrum of both the canonical (with three degenerated bands) and the breathing phases (with single+degenerated bands):

$$W^{m,n}_{(k_1+2\pi,k_2)\leftarrow(k_1,k_2)} = \mathcal{P}\,\exp\left\{-\mathrm{i}\int_{\ell}\mathbf{A}_{m,n}\cdot\mathrm{d}\ell\right\}, \tag{3.7}$$

where $m, n$ are the band indices, the symbol $\mathcal{P}$ represents path ordering operation and $\ell$ is the path between points $(k_1, k_2)$ and $(k_1 + 2\pi, k_2)$. For the single band case, we just take $m = n$. We work with the discrete version of Eq. (3.7) by discretizing the reciprocal space along the two reciprocal space directions [88]. See Sec. 2.8 for a detailed formulation of discrete expressions of topological invariants.

Since the Wilson loop along $\mathbf{b}_1$ is a function of $k_2$, we can evaluate the Wilson loop for all the steps in the discretization along $k_2$. This is called Wilson spectrum, and it is related to the shifting of the Wannier center along the $\mathbf{a}_2$ direction. Due to $m_{\bar{1}1}$ symmetry, the Wilson spectrum along $\mathbf{b}_1$ is the same as along $\mathbf{b}_2$, and so will be the Wannier center [17]. The position of the Wannier center

[1] This will be useful when we talk about bulk polarization in terms of relative displacement of the charge centers.

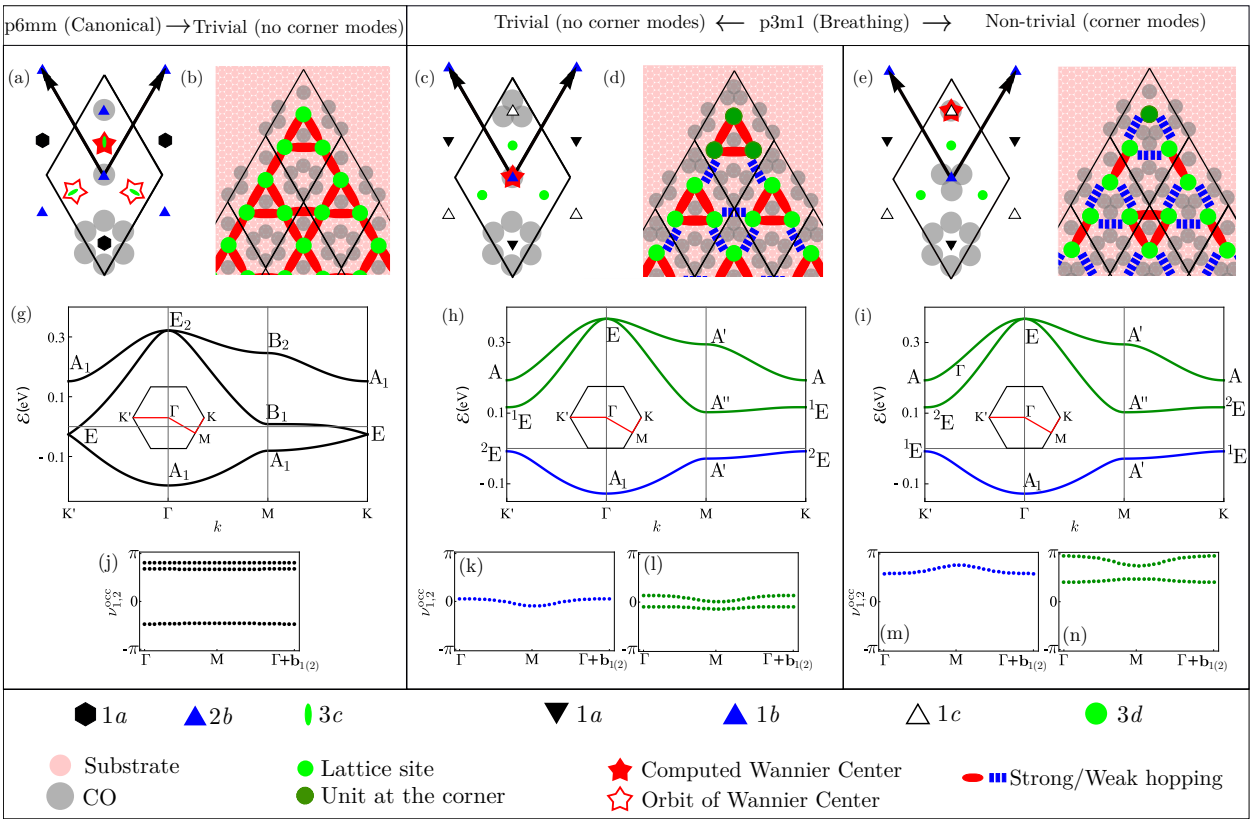


*Figure 3.7:* Summary of the results obtained for the muffin-tin calculation of the canonical/breathing kagome lattice. The overall legend affects the three cases, while each column has its legend for the Wyckoff positions, which are called differently due to the group/subgroup relation. Potential wells defining the unit cells for the non-breathing (a) and breathing phases (c,e). The Wyckoff positions have been represented with an element with the same symmetries as in the point group associated with each Wyckoff position: hexagon, $C_{6v}$, triangle, $C_{3v}$, and ellipse, $C_{2v}$. In the case of the $3d$ Wyckoff position, we have used a circle for simplicity due to the reduced symmetry of this Wyckoff position (the point group associated is $C_m$, which includes just mirror and identity). Upper corner of a finite size sample of kagome lattice; non-breathing (b) and breathing phases (d,f). Panels (g) to (i) show the corresponding band structures plus the irreducible representation assignment at each high-symmetry point. Finally, panels (j) to (n) show the Wilson spectra obtained for the first three bands of each configuration.

is equivalent to the value of the bulk polarization since the Wannier center represents the center of the negative electronic cloud. For $C_n$-symmetric insulators, the bulk polarization is a $\mathbb{Z}_n$-quantized topological invariant [73, 91, 92, 93], where $n$ is the order of the rotation that characterizes the space group. In our case, we expect to find a $\mathbb{Z}_3$ index for the breathing phases due to the $C_{3v}$ symmetry of the lattice. In the case of the canonical kagome lattice, the bulk polarization is always zero.

To compute the position of the Wannier center or, equivalently, the bulk polarization, we connect the bulk polarization to the value of the averaged Wilson loop spectrum, as in Sec. 2.8:

$$p = \frac{1}{2\pi N_k} \sum_{j=1}^{N_k} \sum_{m=1}^{N_{\text{occ}}} \nu_{1,2}^{m}(k_{2,1}^{j}), \qquad \text{mod } 1, \tag{3.8}$$

that is, the average of the (non-Abelian) Wilson spectrum along the reciprocal lattice vectors [94].

We have characterized the first three bands of the canonical and breathing kagome lattice in the electronic quantum simulator, using the Abelian/non-Abelian Wilson loop, since the rest of the bands are very high in energy. We obtained different values for $p$ for the three different phases. Figures 3.7(j to 3.7(n) show the Wilson spectra obtained for the three different phases. In the case of the canonical kagome lattice, we obtain a value of $p = 1/6$, which places the Wannier center at position $\bar{\mathbf{r}}_n = (\mathbf{a}_1 + \mathbf{a}_2)/6$. Given the basis of lattice vectors, we can state that the Wannier center is located at the $3c$ Wyckoff position, precisely where the lattice sites are placed. Since inside the unit cell there are three equivalent $3c$ Wyckoff positions, there are three Wannier centers located at the orbit[1] of the $3c$ Wyckoff position. Since the average position of the Wannier center lies at the origin of the unit cell, there is no displacement in the charge, and the polarization is thus zero (even if the computed value is above zero).

For the breathing sets of molecules, we obtained $p = 0$ for the trivial phase and $p = 1/3$ for the non-trivial phase. These two values allow us to locate the Wannier center at the $1b$ Wyckoff position for the trivial phase and at the $1c$ Wyckoff position for the non-trivial phase. This result is expected because in the trivial phase, the intra-cell hopping is stronger than the inter-cell, and thus the surface state concentrates more around the $1b$ Wyckoff position. This results in a Wannier center placed at the origin, thus coinciding with the center of positive charge (at the $1b$ Wyckoff position). Similarly, in the non-trivial phase, the surface state concentrates more around the $1c$ Wyckoff position, yielding a negative charge center out of the center of positive charge at the $1b$ Wyckoff position. In the case of the composite group, we obtain exactly the same Wannier center as the isolated band, for each of the breathing phases. The filled star in Fig. 3.7(a), 3.7(c), and 3.7(e) represents the Wannier centers

[1] See Sec. 2.6 for a definition of the orbit of a Wyckoff position.

of the first three bands obtained via the Wilson spectrum. In Fig. 3.7(a), the empty stars are the Wannier centers generated by the orbit of the $3c$ Wyckoff position.

The results that we have obtained are general since we have performed the Wilson spectrum calculation using wave functions coming from the plane wave expansion of a potential, not from a tight-binding Hamiltonian. In this way, our Wilson spectra account for all possible hopping terms between lattice sites, and their behavior depends only on the symmetry properties of the lattice.

### 3.5.5 Topological Quantum Chemistry interpretation

| Real space | | | | | |
|---|---|---|---|---|---|
| $p6mm$ (#183) | | | $p3m1$ (#156) | | |
| MWP ($q$) | $G_q$ | irreducible representations | MWP ($q$) | $G_q$ | irreducible representations |
| $3c$ | $C_{2v}$ | $A_1, A_2,$ $B_1, B_2$ | $1b,\ 1c$ | $C_{3v}$ | $A_1, A_2, E$ |

| Reciprocal space | | | | | |
|---|---|---|---|---|---|
| $p6mm$ (#183) | | | $p3m1$(#156) | | |
| $k$ point | $G_{\mathbf{k}}$ | irreducible representations | $k$ point | $G_{\mathbf{k}}$ | irreducible representations |
| $\Gamma$ | $C_{6v}$ | $A_1, A_2,$ $B_1, B_2$ $E_1, E_2$ | $\Gamma$ | $C_{3v}$ | $A_1, A_2, E$ |
| $K,\ K'$ | $C_{3v}$ | $A_1, A_2, E$ | $K, K'$ | $C_3$ | $A,{}^1E,{}^2E$ |
| $M$ | $C_{2v}$ | $A_1, A_2,$ $B_1, B_2$ | $M$ | $C_s$ | $A',\ A''$ |

*Table 3.1:* Symmetry properties of the maximal Wyckoff positions (MWP) and $k$ points involved in the quantum simulator approach of the canonical/breathing kagome lattice. Symbols $G_q$ and $G_{\mathbf{k}}$ correspond to the point groups of the Wyckoff positions and $k$ vectors, respectively.

To conclude, we will use a different approach to study the topological features of a system, which is based on the symmetry eigenvalues of the Bloch wave functions at high-symmetry points in the reciprocal space. Topological Quantum Chemistry [1] is a powerful theory, that allows to classify and diagnose topological phases of matter based solely on group theory arguments. We refer the reader to Sec. 2.6 for a full explanation of the concepts that we will use in this section.

Even if the Wilson loop spectrum already has revealed where the Wannier center lies in each of the phases of the kagome lattice, let's take the following approach: by studying the symmetry properties of the wave functions in reciprocal space, let's try to determine the Wannier center and see

if it coincides with the Wilson loop prediction. This is the usual procedure that allows to characterize a system that is not built out of atomic species or orbitals. We refer the reader to Sec 2.6.3.

Starting from the canonical kagome lattice, the irreducible representation assignment shown in Fig. 3.7(g) is compatible with the three-dimensional band representation $(A_1 \uparrow G)_{3c}$, induced from the $3c$ Wyckoff position. This band representation is three-dimensional and thus 3 bands are touching in total. Topological Quantum Chemistry reveals that the canonical kagome lattice corresponds to a truly trivial atomic limit because the Wannier center lies at an occupied maximal Wyckoff position (lattice sites). The band structure shows features that correspond to a $C_{6v}$-symmetric lattice, *i. e.*, the gap closes at **K** and **K′** points. This can be understood from symmetry arguments: the little group of the **K**, **K′** points in $p6mm$ is $C_{3v}$, which shows two one-dimensional irreducible representations $(A_1, A_2)$ and a single two-dimensional irreducible representation $(E)$ (see Table 3.1).

After breaking the $C_6$ symmetry by introducing the breathing distortion, the symmetry of the space group is reduced to $p3m1$. In reciprocal space, the little group of the **K**, **K′** points reduces from $C_{3v}$ to $C_3$. Since $C_3$ does not have two-dimensional irreducible representations, the two-dimensional irreducible representation from $C_{3v}$ decomposes into irreducible representations of the new little group, which translates into a gap opening of the Dirac cones at the **K** and **K′** points. This decomposition can be studied from compatibility relations in the respective **k** points after a symmetry reduction, revealing the pure symmetry origin of this splitting.

On the one hand, figure 3.7(h) corresponds to the band structure of the trivial breathing phase with zero bulk polarization. The irreducible representation assignment of the lowest band is compatible with the band representation $(A_1 \uparrow G)_{1b}$, which is one-dimensional. The upper two bands are compatible with the band representation $(E \uparrow G)_{1b}$, which is two-dimensional. Both representations come from the $1b$ Wyckoff position, which is maximal, and coincides with the result obtained via the Wilson spectrum approach since we have chosen the origin to lie in the 1b Wyckoff position. Due to the fact that at this maximal Wyckoff position there is a CO molecule, thus it is an unoccupied maximal Wyckoff position[1], and the trivial phase of the breathing kagome lattice is in an obstructed atomic limit [1].

On the other hand, figure 3.7(i) shows the band structure and irreducible representation assignment for the non-trivial phase with non-zero bulk polarization and corner states. The band representations in this case are $(A_1 \uparrow G)_{1c}$ for the lowest band and $(E \uparrow G)_{1c}$ for the upper group of bands. As in the previous case, the Wannier center lies in an unoccupied maximal Wyckoff position, and so, the

[1]The actual kagome lattice does not show any feature in the $2b/1b/1c$ maximal Wyckoff positions, neither in the canonical nor breathing phases.

non-trivial phase corresponds to a *different* obstructed atomic limit, connected by a gap closing to the one presented in the paragraph above.

If we go back to Sec. 2.7, we conclude that we have found a similar set-up to the SSH model: the trivial phase shows a Wannier center in the middle of the unit cell (the origin), which would correspond to a Wilson loop spectrum average equal to zero. In contrast, the non-trivial phase shows a Wannier center (in this case near) the edge of the unit cell, which corresponds to a Wilson loop spectrum average of 1/3. In terms of atomic limits, the two phases are obstructed atomic limits separated by a gap closing, and thus cannot be connected adiabatically. One of them is trivial, in the sense that it displays zero bulk polarization and no corner modes, whereas the other phase is non-trivial in the sense that it displays a non-zero bulk polarization and corner modes, exactly the same as in the SSH. Both phases present a band inversion of the symmetry eigenvalues at the **K**, **K′** points.

### 3.5.6 Wave functions for trivial/non-trivial set-ups

Once we have solved the Schrödinger equation, we can reconstruct the Bloch wave function and plot it in real space. We are showing in Fig. 3.8 the modulo squared of the wave functions for the first two bands at **K**, **K′** points, where the band inversion occurs. The left and right panels show the band structures and irreducible representation assignments of the trivial and non-trivial phases of the breathing kagome lattice in the muffin-tin set-up. The middle panel shows the plot of the wave function inside the unit cell for the first two bands right at the point where the band inversion occurs. We can see that the wave functions transforming as the ${}^2E$ irreducible representation looks like a triangle pointing up, while the wave functions transforming as the ${}^1E$ irreducible representation resembles a triangle pointing down plus a translation of $(\mathbf{a}_1 + \mathbf{a}_2)/3$.

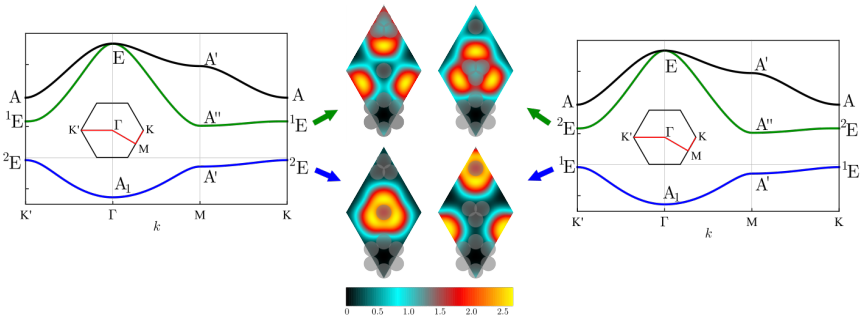


*Figure 3.8:* Wave functions for the first and second bands of the trivial (left) and non-trivial (right) configurations of the muffin-tin set-up.

## 3.6 Discussion and Conclusion

In this chapter, we have studied the different phases of the breathing kagome lattice. We start by tuning a dimerization parameter that we have introduced between the intra- and inter-cell hopping terms in a tight-binding Hamiltonian. When this parameter is set to zero, we recover the traditional kagome lattice, which has a gapless spectrum. When the dimerization parameter changes sign, a band inversion occurs at the **K** and **K′** points and the two breathing phases are distinct while showing the same spectral properties.

A finite-size flake of the non-trivial phase has bulk, edge, and corner localized modes. These edge modes appear in the bulk gap. However, to realize a true higher-order topological insulator, the bulk gap should host only corner modes. Hence, the breathing kagome lattice does not encode higher-order topology. To study the origin, symmetries, and properties protecting such corner modes, we have introduced several perturbations to the non-trivial phase of a finite-size triangular-shaped flake using a tight-binding formalism. We have chosen this geometry to ensure that the sample respects the $C_{3v}$ symmetry group of the lattice. We have shown that the corner modes are trivial and that three ingredients are needed to pin the modes to zero energy and to localize a corner state at one sublattice. First of all, the symmetries imposed by the space group should be respected. Breaking spatial symmetries would lead to, for example, non-degenerate corner modes, as we saw by introducing random onsite energies in the flake while respecting the kagome pattern–see Fig. 3.4(a). Second, we cannot connect sites belonging to the same sublattice, *i. e.*, this is the same as preserving generalized chiral symmetry, which strongly affects how the modes move away from zero, as we saw in Fig. 3.4(b). Finally, the connectivity between lattice sites of different species must be done in a consecutive way, constructing a closed triangle of vertices ABC (see Fig. 3.5). Importantly, if and only if these conditions are fulfilled, the corner modes are truly localized in the corner sublattice, tightly pinned to zero. We have also confirmed that these rules can be extended up to the second, third, etc., nearest neighbors while increasing accordingly the size of the flakes. Otherwise, the corner modes would move away from zero due to overlap.

Finally, we have performed a study of the kagome lattice based on a muffin-tin calculation. In this picture, with no concept of individual hopping terms, all possible overlaps between all the lattice sites are included in the calculation. By solving the Schrödinger equation, we obtained the Bloch wave functions, which inherit all the symmetry properties from the periodic potential. After applying a Wilson spectrum characterization and symmetry markers, we have been able to identify the band representation to which each phase corresponds (canonical, trivial, and non-trivial). We found that the two breathing phases correspond to two different obstructed atomic limits, connected

through a gap closing. Hence, these two phases are not adiabatically connected. This gap closing reveals a band inversion between the two phases. It also accounts for the recovery of a six-fold rotation, characteristic of the canonical kagome lattice. This setup corresponds to a trivial atomic limit in which, up to a point group operation, the Wannier centers lie exactly at the lattice sites.

These results may shed light on the protection of the corner modes of two-dimensional lattices, as well as on understanding what a higher-order topological insulator is and what is not. Within a more general framework than a tight-binding Hamiltonian, we have demonstrated the trivial/non-trivial distinction between the two phases of the breathing kagome lattice, as well as the source of the existence and protection of the corner modes. Since the muffin-tin technique accounts for all the possible hopping terms between all lattice sites, we believe that both the existence and protection of corner modes are a consequence of the symmetry properties of the non-trivial phase hosting the corner modes. In addition, the Wilson spectrum characterization of all the phases of the kagome lattice is determined exclusively by the symmetries of the lattice. However, the appearance of edge modes in the bulk gap of the finite-size system suggests that this protection does not have any topological character while being robust to some extent. We conclude that the corner modes of the breathing kagome lattice have some robustness but are not topological.

Robust protection of corner modes may have potential applications for lasing techniques [123, 124, 130]. These references are based on a kagome pattern, so we believe that the corner modes that they propose do not possess any topological protection while being robust by the symmetry of the lattice.

# CHAPTER 4

# Tunable Dirac points in a two-dimensional non-symmorphic wallpaper group lattice

This chapter is devoted to a deep and descriptive study of the electronic properties of the herringbone lattice in different geometries. The study is based on different distortions that are applied to the lattice, in terms of symmetry-breaking onsite energies and breathing hopping amplitudes, which will allow us to comprehend how the non-symmorphic symmetries affect the spectral properties of the lattice. From the results presented in this chapter, only the bulk results are published under reference [131]. The Chapter is organized in the following way: Section 4.1 is a short introduction to the herringbone lattice, and a state of the art about the two-dimensional lattices displaying non-symmorphic symmetries, which characterize the present lattice. In Section 4.2 we present the herringbone lattice and the tight-binding Hamiltonian we will use to describe the bulk of the lattice. As well, we present the ribbon and flake geometries of the lattice and compare the different spectra concerning the different geometries. We will use the projected spectral function introduced in Section 2.9 to study the localization of the states in the ribbon configurations. In Section 4.3 we present a study on the symmetries of the herringbone lattice and how to write the symmetry operators we are interested in: the glide symmetries. Along this line, we present in Section 4.4 different strategies for breaking the glide symmetries based on the addition of mass-terms to the Hamiltonian (onsite energies). Once the individual effects of the different onsite energies are presented, we combine them in Section 4.5. Additionally, we show in section 4.6 another possible procedure for breaking the symmetries based on a dimerization technique. We sum up all the different effects in section 4.7. Finally, section 4.8 presents a possible realization of this two-dimensional lattice in the CO/Cu(111) electronic quantum simulator platform.

## 4.1 Introduction

Since the isolation of single-layer graphene, there has been a growing interest in analyzing two-dimensional lattices with low-energy physics described by a Dirac-like Hamiltonian [132, 133], but also beyond graphene [134, 135]. The quest for systems hosting Dirac-like features is not only within condensed matter but extended to cold-atoms [136] and electronic quantum simulators [32, 137]. Most of these systems have a crystal structure that belongs to a symmorphic space group [18]. However, there has been an increasing research interest in Dirac-like physics in non-symmorphic crystalline systems [18, 139, 140, 141, 142, 143, 144, 145, 68, 138]. A peculiar property of Dirac cones is that they can merge into a so-called semi-Dirac cone [133, 146, 147, 148, 149]. These points in energy space are distinguished by an energy dispersion that is linear in one direction and parabolic in the perpendicular. They are particularly interesting for their topological [150] and anisotropic transport properties [151, 152]. Semi-Dirac physics are also realizable in three-dimensional crystals such as $SrNbO_3$ [153], where at specific points in reciprocal space, the energy dispersion is linear in a two-dimensional plane and quadratic along an additional axis, thus showing massless/massive electron behaviors.

As introduced in Sec. 2.6 non-symmorphic space groups contain at least a fractional lattice translation combined with either a mirror reflection (glide plane) or a rotation (screw axis). In reciprocal space, this results in band-foldings with crossings inside the first Brillouin zone boundaries that are protected against hybridization [154, 68, 155, 156, 157, 158].

We begin this chapter by presenting the tight-binding model used to study the spectral properties of the herringbone lattice. We will present as well the different distortions and perturbations that we studied, for bulk, ribbon, and flake geometries.

## 4.2 The herringbone lattice model

The herringbone lattice is a two-dimensional lattice containing four sites in its unit cell, all of them with coordination number 3 as shown in Fig. 4.1(a). The primitive lattice vectors are $\mathbf{a}_1 = (1, 1)\, a_0$ and $\mathbf{a}_2 = (-2, 2)\, a_0$, where $a_0$ is the interatomic distance. It is noticeable how $|\mathbf{a}_2| = 2|\mathbf{a}_1|$. To keep the notation used in Chapter 2, we label each unit cell by $(m, n) = m\mathbf{a}_1 + n\mathbf{a}_2$. The herringbone lattice can be regarded as a square lattice with an enlarged unit cell, including four lattice sites, but each atom is missing a link. We thus name the four sites in the unit cell according to the link in the opposite direction to the one that is missing. On the one hand, $r_{mn}$ and $l_{mn}$ miss a link along the horizontal direction, $r$ on its left, but it's connected to its right and $l$ on its left. On

the other hand, $u_{mn}$ and $d_{mn}$ present a missing link along the vertical direction, with a missing link downwards and upwards, respectively.

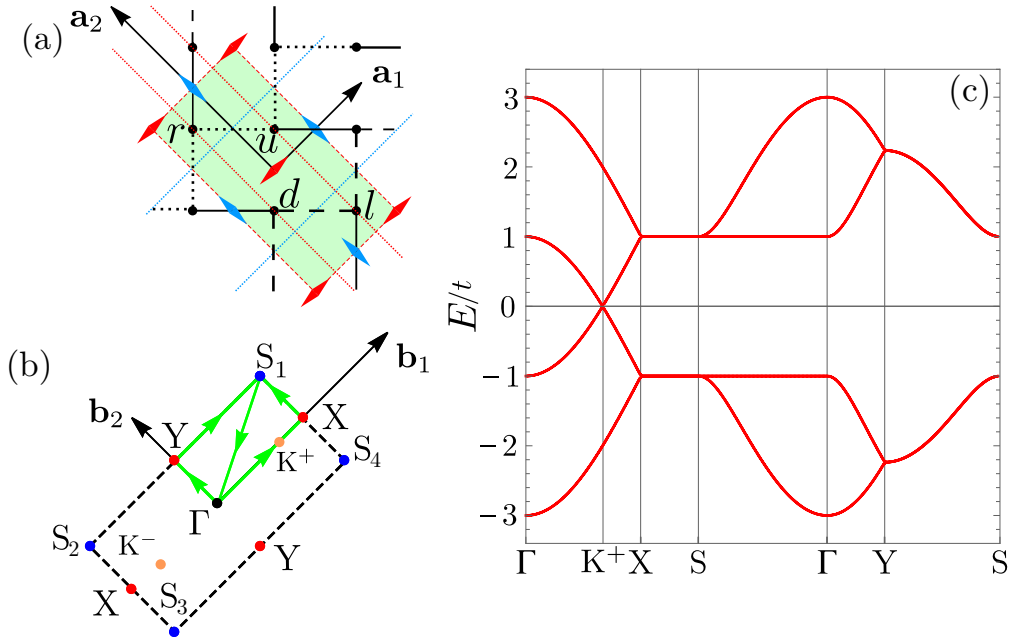


*Figure 4.1:* (a) Unit cell of the herringbone lattice with the naming of the lattice sites $(r, d, u, l)$, direct lattice vectors $\mathbf{a}_1$ and $\mathbf{a}_2$, and the two sets of glides: the dashed blue lines correspond to $\mathcal{G}_{1\alpha}$ while the red ones to $\mathcal{G}_{2\alpha}$. The red and blue diamonds represent the $2a$ and $2b$ maximal Wyckoff positions, respectively. The central red 2a Wyckoff position represents the center of inversion. Additionally, the Su-Schieffer-Heeger-like chains have been highlighted by two different densities of the dashing. (b) First Brillouin zone, reciprocal lattice vectors $\mathbf{b}_1$ and $\mathbf{b}_2$, high-symmetry points and high-symmetry path, plus the position of the Dirac cones appearing in the irreducible Brillouin zone. (c) Spectrum of the herringbone lattice across the high-symmetry path shown in green in panel (b).

### 4.2.1 Bulk Hamiltonian

We now write the tight-binding Hamiltonian in the nearest-neighbor approximation. For simplicity, we assume that there is a single $s$-like orbital at each lattice site. As introduced in Section 2.2, we use fermionic operators, but the naming of the operators corresponds to the labeling of the lattice sites to simplify the notation: in unit cell $m, n$, we find the operators $r_{m,n}$, $d_{m,n}$, $u_{m,n}$, $l_{m,n}$. The tight-binding Hamiltonian, including onsite energies and hopping amplitudes, then reads:

$$\hat{\mathcal{H}} = \sum_{\langle mn \rangle} \left( \varepsilon_r r^\dagger_{mm} r_{mm} + \varepsilon_d d^\dagger_{mm} d_{mm} + \varepsilon_u u^\dagger_{mm} u_{mm} + \varepsilon_l l^\dagger_{mm} l_{mm} \right) + \\ + t_0 (r^\dagger_{m,n} u_{m,n} + d^\dagger_{m,n} l_{m,n} + u^\dagger_{m,n} d_{m+1,n} + d^\dagger_{m,n} l_{m-1,n} + r^\dagger_{m,n} l_{m,n+1}) + \text{h.c.}, \tag{4.1}$$

where $\varepsilon_\alpha$ represents the onsite energy of species $\alpha, \alpha' = r, d, u, l$. We assume that the hopping amplitude between nearest-neighboring sites is the same for all orientations and species, and it is

fixed to $t_0$. The symbol $\langle mn \rangle$ indicates nearest-neighbor unit cells. The first line represents the onsite energies, which will be used to break the symmetries of the herringbone lattice selectively. The second line represents the hopping terms, which can be classified into intra-cell, where we only find horizontal terms, and inter-cell hoppings, where we find horizontal and vertical terms.

At first, we neglect the onsite energies and introduce $k_i = \mathbf{k} \cdot \mathbf{a}_i$. Now, we Fourier transform the Hamiltonian using the basis $\Psi_{\mathbf{k}} = (r_{\mathbf{k}}, d_{\mathbf{k}}, u_{\mathbf{k}}, l_{\mathbf{k}})^{\mathrm{T}}$. We can write $\hat{\mathcal{H}} = \sum_{\mathbf{k}} \hat{\Psi}^{\dagger}_{\mathbf{k}}(h)(\mathbf{k})\hat{\Psi}_{\mathbf{k}}$, where

$$h(\mathbf{k}) = \begin{pmatrix} 0 & q(\mathbf{k}) \\ q(\mathbf{k})^{\dagger} & 0 \end{pmatrix} = \tau_+ \otimes q(\mathbf{k}) + \tau_- \otimes q^{\dagger}(\mathbf{k}), \tag{4.2a}$$

$$q(\mathbf{k}) = t_0 \begin{pmatrix} 1 + \mathrm{e}^{-\mathrm{i}k_1} & \mathrm{e}^{\mathrm{i}k_2} \\ \mathrm{e}^{-\mathrm{i}k_1} & 1 + \mathrm{e}^{-\mathrm{i}k_1} \end{pmatrix} = \sigma_0(1 + \mathrm{e}^{\mathrm{i}k_1}) + \sigma_+ \mathrm{e}^{\mathrm{i}k_2} + \sigma_- \mathrm{e}^{-\mathrm{i}k_1}. \tag{4.2b}$$

On the one hand, in Eq. (4.2a), the matrices $\tau_\pm$ are symmetric/anti-symmetric linear combinations of the $x, y$ Pauli matrices. These matrices differentiate between $r \leftrightarrow u$ and $d \leftrightarrow l$ sites. On the other hand, in Eq. (4.2b), the matrices $\sigma_\pm$ are *also* symmetric/anti-symmetric linear combinations of the $x, y$ Pauli matrices, but this time, these matrices differentiate between sites $r \leftrightarrow d$ and $u \leftrightarrow l$. In analogy with Sec. 2.7, the Hamiltonian has been written with a choice of basis that makes explicit the chirality of the model, this time, with 4 lattice sites per unit cell. The chiral operator is $C = \tau_z \otimes \sigma_0$. This operator hints at an interpretation of the herringbone lattice as two coupled SSH chains, each with its chiral symmetry [159, 160], as in the kagome lattice model[1]. The SSH chains are formed by pairs of sets $s_1 = \{r, u\}$ and $s_2 = \{d, l\}$, respectively. In terms of Pauli matrices, the $\tau_i$ matrices represent intra-chain degrees of freedom while $\sigma_i$ matrices act on the $\{s_1, s_2\}$, and so represent the inter-chain degrees of freedom. Finally, the chains are thus connected along the horizontal direction via $u, d$ atoms and along the vertical direction via $r, l$ atoms. The chains are presented in Fig. 4.1(a) as the black dotted line ($s_1$ chain) and the black dashed line ($s_2$ chain). We will address this discussion further in the text when breaking the various symmetries.

The energy spectrum associated to Eq. (4.2a) reads:

$$\mathcal{E}_{\alpha,\beta}(\mathbf{k}) = \alpha t_0 \sqrt{3 + 2\cos k_1 + 4\beta \cos\left(\frac{k_1}{2}\right)\cos\left(\frac{k_2}{2}\right)} \tag{4.3}$$

with $\alpha, \beta = \pm$. It presents a total of four energy-symmetric bands, with several features that can be seen in Fig. 4.1(c). To begin with, it displays Dirac cones between bands 2 and 3 located at $\mathbf{K}^{\pm} = \pm\mathbf{b}_1/3$[2]. These cones are characterized by a $\pm\pi$ Berry phase. Additionally, we observe flat

[1] We refer the reader to Appendix B for the interpretation of the kagome lattice as coupled SSH chains. This interpretation also applies to the bulk of the system, but the method in the Appendix B is applied in a finite-size flake.

[2] These points are marked inside the first Brillouin zone in Fig. 4.1(b), and fall in the high-symmetry path [68]

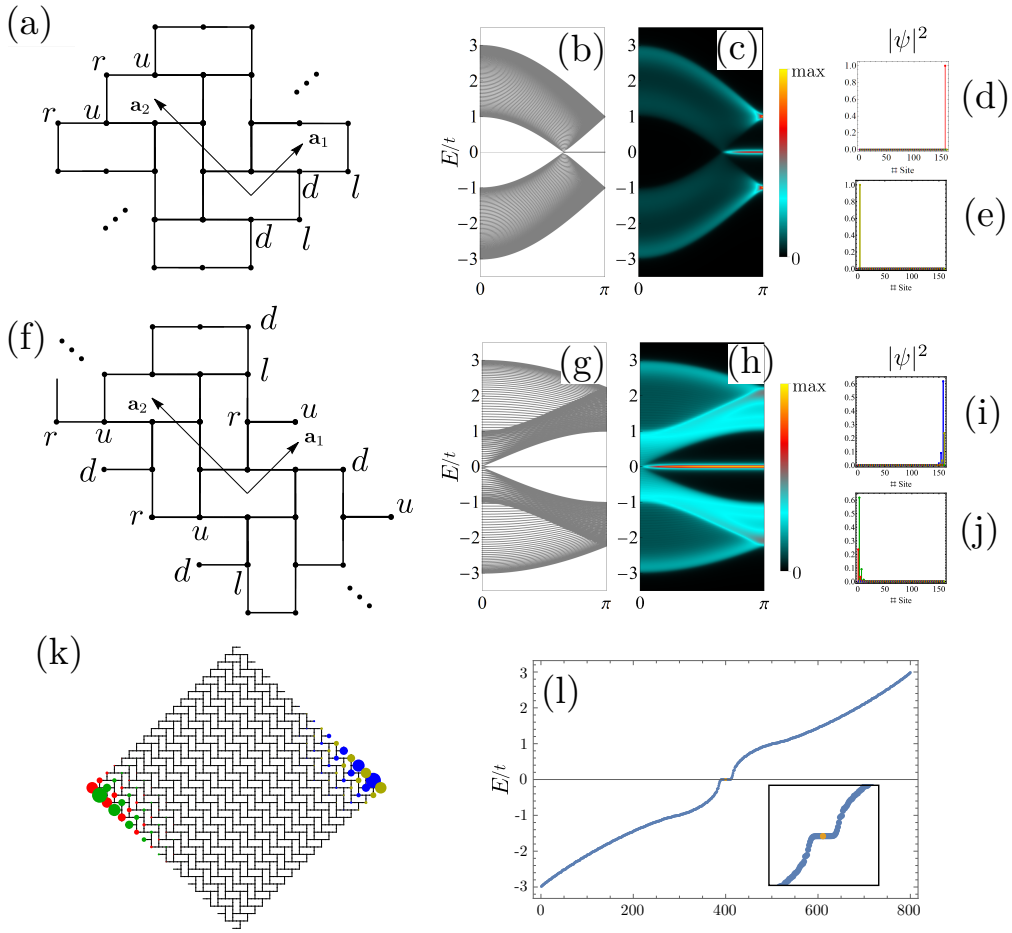


*Figure 4.2:* (a) Sketch of the $\mathbf{a}_1$ ribbon in real space. The dots represent the translational invariance of the system along the $\mathbf{a}_1$ direction. The edges of the ribbon are formed by different species of lattice sites, which have been made explicit. (b) Band structure of the $\mathbf{a}_1$ ribbon geometry. (c) Edge-projected spectral function applied to the spectrum of the $\mathbf{a}_1$ ribbon geometry. Panels (d) and (e) represent the localization of the states at zero energy and at $k = \pi$. (f) Sketch of the $\mathbf{a}_2$ ribbon in real space. The dots represent the translational invariance of the system along the $\mathbf{a}_2$ direction. The edges of the ribbon are formed by different species of lattice sites, which have been made explicit. (b) Band structure of the $\mathbf{a}_2$ ribbon geometry. (c) Edge-projected spectral function applied to the spectrum of the $\mathbf{a}_2$ ribbon geometry. Panels (d) and (e) represent the localization of the states at zero energy and at $k = \pi$. (k) Sketch of the flake cut from the bulk displaying a corner-like state located at zero energy. (l) Spectrum of the real space Hamiltonian written for a flake geometry. The inset shows in orange the eigenvalue of the state represented in panel (k). Finally, the edge-projected spectral functions have been calculated using a $\delta = 0.04$ (see Sec. 2.9).

nodal lines along SXS lines and dispersive ones along SYS, both between bands 1&2 and 3&4. All these features are rooted in the symmetries of the herringbone lattice, which are presented in Sec. 4.3.

### 4.2.2 Ribbon and flake geometries

As introduced in Sec. 2.2, a two-dimensional lattice can be cut to realize finite-size systems, namely ribbons and flakes. For the case of the herringbone lattice, we have chosen the directions along the primitive lattice vectors to cut the lattice and build two different species of ribbons. We present now the spectra corresponding to each of them.

On the one hand, the ribbon along $\mathbf{a}_1$ is built by assuming that the system is periodic along $\mathbf{a}_1$, so that the ribbon unit cell is composed of a set of $N_2$ lattice unit cells along the $\mathbf{a}_2$ direction. In this way, we perform Fourier transform to the operators only along the $\mathbf{a}_1$ direction. Figure 4.2(d) presents the spectrum of the ribbon along $\mathbf{a}_1$, which is completely identical to the spectrum of a graphene zig-zag ribbon [161, 162, 163]. The spectral function projected over the edges–Figure 4.2(e)– reveals that the two states appearing around zero energy are localized over the edges, which is shown in panel 4.2(f).

On the other hand, the process for building ribbons along the $\mathbf{a}_2$ direction is the opposite: we consider $N_1$ lattice unit cells along the $\mathbf{a}_1$ direction and perform the Fourier transform along the $\mathbf{a}_2$ direction. Figure 4.2g presents the spectrum of the ribbon, which is similar to the graphene armchair ribbon [161]. However, in this case, we have not found a condition for the metallic character of the ribbon according to its size, so the gap at $k = 0$ closes only in the thermodynamic limit. The spectral function projected over the edges–Figure 4.2(h)– reveals that the two states appearing around zero energy are localized over the edges, which is shown in panel 4.2(i).

In order to apply the projected spectral function to the ribbon spectrum, we have defined the projection operator in the following way: we compute the weight of the wave function in the lattice unit cells located at the edges of the ribbon unit cell and sum their contributions. This choice is based on the fact that due to inversion symmetry, the bulk states of the ribbon are evenly distributed across the ribbon unit cell. On the contrary, the edge states present non-zero weight in only one of the edges, as it can be seen in panels 4.2(f) and 4.2(i). If, instead, we compute the difference between the contributions, we would obtain a zero contribution from the bulk bands, so they would not be distinguishable from the background. In this case, the contribution from the edge states would not change since one of the edges is always zero. In the following sections, we introduce a different criterion, which is associated with a different color scale since it will help us distinguish between states localized on different edges.

Finally, we diagonalize the real-space Hamiltonian written over a square-shaped flake, with $N_1 = 2N_2 = 20$ unit cells along each primitive lattice vector, to achieve a square flake. The spectrum

is shown in Figure 4.2(b), where no gap opens. However, we find several states at zero energy. In panel 4.2(c) we present a sketch of the flake plus the localization of the state #400, which is localized towards the corners. The spatial distribution of those corners is related by inversion symmetry, present in the flake.

## 4.3 Symmetries of the herringbone lattice

The herringbone lattice belongs to the $pgg$ wallpaper group [164]. This plane space group is non-symmorphic, meaning that some symmetry operators do not leave any point of the space invariant since they include fractional translations along direct lattice vectors (see Section 2.6). These symmetries are called *glide* symmetries and the herringbone lattice presents a total of four different glide operations, which can be classified into two different sets. Since each set acts on different sites, we label each glide with two indices, $\mathcal{G}_{i\alpha}$, where $i$ corresponds to the index of the lattice vector involved in the fractional translation, and $\alpha = \{\text{A,B}\}$ depending on whether the $r$ lattice site is closest to the mirror plane (A) or not (B). We want to point out that, in Section 2.6, the symbol $\mathcal{G}$ represented a space group. However, in this chapter, we use the same symbol $\mathcal{G}$ to represent a glide symmetry, and we add the subindices to distinguish between them. Using the same notation introduced in Sec. 2.6, we represent symmetry operations belonging to space groups with Seitz symbols [165]. In this case, these glide operators can be written as $\mathcal{G}_{1\alpha} = \left\{m_{01}|\frac{1}{2}0\right\}$ and $\mathcal{G}_{2\alpha} = \left\{m_{10}|0\frac{1}{2}\right\}$. The glide operators have been represented in Fig. 4.1(a) with blue and red lines, representing both the direction along which the half translation is performed and the mirror.

The unit cell of the herringbone lattice contains four maximal Wyckoff positions grouped in two non-equivalent sets: $2a$, $2b$. These have been displayed in Figure 4.1(a) as red and blue rhombi. It is remarkable that none of the glide planes goes through any of the maximal Wyckoff positions. Also, none of the lattice sites falls in maximal Wyckoff positions. However, the set of glides $\{\mathcal{G}_{2\alpha}\}$ do go through the lattice sites, while $\{\mathcal{G}_{1\alpha}\}$ do not. This affects how lattice sites transform under these symmetries: when applying the set of glides $\{\mathcal{G}_{1\alpha}\}$, no matter which symmetry operation is performed first (mirror or half translation), the transformed lattice site falls on empty space, whereas for $\{\mathcal{G}_{2\alpha}\}$, the half translation already maps $r$ into $d$, and $u$ into $l$, while the mirror operation will map the lattice site to another one from an adjacent unit cell. These properties affect how the spectrum behaves after breaking $\{\mathcal{G}_{2\alpha}\}$ *vs.* $\{\mathcal{G}_{1\alpha}\}$, as we will see further in the text.

We study now the action of the four glide operators $\mathcal{G}_{i\alpha}$ over the spinor $\Psi(\mathbf{r}) =$

$(\psi_r(\mathbf{r}), \psi_d(\mathbf{r}), \psi_u(\mathbf{r}), \psi_l(\mathbf{r}))^{\mathrm{T}}$ in real space. We obtain:

$$\mathcal{G}_{1A}\Psi(\mathbf{r}) = \begin{pmatrix} \psi_u(\mathbf{r}) \\ \psi_l(\mathbf{r}+\mathbf{a}_2) \\ \psi_r(\mathbf{r}+\mathbf{a}_1) \\ \psi_d(\mathbf{r}+\mathbf{a}_1+\mathbf{a}_2) \end{pmatrix}, \qquad \mathcal{G}_{1B}\Psi(\mathbf{r}) = \begin{pmatrix} \psi_u(\mathbf{r}-\mathbf{a}_2) \\ \psi_l(\mathbf{r}) \\ \psi_r(\mathbf{r}+\mathbf{a}_1-\mathbf{a}_2) \\ \psi_d(\mathbf{r}+\mathbf{a}_1) \end{pmatrix}, \tag{4.4a}$$

$$\mathcal{G}_{2A}\Psi(\mathbf{r}) = \begin{pmatrix} \psi_d(\mathbf{r}+\mathbf{a}_2) \\ \psi_r(\mathbf{r}) \\ \psi_l(\mathbf{r}+\mathbf{a}_2-\mathbf{a}_1) \\ \psi_u(\mathbf{r}-\mathbf{a}_1) \end{pmatrix}, \qquad \mathcal{G}_{2B}\Psi(\mathbf{r}) = \begin{pmatrix} \psi_d(\mathbf{r}+\mathbf{a}_1+\mathbf{a}_2) \\ \psi_r(\mathbf{r}+\mathbf{a}_1) \\ \psi_l(\mathbf{r}+\mathbf{a}_2) \\ \psi_u(\mathbf{r}) \end{pmatrix}. \tag{4.4b}$$

If we Fourier transform these equations, we obtain the action of the glides in reciprocal space. Defining the $\mathcal{S}_i$ matrix as

$$\mathcal{S}_i = \begin{pmatrix} 1 & 0 \\ 0 & \mathrm{e}^{\mathrm{i}k_i} \end{pmatrix}, \tag{4.5}$$

we now can write a closed expression for each of the reciprocal space operators:

$$\mathcal{G}_{1A}(\mathbf{k}) = (\mathcal{S}_1\sigma_x) \otimes \mathcal{S}_2, \tag{4.6a}$$

$$\mathcal{G}_{1B}(\mathbf{k}) = \mathrm{e}^{-\mathrm{i}k_2}\mathcal{G}_{1A}(\mathbf{k}), \tag{4.6b}$$

$$\mathcal{G}_{2A}(\mathbf{k}) = \mathcal{S}_1^{\dagger} \otimes (\sigma_x\mathcal{S}_2), \tag{4.6c}$$

$$\mathcal{G}_{2B}(\mathbf{k}) = (\sigma_x\mathcal{S}_1\sigma_x) \otimes (\sigma_x\mathcal{S}_2). \tag{4.6d}$$

The Kronecker product operator has been made explicit since the usual matrix product is also used in the expressions above. With these expressions, we will understand the band structure features shown in the spectrum in Fig.4.1(c) and how the breaking of them leads to the different features we will see in the following sections. On the one hand, along the lines SXS, $k_1 = \pi$, and the Hamiltonian commutes with $\mathcal{G}_{2\alpha}(\mathbf{k})$. Since along this line this operator has two sets of degenerated eigenvalues, so does the Hamiltonian, and we see the degeneracies along these lines. On the other hand, along the lines SYS, $k_2 = \pi$, and the Hamiltonian commutes with $\mathcal{G}_{1\alpha}(\mathbf{k})$. Again, the symmetry operator has two sets of two degenerated eigenvalues, and so does the Hamiltonian.

## 4.4 Breaking symmetries with onsite potentials

We now study the effects of breaking the symmetries in the pristine herringbone lattice spectrum. We will add onsite energies to the Hamiltonian in Eq (4.2a). These onsite energies are represented by diagonal matrices written in terms of a single parameter $\delta_i$ that will represent the onsite energy

of each site. Finally, diagonalizing the Hamiltonian, we can study the spectrum in terms of this perturbation parameter $\delta_i$.

We cover three onsite energy choices that show how to gap the cones, move them within the first Brillouin zone, and eventually merge them into a semi-Dirac cone. We will present bulk and ribbon geometries together for the three different perturbations. Next, the flake results will be shown together for the three different onsite energy choices.

Finally, we use the three onsite energies as building blocks for creating new onsite energy combinations. By mixing the individual perturbations, we will cover deeper effects in the bulk of the herringbone lattice and represent them in phase diagrams according to the presence of Dirac cones, semi-Dirac cones, or gapped phases.

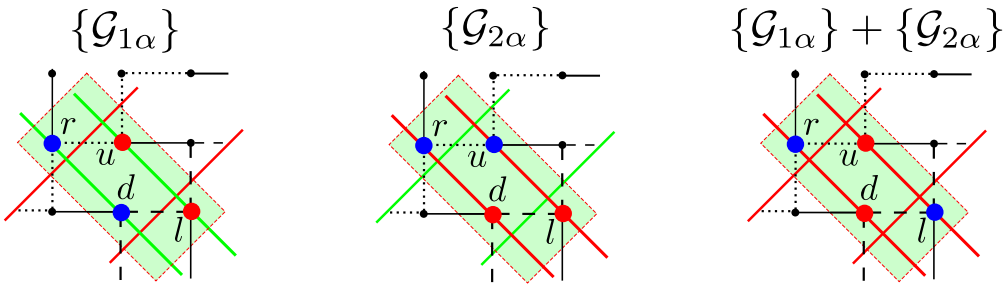


*Figure 4.3:* From left to right, different choices for the onsite energy perturbations that will be covered in the following sections. In the left panel, the onsite energies are not respecting the constraints of the $\{\mathcal{G}_{1\alpha}\}$ glide symmetries, presented as the red lines, since $r, d$ are not mapped into $u, l$. We have presented in green the set of glides $\{\mathcal{G}_{2\alpha}\}$ that are respected, since $r, d$ are mapped into each other, as well as $u, l$. This choice is studied in section 4.4.1. The middle panel shows the configuration for the breaking of the $\{\mathcal{G}_{2\alpha}\}$ set of glides, presented as the red lines, since $r, u$ are not mapped into $d, l$. We have presented in green the set of glides $\{\mathcal{G}_{1\alpha}\}$ that are respected, since $r, u$ are mapped into each other, as well as $d, l$. This choice is studied in section 4.4.2 Finally, the right panel shows the configuration where both glides are broken at the same time, both represented as red lines. This choice does respect inversion symmetry, though, and its consequences will be studied in section 4.4.3.

### 4.4.1 Breaking of $\{\mathcal{G}_{1\alpha}\}$

We start by fixing opposite onsite energies $\varepsilon_\alpha = \pm\delta_1 t_0$ at lattice sites $r$ and $u$, $d$ and $l$. This can be written as $(\varepsilon_r, \varepsilon_d, \varepsilon_u, \varepsilon_l) = \delta_1(1, 1, -1, -1)t_0$. The spatial representation of this choice is present in the left panel of Fig. 4.3. In a diagonal matrix form, we can write:

$$\mathcal{M}_1(\delta_1) = \delta_1 \left(\tau_z \otimes \sigma_0\right) t_0 \tag{4.7}$$

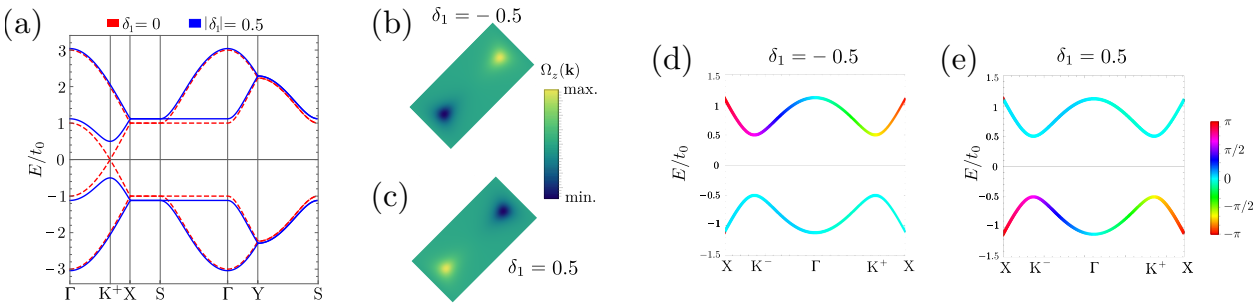


*Figure 4.4:* (a) Bulk spectrum for the pristine herringbone lattice (dashed red line) and with $\mathcal{M}_1(0.5)$ onsite potential (solid blue line); (b), (c) Berry curvature of the lower set of bands revealing a valley distribution of the charge around the gapped Dirac points. (d), (e) Energy spectrum of the herringbone lattice with $\mathcal{M}_1(\delta_1)$ for $|\delta_1| = 0.5$, but colored according to the phase of the symmetry eigenvalue of the $\mathcal{G}_{2A}(\mathbf{k})$ operator, revealing a band inversion when the gap closes and reopens.

where $\mathcal{M}_1(\delta_1)$ denotes the $\{\mathcal{G}_{1\alpha}\}$-breaking mass term that is added to the Hamiltonian in Eq. 4.2a as a function of the perturbation parameter $\delta_1$. In terms of SSH chains, this configuration differentiates between lattice sites inside each chain, thus respecting interchain symmetry and breaking inversion symmetry.

**Bulk spectral properties** We start by discussing the bulk spectral properties for different values of $\delta_1$, present in Fig. 4.4. Panel 4.4(a) shows the spectrum of both the pristine herringbone lattice–setting $\delta_1 = 0$, as shown in Fig. 4.1(c)– and for $|\delta_1| = 0.5$. For any $|\delta_1| > 0$ the band structure splits into two gapped composite sets of two bands. The rest of the spectral features (flat and degenerate lines) are shifted in energy, preserving the degeneracies.

The energy spectrum is symmetric with respect to $\delta_1 = 0$, in the sense that the spectra for $\pm\delta_1$ are identical. However, the eigenfunctions behave differently after a change in sign of $\delta_1$: the Berry curvature shows a valley distribution with opposite signs at the $\mathrm{K}^{\pm}$ points. When the gap closes and reopens, the distribution inverts, as shown in panels 4.4(b) and 4.4(c). The Berry curvature displays a dipolar-like distribution with a fixed length $L_\Omega = 2|\mathbf{K}^{\pm}|$. Given $\{\mathcal{G}_{1_\alpha}\}$ involves the mirror $m_{01}$ in real space, the same mirror in reciprocal space is conserved, and the dipolar distribution is oriented along $\mathbf{b}_1$.

Finally, we study the breaking of $\{\mathcal{G}_{1\alpha}\}$ from the symmetry eigenvalues of $\{\mathcal{G}_{2\alpha}\}$ before and after the closing of the gap. We observe that the eigenvalues of bands 2 and 3 invert before and after the closing of the gap, which reflects a band inversion. This is shown in Figs. 4.4(d) and 4.4(e).

**Ribbon spectral properties** Now we discuss the results in the ribbon geometry. As we introduced in Sec. 2.2.6, the spectrum of ribbon geometries corresponds to the projection of the bulk spectrum

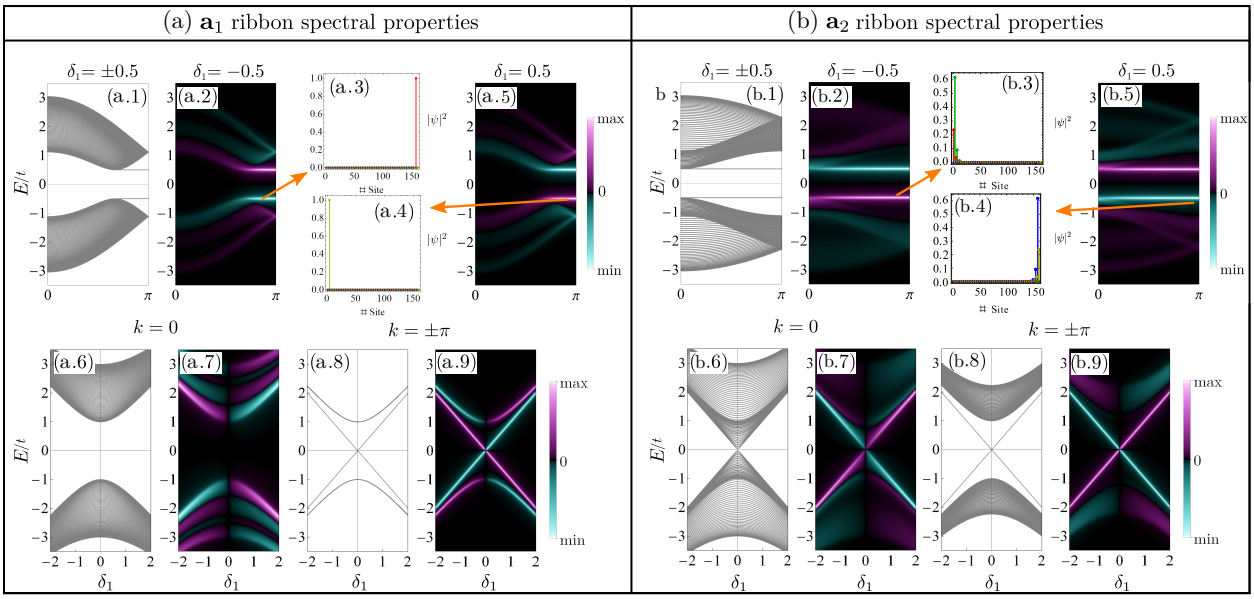


*Figure 4.5:* (a) Spectral properties of the $\mathbf{a}_1$ ribbon. (a.1) Spectrum of the ribbon, (a.2) and (a.5) edge projected spectral functions for opposite values of the onsite potential. The projection reveals a different localization of the edge states. The color of the plot is related to the localization of the wave function (blue for localization on the right and fuchsia for localization on the left). Panels (a.3) and (a.4) reveal the localization of the states marked in panels (a.2) and (a.5). Panels (a.6) and (a.8) show the spectrum of the ribbon versus the $\delta_1$ parameter ($\delta_1$-spectrum), at $k = 0$ and $k = \pi$ respectively. Panels (a.7) and (a.9) show the edge-projected spectral function associated with each $\delta_1$-spectra. (b) Spectral properties of the $\mathbf{a}_2$ ribbon. Panels (b.1) to (b.9) correspond to the same information as the panels from (a.1) to (a.9) but related to the $\mathbf{a}_2$ ribbon geometry. Respectively: (b.1) spectrum of the $\mathbf{a}_2$ ribbon with $|\delta_1| = 0.5$, (b.2) edge-projected spectral function for $\delta_1 = -0.5$, (b.3), (b.4) localization of states across the ribbon, (b.5) edge-projected spectral function for $\delta_1 = 0.5$, (b.6) $\delta_1$-spectrum for $k = 0$, (b.7) edge-projected spectral function applied to the $\delta_1$-spectrum for $k = 0$, (b.8) $\delta_1$-spectrum for $k = \pi$, (b.9) edge-projected spectral function applied to the $\delta_1$-spectrum for $k = \pi$.

over the periodic direction in the two-dimensional first Brillouin zone. Hence, in the ribbon geometry, we then observe the same gapping of the band structure for $\delta_1 \neq 0$ that we see in the bulk. Panels 4.5(a.1) and 4.5(b.1) show the spectrum of ribbons along $\mathbf{a}_1$ and $\mathbf{a}_2$ (respectively). We have shown only the spectrum for $k \in [0, \pi]$ since both the spectrum and the (edge-projected) spectral function are symmetric with respect to $k = 0$.

Panels 4.5(a.2), 4.5(a.5), 4.5(b.2), 4.5(b.5), show the edge-projected spectral function applied to the two ribbon configurations, with $\delta = \pm 0.5$. The localization of the edge states of the ribbons occurs on opposite edges after the closing of the gap. This localization can be seen in panels 4.5(a.3) and 4.5(a.4) for the $\mathbf{a}_1$ ribbon and in panels 4.5(b.3) and 4.5(b.3) for the $\mathbf{a}_2$ ribbon. Panels 4.5(a.6) and 4.5(a.8) show the spectrum of the $\mathbf{a}_1$ ribbon but plotting the eigenvalues computed respectively

at $k = 0$ and $k = \pi$ versus the perturbation parameter $\delta_1$. Similarly, panels 4.5(b.6), and 4.5(b.8) show the $\delta_1$-spectrum of the $\mathbf{a}_2$ ribbon geometry under the same conditions. In these plots, we confirm that the spectrum is symmetric with respect to the $\delta_1$ perturbation parameter. Finally, panels 4.5(a.7), 4.5(a.9), 4.5(b.7), 4.5(b.9) show the projected spectral function applied to the $\delta_1$-spectrum, and reveal that the localization inverts after the change in sing of $\delta_1$. As we mentioned in Sec. 4.2.2, to distinguish between localization on different edges, we can redefine the projection operator present in the edge-projected spectral function. Since we have broken inversion symmetry, the bulk states are not evenly distributed, and thus, they present different localizations across the ribbon. For this reason, we computed the weight of the wave function on the lattice unit cell located at the two edges of the ribbon unit cell. Next, we take the difference between the two values, so if the total is positive, the associated wave function is located on one edge, and if it is negative, it is located on the opposite edge. The color scale now includes negative values (in light blue) to distinguish the differences in localization.

### 4.4.2 Breaking of $\{\mathcal{G}_{2\alpha}\}$

Next, we fix opposite onsite energies $\varepsilon_\alpha = \pm\delta_2 t_0$ at lattice sites $r$ and $d$, $u$ and $l$. This assignation can be written as $(\varepsilon_r, \varepsilon_d, \varepsilon_u, \varepsilon_l) = \delta_2(1, -1, 1, -1)t_0$. The spatial representation of this choice is present in the middle panel of Fig. 4.3. In a diagonal matrix form, we can write:

$$\mathcal{M}_2(\delta_2) = \delta_2 \left(\sigma_0 \otimes \sigma_z\right) t_0, \tag{4.8}$$

where $\mathcal{M}_2(\delta_2)$ denotes the $\{\mathcal{G}_{2\alpha}\}$-breaking mass term that is added to the Hamiltonian in Eq. 4.2a as a function of the perturbation parameter $\delta_2$. In terms of SSH chains, we are differentiating between chains by placing the same onsite energy in lattice sites related by the intra-chain chiral symmetry. Same as before, we are breaking both the $\{\mathcal{G}_{2\alpha}\}$ set of glides and inversion symmetry.

**Bulk spectral properties** We start by discussing the results in the bulk, presented in Figure 4.6. For $\delta_2 = 0$, the pristine herringbone lattice is recovered–red line in Figure 4.6(a). The spectrum is also symmetric with respect to the change in sign of $\delta_2$. However, contrary to the previous section, the band structure remains gapless within the interval $|\delta_2| \leq \sqrt{3}$ (degeneracy interval). As soon as $\delta_2 \neq 0$ the Dirac cones move away from $\mathrm{K}^\pm$ towards $\Gamma$. We can find their position $\mathbf{k}_2^{\mathrm{D}}(\delta_2)$ as a function of $\delta_2$ by solving $E_3[\delta_2, \mathbf{k}_2^{\mathrm{D}}(\delta_2)] = 0$, where $E_3$ is the third band, corresponding to $(\alpha, \beta) = (+, -)$ in Eq. (4.3)[1]. It yields:

$$\mathbf{k}_2^{\mathrm{D}}(\delta_2) = \frac{1}{a_0} \arccos\left(\frac{1}{2}\sqrt{1 + \delta_2^2}\right) \mathbf{u}_1, \tag{4.9}$$

[1]The same expression is obtained if instead we work with band 2, corresponding to $(\alpha, \beta) = (-, +)$ in Eq. (4.3) since the spectrum is energy-symmetric. We refer the reader to Sec. 4.7 for a study on the energy symmetry of the spectrum.

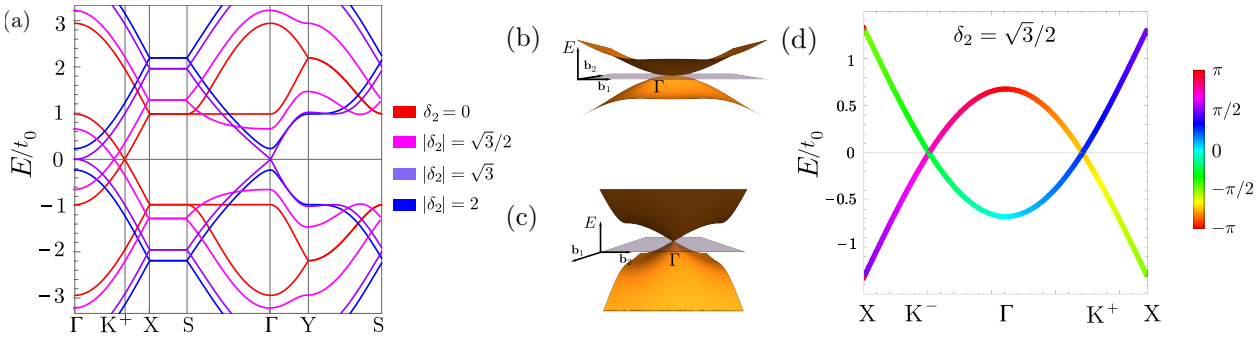


*Figure 4.6:* (a) Bulk spectrum for the pristine herringbone lattice and with the $\mathcal{M}_2(\delta_2)$ onsite potential. The values of $\delta_2$ are explicitly shown and reveal the movement of the Dirac cones. Only the Dirac cone at $\mathbf{K}^+$ has been plotted since it falls in the choice of high-symmetry path; (b), (c) Overview of the semi-Dirac point appearing at Γ when the two cones merge, displaying the parabolic/linear behavior respectively; (d) Energy spectrum of the herringbone lattice with $\mathcal{M}_2(\sqrt{3}/2)$, but colored according to the phase of the symmetry eigenvalue of the $\mathcal{G}_{1A}(\mathbf{k})$ operator, revealing that at the crossings, the eigenvalues are different, allowing a real crossing and not an anti-crossing of the bands.

where $\mathbf{k}_2^{\mathrm{D}}(\delta_2)$ represents the $(k_x, k_y)$ components of the position of the Dirac cones as a function of the $\delta_2$ parameter, $a_0$ is the interatomic distance, taken to be unity but made explicit in the equation, and $\mathbf{u}_1 = \mathbf{b}_1/|\mathbf{b_1}|$ represents the unitary vector along the direction of the first reciprocal lattice vector $\mathbf{b}_1$. The motion of the Dirac cones is captured in Figure 4.6(a). Since the spectrum is symmetric with respect to $\delta_2$, we start from the pristine herringbone lattice and increase $\delta_2$. As mentioned before, the cones move symmetrically towards each other along the $\mathbf{b}_1$ direction until $|\delta_2| = \sqrt{3}$. At this value, the two Dirac cones have shifted away from $\mathbf{K}^{\pm}$ (at $\delta_2 = 0$) and have merged at Γ into a semi-Dirac cone. Figures 4.6(b) and 4.6(c) show the semi-Dirac cone at Γ with the parabolic/linear behavior explicitly displayed. For $|\delta_2| > \sqrt{3}$, the semi-Dirac cone is gapped, and the band structure again splits into two composite sets of two bands. The flat degeneracy present at SXS remains untouched, but the dispersive degeneracy at SYS is broken.

The breaking of these glides can also be studied from the symmetry eigenvalues of $\{\mathcal{G}_{1\alpha}\}$ for different values of $\delta_2$. We observe that the eigenvalues of bands 2 and 3 remain different for all values of $\delta_2$, so the crossing is still protected by the first set of glides. We have presented bands 2 and 3 colored according to the phase of the eigenvalue of the $\{\mathcal{G}_{1\alpha}\}$ symmetry eigenvalue in Fig. 4.6(d).

**Ribbon spectral properties** We present now the results on the ribbons. As we discussed previously, the band structure of ribbons is the projection of the bulk one. We present the ribbon spectrum for $|\delta_2| = \sqrt{3}$, precisely at the appearance of the semi-Dirac cone in the bulk. As expected, we obtain the two different slopes of the semi-Dirac cone along the two different orientations of the ribbons.

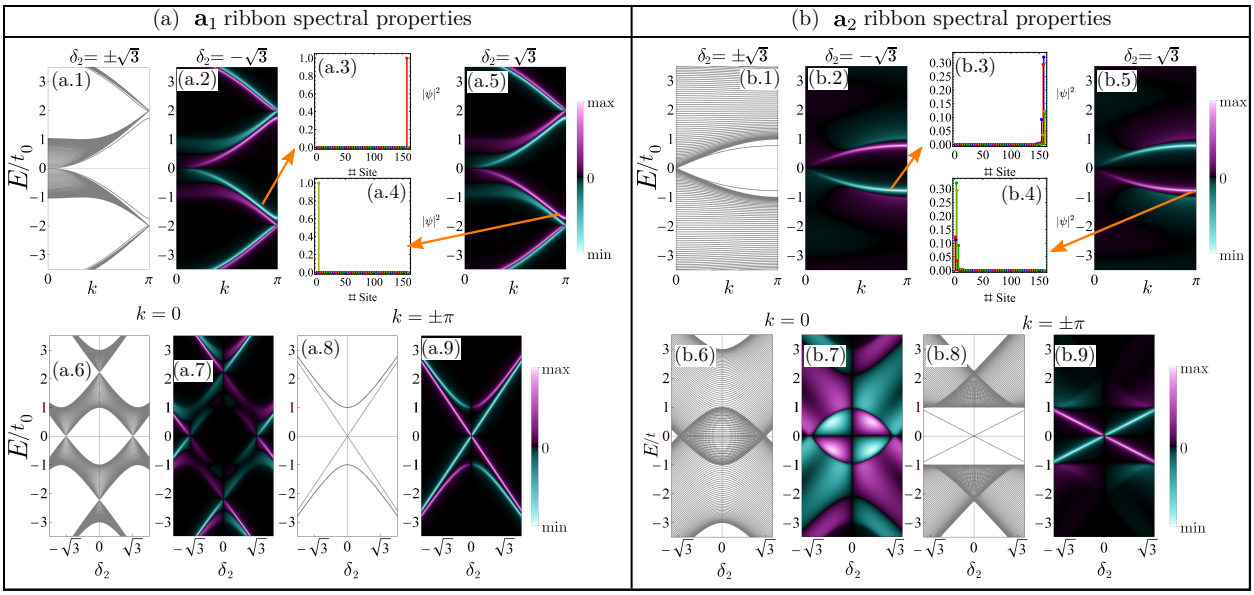


*Figure 4.7:* (a) $\mathbf{a}_1$ ribbon spectral properties with $\mathcal{M}_2(\delta_2)$; (a.1) Spectrum of the ribbon at the semi-Dirac point, (a.2) and (a.5) edge-projected spectral functions for opposite values of the onsite potential. The projection reveals a different localization of the edge states. The color of the plot is related to the localization of the wave function (blue for localization on the right and fuchsia for localization on the left). Panels (a.2) and (a.4) reveal the localization of the states marked in panels (a.2) and (a.5). Panels (a.6) and (a.8) show the $\delta_2$-spectrum at $k = 0$ and $k = \pi$ respectively. Panels (a.7) and (a.9) show the edge-projected spectral function associated with each of the $\delta_2$-spectra. At $k = 0$ the gap closes for $\delta_2$, right where the semi-Dirac cone forms. Panels (b.1) to (b.9) correspond to the same information as the panels from (a.1) to (a.9) but related to the $\mathbf{a}_2$ ribbon geometry. Respectively: (b.1) spectrum of the $\mathbf{a}_2$ ribbon with $|\delta_2| = \sqrt{3}$, (b.2) edge-projected spectral function for $\delta_2 = -\sqrt{3}$, (b.3), (b.4) localization of states across the ribbon, (b.5) edge-projected spectral function for $\delta_2 = \sqrt{3}$, (b.6) $\delta_2$-spectrum for $k = 0$, (b.7) edge-projected spectral function applied to the $\delta_2$-spectrum for $k = 0$, (b.8) $\delta_2$-spectrum for $k = \pi$, (b.9) edge-projected spectral function applied to the $\delta_2$-spectrum for $k = \pi$.

The ribbon along $\mathbf{a}_1$ displays the parabolic behavior, corresponding to the projection present in Figure 4.6(b). In the ribbon spectrum, along the parabolic bands, there are two of them that are detached from the rest. These bands correspond to two states tightly localized in just one atom at the edge, as shown in panels 4.7(a.3) and 4.7(a.4). Again, the localization changes after closing the gap. The $\delta_2$-spectrum for $k = 0$ is shown in panel 4.7(a.6) where we see how the gap closes at $\delta_2 = \pm\sqrt{3}$. The behavior of the closing and reopening of the gap at $k = 0$ is linear with $\delta_2$. Panel 4.7(a.8) is equivalent to panel 4.7(a.6) but for $k = \pi$. The linearity of the closing and reopening of the gap is also clear in this plot. Panels 4.7(a.7) and 4.7(a.9) represent the projected spectral function applied to the $\delta_2$-spectrum, revealing again the opposite localization with respect to the sign of $\delta_2$. On the contrary, the ribbons along $\mathbf{a}_2$ display the *almost* linear behavior, corresponding to the projection present in Figure 4.6(c). The linearity is achieved around a neighborhood of $k = 0$,

and it is lost as we approach $k = \pi$. Again, the are two bands detached from the rest. The states corresponding to these two bands are still localized in the edge of the ribbon, but not as tightly as in the case of $\mathbf{a}_1$ ribbons, as shown in panels 4.7(b.3) and 4.7(b.4). Again, the localization changes after closing the gap, reflected in the inversion of the color scale between panels 4.7(b.2) and 4.7(b.5). The $\delta_2$-spectrum for $k = 0$ is shown in panel 4.7(c.6), where at $\delta_2 = \pm\sqrt{3}$ we see how the gap closes. This time, the gap at $k = 0$ remains closed for the interval of degeneracy $|\delta_2| < \sqrt{3}$. Panel 4.7(b.8) represents the $\delta_2$-spectrum for $k = \pi$. It is noticeable how the bulk bands remain fixed at $E = \pm 1$ and only the detached state crosses the gap linearly at $k = \pi$. Finally, panels 4.7(b.7) and 4.7(b.9) represent the edge-projected spectral function applied to the $\delta_2$-spectrum, revealing again the opposite localization with respect to the sign of $\delta_2$.

We have used the same projection operator for the projected spectral function as in the previous section, since inversion symmetry is also broken by the addition of the $\mathcal{M}_2(\delta_2)$ mass term.

### 4.4.3 Breaking of $\{\mathcal{G}_{1\alpha}\} + \{\mathcal{G}_{2\alpha}\}$

Now, we present the last strategy to perturbing the lattice by assigning onsite energies to the lattice sites. We have related $r, d$ and $u, l$ in Sec. 4.4.1, and $r, u$ and $d, l$ in Sec. 4.4.2. This time, we relate $r, l$ and $d, u$ by placing $(\varepsilon_r, \varepsilon_d, \varepsilon_u, \varepsilon_l) = \delta_{\mathrm{I}}(1, -1, -1, 1)t_0$. The spatial representation of this choice is present in the right panel of Fig. 4.3. With this parameterization, we are simultaneously breaking both glides while respecting inversion symmetry. We will refer to this mass term as the inversion symmetric term, which can be written as a diagonal matrix:

$$\mathcal{M}_{\mathrm{I}}(\delta_{\mathrm{I}}) = \delta_{\mathrm{I}}\,(\tau_z \otimes \sigma_z)\,t_0, \tag{4.10}$$

where $\mathcal{M}_{\mathrm{I}}(\delta_{\mathrm{I}})$ denotes the $\{\mathcal{G}_{1\alpha}\} + \{\mathcal{G}_{2\alpha}\}$-breaking inversion-symmetric mass term that is added to the Hamiltonian in Eq. (4.2a) as a function of the perturbation parameter $\delta_{\mathrm{I}}$. In terms of SSH chains, we are breaking both the intra- and inter-chain chiral symmetry operators.

**Bulk spectral properties** We begin with the bulk results in Fig. 4.8(a). With this setup, the gap at zero energy closes within the interval $|\delta_{\mathrm{I}}| \leq 1$. Outside of it, the four bands become isolated. For $|\delta_{\mathrm{I}}| = \pm 1$, bands 2 and 3 are degenerated at zero energy along SXS, forming a nodal line showing two different regimes: along the path XΓX, the dispersion is locally parabolic around the X point. At the same time, it is locally linear around the S points along SYS, parallel to XΓX. This is represented in Fig. 4.8(b). These two energy dispersions (parabolic and linear behavior) have been presented before as a semi-Dirac cone. However, those two behaviors appear simultaneously at the same $\mathbf{k}$ point and along two orthogonal directions. This time, the two dispersions occur at different $\mathbf{k}$ points and along parallel lines in the first Brillouin zone. We call this feature *unfolded* semi-Dirac cone as

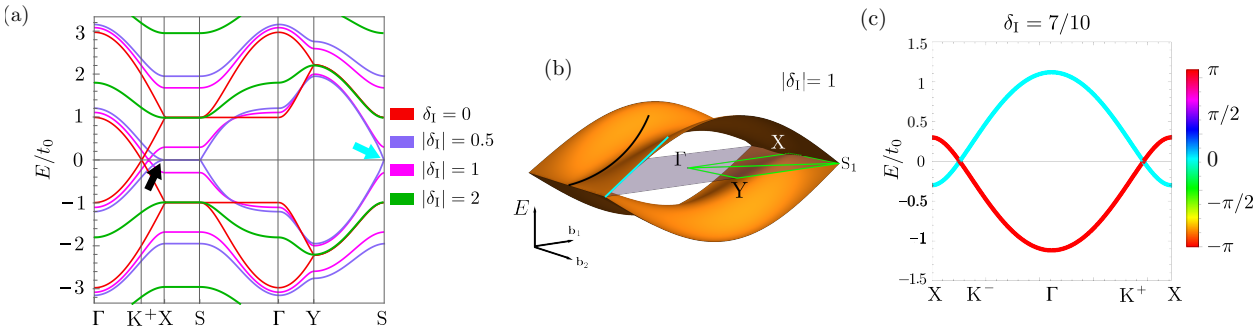


*Figure 4.8:* (a) Bulk spectrum for the fully symmetric case and the one with the $\mathcal{M}_I(\delta_I)$ onsite potential. The values of $\delta_I$ are explicitly shown. The arrows reveal the parabolic/linear behavior of the band structure at different $\mathbf{k}$ points; (b) overview of the unfolded semi-Dirac point appearing at X when the two cones merge; (c) energy spectrum of the Herringbone lattice with $\mathcal{M}_I(1)$, but colored according to the phase of the symmetry eigenvalue of the inversion operator, revealing that at the crossings, the eigenvalues are different ($\pm 1$ for all $\mathbf{k}$ points).

if a semi-Dirac cone was unfolded along SXS, thus forming the nodal line along that path (imposed by the non-symmorphic symmetries) but still preserving the linear and parabolic behaviors.

The bulk spectrum is symmetric under the change of sign of $\delta_I$ so, shifting $\delta_I$ from negative to positive, bands 2 and 3 become degenerated at $\delta_I = -1$ in a nodal line along SXS. Increasing $\delta_I$, the parabolic part of the unfolded semi-Dirac point (at the X point) splits into two Dirac cones that move towards $K^{\pm}$ points, reaching them at $\delta_I = 0$, recovering the pristine herringbone lattice. For positive $\delta_I$, the behavior is the opposite, Dirac cones from $K^{\pm}$ move towards X and merge with the ones from the adjacent first Brillouin zones into unfolded semi-Dirac cones at X and $\delta_I = 1$. Finally, for $\delta_I > 1$, the band structure is formed by four isolated bands.

We obtain the analytical position of the Dirac cones by solving $E_3[\delta_I, \mathbf{k}_I^D(\delta_I)] = 0$, where $E_3$ is the third band, corresponding to $(\alpha, \beta) = (+, -)$ in Eq. (4.3)[1]. It yields:

$$\mathbf{k}_I^D(\delta_I) = \frac{1}{2a_0} \arccos\left(-\frac{1+\delta_I^2}{2}\right) \mathbf{u}_1 \tag{4.11}$$

where $\mathbf{k}_I^D(\delta_I)$ represents the $(k_x, k_y)$ components of the position of the Dirac cones as a function of the $\delta_I$ parameter, $a_0$ is the interatomic distance, taken to be unity but made explicit, and $\mathbf{u}_1 = \mathbf{b}_1/|\mathbf{b_1}|$ represents the unitary vector along the direction of the first reciprocal lattice vector $\mathbf{b}_1$. Figure 4.16 displays the trajectory of the Dirac cones for increasing $\delta_I$.

[1]The same expression is obtained if instead, we work with band 2, corresponding to $(\alpha, \beta) = (-, +)$ in Eq. (4.3) since the spectrum is energy-symmetric. We refer the reader to Sec. 4.7 for a study on the energy symmetry of the spectrum.

**Ribbon spectral properties** Now we discuss the ribbon geometry results, present in Fig. 4.9. We want to point out that with respect to figures 4.5 and 4.7, the color scale of the projected spectral function has changed: now, the projector of the spectral function is the same that the one we used for the pristine herringbone lattice, back in Sec. 4.2.2. This is because the $\mathcal{M}_{\mathrm{I}}(\delta_{\mathrm{I}})$ mass term preserves inversion symmetry, and thus, in order to obtain a non-zero contribution from the bulk states into the projected spectral function, we need to add up the contributions from the lattice unit cells in the boundaries of the ribbon unit cell. Still, the edge states are located on just one edge and so, we cannot distinguish the edges in the edge-projected spectral function.

We begin with the spectral properties of the $\mathbf{a}_1$ ribbon. Panel (a.1) shows the spectrum of the $\mathbf{a}_1$ ribbon for $\delta_{\mathrm{I}} = \pm 1$, right where the unfolded semi-Dirac appears in the bulk. The band structure of the ribbon along $\mathbf{a}_1$ reveals the parabolic and linear behaviors of the unfolded semi-Dirac cone at the same time. In this ribbon, the path SXS projects onto a single point ($k = \pi$), so both the parabolic behavior along XΓX and the linear behavior along SYS are projected along the one-dimensional Brillouin zone. In this way, the bands around zero energy display the parabolic behavior, while the bands closer to the lower and upper gaps display the linear behavior. The spectrum for $\delta_{\mathrm{I}} = -1$ presents two degenerated bands at $k = 0$ in the lower gap detached from the bulk ones, represented in gray. For positive $\delta_{\mathrm{I}} = 1$ these bands merge into the bulk ones, and another two degenerated bands detach from the bulk ones and move inside the upper gap. We have represented these last two bands (for $\delta_{\mathrm{I}} = 1$) in red in panel 4.9(a.1). The rest of the features of the spectrum remain the same between these two situations. Panels 4.9(a.3) and 4.9(a.4) represent the localization of these two degenerated states. In panels 4.9(a.2) and 4.9(a.5) we show the edge-projected spectral function respectively for $\delta_{\mathrm{I}} = \pm 1$, displaying the two in-gap states. In panel 4.9(b.8), where we show the $\delta_{\mathrm{I}}$-spectrum at $k = \pi$, we clearly see how the in-gap states we introduced in panel 4.9(a.1) shift from negative to positive energy. These two in-gap states can also be detected in panel 4.9(b.7), where we plot the $\delta_{\mathrm{I}}$-spectrum but at $k = 0$. At opposite values of $\delta_{\mathrm{I}}$, they appear in different gaps, so now the ribbon spectrum is *not* symmetric under the change of sign of $\delta_{\mathrm{I}}$.

We see a similar behavior along the $\mathbf{a}_2$ direction: the energy spectrum is not symmetric with respect to the change of sing of $\delta_{\mathrm{I}}$. There is an in-gap state at positive energy in the upper gap for negative $\delta_{\mathrm{I}}$, detached from the bulk bands around $k = 0$. For positive $\delta_{\mathrm{I}}$ the in-gap state in the upper gap merges with the bulk bands, and a new in-gap state appears in the lowest gap. The spectrum for both $\delta_{\mathrm{I}} = \pm 1$ are represented 4.9(b.1). The red band appears only for $\delta_{\mathrm{I}} = 1$ while its homologous in the upper gap only appears for $\delta_{\mathrm{I}} = -1$. Panels 4.9(b.3) and 4.9(b.4) show the localization of these states in the two opposite sides of the ribbon unit cell. The unfolded semi-Dirac cone is also present in the band structure of this ribbon. As a reminder, now the one-dimensional first Brillouin

zone is the projection of the SYS path over the S points and the XΓX path over the X points. If one checks the density of bands in the panel 4.9(b.1), near $k = 0$ the bands are closer to each other, corresponding to a parabolic distribution that has been projected over the plane, while near $k = \pi$, the bands are more spaced, which is related to the linear behavior around these $k$ points. Again, in this ribbon, the two-dimensional first Brillouin zone is projected onto the SXS path, so the $k = 0$ corresponds to the X point, where the behavior of the bands is parabolic. In contrast, the $k = \pi$ point corresponds to the S point, where the behavior is linear.

Finally, in panels 4.9(b.6) and 4.9(b.8) we present the $\delta_{\mathrm{I}}$-spectrum respectively at $k = 0$ and $k = \pi$, and their edge-projected spectral functions in panels 4.9(b.7) and 4.9(b.9).

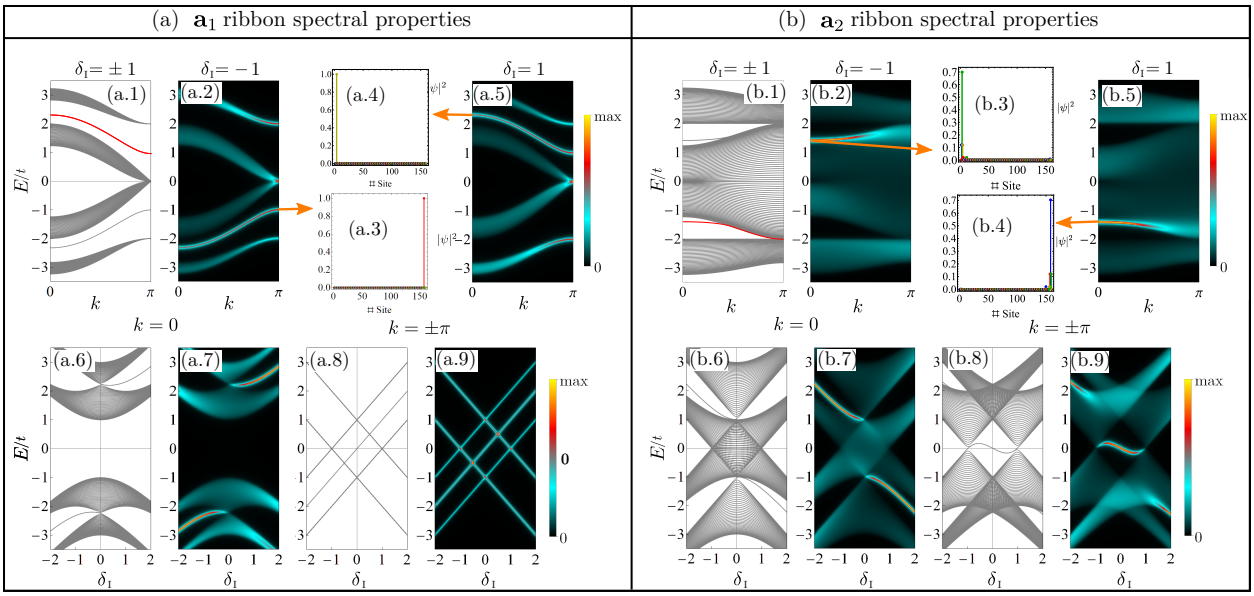


*Figure 4.9:* (b) $\mathbf{a}_1$ ribbon results with $\mathcal{M}_{\mathrm{I}}(\delta_{\mathrm{I}})$; (b.1) Spectrum of the ribbon at the unfolded semi-Dirac point, (b.2) and (b.4) edge projected spectral functions for opposite values of the onsite potential. The projection reveals a different localization of the edge states. Panels (b.3) and (b.5) reveal the localization of the states marked in panels (b.2) and (b.4). Panels (b.6) and (b.8) show the $\delta_{\mathrm{I}}$-spectrum at $k = 0$ and $k = \pi$ respectively. Panels (b.7) and (b.9) show the edge-projected spectral function associated with each of the $\delta_{\mathrm{I}}$-spectra. At $k = \pi$ the gap closes for $\delta_{\mathrm{I}}$, right where the unfolded semi-Dirac cone forms. Panels (c.1) to (c.9) correspond to the same information as the panels from (b.1) to (b.9) but related to the $\mathbf{a}_2$ ribbon geometry. Respectively: (b.1) spectrum of the $\mathbf{a}_2$ ribbon with $|\delta_{\mathrm{I}}|1$, (b.2) edge-projected spectral function for $\delta_{\mathrm{I}} = -1$, (b.3), (b.4) localization of states across the ribbon, (b.5) edge-projected spectral function for $\delta_{\mathrm{I}} = 1$, (b.6) $\delta_{\mathrm{I}}$-spectrum for $k = 0$, (b.7) edge-projected spectral function applied to the $\delta_{\mathrm{I}}$-spectrum for $k = 0$, (b.8) $\delta_{\mathrm{I}}$-spectrum for $k = \pi$, (b.9) edge-projected spectral function applied to the $\delta_{\mathrm{I}}$-spectrum for $k = \pi$.

## 4.5 Combining onsite potentials

Once we have introduced the main perturbations applied to the onsite energies, now we combine them and study the changes in the bulk spectrum. In this way, we study the bulk Hamiltonian with onsite energies controlled by the mass terms we have introduced in the previous sections: the combination $\mathcal{M}_1(\delta_1) + \mathcal{M}_2(\delta_2)$ is present in Sec. 4.5.1; the combination $\mathcal{M}_1(\delta_1) + \mathcal{M}_\mathrm{I}(\delta_\mathrm{I})$ is present in Sec. 4.5.2, and finally, the combination $\mathcal{M}_2(\delta_2) + \mathcal{M}_\mathrm{I}(\delta_\mathrm{I})$ is present in Sec. 4.5.3.

### 4.5.1 Combining $\mathcal{M}_1(\delta_1) + \mathcal{M}_2(\delta_2)$

We begin by adding to the bulk Hamiltonian in Eq. (4.2a) the total mass term $\mathcal{M}_{1,2}(\delta_1, \delta_2) = \mathcal{M}_1(\delta_1) + \mathcal{M}_2(\delta_2)$. The main effect of each term is, respectively, to gap the band structure, and to control the position of the Dirac cones to merge them into a semi-Dirac cone. The combination of the two is thus to gap both the Dirac cones anywhere and the semi-Dirac cone. We have presented the action of the combined onsite potentials in a phase diagram shown in Figure 4.10(c). We have represented $\delta_1$ on the vertical axis, where the gap closes only for $\delta_1 = 0$ at the $\mathbf{K}^\pm$ points. On the horizontal axis, we have represented $\delta_2$, where there is no gap until we leave the interval of degeneracy ($|\delta_2| \leq \sqrt{3}$). Outside of the interval of degeneracy, the gap cannot be closed. Finally, the phase diagram is colored depending on the position of the gap according to the values of $\delta_1$ and $\delta_2$.

Additionally, we have also plotted the band structure for several values of $\delta_1$ and $\delta_2$, which are explicitly shown in the phase diagram. The values for panel 4.10(a) correspond to the bullets in the phase diagram while for panel 4.10(b), the values correspond to the squares in the phase diagram. We have included the plot of the bands at $\delta_1 = 0$, which is already present in Figure 4.6(a), as a guide to the eye. At $\delta_1 = 0$ we find the phase diagram of just $\mathcal{M}_2(\delta_2)$, which is an interval (thick black line), and for $\delta_2 = 0$ we find the phase diagram of just $\mathcal{M}_1(\delta_1)$, which is just the critical point (red triangle).

With this total mass-term, one can shrink the dipolar distribution of the Berry curvature– Fig. 4.10(g). Moreover, we can visualize the Berry curvature of a gapped semi-Dirac cone– Figs. 4.10(f) and 4.10(h). Some final remarks about combining $\mathcal{M}_1(\delta_1) + \mathcal{M}_2(\delta_2)$ are:

- A change in the sign of $\delta_1$ always produces a band inversion. Figures 4.10(e) to 4.10(i) only display the Berry curvature for negative $\delta_1$, since the ones for positive $\delta_1$ differ in an overall sign.
- The gap cannot be closed by using $\mathcal{M}_1(\delta_1)$ when $\delta_2$ falls outside the interval of degeneracy,

which means the gap at the Γ point between the solid blue lines in Fig. 4.10(b) cannot be closed, while the one between the purple ones can.

- The flat degeneracies along SXS remain flat but are completely lifted by a nonzero value of $\delta_1$, so these two degeneracies are protected by both glides at the same time.

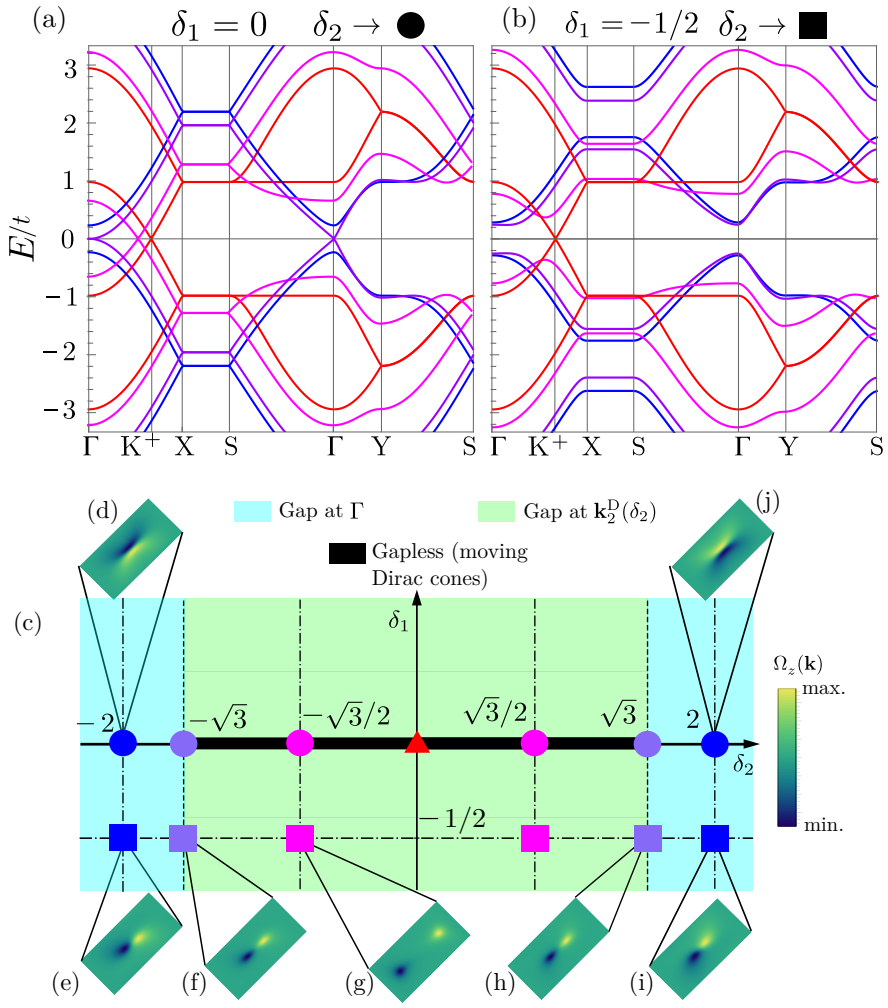


*Figure 4.10:* (a) Energy spectrum for the herringbone lattice with the $\mathcal{M}_2(\delta_2)$ onsite potential. This panel has been added as a guide to understand panel (b). Panel (b) displays the energy spectrum for the herringbone lattice with the combination $\mathcal{M}_1(\delta_1) + \mathcal{M}_2(\delta_2)$ of onsite potentials. Panel (c) represents the phase diagram of the herringbone lattice under the aforementioned onsite potential combination. The symbols correspond to the values of the parameters used to plot the band structures in panels (a) and (b). Panels (d) to (j) Berry curvature profiles for the different combinations of parameters.

### 4.5.2 Combining $\mathcal{M}_1(\delta_1) + \mathcal{M}_\mathrm{I}(\delta_\mathrm{I})$

We now add to the bulk Hamiltonian in Eq. (4.2a) the total mass term $\mathcal{M}_{1,\mathrm{I}}(\delta_1, \delta_\mathrm{I}) = \mathcal{M}_1(\delta_1) + \mathcal{M}_\mathrm{I}(\delta_\mathrm{I})$. The main effect of the $\mathcal{M}_\mathrm{I}(\delta_\mathrm{I})$ onsite potential is to control the position of the Dirac cones and merge them into an unfolded semi-Dirac cone. Hence, the addition of the gapping term $\mathcal{M}_1(\delta_1)$ will gap both the cones, at any position, and the unfolded semi-Dirac cone. We have presented the action of the combined onsite potentials in a phase diagram shown in Figure 4.11(d). On the vertical axis, we represent $\delta_1$, where the gap closes only for $\delta_1 = 0$ at the $\mathbf{K}^\pm$ points. On the horizontal axis, we have represented $\delta_\mathrm{I}$, where there is no gap until we leave the interval of degeneracy ($|\delta_\mathrm{I}| \leq 1$). Finally, outside of the interval of degeneracy, the gap cannot be closed. Same as before, the phase diagram is colored depending on the position of the gap according to the value of $\delta_1, \delta_\mathrm{I}$. We begin by fixing $\delta_1 = 0$, where we recover the individual effects of the $\mathcal{M}_\mathrm{I}(\delta_\mathrm{I})$ perturbation. This case is shown in panel 4.11(a) as a guide to the eye, although it is already present in Figure 4.8(a). If now we let $\delta_1 \neq 0$, we gap the Dirac cones at positions given by expression (4.11), as shown in Fig. 4.11(b) in color magenta.

We discuss now different features we can achieve apart from the gapping of the band structure. First, we refer the reader to panel 4.11(c), where we observe the appearance of degenerate flat bands along SXS. These can be found by setting $\delta_1 = \pm\sqrt{\delta_\mathrm{I}^2 - 1}$ so that $\mathcal{M}_{1,\mathrm{I}}(\delta_\mathrm{I}) = \mathcal{M}_\mathrm{I}(\delta_\mathrm{I}) + \mathcal{M}_1(\pm\sqrt{\delta_\mathrm{I}^2 - 1})$ for any $\delta_\mathrm{I} > 1$.. The lines $\delta_1 = \pm\sqrt{\delta_\mathrm{I}^2 - 1}$ are represented in the phase diagram separating the light pink and light blue regions.

Next, there are two lines of the phase diagram along which the gapped Dirac cones merge totally into the band. In this case, the energy at the position of the Dirac cone, obtained from expression (4.11) since $\delta_1$ does not change the position of the cones, reaches the same value of the energy along the SXS path. We look for the relation between $(\delta_1, \delta_\mathrm{I})$ that makes the energy at $\mathbf{k}_\mathrm{I}^\mathrm{D}(\delta_\mathrm{I})$ equal to the energy along SXS. We obtain:

$$\delta_1(\delta_\mathrm{I}) = \pm\frac{\sqrt{9 - 10\delta_\mathrm{I}^2 + \delta_\mathrm{I}^4}}{4\delta_\mathrm{I}}. \tag{4.12}$$

This relation is represented with the dark blue lines in Figure 4.11(d) separating the green and pink regions. The three colored regions represent different gapped phases. As in the previous case, for $\delta_1 = 0$, we recover the phase diagram of $\mathcal{M}_\mathrm{I}(\delta_\mathrm{I})$, which is an interval. Setting $\delta_\mathrm{I} = 0$ we recover the phase diagram of $\mathcal{M}_1(\delta_1)$.

We now study the Berry curvature for the different combinations of parameters. We begin by the vertical line $\delta_\mathrm{I} = -2$: we observe a change in the sign of the Berry curvature. Remarkably,

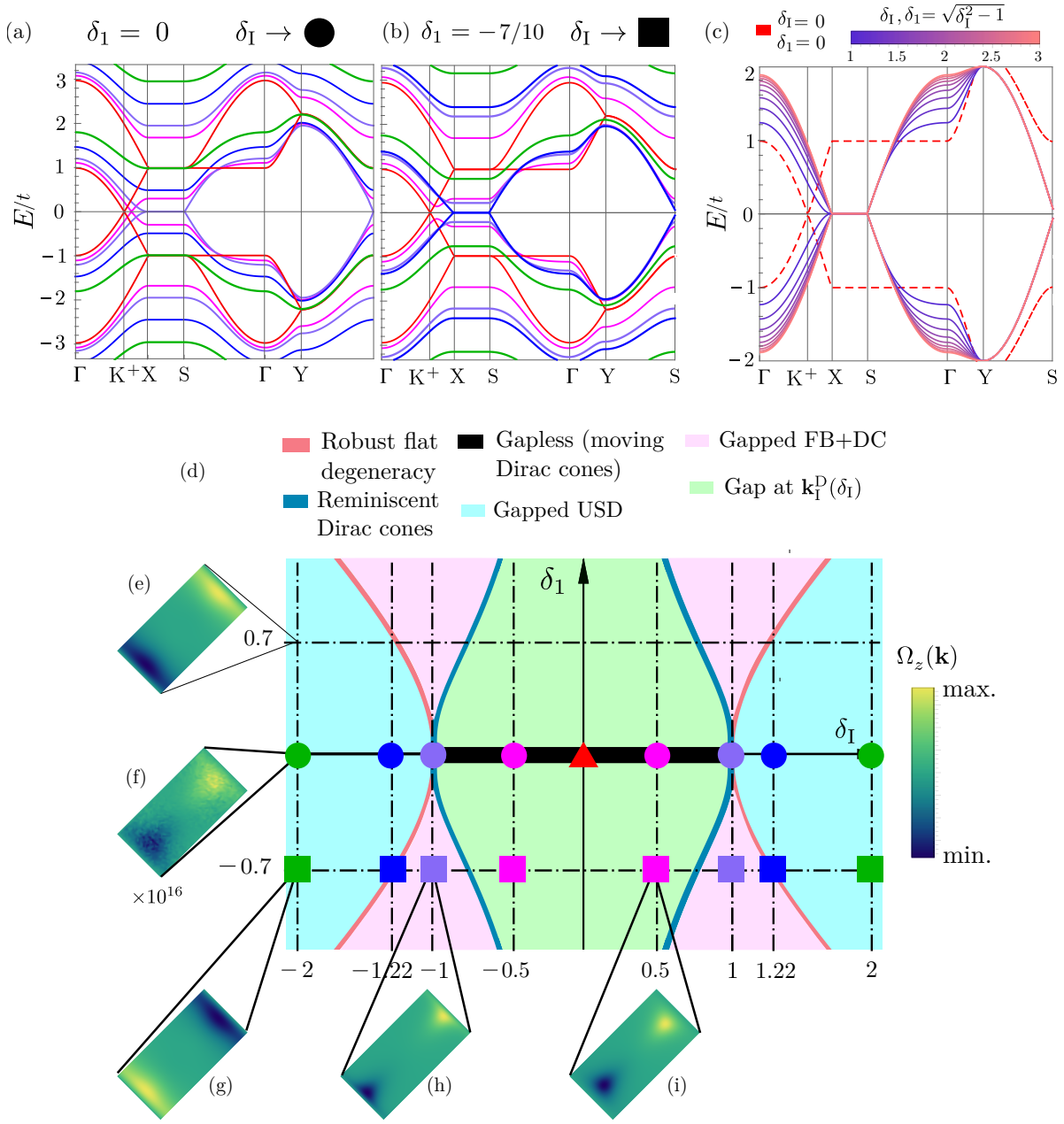


*Figure 4.11:* (a) Energy spectrum for the herringbone lattice with the $\mathcal{M}_I(\delta_I)$ onsite potential. This panel has been added as a guide to understand panel (b). Panel (b) displays the energy spectrum for the herringbone lattice with the combination $\mathcal{M}_1(\delta_1) + \mathcal{M}_I(\delta_I)$ of onsite potentials. The values of the parameters are shown on the panel (d). Panel (c) represents the relation between the parameters such that always yields an unfolded semi-Dirac point, which stretches with the intensity of the onsite potential. The more pink the color of the line, the more stretched the parabolic behavior, thus tending to a linear behavior. Panel (d) represents the phase diagram of the herringbone lattice under the aforementioned onsite potential combination. The symbols correspond to the values of the parameters used to plot the band structures in panels (a) and (b). Clearly, for panel (a), $\delta_1$ is zero.

this change of sign happens without a gap closing since we are outside the degeneracy interval. This is because at $\delta_1 = 0$, the term $\mathcal{M}_{\mathrm{I}}(\delta_{\mathrm{I}})$ preserves inversion symmetry. Since, additionally, time-reversal symmetry is preserved, the Berry curvature is identically zero for all $\delta_{\mathrm{I}}$ values, bands, and $\mathbf{k}$ points. This was claimed back theoretically in Section 2.5, and here, we find a practical example. Figure 4.11(g) shows the Berry curvature under these considerations, where the Berry curvature is around $10^{-16}$ (it has been rescaled to match the color bar). Inside the interval of degeneracy of $\mathcal{M}_{\mathrm{I}}(\delta_{\mathrm{I}})$ and with the gap opened with the non-zero $\delta_1$ value, we observe a dipolar distribution of the Berry curvature that now has stretched with respect to the case with the $\mathcal{M}_1(\delta_1)$ perturbation–shown in Figs. 4.4(b) and 4.4(c). Now the length is given by $L_\Omega = 2|\mathbf{k}_{\mathrm{I}}^{\mathrm{D}}(\delta_{\mathrm{I}})|$, since $\delta_1$ does not affect the position of the (gapped) Dirac cones. Again, the Berry curvature changes under the closing of the gap, so the plots of the Berry curvature for $\delta_1 > 0$ differ in a minus sign from the ones we are displaying, computed for $\delta_1 > 0$ –Figures 4.11(e), and Figures 4.11(g) to 4.11(i).

### 4.5.3 Combining $\mathcal{M}_2(\delta_2) + \mathcal{M}_{\mathrm{I}}(\delta_{\mathrm{I}})$

Finally, we add together the two terms that can change the position of the Dirac cones: $\mathcal{M}_{2,\mathrm{I}}(\delta_2, \mathrm{I}) = \mathcal{M}_2(\delta_2) + \mathcal{M}_{\mathrm{I}}(\delta_{\mathrm{I}})$. We have computed a phase diagram of the system under these potentials, shown in Fig. 4.12. As mentioned previously, the effect of $\mathcal{M}_2(\delta_2)$ is to move the Dirac cones and merge them at $\Gamma$ into a semi-Dirac cone, while the effect of $\mathcal{M}_{\mathrm{I}}(\delta_{\mathrm{I}})$ is to move the Dirac cones and merge them into unfolded semi-Dirac cones at the X points. Panel 4.12(a) shows the band structure for different values of $(\delta_2, \delta_{\mathrm{I}})$, plus the spectrum of the pristine herringbone lattice as a guide to the eye. Figure 4.12(b) shows the phase diagram of this combination of mass terms. Again, by making $\delta_{\mathrm{I}} = 0$ we recover the properties of $\mathcal{M}_2(\delta_2)$, while by making $\delta_2 = 0$ we recover the properties of $\mathcal{M}_{\mathrm{I}}(\delta_{\mathrm{I}})$. We thus expand the phase diagram in the following way. The vertical axis is delimited by the point where the gap closes at $\Gamma$ forming a semi-Dirac cone, so we solve $E_3[\delta_2, \delta_{\mathrm{I}}, \Gamma] = 0$ to obtain the relation between $\delta_2, \delta_{\mathrm{I}}$ that preserves the semi-Dirac cone at $\Gamma$. We obtain:

$$\delta_2(\delta_{\mathrm{I}}) = \pm\sqrt{3 + \delta_{\mathrm{I}}^2}. \tag{4.13}$$

This is represented with the purple line in the phase diagram in Figure 4.12(b), and defines the boundary of gapless/gapped phases in the vertical axis. Fixing $\delta_{\mathrm{I}} = 0$ in expression (4.13) we recover the interval of degeneracy of $\mathcal{M}_2(\delta_2)$, $|\delta_2| \leq \sqrt{3}$. When $\delta_{\mathrm{I}} \neq 0$, the four bands split, and the semi-Dirac at $\Gamma$ is formed only by the two intermediate bands. This new[1] semi-Dirac cone can be

[1]We call it "new" since the previous one was formed also between bands 2 and 3, but they were degenerated also with bands 1 and 4, forming two sets touching in a semi-Dirac cone.

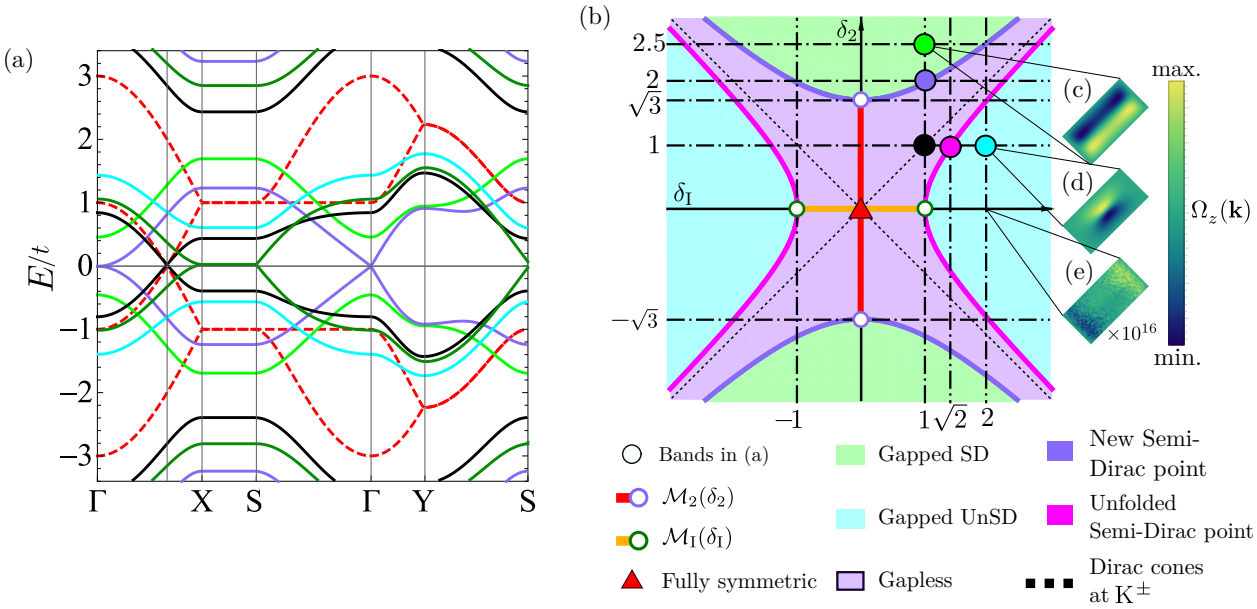


*Figure 4.12:* (a) Energy spectrum for the herringbone lattice with the combination $\mathcal{M}_2(\delta_2)+\mathcal{M}_1(\delta_1)$ of onsite potentials. The values of the parameters are shown on the panel (b). Panel (b) represents the phase diagram of the herringbone lattice under the aforementioned onsite potential combination. The symbols correspond to the values of the parameters used to plot the band structures in panel (a).

gapped by adding a $\mathcal{M}_1(\delta_1)$. However, the bands would not be energy-symmetric anymore. More about this in Sec. 4.7.

Regarding the horizontal axis, we expand it by taking into account the interval of degeneracy of $\mathcal{M}_1(\delta_1)$, $|\delta_1| \leq 1$. Hence, for $(\delta_2, \delta_1) = (0, \pm 1)$, the gap closes along SXS in an unfolded semi-Dirac cone. We solve $E_3[\delta_2, \delta_1, X] = 0$ to obtain the relation between $\delta_2, \delta_1$ that preserves the unfolded-Dirac cone along SXS. This is an extension of the unfolded semi-Dirac cone for non-zero $\delta_2$. We obtain:

$$\delta_2(\delta_1) = \pm\sqrt{\delta_1^2 - 1}. \tag{4.14}$$

This is represented with the fuchsia line in the phase diagram in Figure 4.12(b), and defines the boundary of gapless/gapped phases in the horizontal axis. Finally, the gap at zero energy closes in a pair of Dirac-cones for generic $\delta_2, \delta_1$ inside the region $\mathcal{R}$ defined by the two limiting curves given by expressions (4.13) and (4.14):

$$\mathcal{R} = \left\{(\delta_2, \delta_1) : \delta_2^2 - \delta_1^2 < |3| \cup \delta_1^2 - \delta_2^2 < 1\right\} \tag{4.15}$$

The Dirac cones inside this region appear at generic positions that can be computed similarly as we did in sections 4.4.2 and 4.4.3. We solve $E_3\left[\delta_2, \delta_1, \mathbf{k}^{\mathrm{D}}_{2,1}\right] = 0$ and obtain

$$\mathbf{k}^{\mathrm{D}}_{1,2}(\delta_1, \delta_2) = \frac{1}{2a_0}\arccos\left(\frac{\delta_2^2 - \delta_1^2 - 1}{2}\right)\mathbf{u}_1, \tag{4.16}$$

| + | $\mathcal{M}_1(\delta_1)$ | $\mathcal{M}_2(\delta_2)$ | $\mathcal{M}_{\mathrm{I}}(\delta_{\mathrm{I}})$ |
|---|---|---|---|
| $\mathcal{M}_1(\delta_1)$ | Gap at $\mathrm{K}^{\pm}$ | • gapped SDC<br>• Shrunken BC dist. | • gapped UnSDC<br>• Stretched BC dist.<br>• Robust flat degeneracy |
| $\mathcal{M}_2(\delta_2)$ | | • SDC<br>• Cones at $\mathbf{k}_2^{\mathrm{D}}(\delta_2)$ | • new SD +UnSD<br>• Cones inside $\mathcal{R}$ at $\mathbf{k}_{\mathrm{I}+2}^{\mathrm{D}}(\delta_{\mathrm{I}})$ |
| $\mathcal{M}_{\mathrm{I}}(\delta_{\mathrm{I}})$ | | | • UnSDC<br>• Cones at $\mathbf{k}_{\mathrm{I}}^{\mathrm{D}}(\delta_{\mathrm{I}})$ |

*Table 4.1:* Summary of the main features of the combination of mass terms. Only the upper triangle has been filled so as not to overload the table. Adding only $\mathcal{M}_1(\delta_1)$ to the Hamiltonian, the bands are gapped at $\mathrm{K}^{\pm}$. Adding only $\mathcal{M}_2(\delta_2)$ to the Hamiltonian, a semi-Dirac cone (SDC) appears and can be split into Dirac cones that move according to $\mathbf{k}_2^{\mathrm{D}}(\delta_2)$. Adding only $\mathcal{M}_{\mathrm{I}}(\delta_{\mathrm{I}})$ to the Hamiltonian an unfolded semi-Dirac cone (UnSDC) appears and can be split into Dirac cones that move along $\mathbf{k}_{\mathrm{I}}^{\mathrm{D}}(\delta_{\mathrm{I}})$. Combining $\mathcal{M}_1(\delta_1) + \mathcal{M}_2(\delta_2)$ the SDC gaps and the Berry curvature (BC) is shrunken. Combining $\mathcal{M}_1(\delta_1) + \mathcal{M}_{\mathrm{I}}(\delta_{\mathrm{I}})$, the UnSDC gaps, the BC is stretched and there is a robust flat degeneracy between the bands. Combining $\mathcal{M}_2(\delta_2) + \mathcal{M}_{\mathrm{I}}(\delta_{\mathrm{I}})$ a new SD point is found that can be split into Dirac cones that move across the FBZ. Additionally, there is a region of parameters where the band structure shows Dirac cones.

where $\mathbf{k}_{\mathrm{I},2}^{\mathrm{D}}(\delta_{\mathrm{I}}, \delta_2)$ represents the $(k_x, k_y)$ components of the position of the Dirac cones as a function of the $\delta_{\mathrm{I}}, \delta_2$ parameters, $a_0$ is the interatomic distance, taken to be unity but made explicit, and $\mathbf{u}_1 = \mathbf{b}_1/|\mathbf{b_1}|$ represents the unitary vector along the direction of the first reciprocal lattice vector $\mathbf{b}_1$. We obtain a general expression that encodes equations 4.9 and 4.11[1] In this expression, by fixing $\delta_2 = \pm|\delta_{\mathrm{I}}|$ the Dirac cones always locate at $\mathbf{K}^{\pm}$.

With this, we complete the final phase diagram and our study of the onsite energies and their effects on the bulk spectrum. In the Appendix D.2 we present a low-energy theory [166] for all the cases studied so far. In table 4.1 we present a summary of the features we have studied so far in this lattice. Only the upper half of the table has been filled for the sake of clarity.

## 4.6 Dimerization technique

We present a completely different strategy for moving the Dirac cones inside the first Brillouin zone. It is based on differentiating between the horizontal and vertical hopping amplitudes in a

[1]We refer the reader to Appendix E for the full discussion about the equality between the particular cases of the expression 4.16 and equations 4.9 and 4.11, since they are written different but are analytically the same.

*breathing* form $t_{h/v} = t_0(1 \pm \delta_D)$ [160, 167]. We used the breathing dimerization in the SSH chain in Section 2.7 and in the breathing kagome model in Chapter 3. Figure 4.13(a) shows the real-space interpretation of this choice of breathing distortion. This particular choice of breathing respects inversion symmetry. However, there are several other choices of breathing distortions that also preserve some of the glides or a combination of them. The usual breathing distortion accounts for differentiating between intra- and inter-cell hoppings. In our case, we have differentiated between horizontal and vertical hopping amplitudes in order to break both glides while preserving inversion symmetry. In order to implement this particular breathing distortion, we add to Eq. (4.2b) the matrix:

$$q_B(\mathbf{k}) = t_0\delta_D \begin{pmatrix} 1 - e^{-ik_1} & -e^{ik_2} \\ e^{-ik_1} & 1 - e^{-ik_1} \end{pmatrix} = (1 - e^{-ik_1})\sigma_0 - e^{ik_2}\sigma_+ + e^{-ik_1}\sigma_-, \tag{4.17}$$

where $\delta_D$ is the dimerization parameter in units of the hopping amplitude $t_0$ and $\sigma_\pm$ are a symmetric/antisymmetric linear combinations of the Pauli matrices.

**Bulk spectral properties** We begin by studying the effects of the dimerization on the bulk spectrum. After diagonalizing the Hamiltonian, we find that the interval of degeneracy is the interval $|\delta_D| < 1/\sqrt{5}$. For $\delta_D = -1/\sqrt{5}$, we find semi-Dirac cones appearing at the $S_{2,4}$ points, which are related by inversion symmetry in reciprocal space. Upon increasing $\delta_D$, these semi-Dirac cones split into Dirac cones that move out from the S points towards the $\mathbf{K}^\pm$, for $\delta_D = 0$, where the pristine herringbone lattice is recovered. By increasing $\delta_D$, the cones keep moving continuously until they reach $S_{1,3}$, also related by inversion symmetry. At these points, the Dirac cones merge into semi-Dirac cones with the Dirac cones coming from the neighboring first Brillouin zones. The trajectory of the cones is quasi-hyperbolic and also respects inversion symmetry. Figure 4.13(b) shows the spectrum along the high-symmetry path for $\delta_D = (2\sqrt{5})^{-1}$, which shows a "gapped" band structure. However, this is not true since, for all values inside the interval of degeneracy, there is a pair of two Dirac cones inside the first Brillouin zone, but outside the high-symmetry path of the pristine herringbone lattice. Figure 4.13(c) shows the two Dirac cones outside of the high-symmetry path for $\delta_D = (2\sqrt{5})^{-1}$.

If we add any of the onsite potentials we have studied so far, the overall effect is to gap the cones at positions along the quasi-hyperbolic curve. This translates into an arbitrary orientation and length of the Berry curvature dipolar distribution as shown in Fig. 4.13(d). We show the trajectory of the Dirac cones as a function of $\delta_D$ in Fig. 4.16.

**Ribbon spectral properties** We study the spectral properties of the ribbon geometries, starting from the $\mathbf{a}_1$ ribbon. We study the spectrum in the limits of the degeneracy interval, present in

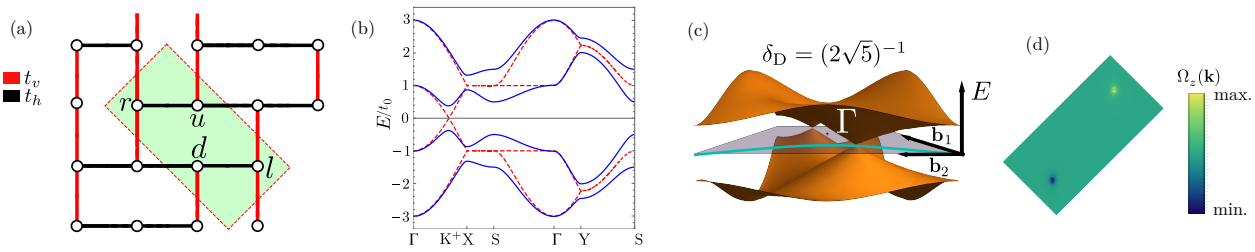


*Figure 4.13:* (a) Real-space interpretation of the horizontal/vertical dimerization applied to the hoppings. The lattice sites have been represented with empty circles to denote that no onsite energy is added to the system. (b) Spectrum of the herringbone lattice along the high-symmetry path for both the pristine case (dashed red line) and the dimerized one (solid blue line). A gap seems to open; however, panel (c) shows the full spectrum, displaying the Dirac cones outside the high-symmetry path. (d) Berry curvature of the dimerized herringbone lattice after adding the $M_1(\delta_1)$ potential to the hopping dimerization.

Figures 4.14(a.1) and 4.14(a.3). We observe that at the negative limit, $\delta_D = -1/\sqrt{5}$, four in-gap states appear totally detached from the bulk-like bands, two degenerated ones in the gap at positive energy and another two degenerated ones in the gap at negative energy. Actually, these states are present for $\delta_D < 0$, and disappear when $\delta_D > 0$. The localization of such states can be seen in the edge projected spectral function in panels 4.14(a.2), and it is plotted explicitly along the ribbon unit cell in panels 4.14(a.5) and 4.14(a.6). The $\delta_D$-spectrum for the $\mathbf{a}_1$ ribbon geometry is present in panels 4.14(a.7), for $k = 0$, and 4.14(a.9), for $k = \pi$. Both plots reveal that the spectrum is not symmetric with respect to the change in sign of the $\delta_D$ parameter. Finally, the edge-projected spectral function is applied to the $\delta_D$-spectrum, revealing the localization of all states for the whole range of $\delta_D$ values. These are shown in panels 4.14(a.8) and 4.14(a.10) respectively for $k = 0$ and $k = \pi$. If we cut the ribbon now along the $\mathbf{a}_2$ direction, we find that for negative $\delta_D$, there are two nearly flat bands around zero energy–Figure 4.14(b.1), that result from the isolation of atoms in the edges of the ribbon, due to the negative sign of $\delta_D$. These bands are present for all $\delta_D < 0$, and disappear when $\delta_D > 0$. The localization of such edge states can be seen in panels 4.14(b.5). For positive $\delta_D$, the flat bands merge with the bulk ones, and edge states at non-zero energy appear, as we can see in the detached bands around $k = 0$ in panel 4.14(b.3). The localization of these states in shown in panel 4.14(b.6) (both show the same distribution). The $\delta_D$-spectrum reveals that the energy spectrum is not symmetric with respect to the change in sign of the $\delta_D$ parameter. Finally, the edge-projected spectral function is applied to the $\delta_D$-spectrum, revealing the localization of all states for the whole range of $\delta_D$ values. These are shown in panels 4.14(b.8) and 4.14(b.10) respectively for $k = 0$ and $k = \pi$.

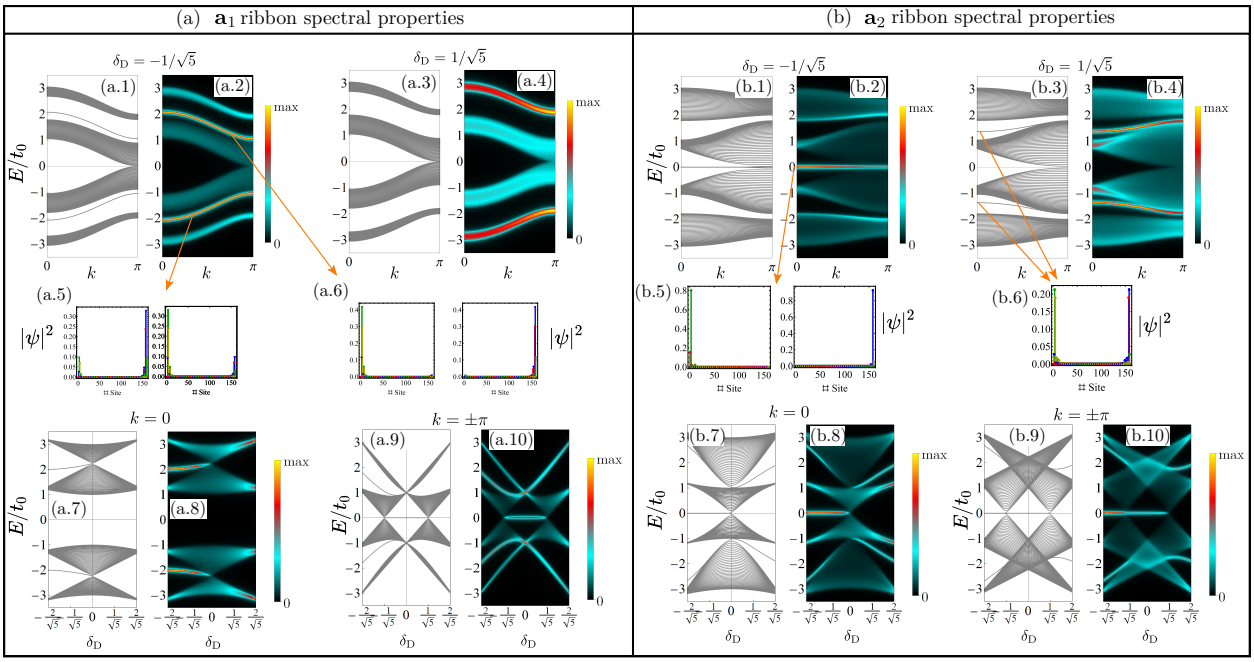


*Figure 4.14:* (b) $\mathbf{a}_1$ ribbon results. (b.1) and (b.2) show the spectra of the ribbon at closing of the gap, (b.4) and (b.6) show the edge projected spectral functions for opposite values of the onsite potential. The projection reveals a different localization of the edge states. Panels (b.2) and (b.3) reveal the localization of the states marked in panel (b.1). Panels (b.7) and (b.9) show the $\delta_D$-spectrum at $k = 0$ and $k = \pi$ respectively. Panels (b.8) and (b.10) show the edge-projected spectral function associated with each of the $\delta_F$-spectra. Panels (c.1) to (c.10) correspond to the same information as the panels from (b.1) to (b.10) but related to the $\mathbf{a}_2$ ribbon geometry. The two states shown in panel (c.5) show the same localization, so only one is shown. Respectively: (b.1) spectrum of the $\mathbf{a}_2$ ribbon with $|\delta_I|1$, (b.2) edge-projected spectral function for $\delta_I = -1$, (b.3), (b.4) localization of states across the ribbon, (b.5) edge-projected spectral function for $\delta_I = 1$, (b.6) $\delta_I$-spectrum for $k = 0$, (b.7) edge-projected spectral function applied to the $\delta_I$-spectrum for $k = 0$, (b.8) $\delta_I$-spectrum for $k = \pi$, (b.9) edge-projected spectral function applied to the $\delta_I$-spectrum for $k = \pi$.

**Flake spectral properties** Finally, in Fig. 4.15 we present the results for the dimerization technique applied to a finite-size square flake of the herringbone lattice. The size of this flake is set to be $N_1 = 2N_2 = 10$ unit cells. Panel 4.15(a) represents the $\delta_D$-spectrum of the flake. The rest of the panels present the localization of the first state of each group of bands: we distinguish bulk state–panel 4.15(b), two different species of edge states-panels 4.15(c) and 4.15(d), and corner modes–panel 4.15(e). We notice how the corner modes are widely spread along the system, more precisely, extended along the edges than into the bulk.

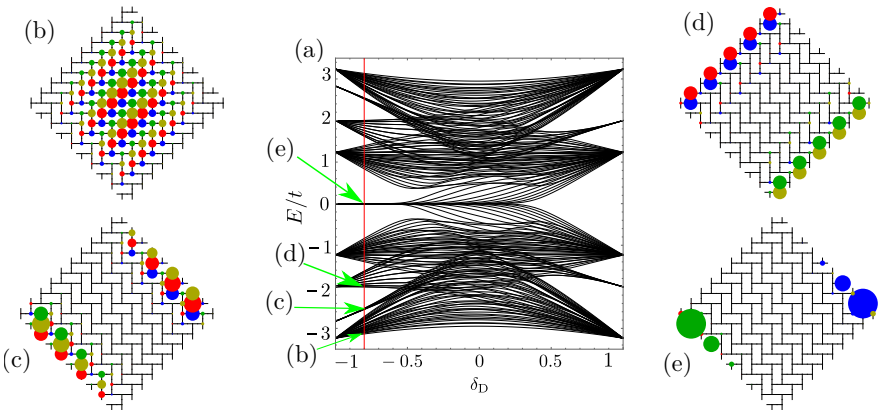


*Figure 4.15:* (a) $\delta_{\mathrm{D}}$-spectrum of a herringbone lattice flake under the dimerization technique. The red line represents the value of $\delta_{\mathrm{D}}$ chosen to plot the states. Along the line, the state with the lowest energy is represented. We have skipped a block of states that are also bulk and have already presented in panel (b). Panels (b) to (e) present the different localization of the chosen states, ordered by bulk, two species of edge, and corners respectively.

## 4.7 Final remarks on the perturbations

So far, we have presented the breaking of the symmetries of the lattices by means of applying onsite potentials to the lattice sites, and by differentiating between horizontal and vertical hoppings. We achieved the gaping of the band structure, movement of the Dirac cones and merging of them into semi-Dirac cones at high-symmetry points. Also, we have found the unfolding of the semi-Dirac cone into a nodal line plus a semi-Dirac cone. Finally, by mixing onsite potentials, we have gapped out all these features and made Dirac cones cross the whole first Brillouin zone.

All these combinations of onsite potentials and/or hopping dimerization leave the spectrum energy symmetric with respect to zero energy. This is true since for a four-band model, there exists an invariant that as long as it remains equal to zero, the band structure is energy symmetric. This invariant is called third Casimir invariant [168] and can be expressed as:

$$C_3 = \mathrm{Tr}(h(\mathbf{k})^3), \tag{4.18}$$

where Tr stands for the trace operator, *i.e.*, the sum of the diagonal elements of a matrix. For all the cases of the onsite potentials shown so far, the Casimir invariant is zero. However, if one computes the Casimir invariant for the combination of all three onsite potentials, we obtain:

$$C_3(\delta_1, \delta_2, \delta_{\mathrm{I}}) = \mathrm{Tr}(h(\delta_1, \delta_2, \delta_{\mathrm{I}}, \mathbf{k})^3) = 24\delta_1\delta_2\delta_{\mathrm{I}}, \tag{4.19}$$

which is different from zero for generic values of the parameters $(\delta_1, \delta_2, \delta_{\mathrm{I}})$ and thus energy symmetry is not recovered. In Table 4.2, we summarize the combinations of all perturbations that

| Perturbation | Spectrum character | Casimir invariant |
|---|---|---|
| $\mathcal{M}_1 + \mathcal{M}_2 + \mathcal{M}_\mathrm{I}$ | $C_3 = 24\delta_1\delta_2\delta_\mathrm{I}$ | No energy symmetry |
| $q_\mathrm{B}(\mathbf{k})$ | 0 | Energy symmetry |
| $q_\mathrm{B}(\mathbf{k}) + \mathcal{M}_1$ | 0 | Energy symmetry |
| $q_\mathrm{B}(\mathbf{k}) + \mathcal{M}_2$ | 0 | Energy symmetry |
| $q_\mathrm{B}(\mathbf{k}) + \mathcal{M}_\mathrm{I}$ | $C_3 = -24\delta_\mathrm{D}\delta_\mathrm{I}$ | No energy symmetry |
| $q_\mathrm{B}(\mathbf{k}) + \mathcal{M}_1 + \mathcal{M}_2$ | 0 | Energy symmetry |
| $q_\mathrm{B}(\mathbf{k}) + \mathcal{M}_1 + \mathcal{M}_\mathrm{I}$ | $C_3 = -24\delta_\mathrm{D}\delta_\mathrm{I}$ | No energy symmetry |
| $q_\mathrm{B}(\mathbf{k}) + \mathcal{M}_2 + \mathcal{M}_\mathrm{I}$ | $C_3 = -24\delta_\mathrm{D}\delta_\mathrm{I}$ | No energy symmetry |
| $q_\mathrm{B}(\mathbf{k}) + \mathcal{M}_1 + \mathcal{M}_2 + \mathcal{M}_\mathrm{I}$ | $C_3 = -24(\delta_\mathrm{D} - \delta_1\delta_2)\delta_\mathrm{I}$ | No energy symmetry |

*Table 4.2:* Table summarizing the possible combinations of onsite potentials and dimerization techniques that break energy symmetry in the bulk herringbone lattice.

respect or break the energy symmetry, with the corresponding Casimir invariant associated. Finally, we present figure 4.16 which shows the possible positions of the Dirac cones, controlled by the different perturbations that we have covered so far in this chapter.

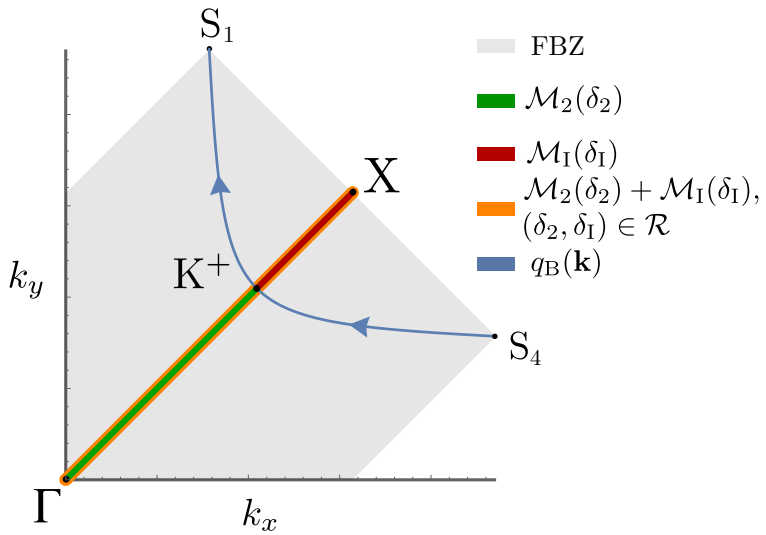


*Figure 4.16:* Representation of all trajectories of the Dirac cones as they move across the first Brillouin zone as a function of the different perturbations (only showing positive values of $k_x, k_y$).

## 4.8 Quantum simulator proposal

We propose here a realization of the herringbone lattice within the synthetic platform known as the artificial electron lattice [33]. We use the two-dimensional electron gas hosted on the (111) surface state of Cu, confined to a potential well designed with a set of CO molecules, which are

placed with atomic precision at certain positions with the help of the tip of a scanning tunneling microscope [32, 44, 45, 46, 53, 58, 129, 137]. We refer the reader to Sec. 2.3 for a full theoretical framework on this systems. Symmetry plays a crucial role: if the space groups of the substrate and the simulated lattice have common generators (one space group is a subgroup of the other), then the electronic structure of the lattice is well recovered. However, if this condition is not met, describing accurately a lattice with this technique is more difficult. In our case, we expect something similar for our proposal. The space group of the Cu(111) substrate is $p6mm$, while for the herringbone lattice it is $pgg$. In order to overcome this issue, we look for a unit cell choice that respects the orientation of lattice vectors. We present the design of the muffin-tin potential that reproduces the herringbone lattice in Fig. 4.17(a). Figure 4.17(b) shows the 8 lower bands obtained for the unit cell potential. Only the lowest four bands come from the inner electronic levels of the artificial electronic lattice, and so they represent the bands closer to our spectrum. Figure 4.17(c) shows bands 2&3 inside the FBZ, and we can see how two Dirac cones appear at opposite $k$ points. From the discussion in the previous sections, we can already see that the proposed unit cell will shows some dimerization plus some onsite energies that will return to the position of the Dirac cones. To fit these bands to a tight-binding Hamiltonian, next-nearest neighbors may be included, and even longer range hoppings, since the nearly-free electron method does not involve atomic orbitals or species, nor chemical bonds between them. The lattice sites are built with artificial interacting artificial atoms [58] connected by hopping amplitudes which are always long-range and modeled by potential wells or barriers.

## 4.9 Conclusions

In conclusion, we have presented the spectral properties of a 2D non-symmorphic lattice. In the bulk, we have shown that the system is characterized by two Dirac cones along a high-symmetry line that can either gap or move within the FBZ. We also can merge these Dirac cones into a semi-Dirac cone or, in a special case, into an unfolded semi-Dirac cone that respects the nodal line degeneracy imposed by a glide symmetry. The moving and the merging of the Dirac cones has been experimentally observed in black phosphorous [169, 170]: a 2D layered material characterized by non-symmorphic symmetries.

In the ribbon and flake geometries, we have observed the appearance of boundary modes whose localization is controlled by the perturbation parameter, both with the onsite potentials and with the dimerization technique. The projected spectral function allows us to study the localization of the states in the energy spectrum, but more interestingly, in the $\delta_{\mathrm{D}}$-spectrum, which has allowed us to see the changes in the localization of the states.

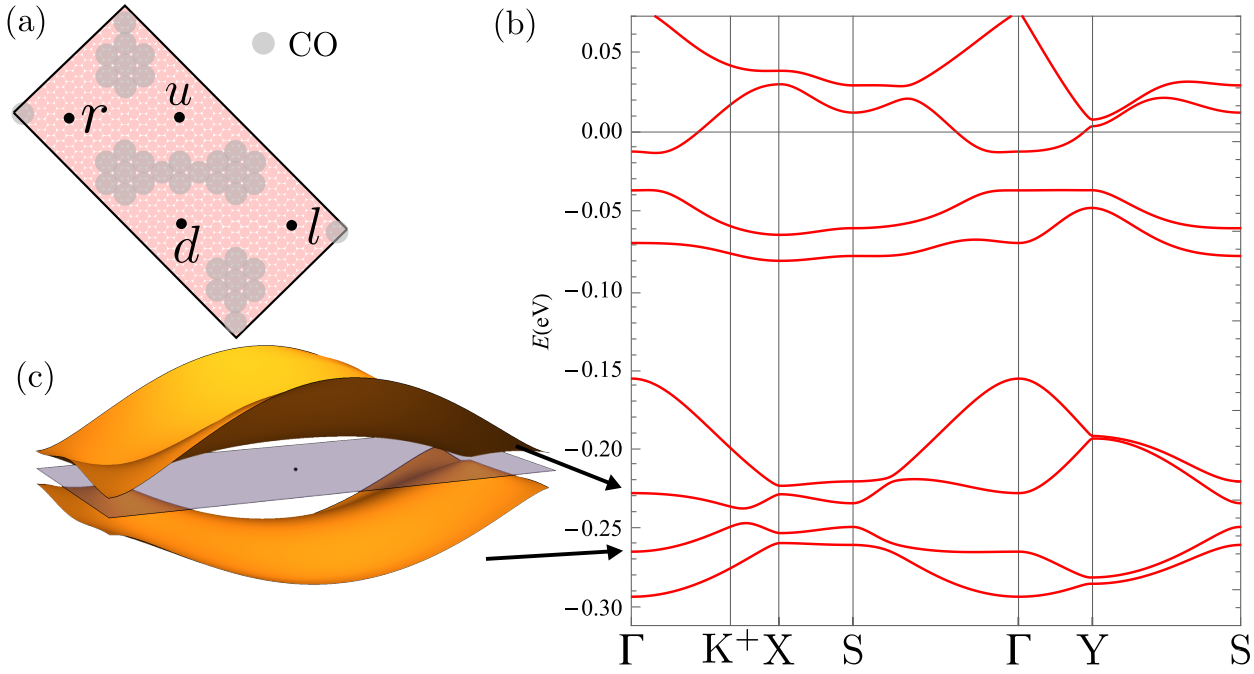


*Figure 4.17:* (a) Proposal for the unit cell of the Herringbone lattice in the nearly-free electron simulator. (b) Energy spectrum along a high-symmetry path for the Herringbone lattice according to the proposal. (c) Bands 2&3 of the proposal, underlining the presence of the Dirac cones outside a high-symmetry path.

Finally, a proposal for realizing the system in a quantum simulator is presented. The low energy band structure resembles the bulk one, presented in Figure 4.13(b), so we can guess that the fitting of the band structure will show dimerization. Many other parameters can also be fit, like longer range hoppings and overlap between the wavefunctions.

# CHAPTER 5

# Fragile topology in electronic quantum simulator

This chapter is devoted to the study of a topological phase dubbed "fragile" [171]. We present in Section 5.1 an introduction to robust or stable topology, in contrast to the fragile one, and we characterize both of them in terms of topological invariants and symmetry arguments, pointing out the differences and similarities between those two approaches. In Section 5.2, we introduce a particular case of a two-dimensional electronic lattice, which we call triangular Lieb lattice, that displays a fragile topological flat band structure and study it by adding nearest-neighbors hoppings to the tight-binding Hamiltonian. Next, in Section 5.3, we present the symmetries of the lattice and write explicitly the representations of the symmetry operators in real and reciprocal space. Additionally, we characterize the irreducible representations at each high-symmetry point in reciprocal space to assign a band representation to each set of bands. We describe in Section 5.4 the diagnosis of the fragile topology by means of both group theory and topological quantum chemistry [1] and topological invariants, more precisely, the Wilson loop operator and its spectrum. In Section 5.5, we study the breakdown of the bulk-boundary correspondence in fragile topological phases and present the results for the triangular Lieb lattice as it is cut into a finite-size flake that respects the symmetries of the lattice. Finally, in Section 5.6, we present a possible quantum simulation of the triangular Lieb lattice in the CO/Cu(111) platform and present different arrangements of molecules that may give rise to a fragile band structure. In this case, the diagnosis is done just by checking the Wilson loop spectrum operator of each configuration.

## 5.1 Robust versus fragile topology

Topology is related to the properties of a system that are robust against small perturbations. As mentioned in Chapter 2, the topology of a system can be diagnosed using both topological invariants

and group theory. The underlying idea is that a topologically trivial system can always be mapped to an atomic limit with exponentially localized Wannier functions that respect the symmetries of the lattice. On the contrary, a topologically non-trivial system will never have a set of exponentially localized Wannier functions that respect *all* the symmetries of the lattice since the topological character is an obstruction to the definition of a smooth gauge in the reciprocal space.

However, it exists a third case where we can *trivialize* a set of *a priori* topological bands by adding trivial degrees of freedom to it. This is the case of fragile topology, where the usual bulk-boundary correspondence breaks down even if the system is indeed topological.

Let's cover the differences between robust and fragile topology in terms of the tools we have used previously for the diagnosis of the topological character of bands: topological invariants (mainly the Wilson loop operator and its spectrum) and topological quantum chemistry.

### 5.1.1 Topological invariants of the fragile phase

We introduced in Sec. 2.5 several tools for diagnosing the topology of a system. We can state that the main one is the Wilson loop operator and its spectrum since other topological invariants, like the Chern number, can be obtained from the spectrum of this operator. Nevertheless, there are other topological invariants that have not been introduced yet in this work, as the $\mathbb{Z}_2$ invariant, which can also be diagnosed via the Wilson loop spectrum. Such invariant is related to systems with spin-orbit coupling that show topological boundary modes when time-reversal symmetry is present. For instance, a layer of graphene with spin-orbit coupling acts as a quantum spin Hall system that displays robust and spin-polarized boundary states, protected by inversion and time reversal symmetry [172]. This topological invariant can be detected via inversion eigenvalues or by a characteristic Wilson loop spectrum. Such Wilson loop spectrum shows two windings in opposite directions with a crossing in the middle point of the Wilson loop spectrum (usually the M point in reciprocal space). In other words, it is as if each band had an independent Chern number of $\pm 1$, but since they are degenerated, the total Chern number is zero, which is imposed by the conservation of time-reversal symmetry. In terms of propagating edge states (bulk-boundary correspondence), there are two states that counterpropagate, reflecting the difference in sign of the Chern numbers.

Back to fragile topology, the Wilson loop spectrum of the fragile bands is identical to the one from the $\mathbb{Z}_2$ topology: two opposite lines in the spectrum that cross in the middle. However, here is where the fragility of the topology comes into play: when we add a trivial band to the Wilson loop spectrum (trivial+fragile bands), the total Wilson loop spectrum does not show any winding anymore. In other words, the enlarged set of bands behaves as a trivial one with no winding in the

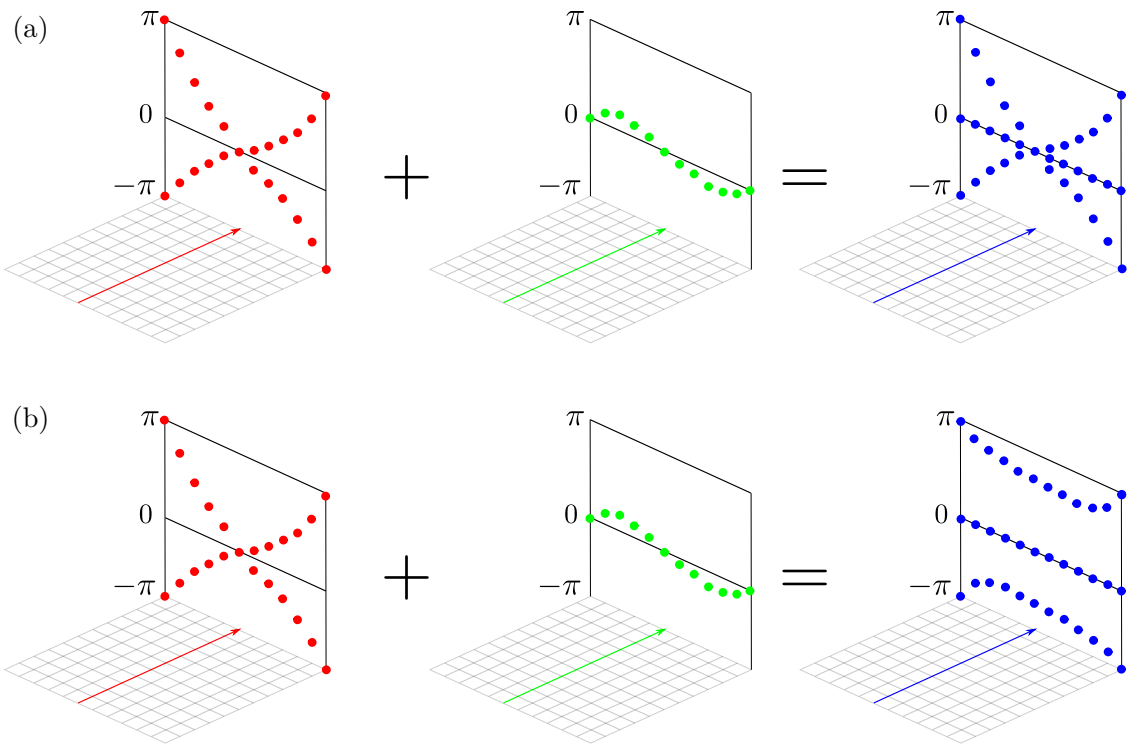


*Figure 5.1:* Two possible scenarios for the diagnosis of an electronic phase showing two windings in its Wilson loop spectrum. By adding a trivial band to these two scenarios we can distinguish between robust topology–panel (a), or fragile topology–panel(b).

Wilson loop spectrum. Hence, the topology is thus broken, and so it is called fragile, contrary to the robust topology, where the addition of trivial bands does not alter the topological behavior of the first set of bands. If one studies the Wilson loop spectrum of the fragile phase with the trivial band added, it resembles the Wilson loop spectrum of an obstructed atomic limit, displaying flat lines outside the origin due to the displacement of the charge.

In figure 5.1, we sketch what would happen if we add a trivial band (green Wilson loop spectra showing no winding) to a Wilson loop spectrum that is being diagnosed (red panels). The first case–panel 5.1(a)– shows the effect of adding a trivial band to a set of bands with $\mathbb{Z}_2$ topology: the trivial band does not alter the crossing of the topological bands, and thus the topology is robust. On the contrary, the total Wilson loop of the panel 5.1(b) is trivialized after adding the trivial band, thus revealing the fragility of the topology.

The fact that a non-trivial winding of a Wilson loop spectrum can reveal the topology of an isolated set of two bands was introduced in Ref. [173]. These Wilson loop spectra are computed along straight lines in the first Brillouin zone. However, in some cases (as spinful systems), these Wilson loop spectra fail to detect the topology [174, 175]. Fragile topology is intimately related to

topological crystalline insulators, where the spatial symmetries protect the topology of the bands. Actually, the crossings in the Wilson loop spectra are protected by a combination of $C_2$ symmetry and time-reversal symmetry. If these symmetries are broken, then the Wilson loop spectra along straight lines may not reveal the fragile topology as we have shown so far. Hence, a more exotic Wilson loop needs to be introduced in relation to the symmetries of the crystal. We refer the reader to references [174, 175] for the use of these Wilson loops.

Finally, another consequence of the fragile topology is that the set of fragile bands does not admit a representation in terms of maximally localized Wannier functions that respect all the symmetries from the system because even if the Chern number is zero, the Wilson loop spectrum displays windings. However, after the addition of trivial degrees of freedom, this whole set of bands *can* be described in terms of exponentially localized Wannier functions. On the contrary, robust topological phases are characterized by non-trivial topological invariants that are robust, hence presenting a Wannier obstruction that is stable against adding trivial degrees of freedom.

### 5.1.2 Topological quantum chemistry of fragile topology

As we introduced in Sec. 2.6, a system is said to be topological if its band representation cannot be decomposed into a linear combination of elementary band representations with positive coefficients (multiplicities). In the fragile topology, the band representation associated is decomposable into elementary band representations, but at least one of the coefficients has to be necessarily negative. This is a formal definition in order to match the irreducible representations present at the **k** points [171, 176]. In general, the diagnosis of topology is done by relating band representations to several atomic limits using an addition operation. A possible example can be:

$$EBR = (A_1 \uparrow G)_{1a} \oplus (A_2 \uparrow G)_{2b}, \tag{5.1}$$

where we are "adding" the atomic limit formed by a crystal orbital with $A_1$ symmetry placed at Wyckoff position $1a$, with the one formed by a crystal orbital with $A_2$ symmetry placed at Wyckoff position $2b$. This is why the addition of atomic limits gives rise to a trivial band structure since the band representation $EBR$ is decomposed into a formal sum of elementary band representations with positive multiplicities. In this line, we can formally define the band representation $(A_2 \uparrow G)_{2b}$ as the subtraction of $EBR \ominus (A_1 \uparrow G)_{1a}$. Generally, this is the simplest band representation for a fragile phase. Actually, all fragile phases in two-dimensional lattices with time-reversal symmetry and without spin-orbit coupling are formed by two bands [177].

The addition of a trivial band discussed in the previous section can be studied as well in the topological quantum chemistry formalism. Given that the fragile bands do not admit a representation

in terms of maximally localized Wannier functions, once a trivial atomic limit is added to the set of fragile bands, the topology is broken and the whole band representation admits a description in terms of maximally localized Wannier functions. In general, a fragile phase is usually written as the formal difference between an obstructed atomic limit and a trivial atomic limit [177], and thus, the addition of the trivial atomic limit results in the obstructed atomic limit. That is the reason behind the Wilson loop spectrum we showed in Figure 5.1b.

## 5.2 Tight-binding model realizing a fragile phase

We present the tight-binding model we have studied in order to realize a fragile phase. The model has been adapted from Ref. [178]. It is a tight-binding model based on the kagome pattern, already shown in Chapter 3, but with an extra $s$ orbital in $1a$ Wyckoff position, as shown in Fig. 5.2(a). The lattice vectors this time have been chosen as $\mathbf{a}_1 = a_0(1, 0)$ and $\mathbf{a}_2 = a_0/2(1, \sqrt{3})$, where $a_0$ is the interatomic distance which is taken to be unity. The unit cell is formed by lattice sites A, B, C, and D, located at positions $(0, 0)$, $\mathbf{a}_1/2$, $\mathbf{a}_2/2$, $(\mathbf{a}_1 + \mathbf{a}_2)/2$, respectively. The lattice sites have the same coordination number, and within the nearest-neighbor approximation, the connectivity of the lattice sites has been chosen to be different: lattice site A has 6 connected neighboring lattice sites, while B, C, are connected to only two lattice sites being both of A nature. Indeed, sites B, C, and D are also nearest-neighbors in terms of distance between them, but we will consider such kind of hopping to be of next-to-nearest neighbor nature.

Throughout this chapter we will refer to this model as the triangular Lieb lattice [44], since the distribution of lattice sites reminds of that of such lattice but in a triangular fashion.

The nearest-neighbor Hamiltonian $\hat{\mathcal{H}}_0$ can be written as:

$$\hat{\mathcal{H}}_0 = -t_0 \sum_{mn} a^\dagger_{m,n} \left( b_{m,n} + b_{m-1,n} + c_{m,n} + c_{m,n-1} + d_{m,n} + d_{m-1,n-1} \right) + \text{h.c.} \tag{5.2}$$

In reciprocal space using the basis $\Psi = (a_\mathbf{k}, b_\mathbf{k}, c_\mathbf{k}, d_\mathbf{k})^\mathrm{T}$, the Bloch Hamiltonian matrix $h_0(\mathbf{k})$ takes the form:

$$h_0(k) = -2t_0 \begin{pmatrix} 0 & \cos\frac{k_x}{2} & \cos\frac{1}{4}\left(k_x - \sqrt{3}k_y\right) & \cos\frac{1}{4}\left(k_x + \sqrt{3}k_y\right) \\ \cos\frac{k_x}{2} & 0 & 0 & 0 \\ \cos\frac{1}{4}\left(k_x - \sqrt{3}k_y\right) & 0 & 0 & 0 \\ \cos\frac{1}{4}\left(k_x + \sqrt{3}k_y\right) & 0 & 0 & 0 \end{pmatrix}. \tag{5.3}$$

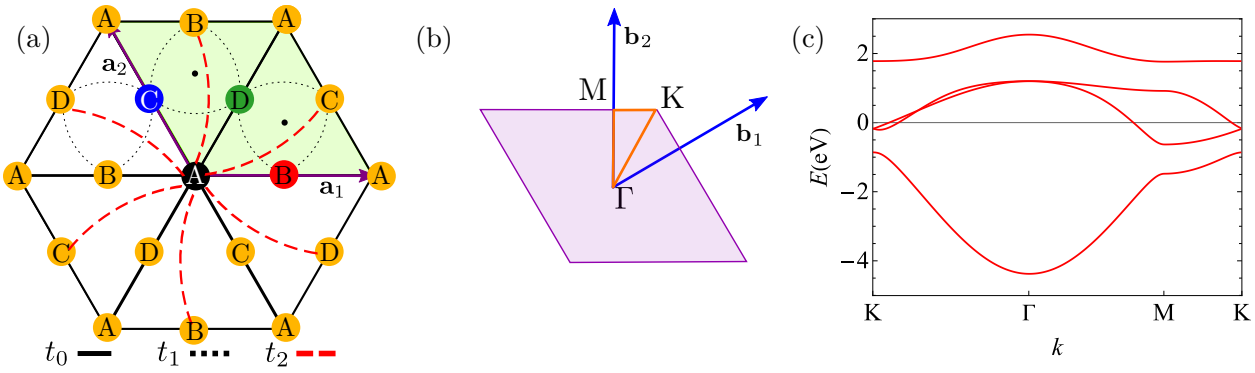


*Figure 5.2:* (a) Unit cell, lattice sites, direct lattice vectors and hoppings of the triangular Lieb lattice displaying a fragile phase. The lattice site A is located at the 1a Wyckoff position and is colored in black, while the sites B, C, and D are located at the 3c Wyckoff positions, each colored respectively in red, blue, and green. The black dots represent the 2b Wyckoff positions, which are unoccupied. The solid black line represents the nearest-neighbor hopping, the dotted black one, the next-nearest-neighbor hoppings, and the dashed red line the next order in nearest-neighbor hoppings. It has been only displayed in the A lattice site for the sake of clarity, but it has been applied in all lattice sites. (b) First Brillouin zone, reciprocal lattice vectors, high-symmetry points, and high-symmetry path of the triangular Lieb lattice. (c) Spectrum of the triangular Lieb lattice with $t_0 = 1$, $t_1 = 0.5$, and $t_2 = 0.1$, in units of $t_0$.

The spectrum of this Hamiltonian is characterized by four bands: two flat bands at zero energy, plus two energy symmetric bands at finite energy. We can add a small perturbation $t_1$ according to $\hat{\mathcal{H}}_1$, which conforms the next-to-nearest neighbor hopping we introduced at the beginning of this section:

$$\hat{\mathcal{H}}_1 = -t_1 \sum_{mn} b^\dagger_{m,n}(c_{m+1,n} + c_{m,n-1} + d_{m,n} + d_{m,n-1}) + c^\dagger_{m,n}(d_{m,n} + d_{m-1,n}) + \text{h.c.} \tag{5.4}$$

If we Fourier transform $\hat{\mathcal{H}}_1$ using the same basis as before, we obtain:

$$h_1(k) = -2t_1 \begin{pmatrix} 0 & 0 & 0 & 0 \\ 0 & 0 & \cos\frac{1}{4}\left(k_x + \sqrt{3}k_y\right) & \cos\frac{1}{4}\left(k_x - \sqrt{3}k_y\right) \\ 0 & \cos\frac{1}{4}\left(k_x + \sqrt{3}k_y\right) & 0 & \cos\frac{k_x}{2} \\ 0 & \cos\frac{1}{4}\left(k_x - \sqrt{3}k_y\right) & \cos\frac{k_x}{2} & 0 \end{pmatrix}. \tag{5.5}$$

Finally, we add the next order in nearest-neighbor hopping as it is shown in Figure 5.2. We compute the Hamiltonian with this hopping term applied in all lattice sites; however in the picture we have shown only the hoppings regarding the lattice sites of species A, for the sake of clarity. The Hamiltonian $\mathcal{H}_2$ reads:

$$\hat{\mathcal{H}}_2 = -t_2 \sum_{mn} a^\dagger_{m,n}(b_{m,n+1} + c_{m+1,n} + d_{m-1,n}) + b^\dagger_{m,n}(c_{m,n} + d_{m+1,n}) + c^\dagger_{m,n} d_{m,n+1} + \text{h.c.} \tag{5.6}$$

If we Fourier transform $\hat{\mathcal{H}}_2$ using the same basis as before, we obtain:

$$h_2(k) = -2t_2 \begin{pmatrix} 0 & a & b & c \\ a & 0 & c & b \\ b & c & 0 & a \\ c & b & a & 0 \end{pmatrix}, \tag{5.7}$$

where $a = \cos\frac{\sqrt{3}k_y}{2}$, $b = \cos\frac{1}{4}\left(3k_x + \sqrt{3}k_y\right)$, and $c = \cos\frac{1}{4}\left(3k_x - \sqrt{3}k_y\right)$ are real valued functions of the crystal momentum. We write the total Hamiltonian as $\hat{\mathcal{H}} = \hat{\mathcal{H}}_0 + \hat{\mathcal{H}}_1 + \hat{\mathcal{H}}_2$. The spectrum of this Hamiltonian is presented in Fig. 5.2(c), where we have taken $t_0 = 1$, $t_1 = 0.5$ and $t_2 = 0.1$, in units of $t_0$. The effect of the $\mathcal{H}_1$ Hamiltonian is to curve the two flat bands, and as long as $t_1 < t_0$, the gaps will not close, so the two middle bands will remain detached from the other two. For $t_0 = t_1$, we recover the spectrum of a triangular lattice with an enlarged unit cell containing four equivalent atoms. Hence, the spectrum shows degeneracies coming from the band folding caused by the enlargement of the unit cell. Finally, the effect of the $\mathcal{H}_2$ Hamiltonian is to lower the energy of the intermediate bands at the M point, as well as increase the curvature of the lowest band.

## 5.3 Symmetries of the triangular Lieb lattice

We study now the symmetries of the triangular Lieb lattice. The triangular Lieb lattice belongs to the *p*6*mm* space group, which has three sets of maximal Wyckoff positions. According to the distribution of the lattice sites, we can state that the lattice site A is located at the 1*a* maximal Wyckoff position. The rest of lattice sites are located at the 3*c* maximal Wyckoff positions, thus leaving the 2*b* maximal Wyckoff positions empty. In Fig. 5.2(a) we have presented the 2b maximal Wyckoff positions as black dots, but there are no orbitals placed there.

In order to study the symmetries of the lattice, we write the representation of the generators of the space group, which in this case are the operations $C_3$, $C_2$, and $m_{11}$, where the notation for the mirror stands for the direction that is inverted, thus the direction $\mathbf{a}_1 + \mathbf{a}_2$. The representation for the symmetry operators is done in the orbital space, the same as in the Hamiltonians we have shown so far. Taking the basis (A,B,C,D), we can write:

$$\rho(C_3) = \begin{pmatrix} 1 & 0 & 0 & 0 \\ 0 & 0 & 0 & 1 \\ 0 & 1 & 0 & 0 \\ 0 & 0 & 1 & 0 \end{pmatrix}, \qquad \rho(C_2) = \begin{pmatrix} 1 & 0 & 0 & 0 \\ 0 & 1 & 0 & 0 \\ 0 & 0 & 1 & 0 \\ 0 & 0 & 0 & 1 \end{pmatrix}, \qquad \rho(m_{11}) = \begin{pmatrix} 1 & 0 & 0 & 0 \\ 0 & 0 & 1 & 0 \\ 0 & 1 & 0 & 0 \\ 0 & 0 & 0 & 1 \end{pmatrix} \tag{5.8}$$

Once we have presented the representations for the generators in real space, we are able to characterize the irreducible representations in reciprocal space. We follow the usual procedure, as described in

Ref. [79]. The action in reciprocal space of the previously introduced operators can be obtained as:

$$\rho^{\mathbf{k}}(C_3) = \begin{pmatrix} 1 & 0 & 0 & 0 \\ 0 & 0 & 0 & e^{-\frac{i}{2}(k_x+\sqrt{3}k_y)} \\ 0 & 1 & 0 & 0 \\ 0 & 0 & e^{\frac{i}{2}(k_x-\sqrt{3}k_y)} & 0 \end{pmatrix}, \tag{5.9a}$$

$$\rho^{\mathbf{k}}(C_2) = \begin{pmatrix} 1 & 0 & 0 & 0 \\ 0 & e^{ik_x} & 0 & 0 \\ 0 & 0 & e^{-\frac{i}{2}(-k_x+\sqrt{3}k_y)} & 0 \\ 0 & 0 & 0 & e^{-\frac{i}{2}(k_x+\sqrt{3}k_y)} \end{pmatrix}, \tag{5.9b}$$

$$\rho^{\mathbf{k}}(m_{11}) = \begin{pmatrix} 1 & 0 & 0 & 0 \\ 0 & 0 & e^{\frac{i}{2}(k_x-\sqrt{3}k_y)} & 0 \\ 0 & e^{ik_x} & 0 & 0 \\ 0 & 0 & 0 & e^{-\frac{i}{2}(k_x+\sqrt{3}k_y)} \end{pmatrix}. \tag{5.9c}$$

Then, by evaluating the symmetry eigenvalues of these operators at each high-symmetry point for each band, we can extract what is the associated irreducible representation. The results are tabulated in table 5.1.

| | Γ | K | M |
|---|---|---|---|
| Band 1 | $A_1$ | $A_1$ | $A_1$ |
| Bands 2&3 | $E_2$ | $E$ | $B_2 \oplus B_1$ |
| Band 4 | $A_1$ | $A_1$ | $A_1$ |

*Table 5.1:* Table summarizing the irreducible representations obtained in the tight-binding model of the triangular Lieb lattice.

In order to determine the band representation from each irreducible representation assignment, we consult the Bilbao Crystallographic server and compare our irreducible representation assignment with the tabulated band representations. The first and fourth bands correspond to the $(A_1 \uparrow G)_{1a}$ elementary band representation. This result is very much expected since the $s$ orbital, due to its spherical character, transforms trivially under all symmetry operations of the point group, and so does the $A_1$ irreducible representation. This band representation is one-dimensional, related to the fact that the first and fourth bands are single and isolated.

However, we cannot assign a band representation to the irreducible representation assignment we find for the second and third bands, which suggests that they may be topological.

## 5.4 Fragile topology diagnosis in the triangular Lieb lattice

We study now how the fragile topology is encoded in the triangular Lieb lattice. We begin by studying the irreducible representation assignment and the possible band representations present in the Bilbao Crystallographic server. We find that the band representation $(A_1 \uparrow G)_{3c}$ contains the irreducible representations we have found plus the irreducible representation assignment of the band representation $(A_1 \uparrow G)_{1a}$. Hence, we can formally subtract the two band representations to retain only the irreducible representations that we are interested in. As a consequence, we claim that the band representation of the middle bands is $(A1 \uparrow G)_{3c} \ominus (A1 \uparrow G)_{1a}$. In table 5.2, we show the irreducible representations associated with each of the elementary band representations presented so far. The formal subtraction we have found for the band representation is done by removing the irreducible representations at each **k** point.

| | Γ | K | M |
|---|---|---|---|
| $(A_1 \uparrow G)_{1a}$ | $A_1$ | $A_1$ | $A_1$ |
| $(A_1 \uparrow G)_{3c}$ | $A_1 \oplus E_2$ | $A_1 \oplus E$ | $A_1 \oplus B_2 \oplus B_1$ |

*Table 5.2:* Table summarizing the irreducible representations associated to the elementary band representations found in the Bilbao Crystallographic Server.

With this, we have successfully concluded the symmetry diagnosis of fragile topology.

Now, we apply the Wilson loop operator to the band structure. Figure 5.3 shows respectively the Wilson loop spectra of bands 1 or 4, 2 and 3, and 1, 2, and 3 altogether in panels (a), (b), and (c)[1]. The first and fourth bands are topologically trivial, and we see how the associated Wannier center (or the **k**-averaged Wilson loop spectrum) is 0, coinciding with the origin of the unit cell, exactly where the $1a$ Wyckoff position is placed. The panel 5.3(b) represents the two windings we expected from the fragile topology that the intermediate set of bands displays. We cannot compute a Wannier associated with this Wilson loop due to the winding; hence, no maximally localized Wannier function can be computed. Finally, panel 5.3(c) represents the breaking of the fragile topology after adding to the calculation of the Wilson loop spectrum the trivial band shown in panel 5.3(a). The result does not change if we add either the first band or the fourth one since both of them are trivial and correspond to the same elementary band representation.

[1]This is a realistic example of figure 5.1(b)

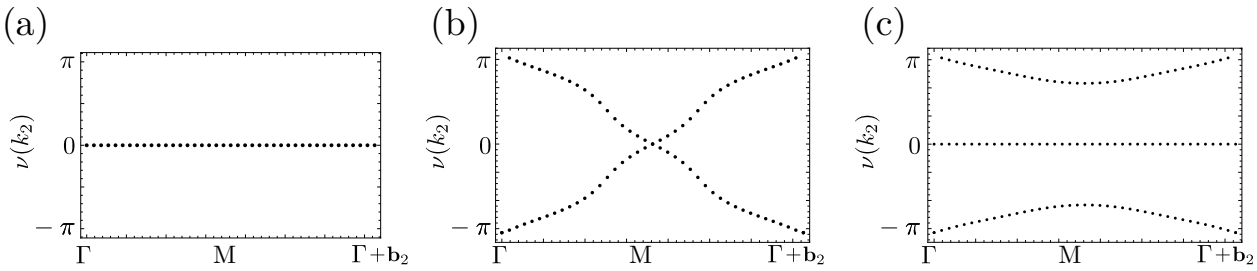


*Figure 5.3:* Wilson loop spectrum of (a) the first or fourth band, (b) the second and third bands, which are degenerated and thus have to be computed together, and (c) the second and third bands plus the first or the fourth bands. We see how the topological character is lost after the addition of a trivial band, thus revealing the fragility of the topological character of bands 2 & 3.

## 5.5 The breakdown of bulk-boundary correspondence: filling anomaly of the fragile phase

Fragile topology is deeply connected to the crystalline symmetries of the lattice. Topological insulators whose ground state is protected by crystalline symmetries and cannot be connected to any atomic limit are called topological crystalline insulators. However, as we claimed before, the addition of trivial degrees of freedom makes the fragile phase adiabatically deformable to an atomic limit, so the ground state is not topological anymore, even in the presence of crystalline symmetries.

As we commented at the beginning of this chapter, whenever a system with fragile topology is cut into a finite-size sample, the bulk boundary correspondence breaks down, and no boundary modes can be related to the fragile bulk topology. This is because the boundary energy spectrum is unchanged after the addition of trivial bands that lie beneath the energy gap. However, crystalline symmetries play an interesting role here since fragile topological phases in two dimensions, with rotational symmetries or inversion symmetry, may display fractional charges in the corners of a finite-size sample whenever the shape of the flake respects the symmetries of the lattice, both rotational and/or inversion symmetries [179, 180, 181]. The origin of corner charges in fragile topological insulators has been attributed to the filling anomaly, an obstruction to fulfill the electron filling for charge neutrality when the crystalline symmetries are preserved [73]. This implies that if the point group is characterized by rotations of $2\pi/n$, the system displays $n$ degenerate in-gap states that, at charge neutrality, are only partially occupied.

We present in the following lines the results of the triangular Lieb lattice inspired by Ref. [182]. In that work, the authors study the bulk, ribbon, and flake geometries of a single layer of graphene with a set of adatoms forming a supercell. There, by comparing the spectra of the flake, ribbon, and bulk geometries, they are able to find $C_6$-symmetric in-gap states that result from the fragile

topology of the lattice and present filling anomaly due to the crystalline symmetries of the sample. In our case, the lattice also presents $C_6$ symmetry, so we expect to find similar physics in our system.

Using the tight-binding model we presented in Section 5.2, we write it into a $\mathbf{a}_1$-ribbon geometry and into an exact hexagonal flake. For the case of the hexagonal flake, we fix the lower edge of the hexagon to 10 unit cells. It is formed by orbitals of A-B type, so to ensure the symmetry of the flake, we remove the extra orbitals so that the six corners of the hexagon are formed by A orbitals. Since the orbitals B, C, and D are placed at equivalent Wyckoff positions, we can ignore the fact that the edges are formed by combinations of either A-B, A-C, or A-D orbitals. The total number of atomic orbitals is 1027, after removing the extra ones.

We present the results in Figure 5.4. In the first place, we present in panel 5.4(a) the results for the bulk, ribbon and flake geometries with only nearest-neighbour interaction, that is, $t_0 = 1, t_1 = 0$, and $t_2 = 0$. The left subfigure shows the bulk spectrum with the gaps shaded in yellow. The middle subfigure presents the spectrum of the ribbon geometry with both the position of the bulk gap (again in yellow) and the position of the ribbon gap in green. On the right margin of each of the subfigures, we present the spectrum of the flake geometry under the same conditions. We observe that there is a set of in-gap states in each of the gaps that do not correspond to either the bulk bands or the ribbon bands. According to Ref. [182], we study the spatial distribution of those states to check if they are boundary states localized in the corners. Surprisingly, this is not the case, as the states are delocalized in the whole flake. We present in the left subfigure the states associated with eigenvalues #271 and #757 since they correspond to the highest and lowest eigenvalues that belong to the in-gap states.

Panels 5.4(b) and 5.4(c) correspond to the same results as panel 5.4(a) but where we have included first the $t_1$ and then the $t_2$ hoppings, respectively. In neither of the cases we find in-gap states related to the fragile topology of the bulk.

A more precise search reveals that there are indeed $C_6$-symmetric states in the flake geometry for the different hopping parameterswe have considered. Figure 5.5 is inspired by Ref. [182], where we study the spatial distribution of the lowest eigenstate that presents $C_6$-symmetric properties. We notice how the index of the lowest eigenstate changes when we add hoppings. As in figure 5.4, each panel corresponds to the addition of a longer-range hopping. On the left subfigure of each panel we present the spatial distribution of the eigenstate, and on the right subfigure, we plot the square of the absolute value (Local Density of States) of the eigenstate along the red and blue lines crossing the flake. The blue line runs through one edge of the flake, while the red one runs from the center of the flake towards the corner. Due to the $C_6$ symmetry, the plots do not change regardless of the

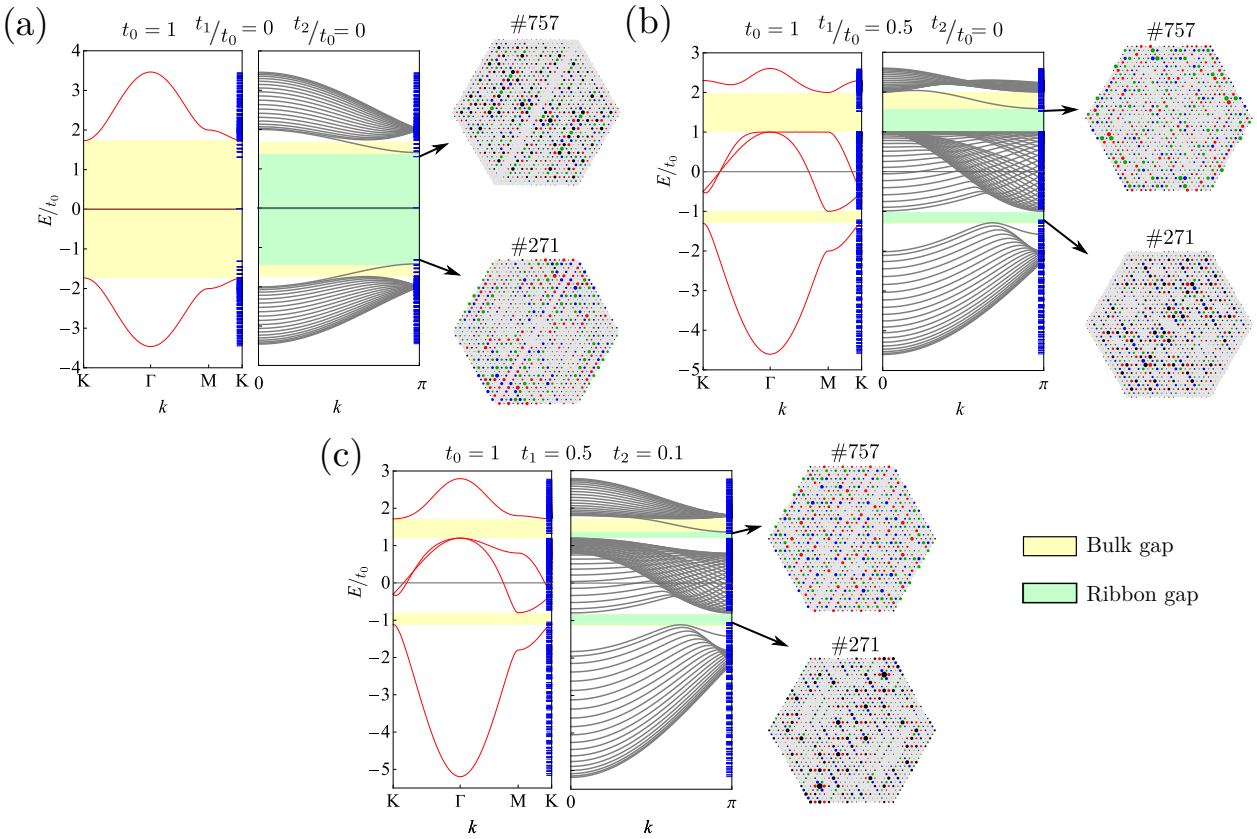


*Figure 5.4:* Bulk, ribbon and flake results on the detection of $C_6$-symmetric in-gap states, product of the broken bulk-boundary correspondence of the fragile topology. Each panel presents the bulk and ribbon results compared to the flake spectrum. The width of the bulk and ribbon gap have been highlighted in yellow and light green respectively, to keep track of the in-gap states that are not associated to either bulk nor ribbon states. Additionally, the spatial distribution of the in-gap states is shown, revealing that they are not connected to the fragile topology of the bulk, that remains unperturbed in the three cases.

orientation of the red and blue lines.

## 5.6 Electronic quantum simulation of the fragile phase

In this section, we present the results obtained for the quantum simulation of the triangular Lieb lattice based on the CO/Cu(111) platform. As we presented in section 2.3, the electronic quantum simulator based on muffin-tin potentials is a good platform to reproduce almost any two-dimensional electronic lattice and study experimentally those features that can be predicted using a tight-binding model.

We show the different muffin-tin potentials we have designed to study the triangular Lieb lattice. The procedure for building those potentials is the same as we introduced in the guide present in

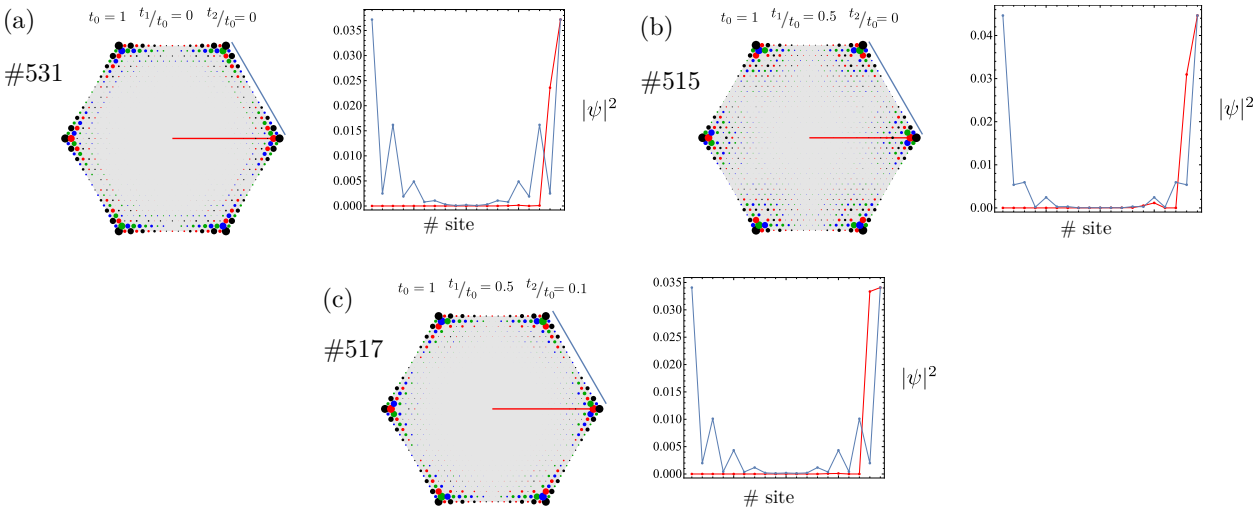


*Figure 5.5:* Spatial distribution across the flake and along certain paths of the lowest state that preserves the $C_6$ symmetry of the lattice. The order of the eigenvalue is shown since it is different for each case. Only in the first plot, the eigenvalue of the associated eigenstate is zero, while for the rest, the associated eigenvalues depart from zero. Additionally, the states have been plotted along two lines that cross the flake. For the sake of clarity, the plot of the local density of states has been colored according to the color of the path.

section 3.5.1. We begin by blocking the empty Wyckoff positions and leaving the occupied ones free. This general procedure ensures that artificial atoms will be created around the occupied lattice sites. For the particular case of the triangular Lieb lattice, we need to block the 2*b* Wyckoff position and reduce, at the same time, the connectivity of the 3*c* Wyckoff positions, right where lattice sites $B, C, D$ lie. As we mentioned in Section 2.3, the main restriction for building the potentials is that the number of molecules must be as small as possible to ensure the stability of the experiment. We will also discriminate between different choices of unit cells depending on the resolution of the band gaps. In the tight-binding model, we have a certain freedom in the width of the band gap since we can manipulate the hopping parameters arbitrarily. However, in the muffin-tin experiment, the hopping amplitudes are controlled by the width and shape of the potential wells, which depend on how they are built. Hence, all possible arrays of molecules may correspond to different sets of hopping parameters corresponding all to the same tight-binding model. At the same time, since the number of molecules also changes the size of the unit cell, the real space parameters of each choice are different, and so are the reciprocal spaces of each configuration. Hence, to reproduce the muffin-tin results, we must properly define the lattice vectors and sites, together with the hopping parameters.

Figure 5.6 shows the different arrangements of molecules we have studied in order to realize the triangular Lieb lattice in the CO/Cu(111) quantum simulator. In order to block the 2*b* Wyckoff

position, we place sets of molecules in this position. They are positioned in a triangular shape since the 2*b* Wyckoff position is surrounded by 3 Wyckoff positions (the 3*c* ones). In this way, by placing a triangular set of molecules at the 2*b* Wyckoff position, we block such Wyckoff position and reduce the connectivity of the 3*c* Wyckoff positions. In panel 5.6(a), we present the first set of molecules in the left subfigure. This is the set with the minimal amount of molecules that display a spectrum–middle subfigure– that is similar to the one obtained with the tight-binding model. The right subfigure shows the corresponding Wilson loop spectra of bands 1, 2 & 3, and 1&2& 3 from bottom to top. We can appreciate how bands 2&3 are not fragile since there is no winding. This is quite interesting since this choice may suggest that the fragile phase may vanish for a certain set of parameters.

We continue with panels 5.6(b) and 5.6(c), where we show other possible configurations with more molecules. For the two situations, we observe that the energy gap between bands 2&3 and 4 is very small at Γ. This is not favorable for our purposes since bands 2&3 have to be well separated from the rest. Nevertheless, the windings of the Wilson loop spectra seem to yield a fragile phase.

Finally, in panel 5.6(d), we show the last configuration where we recover an energy spectrum that resembles quite closely the tight-binding result. The main difference is on the path KΓ, where the crossing between bands 2&3 seems to have displaced from the tight-binding spectrum. The distribution of the gaps is quite clear, so the sets of bands are well isolated from the rest. The Wilson loop spectra of this configuration are strikingly close to the ones obtained with the tight-binding model, revealing a clear winding with the crossing at the M point. Finally, the addition of the first band transforms the fragile Wilson loop spectrum into the usual Wilson loop spectrum of an obstructed atomic limit, right as we claimed at the beginning of this Chapter.

## 5.7 Conclusions and outlook

In this Chapter, we have presented the research we have done around the fragile phase of a two-dimensional electronic lattice called the triangular Lieb lattice. First, we obtain the energy spectrum from a tight-binding perspective using different orders of nearest-neighbor hoppings. From the four bands that form the spectrum, the second and third ones are isolated from the rest, so we are able to characterize them using topological invariants and topological quantum chemistry. From both perspectives, this set of two bands realizes a fragile topological phase characterized, first, by a winding of the Wilson loop spectrum that breaks down after the addition of a trivial band below the gap and second, by the formal subtraction of elementary band representations of the space group.

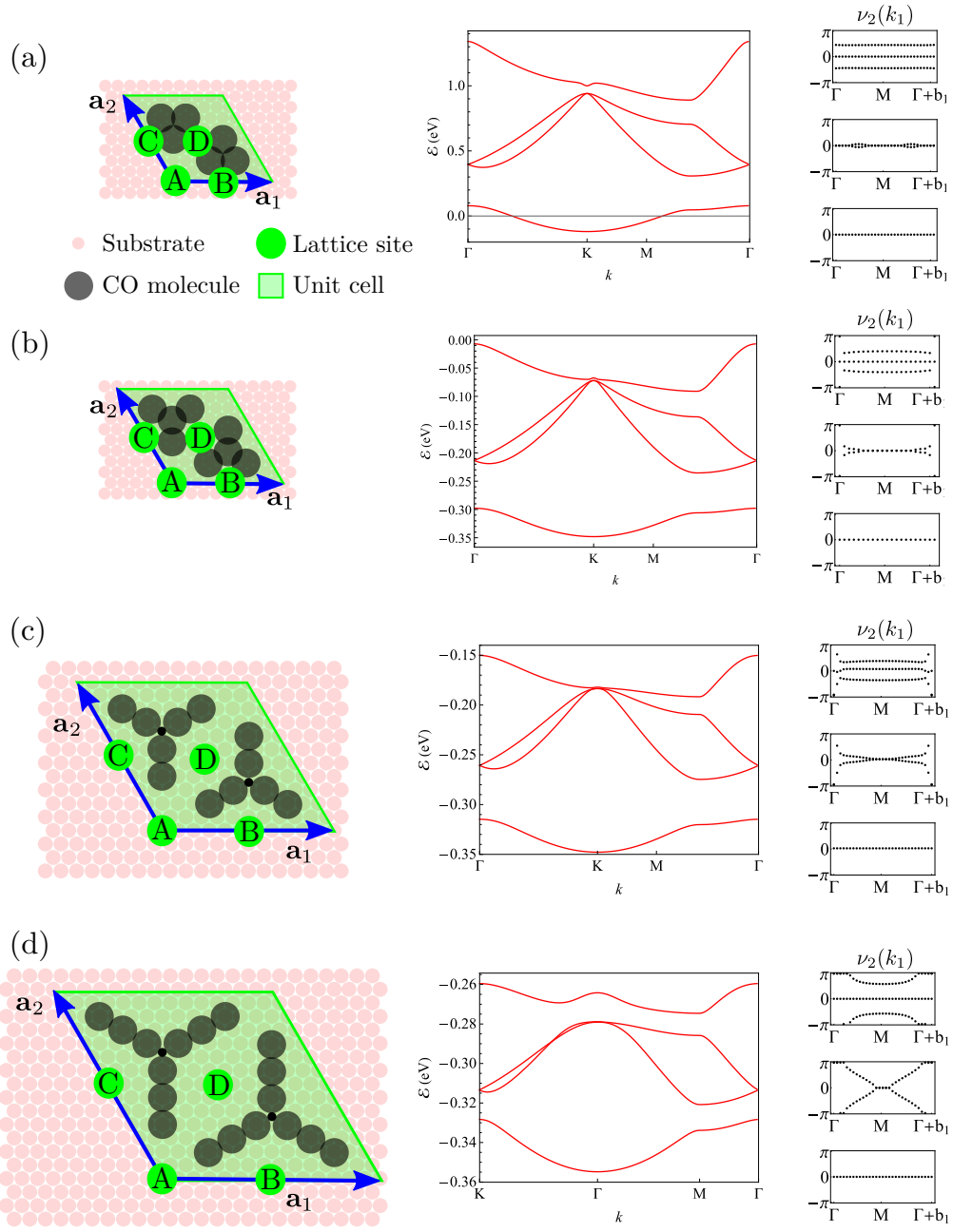


*Figure 5.6:* Posible configurations of CO molecules that realize the triangular Lieb lattice in the CO/Cu(111) quantum simulator. Each panel shows the array of molecules on the left panel, the spectrum in the middle and the Wilson loop operator spectrum of bands 1, 2 & 3, and 1&2& 3 from bottom to top.

The triangular Lieb lattice belongs to a space group with six-fold rotations. These crystalline symmetries are responsible for the appearance of electronic states that respect the symmetry of the lattice when it is cut into finite-size samples, like ribbons and flakes. Inspired by Ref. [182], we build both ribbon and hexagonal flake geometries and study conjointly their spectra. We find

extra in-gap states that do not belong to the bulk or the ribbon spectra but are unrelated to the six-fold symmetry operator. One possible solution may be to study a flake that preserves the six-fold rotation but breaks any other symmetry in the lattice, like mirror symmetries. At the same time, the addition of longer-range hoppings may help open an energy gap since, by inspection, we have found electronic states that respect the six-fold symmetry operator that do not lie in the energy gap [183].

Finally, we study the triangular Lieb lattice in the CO/Cu(111) quantum simulator and present several arrangements of molecules that may give rise to a fragile phase. We characterize them using the Wilson loop operator since it is the most direct way to diagnose fragile topology. We do find fragile configurations with a reasonably low number of molecules that resemble quite closely the tight-binding spectrum.

We believe that by the addition of longer-range hoppings or by changing the shape of the finite-size flake, the proposed tight-binding model may keep the fragility of the topological phase while allowing a more easy detection of the six-fold in-gap states. At the same time, different orbital species can be included both in the tight-binding model and engineered into the muffin-tin potentials, in order to increase the complexity of the model and have access to more parameters.

# Appendices

# APPENDIX A

# Coefficients for the Fourier transform of muffin-tin potentials

In Sec. 2.3 two different potentials were introduced to model the repulsive/attractive nature of the features placed on top of the surfaces in the quantum simulator platforms. Here we present the detailed analytic derivation of the coefficients of the Fourier transform of the potentials.

## A.1 Repulsive potential of CO molecules

We begin by taking Eq. 2.15b and applying it to Eq. 2.38:

$$V_{\mathbf{G}}^{\mathrm{CO}} = \frac{V_0}{A_{\mathrm{UC}}} \int_{\mathbf{r}<a} \mathrm{e}^{-\mathrm{i}\mathbf{G}\cdot\mathbf{r}} d\mathbf{r} \tag{A.1}$$

$$= \frac{V_0}{A_{\mathrm{UC}}} \int_0^a \int_0^{2\pi} \mathrm{e}^{-\mathrm{i}|\mathbf{G}|r\cos\theta} \mathrm{d}\theta r \mathrm{d}r \tag{A.2}$$

The integral over the $\theta$ angle is the definition of Bessel function of the first kind and order zero (Bessel's first integral):

$$V_{\mathbf{G}}^{\mathrm{CO}} = \frac{2\pi V_0}{A_{\mathrm{UC}}} \int_0^a J_0(|\mathbf{G}|r) r \mathrm{d}r \tag{A.3}$$

$$= \frac{2\pi V_0 a}{A_{\mathrm{UC}}|\mathbf{G}|} J_1(|\mathbf{G}|a) \tag{A.4}$$

## A.2 Attractive potential of In adatoms (Gaussian)

We begin by rearranging Eq. 2.41a into an exponential expression and applying Eq. 2.15b to it. Renaming $d$ =FWHM:

$$V_{\mathbf{G}}^{\mathrm{In,G}} = \frac{V_0}{A_{\mathrm{UC}}} \int \exp\left(-4\ln 2 \left(\frac{r}{d}\right)^2\right) \exp\left(-\mathrm{i}\mathbf{G}\cdot\mathbf{r}\right) d\mathbf{r} \tag{A.5}$$

$$= \frac{V_0}{A_{\mathrm{UC}}} \int_0^{\infty} r \exp\left(-4\ln 2 \left(\frac{r}{d}\right)^2\right) \int_0^{2\pi} \exp\left(-\mathrm{i}|\mathbf{G}| r\cos\theta\right) d\theta dr \tag{A.6}$$

$$= \frac{2\pi V_0}{A_{\mathrm{UC}}} \int_0^{\infty} r \exp\left(-4\ln 2 \left(\frac{r}{d}\right)^2\right) J_0(|\mathbf{G}|r)\mathrm{d}r \tag{A.7}$$

In this last expression, we change the variables to:

$$K = \frac{2\sqrt{\ln 2}}{d}, \quad t = 2\sqrt{\ln 2}\,\frac{r}{d} = Kr, \quad r = \frac{t}{K}, \quad \mathrm{d}r = \frac{\mathrm{d}t}{K}, \quad r\mathrm{d}dr = \frac{1}{K^2} t\mathrm{d}t \tag{A.8}$$

Hence,

$$V_{\mathbf{G}}^{\mathrm{In,G}} = \frac{2\pi V_0}{A_{\mathrm{UC}} K^2} \int_0^{\infty} t \exp\left(-t^2\right) J_0\left(\frac{|\mathbf{G}|}{K} t\right) \mathrm{d}t \tag{A.9}$$

Integrating by parts we have:

$$\begin{cases} u = J_0\left(\frac{|\mathbf{G}|}{K} t\right) & \Rightarrow \quad \mathrm{d}u = -\frac{|\mathbf{G}|}{K} J_1\left(\frac{|\mathbf{G}|}{K} t\right) \mathrm{d}t \\ \mathrm{d}v = t\exp\left(-t^2\right)\mathrm{d}t & \Rightarrow \quad v = -\frac{1}{2}\exp(-t^2) \end{cases} \tag{A.10}$$

$$V_{\mathbf{G}}^{\mathrm{In,G}} = \frac{2\pi V_0}{A_{\mathrm{UC}} K^2} \left[ \left(-\frac{1}{2}\exp(-t^2)\right) J_0\left(\frac{|\mathbf{G}|}{K} t\right) \Big|_0^{\infty} - \int_0^{\infty} \frac{1}{2}\exp(-t^2) \frac{|\mathbf{G}|}{K} J_1\left(\frac{|\mathbf{G}|}{K} t\right) \mathrm{d}t \right] \tag{A.11}$$

The first term of the right-hand side is -1/2 and the second term can be rearranged using the following property:

$$\alpha J_1(\alpha t) = \int_0^{\alpha} a t J_0(at)\mathrm{d}a. \tag{A.12}$$

Hence, by defining $\alpha = |\mathbf{G}|/K$:

$$V_{\mathbf{G}}^{\mathrm{In,G}} = \frac{2\pi V_0}{A_{\mathrm{UC}} K^2} \left( \frac{1}{2} - \frac{1}{2} \int_0^{\infty} \exp(-t^2) \alpha J_1\left(\alpha t\right) \mathrm{d}t \right) \tag{A.13}$$

$$= \frac{2\pi V_0}{A_{\mathrm{UC}} K^2} \left( \frac{1}{2} - \frac{1}{2} \int_0^{\infty} \exp(-t^2) \int_0^{\alpha} a J_0(at)\mathrm{d}a\mathrm{d}t \right) \tag{A.14}$$

$$= \frac{2\pi V_0}{A_{\mathrm{UC}} K^2} \left( \frac{1}{2} - \frac{1}{2} \int_0^{\alpha} a \left[ \int_0^{\infty} t\exp(-t^2) J_0(at)\mathrm{d}t \right] \mathrm{d}a \right) \tag{A.15}$$

In A.9 we can define $f(\alpha)$ as:

$$f(\alpha) = \int_0^{\infty} t\exp\left(-t^2\right) J_0\left(\alpha t\right) \mathrm{d}t \quad \Rightarrow \quad V_{\mathbf{G}}^{\mathrm{In,G}} = \frac{2\pi V_0}{A_{\mathrm{UC}} K^2} f\left(\frac{|\mathbf{G}|}{K}\right) \tag{A.16}$$

We can see how the expression in square brackets in A.15 is precisely the definition of $f(a)$. Hence we can write an integral equation for $f(a)$:

$$f(\alpha) = \frac{1}{2} - \frac{1}{2} \int_0^{\alpha} a f(a)\mathrm{d}a, \quad \text{for } f(0) = \frac{1}{2} \tag{A.17}$$

Solving for $f(\alpha)$ we obtain:

$$f(\alpha) = -\frac{1}{2}\exp\left(-\frac{\alpha^2}{4}\right) \tag{A.18}$$

Substituting back the constants we obtain:

$$V_{\mathbf{G}}^{\mathrm{In,G}} = \frac{2\pi V_0}{A_{\mathrm{UC}}K^2}\left(\frac{1}{2}\exp\left(-\frac{1}{4}\left(\frac{|\mathbf{G}|}{K}\right)^2\right)\right) = \frac{\pi V_0 d^2}{4A_{\mathrm{UC}}\ln 2}\exp\left(-\frac{d^2|\mathbf{G}|^2}{16\ln 2}\right) \tag{A.19}$$

# APPENDIX B

# Interpretation of the kagome lattice as stacked SSH chains

A possible interpretation of the (breathing) kagome lattice in terms of SSH chains is given in Figure B.1. Each unit cell is decomposed as an SSH unit cell plus an extra orbital, which acts as an intermediate between the SSH chains. The breathing distortion is precisely the breathing of the SSH chain, plus a breathing interaction with such extra orbital. This distortion can be also applied in the bulk, where the Hamiltonian present in Eq. (3.2) can be decomposed into $h(\mathbf{k}) = h_{\text{SSH}}(\mathbf{k}) \oplus h_{\text{coupling}}(\mathbf{k})$. Clearly, this interpretation is done in two dimensions, even though the SSH model is done in one dimension.

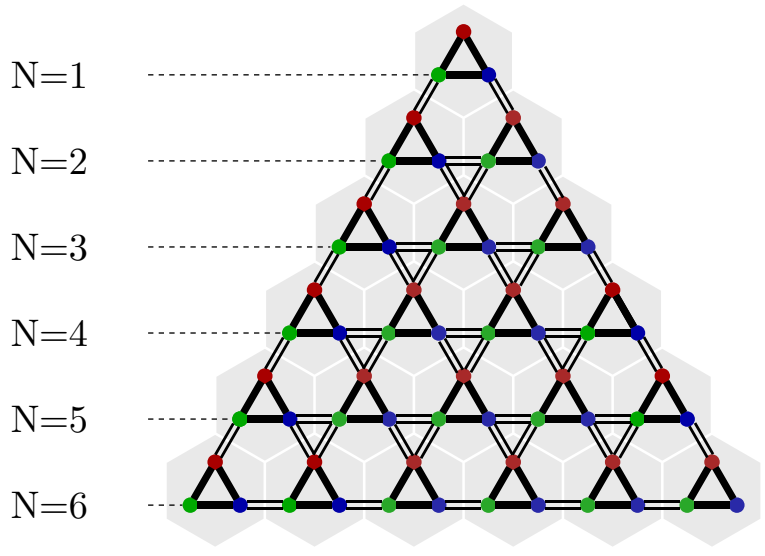


*Figure B.1:* SSH interpretation of a finite size flake of the breathing kagome lattice. The chains are formed by the green and blue atoms, while the red one acts as an intermediate between chains.

# APPENDIX C

# Destructive interference interpretation of the corner modes

A different way to interpret the zero modes in the breathing kagome lattice is by considering them as due to destructive interference [184, 185, 186]. To illustrate this approach, we will follow Ref. [184]: we start by considering the case of a one-dimensional (1D) bipartite lattice with two sites in the unit cell, A and B, such as the SSH chain. When considering a Hamiltonian in which the A-sites only couple to one B site, it is possible to find a wave function that completely localizes on the A sublattice due to destructive interference.

In this perspective, the non-trivial phase of the SSH model can be understood in terms of destructive interference. To describe the zero-energy modes of the breathing kagome lattice within this approach, we will start by analysing destructive interference in a SSH-like model. In fact, the model of destructive interference admits an analytical solution if the chain starts and ends with the same type of lattice site, *e.g.* A [186, 187].

In order to find the zero-energy wave function that interferes destructively on the B sublattice, we use the *ansatz*:

$$|\psi\rangle = N_i \sum_{m}^{M} r_i^m c^\dagger_{\mathrm{A}_i,m} |0\rangle, \tag{C.1}$$

where $r$ is a complex number describing the wave function decay, $N_i$ a normalization constant, $M$ the total number of unit cells, and $c^\dagger_{\mathrm{A}_i,m}$ creates an electron on an A-site of cell $i$.

If the A sites only couple to the B sites and vice versa, the Hamiltonian for this 1D lattice with

open boundaries reads

$$\mathbf{H}_{1\mathrm{D}} = \begin{pmatrix} e_{\mathrm{A}} & t_{\mathrm{A,B}} & 0 & 0 & 0 \\ t^{\dagger}_{\mathrm{A,B}} & e_{\mathrm{B}} & t_{\mathrm{B,A}} & 0 & 0 \\ 0 & t^{\dagger}_{\mathrm{B,A}} & e_{\mathrm{A}} & \cdots & 0 \\ 0 & 0 & \vdots & \ddots & t_{\mathrm{B,A}} \\ 0 & 0 & 0 & t^{\dagger}_{\mathrm{B,A}} & e_{\mathrm{A}} \end{pmatrix}, \tag{C.2}$$

where $e_{\mathrm{A,(B)}}$ is the on-site energy for the A (B) lattice site and, $t_{\mathrm{A,B}}$ and $t_{\mathrm{B,A}}$ are the intra- and inter-hopping terms between the lattice sites. We can rewrite Eq. (C.1) as

$$|\psi\rangle = \left(1, 0, r, 0, r^2, 0, r^3, \ldots\right)^{\mathrm{T}}, \tag{C.3}$$

localized only on the A sites, where we have omitted the normalization factor. The action of Hamiltonian (C.2) on this wave function is

$$\mathbf{H}_{1\mathrm{D}}|\psi\rangle = \tag{C.4}$$
$$\left(e_{\mathrm{A}}, t^{\dagger}_{\mathrm{A,B}} + r t_{\mathrm{B,A}}, r e_{\mathrm{A}}, r(t^{\dagger}_{\mathrm{A,B}} + r t_{\mathrm{B,A}}), \ldots, e_{\mathrm{A}} r^{M}\right)^{\mathrm{T}}.$$

From this equation, it is clear that if $t^{\dagger}_{\mathrm{A,B}} + r t_{\mathrm{B,A}} = 0$, the wave function (C.3) is an eigenstate of $\mathbf{H}_{1\mathrm{D}}$ with eigenvalues $e_{\mathrm{A}}$. It has the property that the weight on the B sites is 0 and there is a decaying wave function with energy $e_{\mathrm{A}}$ only on the A sites. We find $r = |-t^{\dagger}_{\mathrm{A,B}}/t_{\mathrm{B,A}}|$, and this mode is localized on the left of the chain if $r < 1$, and on the right if $r > 1$. In the case of the SSH model, $e_{\mathrm{A}} = e_{\mathrm{B}} = 0$, $t_{\mathrm{A,B}} = t_a$ and $t_{\mathrm{B,A}} = t_b$. We find $r = |-t_a/t_b|$, leading to the well-known localization of the zero mode on one side of the lattice [186]; this is true if the unbroken cell is on the right edge, the condition is reversed if the unbroken cell is on the opposite edge. A sketch of this wave function is given in Fig. C.1(a). This feature seems to indicate that once the lattice with open boundaries is "long enough", these exact solutions of the wave function can be used to describe the zero modes of the SSH (even though in the SSH model the sites at the beginning and end of the chain are different). Note that these zero modes are now only present when $t_a < t_b$ (the non-trivial phase) because we can then map the zero mode of the SSH model to the one at the end of the chain discussed above. This cannot be done in the trivial phase, where the eigenstate is not starting at the end of the chain [186]. In this perspective, one does not need to invoke chiral symmetry and also when the onsite energy of a site is increased to $E = \epsilon$ [20], there will still be these exponentially decaying modes at energy $\epsilon$.

We now follow the analysis in terms of destructive interference to the breathing kagome model [185]; the two-dimensional nature of the wave function leads to two indices $m$ and $m'$ in Eq. (C.1). The wave function is therefore

$$|\psi\rangle = N_i \sum_{m}^{M} \sum_{m'}^{M'} r_i^m r_i'^{m'} c^{\dagger}_{\mathrm{A}_i,m,m'}|0\rangle. \tag{C.5}$$

The Hamiltonian for the breathing kagome lattice can be expressed as parallel 1D chains coupled to each other via the intermediate site C, Fig. C.1(b). The Hamiltonian for this breathing kagome rhombus reads

$$H^{M,M'} = \begin{pmatrix} \mathbf{H}_{1D} & \mathbf{t}_{AB,C} & 0 & 0 & 0 \\ \mathbf{t}^{\dagger}_{AB,C} & \mathbf{e}_C & \mathbf{t}_{C,AB} & 0 & 0 \\ 0 & \mathbf{t}^{\dagger}_{C,AB} & \mathbf{H}_{1D} & \cdots & 0 \\ 0 & 0 & \vdots & \ddots & \mathbf{t}_{C,AB} \\ 0 & 0 & 0 & \mathbf{t}^{\dagger}_{C,AB} & \mathbf{H}_{1D} \end{pmatrix}, \tag{C.6}$$

where $\mathbf{H}_{1D}$ is the same as for Eq. (C.2) with $t_{A,B} = t_a$ and $t_{B,A} = t_b$, $\mathbf{e}_C$ is the matrix of the onsite energy of the site C, and $\mathbf{t}_{AB,C}$ and $\mathbf{t}_{C,AB}$ are the rectangular matrices containing the hopping elements connecting the 1D-chains to the C sites. These are given by

$$\mathbf{t}_{AB,C} = \begin{pmatrix} t_a & 0 & 0 & 0 \\ t_a & 0 & 0 & 0 \\ 0 & t_a & 0 & 0 \\ 0 & t_a & \cdots & 0 \\ 0 & \vdots & \ddots & 0 \\ 0 & 0 & 0 & t_a \end{pmatrix}, \tag{C.7a}$$

and

$$\mathbf{t}^{\dagger}_{C,AB} = \begin{pmatrix} t_b & 0 & 0 & 0 \\ 0 & t_b & & 0 \\ 0 & t_b & 0 & 0 \\ 0 & \vdots & \ddots & 0 \\ 0 & 0 & 0 & t_b \\ 0 & 0 & 0 & t_b \end{pmatrix}. \tag{C.7b}$$

In this way, the coupling between A and B or C is alternating $t_a$ and $t_b$. Using the same analysis as before, we observe that $t_a + r t_b = 0$ and $t_a + r' t_b = 0$ for these exact wave functions, leading to

$$|\psi\rangle = N_i \sum_{m}^{M} \sum_{m'}^{M'} \left(\frac{-t_a}{t_b}\right)^{m} \left(\frac{-t_a}{t_b}\right)^{m'} c^{\dagger}_{A_i,m,m'} |0\rangle. \tag{C.8}$$

The real amplitude of such a wave function is shown in Fig. C.1(b). The rhombus-shaped flake, adopted from Ref. [106], allows to have the same sublattice in each corner, in order to follow the same approach as in the SSH model explained previously. The three lower panels of Fig. C.1(b) show the amplitude of the wave function along three different directions inside the flake. Along $m$ and $m'$ the weight of the wave function in the sublattice different from the one in the corner is always zero. The case of $m = m'$ is a consequence of the geometry, since we only find sublattice

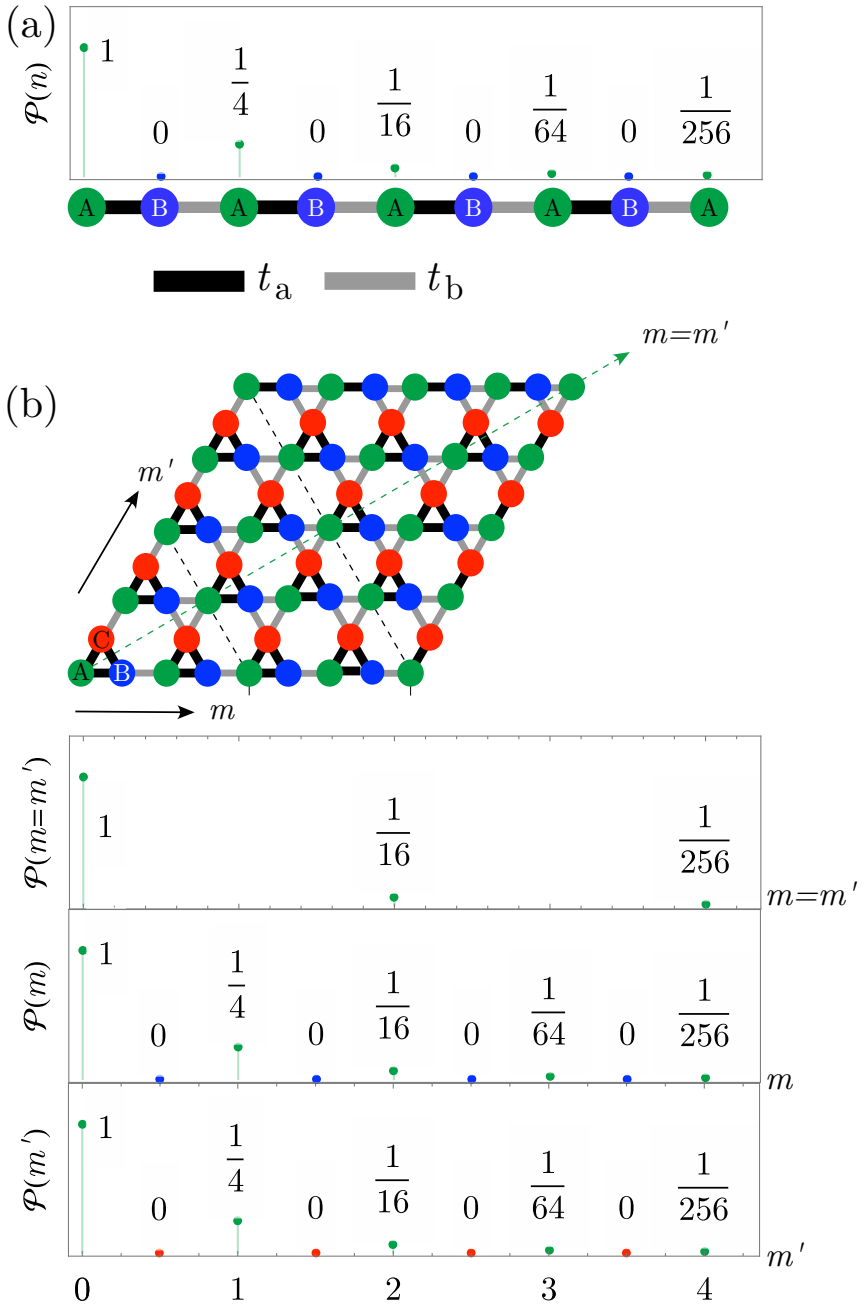


*Figure C.1:* Destructive interference models. (a) In the case of the 1D chain, the probability is finite only in the A sublattice site and decays as $(-t_a/t_b)^{2n}$, where $n$ is the unit-cell index. (b) The breathing kagome rhombus. Due to destructive interference, there is a wave function that has zero amplitude on the B and C sublattices and a finite amplitude on the A, where the probability decays as $(-t_a/t_b)^{(2m')}$ along $m$ (and analogously along $m'$), whereas it decays as $(-t_a/t_b)^{2(m+m')}$ along $m+m'$. In all the panels, we have set $t_2 = 2t_1$.

sites of the same kind as in the corner. Within this setup, we can generalize the hopping parameters connecting the sites by making them different. However, this will only add to the complexity of the model without changing the physics. The key point is that we can always find a solution for a decaying wave function with coefficients determined analytically.

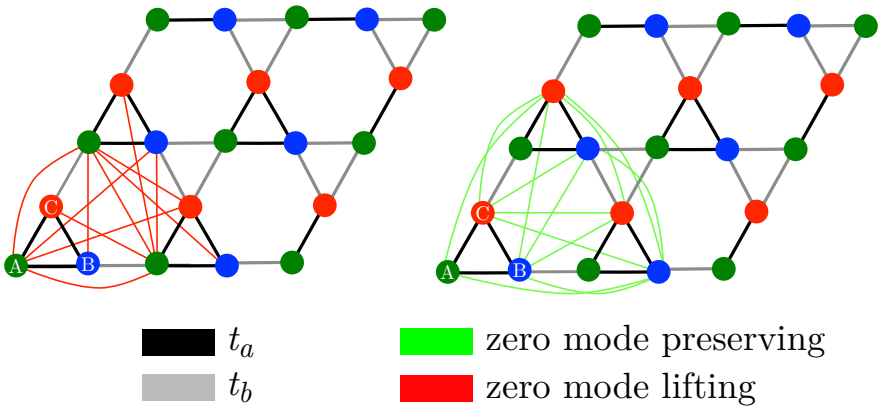


*Figure C.2:* Set of hopping terms that lift (a) or preserve (b) the corner modes pinned to zero energy. Although they are only shown on the lower-left corner of the flake, these hopping terms can be established between any $m$ and $m'$ layers.

A more interesting approach is to determine which additional hopping terms preserve the corner mode at zero energy. We consider all the hopping parameters indicated in Fig. C.2 (see appendix for the explicit expression of the Hamiltonian for a lattice containing 21 sites). For simplicity, we show in Fig. C.2 only the hopping terms between the first three unit cells in the bottom left corner of the flake, but they extend to all the lattice. It turns out from the analysis on this lattice (in which we placed an A site in each of the corners of this breathing kagome rhombus [185]) that only the hopping terms indicated in green preserve the energy of the corner modes, whereas the hopping terms in red change the energy of the corner modes (*i.e.*, there is no consistent solution when we include the red hopping terms). To summarize: all hopping terms between the sites B and C preserve the corner mode energy and additionally one can connect A and B and A and C in the direction $m$ and $m'$, respectively (in the same way as in the SSH chain). However, one cannot connect an A site with another site (A, B or C) when these sites are in different chains: $m$ and $m'$ are both different. This analysis is fully consistent with the numerical analysis for a lattice containing 630 sites presented in Figs. 3.4 and. 3.5. Note that in order to have zero modes in the triangle (with a different sublattice in each corner), we can only have the next-nearest neighbor hopping terms along $m$ (connecting A to B) or $m'$ (connecting A to C); all other perturbations will remove the zero mode since they connect the sublattice of the corner mode with a different site and hence the destructive interference is gone. We note in passing that the destructive interference method has been recently extended to the case of lattice systems characterized by a non-Hermitian Hamiltonian [188].

Now we show an explicit calculation for a similar kagome lattice as shown in Fig. C.2 in the previous appendix, consisting of 21 sites to keep the equation concise.

A solution for the equation $H\psi = e_{\mathrm{A}}\psi$ is found if $t^{m'}_{\mathrm{BA}} = t^{mm'}_{\mathrm{BA}} = t^{mm''}_{\mathrm{BA}} = t^{m'}_{\mathrm{AB}} = t^{m}_{\mathrm{CA}} = t^{m}_{\mathrm{AC}} = t^{m}_{\mathrm{AA}} = t^{m'}_{\mathrm{AA}} = t^{mm'}_{\mathrm{AA}} = t^{mm'}_{\mathrm{AB}} = t^{mm''}_{\mathrm{AB}} = t^{mm'}_{\mathrm{AC}} = t^{mm''}_{\mathrm{AC}} = t^{mm'}_{\mathrm{CA}} = t^{mm''}_{\mathrm{CA}} = 0$. These hopping values are indicated by in green in Fig. C.2. In the following, we decompose the $21 \times 21$ Hamiltonian matrix $H$ into a set of 9 $M$ matrices of dimension $7 \times 7$:

$$\begin{pmatrix} M_{11} & M_{12} & M_{13} \\ M_{21} & M_{22} & M_{32} \\ M_{13} & M_{32} & M_{33} \end{pmatrix} \psi = \chi, \tag{C.9}$$

where each matrix is defined as:

$$M_{11} = \begin{pmatrix} e_{\mathrm{A}} & -t_{\mathrm{AB}} & -t^{m}_{\mathrm{AA}} & -t^{m}_{\mathrm{AB}} & 0 & -t_{\mathrm{AC}} & -t^{m}_{\mathrm{AC}} \\ -t_{\mathrm{AB}} & e_{\mathrm{B}} & -t_{\mathrm{BA}} & -t^{m}_{\mathrm{BB}} & -t^{m}_{\mathrm{BA}} & -t_{\mathrm{BC}} & -t^{m}_{\mathrm{BC}} \\ -t^{m}_{\mathrm{AA}} & -t_{\mathrm{BA}} & e_{\mathrm{A}} & -t_{\mathrm{AB}} & -t^{m}_{\mathrm{AA}} & -t^{m}_{\mathrm{CA}} & -t_{\mathrm{AC}} \\ -t^{m}_{\mathrm{AB}} & -t^{m}_{\mathrm{BB}} & -t_{\mathrm{AB}} & e_{\mathrm{B}} & -t_{\mathrm{BA}} & -t^{m}_{\mathrm{CB}} & -t_{\mathrm{BC}} \\ 0 & -t^{m}_{\mathrm{BA}} & -t^{m}_{\mathrm{AA}} & -t_{\mathrm{BA}} & e_{\mathrm{A}} & 0 & -t^{m}_{\mathrm{CA}} \\ -t_{\mathrm{AC}} & -t_{\mathrm{BC}} & -t^{m}_{\mathrm{CA}} & -t^{m}_{\mathrm{CB}} & 0 & e_{C} & -t_{\mathrm{CC}} \\ -t^{m}_{\mathrm{AC}} & -t^{m}_{\mathrm{BC}} & -t_{\mathrm{AC}} & -t_{\mathrm{BC}} & -t^{m}_{\mathrm{CA}} & -t_{\mathrm{CC}} & e_{\mathrm{C}} \end{pmatrix}, \tag{C.10a}$$

$$M_{12} = \begin{pmatrix} 0 & -t^{m'}_{\mathrm{AA}} & -t^{m'}_{\mathrm{AB}} & 0 & 0 & 0 & -t^{m'}_{\mathrm{AC}} \\ 0 & -t^{m'}_{\mathrm{BA}} & -t^{m'}_{\mathrm{BB}} & -t^{mm''}_{\mathrm{BA}} & 0 & 0 & -t^{m'}_{\mathrm{BC}} \\ -t^{m}_{\mathrm{AC}} & -t^{mm'}_{\mathrm{AA}} & -t^{mm'}_{\mathrm{AB}} & -t^{m'}_{\mathrm{AA}} & -t^{m'}_{\mathrm{AB}} & 0 & -t^{mm'}_{\mathrm{AC}} \\ -t^{m}_{\mathrm{BC}} & -t^{mm'}_{\mathrm{BA}} & -t^{mm'}_{\mathrm{BB}} & -t^{m'}_{\mathrm{BA}} & -t^{m'}_{\mathrm{BB}} & -t^{mm''}_{\mathrm{BA}} & -t^{mm'}_{\mathrm{BC}} \\ -t_{\mathrm{AC}} & 0 & -t^{mm''}_{\mathrm{AB}} & -t^{mm'}_{\mathrm{AA}} & -t^{mm'}_{\mathrm{AB}} & -t^{m'}_{\mathrm{AA}} & 0 \\ 0 & -t_{\mathrm{CA}} & -t^{m'}_{\mathrm{CB}} & -t^{mm''}_{\mathrm{CA}} & 0 & 0 & -t^{m'}_{\mathrm{CC}} \\ -t_{\mathrm{CC}} & -t^{mm'}_{\mathrm{CA}} & -t_{\mathrm{CB}} & -t_{\mathrm{CA}} & -t^{mm'}_{\mathrm{CB}} & -t^{mm''}_{\mathrm{CA}} & -t^{mm'}_{\mathrm{CC}} \end{pmatrix}, \tag{C.10b}$$

$$M_{13} = \begin{pmatrix} 0 & 0 & 0 & 0 & 0 & 0 & 0 \\ 0 & 0 & 0 & 0 & 0 & 0 & 0 \\ -t^{m'}_{\mathrm{AC}} & 0 & 0 & 0 & 0 & 0 & 0 \\ -t^{m'}_{\mathrm{BC}} & 0 & 0 & 0 & 0 & 0 & 0 \\ -t^{mm'}_{\mathrm{AC}} & -t^{m'}_{\mathrm{AC}} & 0 & 0 & 0 & 0 & 0 \\ 0 & 0 & -t^{m'}_{\mathrm{CA}} & 0 & 0 & 0 & 0 \\ -t^{m'}_{\mathrm{CC}} & 0 & -t^{mm''}_{\mathrm{AC}} & -t^{mm^{(3)}}_{\mathrm{CB}} & -t^{m'}_{\mathrm{CA}} & 0 & 0 \end{pmatrix}, \tag{C.10c}$$

$$M_{21} = \begin{pmatrix} 0 & 0 & -t^{m}_{AC} & -t^{m}_{BC} & -t_{AC} & 0 & -t_{CC} \\ -t^{m'}_{AA} & -t^{m'}_{BA} & -t^{mm'}_{AA} & -t^{mm'}_{BA} & 0 & -t_{CA} & -t^{mm'}_{CA} \\ -t^{m'}_{AB} & -t^{m'}_{BB} & -t^{mm'}_{AB} & -t^{mm'}_{BB} & -t^{mm''}_{AB} & -t^{m'}_{CB} & -t_{CB} \\ 0 & -t^{mm''}_{BA} & -t^{m'}_{AA} & -t^{m'}_{BA} & -t^{mm'}_{AA} & -t^{mm''}_{CA} & -t_{CA} \\ 0 & 0 & -t^{m'}_{AB} & -t^{m'}_{BB} & -t^{mm'}_{AB} & 0 & -t^{mm'}_{CB} \\ 0 & 0 & 0 & -t^{mm''}_{BA} & -t^{m'}_{AA} & 0 & -t^{mm''}_{CA} \\ -t^{m'}_{AC} & -t^{m'}_{BC} & -t^{mm'}_{AC} & -t^{mm'}_{BC} & 0 & -t^{m'}_{CC} & -t^{mm'}_{CC} \end{pmatrix}, \tag{C.10d}$$

$$M_{22} = \begin{pmatrix} e_C & 0 & -t^{mm''}_{CB} & -t^{mm'}_{CA} & -t_{CB} & -t_{CA} & 0 \\ 0 & e_A & -t_{AB} & -t^{m}_{AA} & -t^{m}_{AB} & 0 & -t_{AC} \\ -t^{mm''}_{CB} & -t_{AB} & e_B & -t_{BA} & -t^{m}_{BB} & -t^{m}_{BA} & -t_{BC} \\ -t^{mm'}_{CA} & -t^{m}_{AA} & -t_{BA} & e_A & -t_{AB} & -t^{m}_{AA} & -t^{m}_{CA} \\ -t_{CB} & -t^{m}_{AB} & -t^{m}_{BB} & -t_{AB} & e_B & -t_{BA} & -t^{m}_{CB} \\ -t_{CA} & 0 & -t^{m}_{BA} & -t^{m}_{AA} & -t_{BA} & e_A & 0 \\ 0 & -t_{AC} & -t_{BC} & -t^{m}_{CA} & -t^{m}_{CB} & 0 & e_C \end{pmatrix}, \tag{C.10e}$$

$$M_{23} = \begin{pmatrix} -t^{mm'}_{CC} & -t^{m'}_{CC} & 0 & -t^{mm''}_{BC} & -t^{mm''}_{AC} & -t^{mm^{(3)}}_{CB} & -t^{m'}_{CA} \\ -t^{m}_{AC} & 0 & -t^{m'}_{AA} & -t^{m'}_{AB} & 0 & 0 & 0 \\ -t^{m}_{BC} & 0 & -t^{m'}_{BA} & -t^{m'}_{BB} & -t^{mm''}_{BA} & 0 & 0 \\ -t_{AC} & -t^{m}_{AC} & -t^{mm'}_{AA} & -t^{mm'}_{AB} & -t^{m'}_{AA} & -t^{m'}_{AB} & 0 \\ -t^{m}_{BC} & -t^{mm'}_{BA} & -t^{mm'}_{BB} & -t^{m'}_{BA} & -t^{m'}_{BB} & -t^{mm''}_{BA} & 0 \\ -t^{m}_{CA} & -t_{AC} & 0 & -t^{mm''}_{AB} & -t^{mm'}_{AA} & -t^{mm'}_{AB} & -t^{m'}_{AA} \\ -t_{CC} & 0 & -t_{CA} & -t^{m'}_{CB} & -t^{mm''}_{CA} & 0 & 0 \end{pmatrix}, \tag{C.10f}$$

and

$$M_{31} = \begin{pmatrix} 0 & 0 & -t^{m'}_{AC} & -t^{m'}_{BC} & -t^{mm'}_{AC} & 0 & -t^{m'}_{CC} \\ 0 & 0 & 0 & 0 & -t^{m'}_{AC} & 0 & 0 \\ 0 & 0 & 0 & 0 & 0 & -t^{m'}_{CA} & -t^{mm''}_{AC} \\ 0 & 0 & 0 & 0 & 0 & 0 & -t^{mm^{(3)}}_{CB} \\ 0 & 0 & 0 & 0 & 0 & 0 & -t^{m'}_{CA} \\ 0 & 0 & 0 & 0 & 0 & 0 & 0 \\ 0 & 0 & 0 & 0 & 0 & 0 & 0 \end{pmatrix}, \tag{C.10g}$$

$$M_{32} = \begin{pmatrix} -t_{CC}^{mm'} & -t_{AC}^{m} & -t_{BC}^{m} & -t_{AC} & -t_{BC} & -t_{CA}^{m} & -t_{CC} \\ -t_{CC}^{m'} & 0 & 0 & -t_{AC}^{m} & -t_{BC}^{m} & -t_{AC} & 0 \\ 0 & -t_{AA}^{m'} & -t_{BA}^{m'} & -t_{AA}^{mm'} & -t_{BA}^{mm'} & 0 & -t_{CA} \\ -t_{BC}^{mm''} & -t_{AB}^{m'} & -t_{BB}^{m'} & -t_{AB}^{mm'} & -t_{BB}^{mm'} & -t_{AB}^{mm''} & -t_{CB}^{m'} \\ 0 & -t_{BA}^{mm''} & -t_{AA}^{m'} & -t_{BA}^{m'} & -t_{AA}^{mm'} & -t_{CA}^{mm''} & 0 \\ -t_{CB}^{mm^{(3)}} & 0 & 0 & -t_{AB}^{m'} & -t_{BB}^{m'} & -t_{AB}^{mm'} & 0 \\ -t_{CA}^{m'} & 0 & 0 & 0 & -t_{BA}^{mm''} & -t_{AA}^{m'} & 0 \end{pmatrix}, \tag{C.10h}$$

$$M_{33} = \begin{pmatrix} e_C & -t_{CC} & -t_{CA}^{mm'} & -t_{CB} & -t_{CA} & -t_{CB}^{mm'} & -t_{CA}^{mm''} \\ -t_{CC} & e_C & 0 & -t_{CB}^{mm''} & -t_{CA}^{mm'} & -t_{CB} & -t_{CA} \\ -t_{CA}^{mm'} & 0 & e_A & -t_{AB} & -t_{AA}^{m} & -t_{AB}^{m} & 0 \\ -t_{CB} & -t_{CB}^{mm''} & -t_{AB} & e_B & -t_{BA} & -t_{BB}^{m} & -t_{BA}^{m} \\ -t_{CA} & -t_{CA}^{mm'} & -t_{AA}^{m} & -t_{BA} & e_A & -t_{AB} & -t_{AA}^{m} \\ -t_{CB}^{mm'} & -t_{CB} & -t_{AB}^{m} & -t_{BB}^{m} & -t_{AB} & e_B & -t_{BA} \\ -t_{CA}^{mm''} & -t_{CA} & 0 & -t_{BA}^{m} & -t_{AA}^{m} & -t_{BA} & e_A \end{pmatrix}. \tag{C.10i}$$

The vector ansatz for the localized state $\psi$ reads

$$\psi = (1 \quad 0 \quad r_1 \quad 0 \quad r_2 \quad 0 \quad 0 \quad 0 \quad r_3 \quad 0 \quad r_4 \quad 0 \quad r_5 \quad 0 \quad 0 \quad 0 \quad r_6 \quad 0 \quad r_7 \quad 0 \quad r_8)^{T}, \tag{C.11}$$

and finally, the action of the system Hamiltonian of the ansatz vector is given by $\chi = (\chi_1 \quad \chi_2 \quad \chi_3)^{T}$:

$$\chi_1 = \begin{pmatrix} e_A - r_3 t_{AA}^{m'} - r_1 t_{AA}^{m} \\ -t_{AB} - r_3 t_{BA}^{m'} - r_2 t_{BA}^{m} - r_4 t_{BA}^{mm''} - r_1 t_{BA} \\ r_1 e_A - r_4 t_{AA}^{m'} - r_2 t_{AA}^{m} - t_{AA}^{m} - r_3 t_{AA}^{mm'} \\ -t_{AB}^{m} - r_1 t_{AB} - r_4 t_{BA}^{m'} - r_5 t_{BA}^{mm''} - r_3 t_{BA}^{mm'} - r_2 t_{BA} \\ r_2 e_A - r_5 t_{AA}^{m'} - r_1 t_{AA}^{m} - r_4 t_{AA}^{mm'} \\ -t_{AC} - r_6 t_{CA}^{m'} - r_1 t_{CA}^{m} - r_4 t_{CA}^{mm''} - r_3 t_{CA} \\ -t_{AC}^{m} - r_6 t_{AC}^{mm''} - r_1 t_{AC} - r_7 t_{CA}^{m'} - r_3 t_{CA}^{mm'} - r_2 t_{CA}^{m} - r_5 t_{CA}^{mm''} - r_4 t_{CA} \end{pmatrix}, \tag{C.12a}$$

$$\chi_2 = \begin{pmatrix} -r_1 t_{AC}^{m} - r_7 t_{AC}^{mm''} - r_2 t_{AC} - r_8 t_{CA}^{m'} - r_4 t_{CA}^{mm'} - r_5 t_{CA} \\ r_3 e_A - r_6 t_{AA}^{m'} - t_{AA}^{m'} - r_4 t_{AA}^{m} - r_1 t_{AA}^{mm'} \\ -t_{AB}^{m'} - r_2 t_{AB}^{mm''} - r_1 t_{AB}^{mm'} - r_3 t_{AB} - r_6 t_{BA}^{m'} - r_5 t_{BA}^{m} - r_7 t_{BA}^{mm''} - r_4 t_{BA} \\ r_4 e_A - r_1 t_{AA}^{m'} - r_7 t_{AA}^{m'} - r_3 t_{AA}^{m} - r_5 t_{AA}^{m} - r_2 t_{AA}^{mm'} - r_6 t_{AA}^{mm'} \\ -r_1 t_{AB}^{m'} - r_3 t_{AB}^{m} - r_2 t_{AB}^{mm'} - r_4 t_{AB} - r_7 t_{BA}^{m'} - r_8 t_{BA}^{mm''} - r_6 t_{BA}^{mm'} - r_5 t_{BA} \\ r_5 e_A - r_2 t_{AA}^{m'} - r_8 t_{AA}^{m'} - r_4 t_{AA}^{m} - r_7 t_{AA}^{mm'} \\ -t_{AC}^{m'} - r_1 t_{AC}^{mm'} - r_3 t_{AC} - r_4 t_{CA}^{m} - r_7 t_{CA}^{mm''} - r_6 t_{CA} \end{pmatrix}, \tag{C.12b}$$

$$\chi_3 = \begin{pmatrix} -r_1 t^{m'}_{\mathrm{AC}} - r_3 t^{m}_{\mathrm{AC}} - r_2 t^{mm'}_{\mathrm{AC}} - r_4 t_{\mathrm{AC}} - r_6 t^{mm'}_{\mathrm{CA}} - r_5 t^{m}_{\mathrm{CA}} - r_8 t^{mm''}_{\mathrm{CA}} - r_7 t_{\mathrm{CA}} \\ -r_2 t^{m'}_{\mathrm{AC}} - r_4 t^{m}_{\mathrm{AC}} - r_5 t_{\mathrm{AC}} - r_7 t^{mm'}_{\mathrm{CA}} - r_8 t_{\mathrm{CA}} \\ r_6 e_{\mathrm{A}} - r_3 t^{m'}_{\mathrm{AA}} - r_7 t^{m}_{\mathrm{AA}} - r_4 t^{mm'}_{\mathrm{AA}} \\ -r_3 t^{m'}_{\mathrm{AB}} - r_5 t^{mm''}_{\mathrm{AB}} - r_4 t^{mm'}_{\mathrm{AB}} - r_6 t_{\mathrm{AB}} - r_8 t^{m}_{\mathrm{BA}} - r_7 t_{\mathrm{BA}} \\ r_7 e_{\mathrm{A}} - r_4 t^{m'}_{\mathrm{AA}} - r_6 t^{m}_{\mathrm{AA}} - r_8 t^{m}_{\mathrm{AA}} - r_5 t^{mm'}_{\mathrm{AA}} \\ -r_4 t^{m'}_{\mathrm{AB}} - r_6 t^{m}_{\mathrm{AB}} - r_5 t^{mm'}_{\mathrm{AB}} - r_7 t_{\mathrm{AB}} - r_8 t_{\mathrm{BA}} \\ r_8 e_{\mathrm{A}} - r_5 t^{m'}_{\mathrm{AA}} - r_7 t^{m}_{\mathrm{AA}} \end{pmatrix}. \tag{C.12c}$$

# APPENDIX D

# Low-energy description of the system Hamiltonian in the various phases

In the following, we illustrate a general method that we have combined with the Taylor expansion to obtain the low-energy expression for the system Hamiltonian in the various phases presented in the main text.

## D.1 Decimation

We consider the energy eigenvalue equation, and consider separate blocks in the 4×4 Hamiltonian corresponding to low-energy $\lambda = \left(\psi_{A_1}, \psi_{B_2}\right)^T$ and dimer $\Delta = \left(\psi_{A_2}, \psi_{B_1}\right)^T$ components:

$$\begin{pmatrix} h_\lambda & u \\ u^\dagger & h_\Delta \end{pmatrix} \begin{pmatrix} \lambda \\ \Delta \end{pmatrix} = E \begin{pmatrix} \lambda \\ \Delta \end{pmatrix}, \tag{D.1}$$

The second-row of (D.1) allows the dimer components to be expressed in terms of he low-energy ones:

$$\Delta = (E - h_\Delta)^{-1} u^\dagger \lambda, \tag{D.2}$$

Substituting this into the first-row of (D.1) gives an effective eigenvalue equation that is written solely for the low-energy components:

$$\begin{aligned} \left[h_\lambda + u\,(E - h_\Delta)^{-1} u^\dagger\right] \lambda =& E\lambda, \\ \left[h_\lambda - u h_\Delta^{-1} u^\dagger\right] \lambda \approx& E\mathcal{S}\lambda, \end{aligned}$$

where $\mathcal{S} = 1 + uh_\Delta^{-2}u^\dagger$. The second equation is accurate up to linear terms in $E$. Finally, we perform a transformation $\Phi = \mathcal{S}^{1/2}\lambda$:

$$\begin{aligned}\left[h_\lambda - uh_\Delta^{-1}u^\dagger\right]\mathcal{S}^{-1/2}\Phi \approx& E\mathcal{S}^{1/2}\Phi\,,\\ \mathcal{S}^{-1/2}\left[h_\lambda - uh_\Delta^{-1}u^\dagger\right]\mathcal{S}^{-1/2}\Phi \approx& E\Phi\,.\end{aligned} \tag{D.3}$$

This transformation ensures that the normalisation of $\Phi$ is consistent with that of the original states:

$$\begin{aligned}\Phi^\dagger\Phi = \lambda^\dagger\mathcal{S}\lambda =& \lambda^\dagger\left(1 + uh_\Delta^{-2}u^\dagger\right)\lambda\,,\\ \approx& \lambda^\dagger\lambda + \Delta^\dagger\Delta\,,\end{aligned}$$

where we used Eq. (D.2) for small $E$: $\chi \approx -h_\chi^{-1}u^\dagger\lambda$. Thus, the effective Hamiltonian for low-energy components is given by Eq. (D.3):

$$H^{(\text{eff})} \approx \mathcal{S}^{-1/2}\left[h_\lambda - uh_\chi^{-1}u^\dagger\right]\mathcal{S}^{-1/2}\,, \tag{D.4a}$$

$$\mathcal{S} = 1 + uh_\chi^{-2}u^\dagger\,. \tag{D.4b}$$

## D.2 Low-energy Hamiltonians

We obtain a low-energy description of the Hamiltonian in Eq. (4.2a) by performing first a Taylor expansion around the Dirac cones $\mathbf{k} = \mathbf{K}^+ + \mathbf{q}$ of all the entries of the matrix. We identify the orbitals contributing to the low-energy features by checking which hopping term destroys the Dirac cones when removed. At this point, we rearrange the Hamiltonian in a low- and high-energy sector $h_\lambda$ and $h_\Delta$, and perform a decimation as introduced in [166]. For this lattice, we have chosen the orbitals placed at lattice sites $r$, $l$ to be the low-energy sector and $u$, $d$ to be the high-energy one. Figure D.1(a) shows the spectrum of the low-/high-energy sectors, which is the same if the choice of orbitals is reversed. After these two processes, the low-energy Hamiltonian $\tilde{\mathcal{H}}$ for the fully symmetric case reads:

$$\begin{aligned}\tilde{\mathcal{H}}_0 &= v_\text{F}\mathbf{h}\cdot\sigma,\\ &= v_\text{F}\left[\sqrt{3}(3p_x - p_y)\sigma_x - (p_x - 5p_y)\sigma_y\right].\end{aligned} \tag{D.5}$$

where we have introduced the Fermi velocity defined as $\hbar v_\text{F} = t_0 a_0/4$, $p_\alpha = -\mathrm{i}\hbar\partial_\alpha$ is the momentum operator in the direction $\alpha$, and $\sigma$ are the Pauli matrices. This decimated Hamiltonian reproduces the low-energy physics of the herringbone lattice properly since we recover Dirac cones in the low-energy regime. The corresponding spectrum is shown in Fig. D.1(b). The low-energy description of the herringbone with $\{\mathcal{G}_{1\alpha}\}$ broken corresponds to the following Hamiltonian:

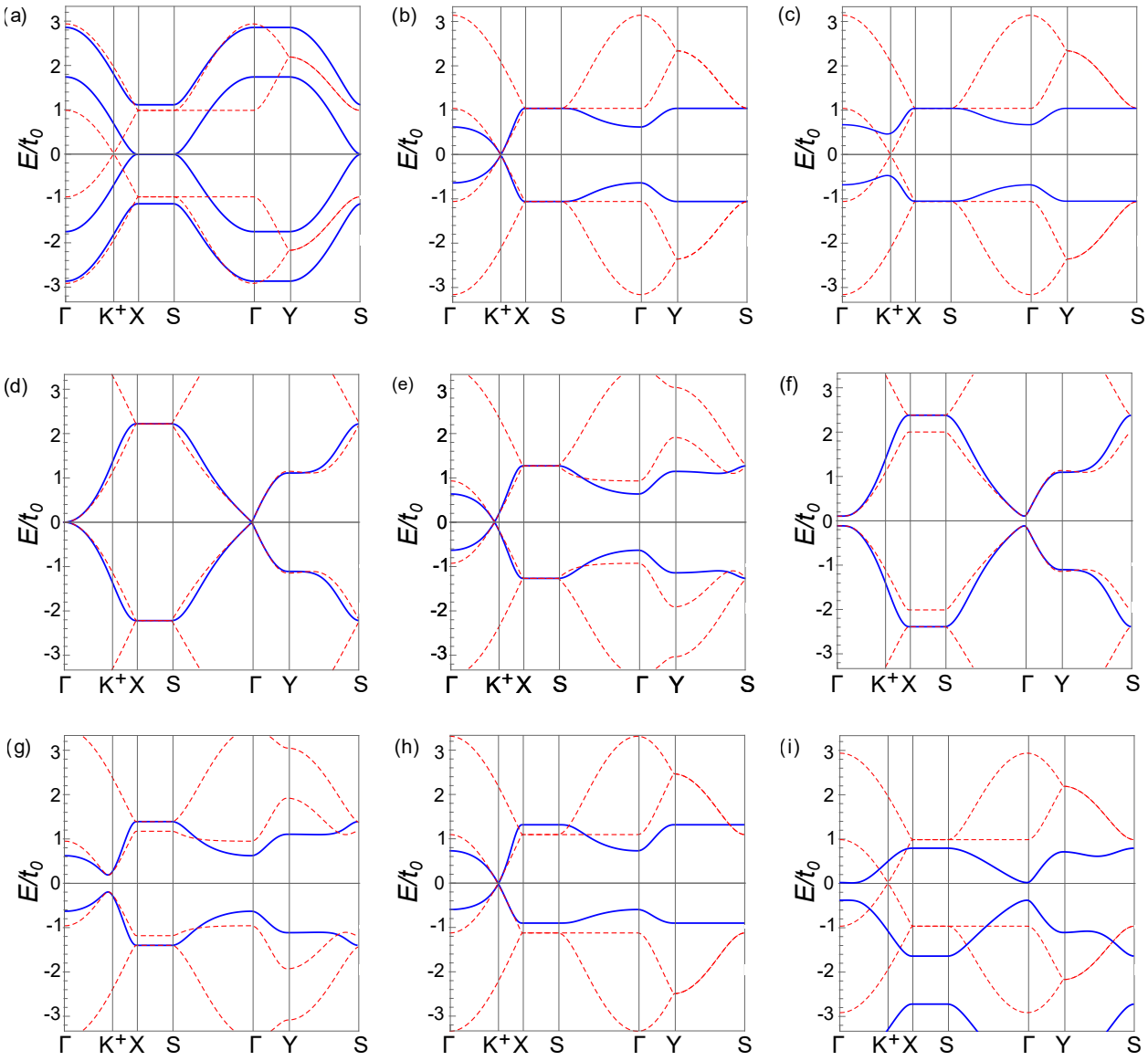


*Figure D.1:* (a) Low-energy and dimer bands after setting $r$, $l$ as low-energy and $u$, $d$ as dimer. Low-energy Hamiltonians for (b) fully symmetric case expanded at $K^+$, (c) in the presence of $\mathcal{M}_1(\delta_1)$ at $K^+$, (d) in the presence of $\mathcal{M}_2(\sqrt{3})$ at $\Gamma$, (e) in the presence of $\mathcal{M}_2(\delta_2)$ for generic $k$ point away from $K^+$ determined by the choice of $\delta_2$, (f) in the presence of $\mathcal{M}_1(\delta_1) + \mathcal{M}_2(\sqrt{3})$, at $\Gamma$, (g) in the presence of $\mathcal{M}_1(\delta_1) + \mathcal{M}_2(\delta_2)$, at generic $k$ point away from $K^+$ given by the set of parameters, (h) in the presence of $\mathcal{M}_I(\delta_I)$ at generic $k$ point given by the set of parameters. This last case is very sensitive to the choice of parameters since it is not able to reproduce properly the flat band. (i) Band structure after adding all three perturbations. Bands are split in energy since the Casimir invariant of this choice is different from zero. See Sec.4.7.

$$\begin{aligned}\tilde{\mathcal{H}}_1 &= v_{\mathrm{F}}\mathbf{h}\cdot\sigma \\ &= v_{\mathrm{F}}\left[f(\mathbf{p},\delta_1)\sigma_x + g(\mathbf{p},\delta_1)\sigma_y\right] + t_0\delta_1\sigma_z\end{aligned} \tag{D.6}$$

where $f(\mathbf{p},\delta_1)$ and $g(\mathbf{p},\delta_1)$ are complex functions of their variables which, at $\delta_1 = 0$, yield the expressions in (D.5). For finite $\delta_1$, the mass term proportional to $\sigma_z$ is finite, thus gaps open at $\mathbf{K}^{\pm}$ points. The corresponding spectrum is shown in Fig. D.1(c).

When breaking the glide $\{\mathcal{G}_{2\alpha}\}$, we obtain a low-energy expansion around $\Gamma$ that recovers the semi-Dirac cone. It reads:

$$\tilde{\mathcal{H}}_2 = v_{\mathrm{F}}\mathbf{h}\cdot\sigma = -\frac{p_x p_y}{m}\sigma_x + v_{\mathrm{F}}(p_x - p_y)\sigma_y, \tag{D.7a}$$

$$E(\mathbf{q}) = \pm\frac{1}{2}\sqrt{16q_y^2 - 32q_xq_y + q_x^2(16+9q_y^2)}. \tag{D.7b}$$

where we have introduced an effective mass defined as $m = t_0/(12v_{\mathrm{F}}^2)$. From Eq. (D.7b) for small $q$, we find that, by fixing $q_x = q_y$ (*i.e.* $\Gamma$X direction), we obtain $E \sim q^2$ behavior while, for $q_x = -q_y$ (*i.e.* $\Gamma$Y direction), we obtain $E \sim |q|$. At any other $\delta_2$, the series expansion of the decimated Hamiltonian has to be done around the $k$ point given by Eq. (4.9) in the main text to recover the Dirac cones.

Since the Hamiltonian in (D.7a) is written only in terms of two Pauli matrices [150], we can gap the semi-Dirac cone by adding a constant term proportional to $\sigma_z$, which breaks the first set of glides. In the total Hamiltonian, this corresponds to an additional mass term given by the one in the main text, *i.e.*, $\mathcal{M}_1(\delta_1)$.

Figures. D.1(d) and (e) show the corresponding spectrum for semi-Dirac dispersion and Dirac cones at positions given by Eq. (4.9), respectively. Figures. D.1(f) and (g) show the previous two situations, plus the $\mathcal{M}_1(\delta_1)$ term, where the spectrum is gapped.

Finally, the Hamiltonian for the last choice of onsite energies displays a similar expression as in Eq. (D.6). The corresponding spectrum is shown in Fig. D.1(h). This spectrum is very sensitive to the choice of parameters. We have chosen a situation where the Dirac cone is very close to the fully symmetric case, but, unlike Fig. D.1(b), the bands are not symmetric in energy.

# APPENDIX E

# Analytical expressions for the position of the Dirac cones

This Appendix is devoted to the study of the analytical expressions for the position of the Dirac cones obtained in expressions (4.9) and (4.11), and how (4.16) captures both of them but with different expressions. We begin by studying the particular cases of expression 4.16, which reads:

$$\mathbf{k}^{\mathrm{D}}_{\mathrm{I},2}(\delta_{\mathrm{I}},\delta_2) = \frac{1}{2a_0}\arccos\left(\frac{\delta_2^2-\delta_{\mathrm{I}}^2-1}{2}\right)\mathbf{u}_1, \tag{E.1}$$

where $\mathbf{k}^{\mathrm{D}}_{\mathrm{I},2}(\delta_{\mathrm{I}},\delta_2)$ represents the $(k_x,k_y)$ components of the position of the Dirac cones as a function of the $\delta_{\mathrm{I}},\delta_2$ parameters, $a_0$ is the interatomic distance, taken to be unity but made explicit, and $\mathbf{u}_1 = \mathbf{b}_1/|\mathbf{b_1}|$ represents the unitary vector along the direction of the first reciprocal lattice vector $\mathbf{b}_1$.

If now we let $\delta_2 = 0$, we recover the expression:

$$\mathbf{k}^{\mathrm{D}}_{\mathrm{I},2}(\delta_{\mathrm{I}},0) = \frac{1}{2a_0}\arccos\left(\frac{-\delta_{\mathrm{I}}^2-1}{2}\right)\mathbf{u}_1, \tag{E.2}$$

which is equal to equation (4.11). On the other hand, if we take $\delta_{\mathrm{I}} = 0$ we obtain the expression:

$$\mathbf{k}^{\mathrm{D}}_{\mathrm{I},2}(0,\delta_2) = \frac{1}{2a_0}\arccos\left(\frac{\delta_2^2-1}{2}\right)\mathbf{u}_1, \tag{E.3}$$

which is quite different from the expression (4.9), given by:

$$\mathbf{k}^{\mathrm{D}}_{2}(\delta_2) = \frac{1}{a_0}\arccos\left(\frac{1}{2}\sqrt{1+\delta_2^2}\right)\mathbf{u}_1, \tag{E.4}$$

which is quite different from expression (E.3). In the following, we find the equivalence between the two expressions. We begin by solving for $\delta_2^2$ in both equations. From Eq. (E.3) we write:

$$x = |\mathbf{k}^{\mathrm{D}}_{\mathrm{I},2}(0,\delta_2)| = \frac{1}{2a_0}\arccos\left(\frac{\delta_2^2-1}{2}\right), \tag{E.5a}$$

$$\delta_2^2 = 2\cos(2x) + 1. \tag{E.5b}$$

Similarly, for Eq. (E.4) we write

$$y = |\mathbf{k}_2^{\mathrm{D}}(\delta_2)| = \frac{1}{a_0}\arccos\left(\frac{1}{2}\sqrt{1+\delta_2^2}\right), \tag{E.6a}$$

$$\delta_2^2 = 4\cos^2 y - 1. \tag{E.6b}$$

Now, if we equal equations (E.5b) to (E.6b), we find the relation of the cosine of the double angle between $2x$ and $y$, which reveals that $x = y$:

$$\cos(2x) = 2\cos y - 1. \tag{E.7}$$

Hence, expression (4.16) gives the position of the Dirac cones for a generic pair of values of $\delta_2, \delta_{\mathrm{I}}$, and captures the particular cases when one of them is taken to 0.

# BIBLIOGRAPHY


[1] Barry Bradlyn et al. “Topological quantum chemistry”. In: *Nature* 547.7663 (2017), p. 298. DOI: 10.1038/nature23268.

[2] George P Thomson and Alexander Reid. “Diffraction of cathode rays by a thin film”. In: *Nature* 119.3007 (1927), pp. 890–890.

[3] Clinton Davisson and Lester H Germer. “The scattering of electrons by a single crystal of nickel”. In: *Nature* 119.2998 (1927), pp. 558–560.

[4] Claus Jönsson. “Elektroneninterferenzen an mehreren künstlich hergestellten Feinspalten”. In: *Zeitschrift für Physik* 161.4 (1961), pp. 454–474.

[5] Claus Jönsson. “Electron diffraction at multiple slits”. In: *American Journal of Physics* 42.1 (1974), pp. 4–11.

[6] Pier Giorgio Merli, Gian Franco Missiroli, and Giulio Pozzi. “On the statistical aspect of electron interference phenomena”. In: *Am. J. Phys* 44.3 (1976), pp. 306–307.

[7] Akira Tonomura et al. “Demonstration of single-electron buildup of an interference pattern”. In: *American Journal of Physics* 57.2 (1989), pp. 117–120.

[8] Erwin Schrödinger. “An undulatory theory of the mechanics of atoms and molecules”. In: *Physical review* 28.6 (1926), p. 1049.

[9] Wikimedia Commons. *Plaques of Lambda Phages on E. coli XL1-Blue MRF*. 16 June 2013. URL: https://upload.wikimedia.org/wikipedia/commons/9/9d/Band_filling_diagram.svg.

[10] David J Thouless et al. “Quantized Hall conductance in a two-dimensional periodic potential”. In: *Physical review letters* 49.6 (1982), p. 405. DOI: 10.1103/PhysRevLett.49.405.

[11] Kubo Ryogo. “Statistical-mechanical theory of irreversible processes. I. General theory and simple applications to magnetic and conduction problems”. In: *Journal of the Physical Society of Japan* 12.6 (1957), pp. 570–586.

[12] Richard P. Feynman. “There’s plenty of room at the bottom”. In: *Resonance* 16.9 (Sept. 2011), pp. 890–905. DOI: 10.1007/s12045-011-0109-x. URL: https://doi.org/10.1007/s12045-011-0109-x.

[13] Richard P Feynman et al. “Simulating physics with computers”. In: *Int. j. Theor. phys* 21.6/7 (2018).

[14] Barry Bradlyn et al. “Topological quantum chemistry”. In: *Nature* 547.7663 (2017), pp. 298–305.

[15] N. W. Ashcroft and N. D. Mermin. *Solid State Physics*. Saunders, 1976.

[16] David Vanderbilt. *Berry Phases in Electronic Structure Theory: Electric Polarization, Orbital Magnetization and Topological Insulators*. Cambridge University Press, 2018. DOI: 10.1017/9781316662205.

[17] Titus Neupert and Frank Schindler. “Topological Crystalline Insulators”. In: *Topological Matter*. Springer International Publishing, 2018, pp. 31–61. DOI: 10.1007/978-3-319-76388-0_2. URL: https://doi.org/10.1007/978-3-319-76388-0_2.

[18] M.S. Dresselhaus, G. Dresselhaus, and A. Jorio. *Group Theory: Application to the Physics of Condensed Matter*. Springer Berlin Heidelberg, 2007. ISBN: 9783540328971. DOI: https://doi.org/10.1007/978-3-540-32899-5.

[19] Titus Neupert and Frank Schindler. “Topological Crystalline Insulators”. In: *Topological Matter*. Springer International Publishing, 2018, pp. 31–61. DOI: 10.1007/978-3-319-76388-0_2.

[20] János K. Asbóth, László Oroszlány, and András Pályi. *A Short Course on Topological Insulators*. Springer International Publishing, 2016. ISBN: 9783319256078. DOI: 10.1007/978-3-319-25607-8. URL: https://doi.org/10.1007/978-3-319-25607-8.

[21] William Shockley. “On the surface states associated with a periodic potential”. In: *Physical review* 56.4 (1939), p. 317.

[22] Igor Tamm. “On the possible bound states of electrons on a crystal surface”. In: *Phys. Z. Sowjetunion* 1 (1932), pp. 733–735.

[23] Gerald D Mahan. *Many-particle physics*. Springer Science & Business Media, 2000.

[24] Henrik Bruus and Karsten Flensberg. *Many-body quantum theory in condensed matter physics: an introduction*. OUP Oxford, 2004.

[25] Mois I Aroyo et al. “Crystallography online: Bilbao crystallographic server”. In: *Bulg. Chem. Commun* 43.2 (2011), pp. 183–197.

[26] Mois Ilia Aroyo et al. “Bilbao Crystallographic Server: I. Databases and crystallographic computing programs”. In: *Z. Kristallogr. Cryst. Mater.* 221.1 (Jan. 2006), p. 15. DOI: 10.1524/zkri.2006.221.1.15. URL: https://doi.org/10.1524%2Fzkri.2006.221.1.15.

[27] M. I. Aroyo et al. “Bilbao Crystallographic Server. II. Representations of crystallographic point groups and space groups”. In: *Acta Cryst.* A62 (2006), p. 115. DOI: 10.1107/S0108767305040286.

[28] Nicola Marzari et al. “Maximally localized Wannier functions: Theory and applications”. In: *Reviews of Modern Physics* 84.4 (2012), p. 1419.

[29] Jacques Des Cloizeaux. “Analytical properties of n-dimensional energy bands and Wannier functions”. In: *Physical Review* 135.3A (1964), A698.

[30] Gheorghe Nenciu. “Existence of the exponentially localised Wannier functions”. In: *Communications in mathematical physics* 91 (1983), pp. 81–85.

[31] Viatcheslav M Silkin et al. “The role of an electronic surface state in the stopping power of a swift charged particle in front of a metal”. In: *Journal of Physics: Condensed Matter* 20.30 (2008), p. 304209.

[32] Kenjiro K Gomes et al. “Designer Dirac fermions and topological phases in molecular graphene”. In: *Nature* 483.7389 (2012), pp. 306–310. DOI: 10.1038/nature10941.

[33] Alexander A Khajetoorians et al. “Creating designer quantum states of matter atom-by-atom”. In: *Nat. Rev. Phys.* 1.12 (2019), pp. 703–715. DOI: 10.1038/s42254-019-0108-5.

[34] Cheol-Hwan Park and Steven G Louie. “Making massless Dirac fermions from a patterned two-dimensional electron gas”. In: *Nano Lett.* 9.5 (2009), pp. 1793–1797. DOI: 10.1021/nl803706c.

[35] Donald M Eigler and Erhard K Schweizer. “Positioning single atoms with a scanning tunnelling microscope”. In: *Nature* 344.6266 (1990), pp. 524–526.

[36] Michael F Crommie, Christopher P Lutz, and Donald M Eigler. “Confinement of electrons to quantum corrals on a metal surface”. In: *Science* 262.5131 (1993), pp. 218–220.

[37] MF Crommie et al. “Quantum corrals”. In: *Physica D: Nonlinear Phenomena* 83.1-3 (1995), pp. 98–108.

[38] MF Crommie, Ch P Lutz, and DM Eigler. “Imaging standing waves in a two-dimensional electron gas”. In: *Nature* 363.6429 (1993), pp. 524–527. DOI: 10.1038/363524a0.

[39] Saw-Wai Hla, Kai-Felix Braun, and Karl-Heinz Rieder. "Single-atom manipulation mechanisms during a quantum corral construction". In: *Phys. Rev. B* 67 (20 May 2003), p. 201402. DOI: 10.1103/PhysRevB.67.201402. URL: https://link.aps.org/doi/10.1103/PhysRevB.67.201402.

[40] Stefan Fölsch et al. "Quantum dots with single-atom precision". In: *Nat. Nanotechnol.* 9.7 (2014), pp. 505–508. DOI: 10.1038/nnano.2014.129.

[41] PO Gartland and BJ Slagsvold. "Transitions conserving parallel momentum in photoemission from the (111) face of copper". In: *Physical Review B* 12.10 (1975), p. 4047.

[42] L Bürgi et al. "Noble metal surface states: deviations from parabolic dispersion". In: *Surface science* 447.1-3 (2000), pp. L157–L161.

[43] F Reinert et al. "Direct measurements of the L-gap surface states on the (111) face of noble metals by photoelectron spectroscopy". In: *Physical Review B* 63.11 (2001), p. 115415.

[44] Marlou R. Slot et al. "Experimental realization and characterization of an electronic Lieb lattice". In: *Nat. Phys.* 13.7 (Apr. 2017), pp. 672–676. DOI: 10.1038/nphys4105. URL: https://doi.org/10.1038%2Fnphys4105.

[45] SN Kempkes et al. "Robust zero-energy modes in an electronic higher-order topological insulator". In: *Nat. Mat.* 18.12 (2019), pp. 1292–1297. DOI: 10.1038/s41563-019-0483-4.

[46] S. N. Kempkes et al. "Design and characterization of electrons in a fractal geometry". In: *Nat. Phys.* 15.2 (Nov. 2018), pp. 127–131. DOI: 10.1038/s41567-018-0328-0. URL: https://doi.org/10.1038%2Fs41567-018-0328-0.

[47] Shin-ichi Ishi, Yuichi Ohno, and B Viswanathan. "An overview on the electronic and vibrational properties of adsorbed CO". In: *Surface Science* 161.2-3 (1985), pp. 349–372.

[48] Gregor Witte. "Low frequency vibrational modes of adsorbates". In: *Surface science* 502 (2002), pp. 405–416.

[49] P Lazić et al. "Density functional theory with nonlocal correlation: A key to the solution of the CO adsorption puzzle". In: *Physical Review B* 81.4 (2010), p. 045401.

[50] Kareem M Gameel et al. "Unveiling CO adsorption on Cu surfaces: new insights from molecular orbital principles". In: *Physical Chemistry Chemical Physics* 20.40 (2018), pp. 25892–25900.

[51] Kenjiro K Gomes et al. "Designer Dirac fermions and topological phases in molecular graphene". In: *Nature* 483.7389 (2012), pp. 306–310.

[52] MR Slot et al. "p-Band engineering in artificial electronic lattices". In: *Phys. Rev. X* 9.1 (2019), p. 011009. DOI: 10.1103/PhysRevX.9.011009.

[53] M. A. J. Herrera et al. “Corner modes of the breathing kagome lattice: Origin and robustness”. In: *Phys. Rev. B* 105 (8 Feb. 2022), p. 085411. DOI: 10.1103/PhysRevB.105.085411. URL: https://link.aps.org/doi/10.1103/PhysRevB.105.085411.

[54] Robert J Celotta et al. “Invited Article: Autonomous assembly of atomically perfect nanostructures using a scanning tunneling microscope”. In: *Review of Scientific Instruments* 85.12 (2014).

[55] Ludwig Bartels, Gerhard Meyer, and K-H Rieder. “Basic steps of lateral manipulation of single atoms and diatomic clusters with a scanning tunneling microscope tip”. In: *Physical Review Letters* 79.4 (1997), p. 697.

[56] Ludwig Bartels et al. “Dynamics of electron-induced manipulation of individual CO molecules on Cu (111)”. In: *Physical Review Letters* 80.9 (1998), p. 2004.

[57] L Bartels, G Meyer, and K-H Rieder. “Controlled vertical manipulation of single CO molecules with the scanning tunneling microscope: A route to chemical contrast”. In: *Applied Physics Letters* 71.2 (1997), pp. 213–215.

[58] Fabian Stilp et al. “Very weak bonds to artificial atoms formed by quantum corrals”. In: *Science* 372.6547 (May 2021), pp. 1196–1200. DOI: 10.1126/science.abe2600. URL: https://doi.org/10.1126/science.abe2600.

[59] J Yang et al. “Vertical manipulation of native adatoms on the InAs (111) A surface”. In: *Journal of Physics: Condensed Matter* 24.35 (2012), p. 354008.

[60] Yi Pan et al. “Reconfigurable quantum-dot molecules created by atom manipulation”. In: *Physical Review Letters* 115.7 (2015), p. 076803.

[61] Kiyoshi Kanisawa, Stefan Fölsch, et al. “Quantum rings engineered by atom manipulation”. In: *Physical review letters* 123.6 (2019), p. 066801.

[62] K v Klitzing, Gerhard Dorda, and Michael Pepper. “New method for high-accuracy determination of the fine-structure constant based on quantized Hall resistance”. In: *Physical review letters* 45.6 (1980), p. 494.

[63] Robert B Laughlin. “Fractional quantization”. In: *Nobel lectures, physics* 2000 (1996), p. 264.

[64] Alexander Altland and Martin R Zirnbauer. “Nonstandard symmetry classes in mesoscopic normal-superconducting hybrid structures”. In: *Physical Review B* 55.2 (1997), p. 1142.

[65] Andreas P Schnyder et al. “Classification of topological insulators and superconductors in three spatial dimensions”. In: *Physical Review B* 78.19 (2008), p. 195125.

[66] Shinsei Ryu et al. “Topological insulators and superconductors: tenfold way and dimensional hierarchy”. In: *New Journal of Physics* 12.6 (2010), p. 065010.

[67] Liang Fu. “Topological crystalline insulators”. In: *Physical review letters* 106.10 (2011), p. 106802.

[68] Jorrit Kruthoff et al. “Topological Classification of Crystalline Insulators through Band Structure Combinatorics”. In: *Phys. Rev. X* 7 (4 Dec. 2017), p. 041069. DOI: 10.1103/PhysRevX.7.041069. URL: https://link.aps.org/doi/10.1103/PhysRevX.7.041069.

[69] Titus Neupert and Frank Schindler. “Topological crystalline insulators”. In: *Topological Matter: Lectures from the Topological Matter School 2017* (2018), pp. 31–61.

[70] Eyal Cornfeld and Shachar Carmeli. “Tenfold topology of crystals: Unified classification of crystalline topological insulators and superconductors”. In: *Physical Review Research* 3.1 (2021), p. 013052.

[71] Tosio Kato. “On the adiabatic theorem of quantum mechanics”. In: *Journal of the Physical Society of Japan* 5.6 (1950), pp. 435–439.

[72] T Thonhauser and David Vanderbilt. “Insulator/Chern-insulator transition in the Haldane model”. In: *Physical Review B* 74.23 (2006), p. 235111.

[73] Wladimir A Benalcazar, Tianhe Li, and Taylor L Hughes. “Quantization of fractional corner charge in $C_n$-symmetric higher-order topological crystalline insulators”. In: *Phys. Rev. B* 99.24 (2019), p. 245151. DOI: 10.1103/PhysRevB.99.245151.

[74] RD King-Smith and David Vanderbilt. “Theory of polarization of crystalline solids”. In: *Physical Review B* 47.3 (1993), p. 1651.

[75] Raffaele Resta and David Vanderbilt. “Theory of polarization: a modern approach”. In: *Physics of ferroelectrics: a modern perspective*. Springer, 2007, pp. 31–68.

[76] Aris Alexandradinata, Xi Dai, and B Andrei Bernevig. “Wilson-loop characterization of inversion-symmetric topological insulators”. In: *Phys. Rev. B* 89.15 (2014), p. 155114. DOI: 10.1103/PhysRevB.89.155114.

[77] Luis Elcoro et al. “Magnetic topological quantum chemistry”. In: *Nature communications* 12.1 (2021), p. 5965.

[78] Yuanfeng Xu et al. “High-throughput calculations of magnetic topological materials”. In: *Nature* 586.7831 (2020), pp. 702–707.

[79] Jennifer Cano and Barry Bradlyn. “Band representations and topological quantum chemistry”. In: *Annual Review of Condensed Matter Physics* 12 (2021), pp. 225–246.

[80] Roald Hoffmann. “How chemistry and physics meet in the solid state”. In: *Angewandte Chemie International Edition in English* 26.9 (1987), pp. 846–878.

[81] J Zak. “Symmetry specification of bands in solids”. In: *Physical Review Letters* 45.12 (1980), p. 1025.

[82] J Zak. “Band representations and symmetry types of bands in solids”. In: *Physical Review B* 23.6 (1981), p. 2824.

[83] J Zak. “Band representations of space groups”. In: *Physical Review B* 26.6 (1982), p. 3010.

[84] H Bacry, L Michel, and J Zak. “Symmetry and classification of energy bands in crystals”. In: *Group Theoretical Methods in Physics: Proceedings of the XVI International Colloquium Held at Varna, Bullgaria, June 15–20, 1987*. Springer. 1988, pp. 289–308.

[85] L Michel and J Zak. “Connectivity of energy bands in crystals”. In: *Physical Review B* 59.9 (1999), p. 5998.

[86] L Michel and J Zak. “Elementary energy bands in crystals are connected”. In: *Physics Reports* 341.1-6 (2001), pp. 377–395.

[87] W. P. Su, J. R. Schrieffer, and A. J. Heeger. “Solitons in Polyacetylene”. In: *Phys. Rev. Lett.* 42 (25 June 1979), pp. 1698–1701. DOI: 10.1103/PhysRevLett.42.1698. URL: https://link.aps.org/doi/10.1103/PhysRevLett.42.1698.

[88] María Blanco de Paz et al. “Tutorial: Computing Topological Invariants in 2D Photonic Crystals”. In: *Adv. Quantum Technol.* 3.2 (Dec. 2019), p. 1900117. DOI: 10.1002/qute.201900117. URL: https://doi.org/10.1002/qute.201900117.

[89] Takahiro Fukui, Yasuhiro Hatsugai, and Hiroshi Suzuki. “Chern numbers in discretized Brillouin zone: efficient method of computing (spin) Hall conductances”. In: *Journal of the Physical Society of Japan* 74.6 (2005), pp. 1674–1677.

[90] Warren Ambrose and Isadore M Singer. “A theorem on holonomy”. In: *Transactions of the American Mathematical Society* 75.3 (1953), pp. 428–443.

[91] Wladimir A. Benalcazar, B. Andrei Bernevig, and Taylor L. Hughes. “Quantized electric multipole insulators”. In: *Science* 357.6346 (2017), p. 61. DOI: 10.1126/science.aah6442.

[92] Wladimir A. Benalcazar, B. Andrei Bernevig, and Taylor L. Hughes. “Electric multipole moments, topological multipole moment pumping, and chiral hinge states in crystalline insulators”. In: *Phys. Rev. B* 96 (24 Dec. 2017), p. 245115. DOI: 10.1103/PhysRevB.96.245115. URL: https://link.aps.org/doi/10.1103/PhysRevB.96.245115.

[93] Guido van Miert and Carmine Ortix. "Higher-order topological insulators protected by inversion and rotoinversion symmetries". In: *Phys. Rev. B* 98 (8 Aug. 2018), p. 081110. DOI: 10.1103/PhysRevB.98.081110. URL: https://link.aps.org/doi/10.1103/PhysRevB.98.081110.

[94] Eunwoo Lee, Akira Furusaki, and Bohm-Jung Yang. "Fractional charge bound to a vortex in two-dimensional topological crystalline insulators". In: *Phys. Rev. B* 101.24 (2020), p. 241109. DOI: 10.1103/PhysRevB.101.241109.

[95] Mamoru Mekata. "Kagome: The story of the basketweave lattice". In: *Physics Today* 56.2 (2003), pp. 12–13.

[96] Yasir Iqbal et al. "Gapless spin-liquid phase in the kagome spin-1 2 heisenberg antiferromagnet". In: *Phys. Rev. B* 87.6 (2013), p. 060405. DOI: 10.1103/PhysRevB.87.060405.

[97] Michael Hermele et al. "Properties of an algebraic spin liquid on the kagome lattice". In: *Phys. Rev. B* 77 (22 June 2008), p. 224413. DOI: 10.1103/PhysRevB.77.224413. URL: https://link.aps.org/doi/10.1103/PhysRevB.77.224413.

[98] Simeng Yan, David A Huse, and Steven R White. "Spin-liquid ground state of the S= 1/2 kagome Heisenberg antiferromagnet". In: *Science* 332.6034 (2011), pp. 1173–1176. DOI: 10.1126/science.1201080.

[99] Laura Messio, Bernard Bernu, and Claire Lhuillier. "Kagome antiferromagnet: a chiral topological spin liquid?" In: *Phys. Rev. Lett.* 108.20 (2012), p. 207204. DOI: 10.1103/PhysRevLett.108.207204.

[100] Jia-Xin Yin, Biao Lian, and M Zahid Hasan. "Topological kagome magnets and superconductors". In: *Nature* 612.7941 (2022), pp. 647–657.

[101] Janne Ruostekoski. "Optical kagome lattice for ultracold atoms with nearest neighbor interactions". In: *Phys. Rev. Lett.* 103.8 (2009), p. 080406. DOI: 10.1103/PhysRevLett.103.080406.

[102] Xing Zhu, Hong Wang, and Li-Xian Zheng. "Defect solitons in kagome optical lattices". In: *Opt. Express* 18.20 (2010), pp. 20786–20792. DOI: 10.1364/OE.18.020786.

[103] Gyu-Boong Jo et al. "Ultracold atoms in a tunable optical kagome lattice". In: *Phys. Rev. Lett.* 108.4 (2012), p. 045305. DOI: 10.1103/PhysRevLett.108.045305.

[104] Motohiko Ezawa. "Higher-order topological electric circuits and topological corner resonance on the breathing kagome and pyrochlore lattices". In: *Phys. Rev. B* 98 (20 Nov. 2018), p. 201402. DOI: 10.1103/PhysRevB.98.201402. URL: https://link.aps.org/doi/10.1103/PhysRevB.98.201402.

[105] Xiang Ni et al. "Observation of higher-order topological acoustic states protected by generalized chiral symmetry". In: *Nat. Mat.* 18 (2019), p. 113. DOI: 10.1038/s41563-018-0252-9.

[106] Haoran Xue et al. "Acoustic higher-order topological insulator on a Kagome lattice". In: *Nat. Mat.* 18 (2019), p. 108. DOI: 10.1038/s41563-018-0251-x.

[107] Qian Chen, Sung Chul Bae, and Steve Granick. "Directed self-assembly of a colloidal kagome lattice". In: *Nature* 469.7330 (2011), pp. 381–384. DOI: 10.1038/nature09713.

[108] Stewart A Mallory and Angelo Cacciuto. "Activity-enhanced self-assembly of a colloidal kagome lattice". In: *J. Am. Chem. Soc.* 141.6 (2019), pp. 2500–2507. DOI: 10.1021/jacs.8b12165.

[109] Mengyao Li et al. "Higher-order topological states in photonic kagome crystals with long-range interactions". In: *Nat. Photonics* 14 (2019), pp. 89–94. DOI: 10.1038/s41566-019-0561-9.

[110] Yafeng Chen et al. "Inverse design of higher-order photonic topological insulators". In: *Phys. Rev. Research* 2 (2 May 2020), p. 023115. DOI: 10.1103/PhysRevResearch.2.023115. URL: https://link.aps.org/doi/10.1103/PhysRevResearch.2.023115.

[111] Marco S. Kirsch et al. "Nonlinear second-order photonic topological insulators". In: *Nat. Phys.* 17 (June 2021), p. 995. DOI: 10.1038/s41567-021-01275-3. URL: https://doi.org/10.1038/s41567-021-01275-3.

[112] Shi-lei Shen, Chao Li, and Jun-Fang Wu. "Investigation of corner states in second-order photonic topological insulator". In: *Opt. Express* 29.15 (June 2021), pp. 24045–24055. DOI: 10.1364/OE.426691. URL: http://www.osapublishing.org/oe/abstract.cfm?URI=oe-29-15-24045.

[113] Zheng Wang et al. "Reflection-Free One-Way Edge Modes in a Gyromagnetic Photonic Crystal". In: *Phys. Rev. Lett.* 100 (1 Jan. 2008), p. 013905. DOI: 10.1103/PhysRevLett.100.013905. URL: https://link.aps.org/doi/10.1103/PhysRevLett.100.013905.

[114] Mikhail I. Shalaev, Wiktor Walasik, and Natalia M. Litchinitser. "Optically tunable topological photonic crystal". In: *Optica* 6.7 (June 2019), pp. 839–844. DOI: 10.1364/OPTICA.6.000839. URL: http://www.osapublishing.org/optica/abstract.cfm?URI=optica-6-7-839.

[115] Frank Schindler et al. “Higher-order topological insulators”. In: *Sci. Adv.* 4.6 (May 2018), eaat0346. DOI: 10.1126/sciadv.aat0346. URL: https://doi.org/10.1126/sciadv.aat0346.

[116] Biye Xie et al. “Higher-order band topology”. In: *Nature Reviews Physics* 3.7 (2021), pp. 520–532.

[117] Motohiko Ezawa. “Higher-Order Topological Insulators and Semimetals on the Breathing Kagome and Pyrochlore Lattices”. In: *Phys. Rev. Lett.* 120 (2 Jan. 2018), p. 026801. DOI: 10.1103/PhysRevLett.120.026801. URL: https://link.aps.org/doi/10.1103/PhysRevLett.120.026801.

[118] Matthew Proctor et al. “Robustness of topological corner modes in photonic crystals”. In: *Phys. Rev. Research* 2 (4 Dec. 2020), p. 042038. DOI: 10.1103/PhysRevResearch.2.042038. URL: https://link.aps.org/doi/10.1103/PhysRevResearch.2.042038.

[119] E. Prince, ed. *International Tables for Crystallography*. International Union of Crystallography, Oct. 2006. DOI: 10.1107/97809553602060000103. URL: https://doi.org/10.1107/97809553602060000103.

[120] A. J. Heeger et al. “Solitons in conducting polymers”. In: *Rev. Mod. Phys.* 60 (3 1988), pp. 781–850. DOI: 10.1103/RevModPhys.60.781.

[121] Guido van Miert and Carmine Ortix. “On the topological immunity of corner states in two-dimensional crystalline insulators”. In: *npj Quantum Mater* 5 (23 2020), p. 63. DOI: 10.1038/s41535-020-00265-7. URL: https://www.nature.com/articles/s41535-020-00265-7.

[122] Matthew Proctor et al. “Higher-order topology in plasmonic Kagome lattices”. In: *Appl. Phys. Lett.* 118.9 (2021), p. 091105. DOI: 10.1063/5.0040955.

[123] Ashraf El Hassan et al. “Corner states of light in photonic waveguides”. In: *Nat. Photonics* 13.10 (Sept. 2019), pp. 697–700. ISSN: 1749-4893. DOI: 10.1038/s41566-019-0519-y.

[124] Hua Zhong et al. “Theory of topological corner state laser in Kagome waveguide arrays”. In: *APL Photonics* 6.4 (2021), p. 040802. DOI: 10.1063/5.0042975.

[125] Changhyun Han, Minsu Kang, and Heonsu Jeon. “Lasing at multidimensional topological states in a two-dimensional photonic crystal structure”. In: *ACS Photonics* 7.8 (2020), pp. 2027–2036. DOI: 10.1021/acsphotonics.0c00357.

[126] Ruirong Gong et al. “Topological photonic crystal fibers based on second-order corner modes”. In: *Opt. Lett.* 46.16 (2021), pp. 3849–3852. DOI: 10.1364/OL.430579.

[127] Yasutomo Ota et al. “Photonic crystal nanocavity based on a topological corner state”. In: *Optica* 6.6 (2019), pp. 786–789. DOI: 10.1364/OPTICA.6.000786.

[128] Xiao-Dong Chen et al. “Direct observation of corner states in second-order topological photonic crystal slabs”. In: *Phys. Rev. Lett.* 122.23 (2019), p. 233902. DOI: 10.1103/PhysRevLett.122.233902.

[129] Saoirse Freeney et al. “Coupling quantum corrals to form artificial molecules”. In: *SciPost Phys.* 9.6 (Dec. 2020), p. 085. DOI: 10.21468/scipostphys.9.6.085. URL: https://doi.org/10.21468/scipostphys.9.6.085.

[130] Ha-Reem Kim et al. “Multipolar lasing modes from topological corner states”. In: *Nat. Comm.* 11.1 (Nov. 2020), p. 5758. DOI: 10.1038/s41467-020-19609-9. URL: https://doi.org/10.1038/s41467-020-19609-9.

[131] Miguel AJ Herrera and Dario Bercioux. “Tunable Dirac points in a two-dimensional non-symmorphic wallpaper group lattice”. In: *Communications Physics* 6.1 (2023), p. 42.

[132] Oskar Vafek and Ashvin Vishwanath. “Dirac Fermions in Solids: From High-$T_C$ Cuprates and Graphene to Topological Insulators and Weyl Semimetals”. In: *Annu. Rev. Condens. Matter Phys* 5.1 (Mar. 2014), pp. 83–112. DOI: 10.1146/annurev-conmatphys-031113-133841. URL: https://doi.org/10.1146%2Fannurev-conmatphys-031113-133841.

[133] Mark Goerbig and Gilles Montambaux. “Dirac fermions in condensed matter and beyond”. In: *Progress in Mathematical Physics*. Progress in mathematical physics. Cham: Springer International Publishing, 2017, pp. 25–53. DOI: 10.1007/978-3-319-32536-1_2.

[134] Jinying Wang et al. “The rare two-dimensional materials with Dirac cones”. In: *Natl. Sci. Rev.* 2.1 (Jan. 2015), pp. 22–39. DOI: 10.1093/nsr/nwu080. URL: https://doi.org/10.1093%2Fnsr%2Fnwu080.

[135] Miriam Galbiati et al. “Group-IV 2D materials beyond graphene on nonmetal substrates: Challenges, recent progress, and future perspectives”. In: *Appl. Phys. Rev.* 6.4 (Dec. 2019), p. 041310. DOI: 10.1063/1.5121276. URL: https://doi.org/10.1063%2F1.5121276.

[136] Leticia Tarruell et al. “Creating, moving and merging Dirac points with a Fermi gas in a tunable honeycomb lattice”. In: *Nature* 483.7389 (Mar. 2012), pp. 302–305. DOI: 10.1038/nature10871. URL: https://doi.org/10.1038%2Fnature10871.

[137] Thomas S Gardenier et al. “$p$-orbital flat band and Dirac cone in the electronic honeycomb lattice”. In: *ACS nano* 14.10 (2020), pp. 13638–13644. DOI: 10.1021/acsnano.0c05747.

[138] Benjamin J Wieder et al. “Wallpaper fermions and the nonsymmorphic Dirac insulator”. In: *Science* 361.6399 (2018), pp. 246–251. URL: 10.1126/science.aan2802.

[139] Lukas Muechler et al. “Topological Nonsymmorphic Metals from Band Inversion”. In: *Phys. Rev. X* 6 (4 Dec. 2016), p. 041069. DOI: 10.1103/PhysRevX.6.041069. URL: https://link.aps.org/doi/10.1103/PhysRevX.6.041069.

[140] Dong-Choon Ryu et al. “Wallpaper Dirac Fermion in a Nonsymmorphic Topological Kondo Insulator: $PuB_4$”. In: *J. Am. Chem. Soc.* 142.45 (Oct. 2020), pp. 19278–19282. DOI: 10.1021/jacs.0c09442. URL: https://doi.org/10.1021%2Fjacs.0c09442.

[141] Chao-Xing Liu, Rui-Xing Zhang, and Brian K VanLeeuwen. “Topological nonsymmorphic crystalline insulators”. In: *Phys. Rev. B* 90.8 (2014), p. 085304. URL: https://doi.org/10.1103/PhysRevB.90.085304.

[142] Steve M. Young and Charles L. Kane. “Dirac Semimetals in Two Dimensions”. In: *Phys. Rev. Lett.* 115 (12 Sept. 2015), p. 126803. DOI: 10.1103/PhysRevLett.115.126803. URL: https://link.aps.org/doi/10.1103/PhysRevLett.115.126803.

[143] Ken Shiozaki, Masatoshi Sato, and Kiyonori Gomi. “$Z_2$ topology in nonsymmorphic crystalline insulators: Möbius twist in surface states”. In: *Phys. Rev. B* 91 (15 Apr. 2015), p. 155120. DOI: 10.1103/PhysRevB.91.155120. URL: https://link.aps.org/doi/10.1103/PhysRevB.91.155120.

[144] Zhijun Wang et al. “Hourglass fermions”. In: *Nature* 532.7598 (Apr. 2016), pp. 189–194. DOI: 10.1038/nature17410. URL: https://doi.org/10.1038%2Fnature17410.

[145] A. Alexandradinata, Zhijun Wang, and B. Andrei Bernevig. “Topological Insulators from Group Cohomology”. In: *Phys. Rev. X* 6 (2 Apr. 2016), p. 021008. DOI: 10.1103/PhysRevX.6.021008. URL: https://link.aps.org/doi/10.1103/PhysRevX.6.021008.

[146] Yasumasa Hasegawa et al. “Zero modes of tight-binding electrons on the honeycomb lattice”. In: *Phys. Rev. B* 74 (3 July 2006), p. 033413. DOI: 10.1103/PhysRevB.74.033413. URL: https://link.aps.org/doi/10.1103/PhysRevB.74.033413.

[147] Petra Dietl, Frédéric Piéchon, and Gilles Montambaux. “New Magnetic Field Dependence of Landau Levels in a Graphenelike Structure”. In: *Phys. Rev. Lett.* 100 (23 June 2008), p. 236405. DOI: 10.1103/PhysRevLett.100.236405. URL: https://link.aps.org/doi/10.1103/PhysRevLett.100.236405.

[148] S. Banerjee et al. “Tight-Binding Modeling and Low-Energy Behavior of the Semi-Dirac Point”. In: *Phys. Rev. Lett.* 103 (1 July 2009), p. 016402. DOI: 10.1103/PhysRevLett.103.016402. URL: https://link.aps.org/doi/10.1103/PhysRevLett.103.016402.

[149] G. Montambaux et al. “Merging of Dirac points in a two-dimensional crystal”. In: *Phys. Rev. B* 80 (15 Oct. 2009), p. 153412. DOI: 10.1103/PhysRevB.80.153412. URL: https://link.aps.org/doi/10.1103/PhysRevB.80.153412.

[150] Gilles Montambaux et al. “Winding vector: How to annihilate two Dirac points with the same charge”. In: *Phys. Rev. Lett.* 121.25 (2018), p. 256402. DOI: 10.1103/PhysRevLett.121.256402.

[151] B. Real et al. “Semi-Dirac Transport and Anisotropic Localization in Polariton Honeycomb Lattices”. In: *Phys. Rev. Lett.* 125 (18 Oct. 2020), p. 186601. DOI: 10.1103/PhysRevLett.125.186601. URL: https://link.aps.org/doi/10.1103/PhysRevLett.125.186601.

[152] Swapnonil Banerjee and Warren E Pickett. “Phenomenology of a semi-Dirac semi-Weyl semimetal”. In: *Physical Review B* 86.7 (2012), p. 075124.

[153] Narayan Mohanta et al. “Semi-Dirac and Weyl fermions in transition metal oxides”. In: *Physical Review B* 104.23 (2021), p. 235121.

[154] YX Zhao and Andreas P Schnyder. “Nonsymmorphic symmetry-required band crossings in topological semimetals”. In: *Phys. Rev. B* 94.19 (2016), p. 195109. URL: https://doi.org/10.1103/PhysRevB.94.195109.

[155] ZF Wang, Bing Liu, and Wei Zhu. “Hourglass Fermion in Two-Dimensional Material”. In: *Phy. Rev. Lett.* 123.12 (2019), p. 126403. URL: https://doi.org/10.1103/PhysRevLett.123.126403.

[156] Shuo-Ying Yang et al. “Symmetry demanded topological nodal-line materials”. In: *Adv. Phys.: X* 3.1 (Jan. 2018), p. 1414631. DOI: 10.1080/23746149.2017.1414631. URL: https://doi.org/10.1080%2F23746149.2017.1414631.

[157] Sebastian Klemenz, Leslie Schoop, and Jennifer Cano. “Systematic study of stacked square nets: From Dirac fermions to material realizations”. In: *Phys. Rev. B* 101 (16 Apr. 2020), p. 165121. DOI: 10.1103/PhysRevB.101.165121. URL: https://link.aps.org/doi/10.1103/PhysRevB.101.165121.

[158] Sebastian Klemenz et al. “The Role of Delocalized Chemical Bonding in Square-Net-Based Topological Semimetals”. In: *J. Am. Chem. Soc.* 142.13 (Mar. 2020), pp. 6350–6359. DOI: 10.1021/jacs.0c01227. URL: https://doi.org/10.1021%2Fjacs.0c01227.

[159] Sunam Jeon and Youngkuk Kim. “Two-dimensional weak topological insulators in inversion-symmetric crystals”. In: *Phys. Rev. B* 105 (12 Mar. 2022), p. L121101. DOI: 10.1103/PhysRevB.105.L121101. URL: https://link.aps.org/doi/10.1103/PhysRevB.105.L121101.

[160] Chang-An Li et al. “Dirac states in an inclined two-dimensional Su-Schrieffer-Heeger model”. In: *Phys. Rev. Research* 4 (2 June 2022), p. 023193. DOI: 10.1103/PhysRevResearch.4.023193. URL: https://link.aps.org/doi/10.1103/PhysRevResearch.4.023193.

[161] Katsunori Wakabayashi et al. “Electronic and magnetic properties of nanographite ribbons”. In: *Physical Review B* 59.12 (1999), p. 8271.

[162] Mitsutaka Fujita et al. “Peculiar localized state at zigzag graphite edge”. In: *Journal of the Physical Society of Japan* 65.7 (1996), pp. 1920–1923.

[163] Kyoko Nakada et al. “Edge state in graphene ribbons: Nanometer size effect and edge shape dependence”. In: *Physical Review B* 54.24 (1996), p. 17954.

[164] J.H. Conway, H. Burgiel, and C. Goodman-Strauss. *The Symmetries of Things*. AK Peters/CRC Recreational Mathematics Series. Taylor & Francis, 2008. ISBN: 9781568812205. DOI: 10.1201/b21368.

[165] A Michael Glazer, Mois I Aroyo, and André Authier. “Seitz symbols for crystallographic symmetry operations”. In: *Acta Cryst.* 70.3 (2014), pp. 300–302. DOI: 10.1107/S2053273314004495.

[166] Edward McCann and Mikito Koshino. “The electronic properties of bilayer graphene”. In: *Rep. Progr. Phys.* 76.5 (2013), p. 056503. DOI: 10.1088/0034-4885/76/5/056503.

[167] Feng Liu and Katsunori Wakabayashi. “Novel Topological Phase with a Zero Berry Curvature”. In: *Phys. Rev. Lett.* 118 (7 Feb. 2017), p. 076803. DOI: 10.1103/PhysRevLett.118.076803. URL: https://link.aps.org/doi/10.1103/PhysRevLett.118.076803.

[168] Ansgar Graf and Frédéric Piéchon. “Berry curvature and quantum metric in $N$-band systems: An eigenprojector approach”. In: *Phys. Rev. B* 104 (8 Aug. 2021), p. 085114. DOI: 10.1103/PhysRevB.104.085114. URL: https://link.aps.org/doi/10.1103/PhysRevB.104.085114.

[169] Ruixiang Fei, Vy Tran, and Li Yang. “Topologically protected Dirac cones in compressed bulk black phosphorus”. In: *Phys. Rev. B* 91 (19 May 2015), p. 195319. DOI: 10.1103/PhysRevB.91.195319. URL: https://link.aps.org/doi/10.1103/PhysRevB.91.195319.

[170] Jimin Kim et al. “Two-Dimensional Dirac Fermions Protected by Space-Time Inversion Symmetry in Black Phosphorus”. In: *Phys. Rev. Lett.* 119 (22 Nov. 2017), p. 226801. DOI: 10.1103/PhysRevLett.119.226801. URL: https://link.aps.org/doi/10.1103/PhysRevLett.119.226801.

[171] Hoi Chun Po, Haruki Watanabe, and Ashvin Vishwanath. “Fragile topology and Wannier obstructions”. In: *Physical review letters* 121.12 (2018), p. 126402.

[172] Charles L Kane and Eugene J Mele. “Quantum spin Hall effect in graphene”. In: *Physical review letters* 95.22 (2005), p. 226801.

[173] Adrien Bouhon, Annica M Black-Schaffer, and Robert-Jan Slager. "Wilson loop approach to fragile topology of split elementary band representations and topological crystalline insulators with time-reversal symmetry". In: *Physical Review B* 100.19 (2019), p. 195135.

[174] Barry Bradlyn et al. "Disconnected elementary band representations, fragile topology, and Wilson loops as topological indices: An example on the triangular lattice". In: *Physical Review B* 99.4 (2019), p. 045140.

[175] Zhida Song et al. "All magic angles in twisted bilayer graphene are topological". In: *Physical review letters* 123.3 (2019), p. 036401.

[176] Jennifer Cano et al. "Topology of disconnected elementary band representations". In: *Physical review letters* 120.26 (2018), p. 266401.

[177] Zhi-Da Song, Luis Elcoro, and B Andrei Bernevig. "Twisted bulk-boundary correspondence of fragile topology". In: *Science* 367.6479 (2020), pp. 794–797.

[178] Valerio Peri et al. "Fragile topology and flat-band superconductivity in the strong-coupling regime". In: *Physical review letters* 126.2 (2021), p. 027002.

[179] Benjamin J Wieder and B Andrei Bernevig. "The axion insulator as a pump of fragile topology". In: *arXiv preprint arXiv:1810.02373* (2018).

[180] Zhijun Wang et al. "Higher-Order Topology, Monopole Nodal Lines, and the Origin of Large Fermi Arcs in Transition Metal Dichalcogenides X Te 2 (X= Mo, W)". In: *Physical review letters* 123.18 (2019), p. 186401.

[181] Yoonseok Hwang, Junyeong Ahn, and Bohm-Jung Yang. "Fragile topology protected by inversion symmetry: Diagnosis, bulk-boundary correspondence, and Wilson loop". In: *Physical Review B* 100.20 (2019), p. 205126.

[182] Anastasiia Skurativska et al. "Flat bands with fragile topology through superlattice engineering on single-layer graphene". In: *Physical Review Research* 3.3 (2021), p. L032003.

[183] Pranav Rao and Barry Bradlyn. "Effective action approach to the filling anomaly in crystalline topological matter". In: *Physical Review B* 107.19 (2023), p. 195153.

[184] Flore K. Kunst, Maximilian Trescher, and Emil J. Bergholtz. "Anatomy of topological surface states: Exact solutions from destructive interference on frustrated lattices". In: *Phys. Rev. B* 96 (8 Aug. 2017), p. 085443. DOI: 10.1103/PhysRevB.96.085443.

[185] Flore K. Kunst, Guido van Miert, and Emil J. Bergholtz. "Lattice models with exactly solvable topological hinge and corner states". In: *Phys. Rev. B* 97.24 (June 2018), 241405(R). ISSN: 2469-9969. DOI: 10.1103/PhysRevB.97.241405.

[186] Flore K. Kunst, Guido van Miert, and Emil J. Bergholtz. "Boundaries of boundaries: A systematic approach to lattice models with solvable boundary states of arbitrary codimension". In: *Phys. Rev. B* 99.8 (Feb. 2019), p. 085426. ISSN: 2469-9969. DOI: 10.1103/PhysRevB.99.085426.

[187] There are also other techniques for obtaining an analytical expression for the wave function associated to the end states of a one-dimensional lattice expressed by a tridiagonal tight-binding matrix, as the SSH model [189, 190, 191, 192, 193].

[188] Stephan Wong and Sang Soon Oh. "Topological bulk lasing modes using an imaginary gauge field". In: *Phys. Rev. Research* 3 (3 July 2021), p. 033042. DOI: 10.1103/PhysRevResearch.3.033042. URL: https://link.aps.org/doi/10.1103/PhysRevResearch.3.033042.

[189] S. Kouachi. "Eigenvalues and eigenvectors of tridiagonal matrices". In: *Electron. J. Linear Algebra* 15 (2006), p. 115. DOI: 10.13001/1081-3810.1223.

[190] C.M. da Fonseca. "On the eigenvalues of some tridiagonal matrices". In: *J. Comput. Appl. Math.* 200.1 (Mar. 2007), pp. 283–286. DOI: 10.1016/j.cam.2005.08.047. URL: https://doi.org/10.1016/j.cam.2005.08.047.

[191] Allan R. Willms. "Analytic Results for the Eigenvalues of Certain Tridiagonal Matrices". In: *SIAM J. Matrix Anal. Appl.* 30.2 (Jan. 2008), pp. 639–656. DOI: 10.1137/070695411. URL: https://doi.org/10.1137/070695411.

[192] S. Kouachi. "Eigenvalues and eigenvectors of some tridiagonal matrices with non-constant diagonal entries". In: *Applicationes Mathematicae* 35.1 (2008), pp. 107–120. DOI: 10.4064/am35-1-7. URL: https://doi.org/10.4064/am35-1-7.

[193] Nico Leumer et al. "Linear and nonlinear transport across a finite Kitaev chain: An exact analytical study". In: *Phys. Rev. B* 103 (16 Apr. 2021), p. 165432. DOI: 10.1103/PhysRevB.103.165432. URL: https://link.aps.org/doi/10.1103/PhysRevB.103.165432.